Geodätisch-geophysikalische
Arbeiten in der Schweiz

(Fortsetzung der Publikationsreihe
«Astronomisch-geodätische Arbeiten in der Schweiz»)

herausgegeben von der

Schweizerischen Geodätischen Kommission
(Organ der Akademie der Naturwissenschaften Schweiz)

Einhundertsechster Band
Volume 106

Automated micro-triangulation for high-precision fiducialization and alignment of particle accelerator components

Vasileios Vlachakis

2021

Adresse der Schweizerischen Geodätischen Kommission:

ETH Zürich
Institut für Geodäsie und Photogrammetrie
Eidg. Technische Hochschule Zürich
8093 Zürich
Switzerland

Internet: http://www.sgc.ethz.ch

ISBN 978-3-908440-53-6

Redaktion des 106. Bandes:
Dr. V. Vlachakis, J. Müller-Gantenbein, Prof. Dr. M. Rothacher
Druck: Print-Atelier ADAG, Zürich

VORWORT

Teilchenbeschleuniger gehören zu den Infrastrukturen mit den grössten Herausforderungen, wenn es um die Genauigkeit der Ausrichtung geht, die für die verschiedenen Beschleunigerkomponenten wie Magnete und Detektoren erreicht werden muss. Die Anforderungen werden für zukünftige Teilchenbeschleuniger wie den Compact Linear Collider (CLIC) oder den Future Circular Collider (FCC), die am CERN geplant werden, sogar noch anspruchsvoller. Um mit den höheren Genauigkeitsansprüchen umgehen zu können, müssen neue Messinstrumente und neue Methoden entworfen, entwickelt und getestet werden. Zusätzlich zur hohen Genauigkeit müssen diese neuen Messsysteme jedoch auch transportierbar sein, damit sie innerhalb des Beschleunigertunnels von Komponente zu Komponente verschoben werden können. Nur ganz wenige Lösungen für diese Problemstellung sind derzeit in Sichtweite.

Mit dem Projekt PACMAN (Particle Accelerator Component's Metrology and Alignment to the Nanometre scale), ein EU Marie Curie Initial Training Network, sind zwei dieser neuen Methoden sehr detaillierten Studien unterworfen worden. Eine dieser Methoden basiert auf der Frequency Scanning Interferometry (FSI) und wurde im Rahmen der Dissertation von Solomon Kamugasa intensiv studiert und getestet. Eine andere Lösung verwendet die Mikrotriangulation mit Theodoliten, wobei diese mit einer zusätzlichen Kamera und einer Bildverarbeitungssoftware ausgerüstet sind, um die Winkel zu den Zielen zu bestimmen, die auf den auszurichtenden Objekten montiert sind. Während die FSI-Methode eventuell etwas genauer ist, hat die Mikrotriangulation den Vorteil, dass sie direkt sowohl die Referenzpunkte auf einem Magneten als auch den Draht, der für die Bestimmung der Hauptachse des Magnetfeldes des Magneten gebraucht wird, im gleichen Koordinatensystem einmessen kann.

Es ist in der Tat das Ziel der Dissertation von Vasileios Vlachakis eine metrologische Lösung basierend auf der Mikrotriangulation für die Ausrichtung von Magneten (und anderen Komponenten) zu entwickeln und zu validieren. Während die Theodolite mit Bilderfassung bereits verfügbar waren, musste Vasileios Vlachakis (1) die Computer-Vision-Algorithmen entwickeln, um den gespannten Draht zu erkennen und seine genaue Position zu ermitteln, (2) neue Objekte wie Geraden und Kettenlinien für die Einmessung des Draht in die Ausgleichungsrechnung für Mikrotriangulationsnetze implementieren und (3) das gesamte Messsystem unter unterschiedlichen Bedingungen, was z.B. Temperaturveränderungen und Lichtverhältnisse angeht, testen.

Als Resultat realisierte Vasileios Vlachakis ein sehr leistungsstarkes und automatisiertes System für die exakte Ausrichtung von Beschleunigerkomponenten. Die hohe Präzision, Robustheit und Effizienz dieses Systems wurden bereits unter den speziellen Umweltbedingungen und der Raumknappheit im Tunnel des Large Hadron Collider (LHC) getestet. Die von Vasileios Vlachakis entwickelte, getestete und automatisierte Methode ist sehr allgemein gehalten und kann für eine Vielzahl von anderen Anwendungen, die eine hochgenaue Ausrichtung von Objekten im Bereich von einigen Mikrometern benötigen, eingesetzt werden.

Die SGK dankt sowohl dem Autor für den wertvollen Beitrag als auch der Schweizerischen Akademie für Naturwissenschaften (SCNAT) für die Übernahme der Druckkosten.

Prof. Dr. Alain Geiger
Institut für Geodäsie & Photogrammetrie
ETH Zürich

Prof. Dr. Markus Rothacher
ETH Zürich
Präsident der SGK

PREFACE

Les accélérateurs de particules font partie des infrastructures les plus exigeantes en matière de précision de l'alignement des composants comme les aimants et les détecteurs. Les exigences vont même encore augmenter pour les futurs accélérateurs en cours de planification au CERN, comme le Compact linear collider (CLIC) ou le Future circular collider (FCC). Afin de pouvoir gérer ces nouvelles exigences de précision, de nouveaux instruments et de nouvelles méthodes doivent être conçus, développés et testés. En plus d'une précision très élevée, ces nouveaux systèmes de mesure doivent être transportables afin d'être déplacés d'un élément de l'accélérateur à un autre. Seul un nombre très réduit de solutions sont actuellement envisageables pour répondre à cette problématique.

Avec le projet PACMAN (Particle accelerator component's metrology and alignment to the nanometre scale), qui s'intègre au Marie curie initial training network de l'Union européenne, deux nouvelles méthodes ont été soumises à une étude détaillée. Une de ces méthodes est fondée sur le principe de l'Interférométrie par balayage de fréquences (IBF) et a été étudiée et testée de manière intensive dans le cadre de la thèse doctorale de Solomon Kamugasa. Une autre solution utilise la microtriangulation par théodolites équipés d'une caméra additionnelle et d'un logiciel de traitement d'image afin de mesurer les angles vers les cibles installées sur les objets à aligner. Alors que l'IBF est quelque peu plus précise, la microtriangulation a l'avantage de mesurer à la fois les points de référence et le fil utilisé pour marquer l'axe magnétique des aimants et cela dans un système de coordonnées commun.

L'objectif de la thèse doctorale de Vasileios Vlachakis est donc de développer et de tester une solution métrologique, basée sur la microtriangulation, pour l'alignement des aimants et des autres éléments. Alors que les théodolites équipés de caméras étaient déjà disponibles, Vasileios Vlachakis a dû (1) développer un algorithme de vision par ordinateur afin de reconnaitre le fil tendu et déterminer sa position exacte, (2) implémenter de nouveaux objets, comme des droites et des chaines de segments droits, dans le logiciel de compensation de réseaux de microtriangulation et (3) tester le système complet dans diverses conditions, par exemple de température et de lumière.

Au final, Vasileios Vlachakis a réalisé un système puissant et automatisé pour l'alignement précis des éléments d'un accélérateur. La grande précision, fiabilité et efficacité de ce système ont d'ores et déjà été mises à l'épreuve dans les conditions environnementales particulières et l'espace confiné du Grand collisionneur de hadrons. La méthode développée, testée et automatisée par les soins de Vasileios Vlachakis est suffisamment générale pour être utilisée pour une pluralité d'applications en lien avec l'alignement d'objets au micromètre près.

La Commission géodésique suisse remercie l'auteur pour cette précieuse publication ainsi que l'Académie suisse des sciences naturelles pour la prise en charge des frais d'impression.

Prof. Dr. Alain Geiger
Institut de Géodésie et Photogrammetrie
ETH Zürich

Prof. Dr. Markus Rothacher
ETH Zürich
Président de la CGS

FOREWORD

Particle accelerators are among the most demanding infrastructures concerning the precision of the alignment required for the different components such as magnets and detectors. These requirements are even getting more challenging for future particle accelerators like the Compact Linear Collider (CLIC) or the Future Circular Collider (FCC) that are planned at CERN. To cope with the more stringent accuracy demands, new instrumentation and new methods have to be designed, developed and tested. In addition to being very accurate, these new measurement systems also have to be portable in order to move them from component to component along the accelerator tunnel. Only a few solutions to this problem are presently in view.

Within the project PACMAN (Particle Accelerator Component's Metrology and Alignment to the Nanometre scale), an EU Marie Curie Initial Training Network, two such methods were studied in detail. One of them is based on Frequency Scanning Interferometry (FSI) and was intensively studied and tested in the framework of the PhD thesis of Solomon Kamugasa. Another solution is making use of micro-triangulation with theodolite systems that are equipped with an additional camera and an image processing software to determine the angles to the targets mounted on the object to be aligned. Whereas the FSI method may be slightly more precise, the micro-triangulation has the advantage that it can directly measure both, fiducial points on the magnet as well as the wire used to measure the principle axis of the magnetic field of the magnet in the same coordinate system.

It is the objective of the PhD thesis of Vasileios Vlachakis to indeed develop and validate a metrology solution for the alignment of the magnets (and other components) using the micro-triangulation approach. Whereas the image-assisted theodolite systems were already available, Vasileios Vlachakis had to (1) develop computer vision algorithms to detect and measure the position of the stretched wire, (2) implement new objects such as lines and catenaries for the wire measurements into a micro-triangulation network adjustment and (3) test the entire system under different conditions concerning, e.g., temperature variations and light conditions.

As a result, Vasileios Vlachakis established a very performing and automated system for the accurate alignment of accelerator components. Its high accuracy, robustness and efficiency has already been demonstrated under the special environmental conditions and space limitations of the Large Hadron Collider (LHC) tunnel. The method developed, tested and automated by Vasileios Vlachakis is quite general and may be used in a variety of other applications, where a high-accuracy alignment of objects is required at the several micron level.

The SGC thanks the author for his valuable contribution as well as the Swiss Academy of Sciences (SCNAT) for covering the printing costs of this volume.

Prof. Dr. Alain Geiger
Institute for Geodesy and Photogrammetry
ETH Zürich

Prof. Dr. Markus Rothacher
ETH Zürich
President of SGC

Summary

Future particle accelerators demand a high-precision alignment, at the level of a few micrometres, in order to maintain high luminosity. The challenge for the fields of Surveying, Geodesy and Large-Scale Dimensional Metrology is to develop new technologies, methods and measuring systems that are capable of achieving the required precision, following the constraints imposed by the nature and magnitude of the application.

This thesis concerns the development, validation and precision evaluation of a portable metrology solution for fiducialization and alignment applications of particle accelerator components that are based on stretched wires. The proposed solution is based on the automated micro-triangulation method and utilizes image-assisted theodolite systems. One major novelty of the proposed methodology is the direct angle observations to the fiducial targets and the stretched wire, at the same time and location. Another important novelty is the least-squares adjustment of these observations according to a unified mathematical model, and in a single coordinate system.

The first objective of this study is the development of an image-processing algorithm that enables the detection and measurement, with sub-pixel precision, of the position of a stretched wire in the image. An important part of this objective is the implementation of the algorithm in accordance to the structure of the existing acquisition software, which is part of the employed QDaedalus measuring system.

The next objective is the experimental evaluation of the developed wire detection algorithm, which aims to ensure the precision and the robustness of the algorithm, and to define the influence that various parameters and conditions may have on the result of the wire measurement.

The performance evaluation of the wire detection algorithm demonstrated that the automated detection is capable of providing high-precision angle measurements with a standard deviation that is at least two times better than the angular accuracy specification of the employed theodolite. Moreover, the algorithm demonstrated excellent robustness against the variation of several parameters that are relevant to the detection process. However, it is shown that the variation of the ambient light conditions and the contrast between the wire and its background intensity in the image may introduce systematic errors to the measurements.

One of the most important objectives of this study is the formulation of an expanded mathematical model that integrates the angle observations to objects such as straight lines and catenaries into a standard triangulation network. An essential part of the objective is the development of a software that is capable of adjusting micro-triangulation networks with targets and stretched wires. This software enabled the simulation and the actual precision evaluation of such surveying networks.

The subsequent objective concerns the validation of the proposed method for magnet fiducialization applications and the experimental evaluation of its accuracy for close-range angle observations in a metrology room.

It is demonstrated that the fiducialization of a quadrupole magnet in a metrology room can be achieved with an accuracy of approximately 10 µm rms, with respect to a high-precision coordinate measuring machine. This result is comparable to the standard fiducialization method applied at CERN for such particle accelerator components.

The last objective of this study is the examination of the feasibility and the efficiency of the proposed method in the special environmental conditions and space limitations of the Large Hadron Collider tunnel for applications of particle accelerator components alignment.

In the Large Hadron Collider tunnel, the proposed micro-triangulation method provided precision of approximately 60 µm for a 95 % confidence level. This result refers to the horizontal offsets between the fiducial targets of the magnets and a stretched wire, for a 55 m long accelerator section. This level of precision is comparable to the standard alignment method at CERN, which is based on the ecartometry technique.

In conclusion, we successfully developed and evaluated a portable metrology solution that is remotely-controlled and able to perform fast, accurate, contactless and automated measurements to the fiducial targets and the stretched wire. From now on, these distinctive features enable the precise measurement of complex configurations with multiple wires being in various directions and height differences, which was not possible beforehand. Moreover, the proposed method is based on a rigorous mathematical model and — in combination with the employed measuring system — is able to provide the necessary accuracy for the fiducialization and the alignment of particle accelerator components for future accelerators, in the three dimensional space.

Finally, the remote operation and the high level of automation render the proposed methodology suitable for applications in hazardous environments. The upgrade of hardware components and the development of software tools will enhance the efficiency of the system, will reduce the preparation time and effort, and will improve the level of automation under demanding conditions, potentially resulting in higher precision.

Résumé

Les futurs accélérateurs de particules exigent un alignement de haute précision, de l'ordre du micromètre, afin de maintenir une haute luminosité. L'enjeu pour les domaines de la topographie, de la géodésie et de la métrologie des grandes dimensions est de développer de nouvelles technologies, des systèmes et des méthodes de mesure qui sont capables d'atteindre la précision requise en fonction des contraintes imposées par la dimension et la nature de l'application.

Cette thèse concerne le développement et l'évaluation de la précision d'une solution de métrologie portable pour les applications de fiducialisation et d'alignement de composants des accélérateurs de particules à base de fils tendus. La solution proposée est basée sur la méthode de micro-triangulation automatique et utilise des systèmes théodolites assistés par caméra. Les nouveautés de la méthodologie proposée incluent l'observation directe des deux cibles de référence et du fil tendu au même moment et au même endroit, et la compensation par la méthode des moindres carrés des observations sur la base d'un modèle mathématique unifié dans un système de coordonnées unique.

Le premier objectif de cette étude est le développement d'un algorithme de traitement d'image permettant la détection et la mesure, avec une précision de l'ordre du sous-pixel, de la position d'un fil tendu dans l'image. Une partie importante de cet objectif est la mise en œuvre de l'algorithme conformément à la structure du logiciel d'acquisition existant, qui fait partie du système de mesure utilisé.

L'objectif suivant est l'évaluation expérimentale de l'algorithme de détection de fils qui a été développé, visant ainsi à assurer la précision et la robustesse de l'algorithme et à définir l'influence que divers paramètres et conditions peuvent avoir sur la mesure des fils.

L'évaluation des performances de l'algorithme de détection de fils démontre que la détection automatisée fournit des mesures d'angle de haute précision avec un écart type qui est meilleur que les caractéristiques de précision angulaire du théodolite utilisé. De plus, l'algorithme a démontré une excellente robustesse face à la variation de plusieurs paramètres pertinents pour la détection. Cependant, il a été démontré que la variation des conditions d'éclairage ambiant et l'intensité du contraste entre le fil et le background de l'image peuvent introduire des erreurs systématiques dans les mesures.

L'un des objectifs les plus importants de cette étude est la formulation d'un modèle mathématique élargi qui intègre les observations d'angle effectuées sur des lignes droites et des chaînettes à un réseau de triangulation standard. Le développement d'un logiciel capable de compenser les réseaux de fiducialisation avec des cibles et des fils tendus est une partie essentielle de l'objectif qui permet d'évaluer la précision de tels réseaux de topométrie.

L'objectif suivant concerne la validation de la méthode proposée pour des applications de fiducialisation d'aimants et l'évaluation expérimentale de sa précision pour les observations d'angles à courte portée dans une salle de métrologie.

Il est démontré que la fiducialisation d'un aimant quadripolaire dans une salle de métrologie peut être réalisée avec une précision d'environ 10 µm rms, par rapport à une machine de mesure de coordonnées (CMM) de haute précision. Ce résultat est comparable à la méthode de fiducialisation standard appliquée au CERN pour de tels composants d'accélérateur de particules.

Le dernier objectif de cette étude est l'examen de la faisabilité et de l'efficacité de la méthode proposée dans des conditions environnementales particulières et des limitations d'espace du tunnel du grand collisionneur de hadrons LHC pour les applications d'alignement de composants d'accélérateur de particules.

Dans le tunnel du grand collisionneur de hadrons LHC, la méthode de micro-triangulation proposée a fourni une précision d'environ 60 µm à un niveau de confiance de 95 %. Ce résultat fait référence aux écarts horizontaux entre les cibles de référence des aimants et un fil tendu, pour un arc détecteur de 55 m de long. Ce niveau de précision est comparable à la méthode d'alignement standard du CERN, qui est basée sur la technique d'écartométrie.

En conclusion, nous avons développé et évalué avec succès une solution de métrologie portable qui est contrôlée à distance et capable d'effectuer des mesures rapides, précises, sans contact et automatisées directement sur les cibles de référence et sur le fil tendu. Pour la première fois, ces caractéristiques distinctives permettent la mesure précise de configurations complexes sur plusieurs fils se trouvant dans différentes hauteurs et orientations. De plus, la méthode proposée est basée sur un modèle mathématique rigoureux et, en combinaison avec le système de mesure d'alignement utilisé, est capable de fournir la précision nécessaire pour la fiducialisation et l'alignement de composants de l'accélérateur de particules pour les futurs détecteurs, dans l'espace tridimensionnel.

Finalement, les technologies appliquées qui permettent le fonctionnement à distance avec un haut niveau d'automatisation rendent cette méthodologie adaptée aux applications dans des environnements dangereux. La mise à niveau des composants matériels et le développement de logiciels outils amélioreront l'efficacité du système, réduiront le temps et les efforts de préparation et amélioreront le degré d'automatisation dans des conditions exigeantes, ce qui engendrera potentiellement une plus grande précision.

Contents

Chapter 1

Introduction

The topic of this thesis is relevant to the *Large-Scale Dimensional Metrology*, which directly refers to the field of *Particle Accelerator Alignment*. According to *Franceschini et al.* (2011), the term was introduced by *Berry* (1961). In the introduction of his paper about the precise measurements for the construction of the 7 GeV Proton Synchrotron at the Rutherford High Energy Laboratory in Harwell Oxford, United Kingdom, we read:

> *"[...] a field of development in which the hitherto separate skills of the surveyor and the engineering metrologist have been brought together in what is becoming known as 'Large-Scale Metrology'. Large-Scale Metrology means the measurement of dimensions usually undertaken by surveyors to limits normally associated with the workshop."*

This study is relevant to the *fiducialization* and to the *alignment* processes of particle accelerator components, which in our case is a prototype quadrupole magnet of the Compact Linear Collider (CLIC). Thus, in Section 1.1, we introduce the CLIC project, its alignment strategy and the tolerances, as they are currently considered. In Section 1.2, we describe the fiducialization process of a particle accelerator component, in our case of a quadrupole magnet, referring to state-of-the-art applications at CERN and other institutes. In this study we develop, validate and evaluate a novel approach for fiducialization and alignment applications based on the *triangulation* method — as considered in the fields of Surveying and Geodesy — which is introduced in Section 1.3. In Section 1.4, we present the QDaedalus measuring system; an image-assisted theodolite system that was employed in the experimental part of our study. Finally, in Section 1.5, we describe the motivation, the aim of the thesis and the methodology that we developed to accomplish the objectives, following the structure of the thesis in chapters.

1.1 The Compact Linear Collider (CLIC) project

The Compact Linear Collider (CLIC) is an international collaboration working on the design and the feasibility study of a multi-TeV, high-luminosity, linear, electron (e^-)–positron (e^+) collider. CLIC is based on a novel two-beam acceleration technique with accelerating field gradients of $100\,\mathrm{MV\,m^{-1}}$, which is 20 times higher than the Large Hadron Collider (LHC). A two-beam accelerator consists of a high-intensity electron *drive beam*, which is decelerated in sequential power extraction and transfer structures (PETS) in order to provide power for the accelerating structures (AS) of the *main beam*.

The CLIC conceptual design report (*Aicheler et al.*, 2012) proposes a three-stage development, which is more appealing for the physics society and more feasible by financial means (Figure 1.2a). The revised staging scenario — optimized after the discovery of the Higgs boson in the LHC experiments — foresees three main centre-of-mass energy stages at 380 GeV, 1.5 TeV and 3 TeV, with progressively increasing luminosity up to $2 \times 10^{34}\,\mathrm{cm^{-2}\,s^{-1}}$ for the final machine (*Boland et al.*, 2016).

In terms of dimensions, the two linear accelerators (*linacs*) are designed to measure about 20 km each, in the final stage, and to be placed in a narrow ∅5.6 m tunnel, at ap-

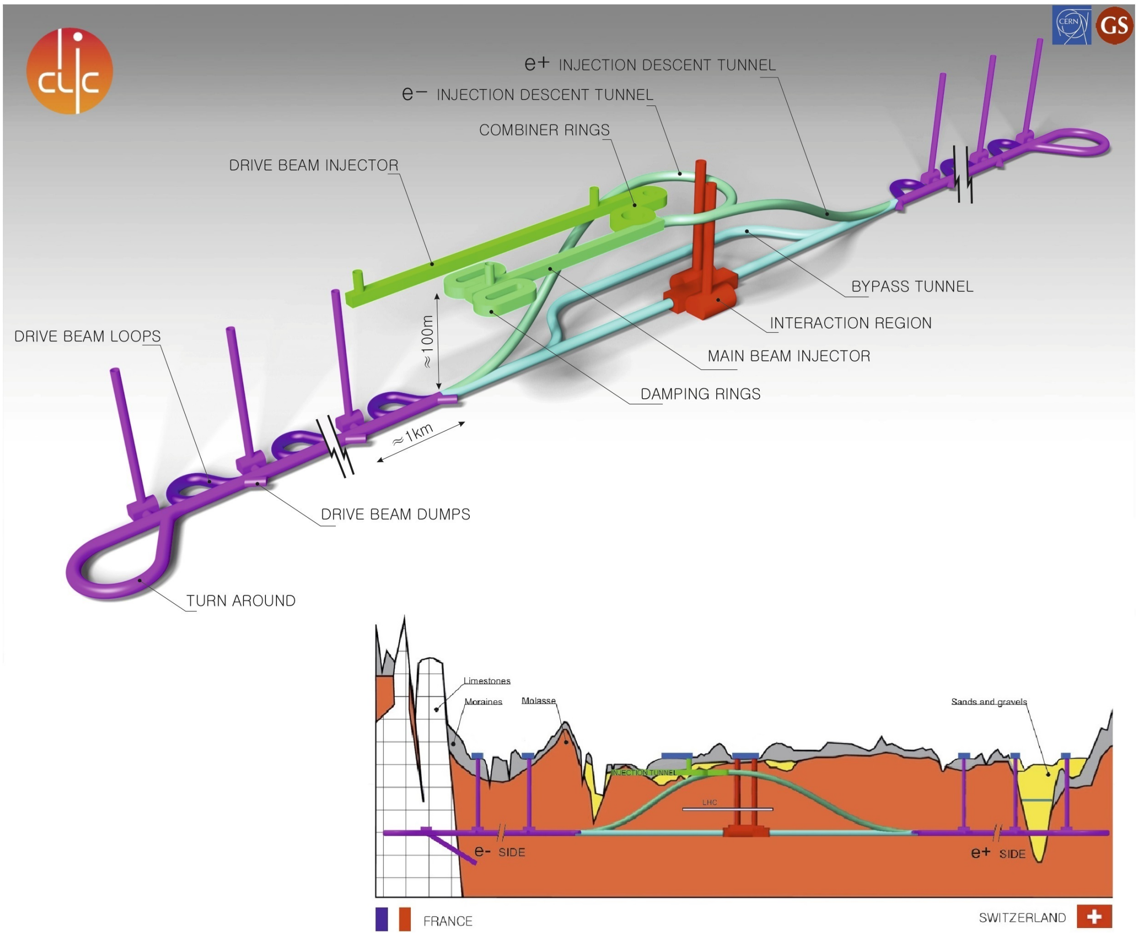

Figure 1.1: 3D schematic and vertical profile of CLIC (*CLIC@CERN*, 2018).

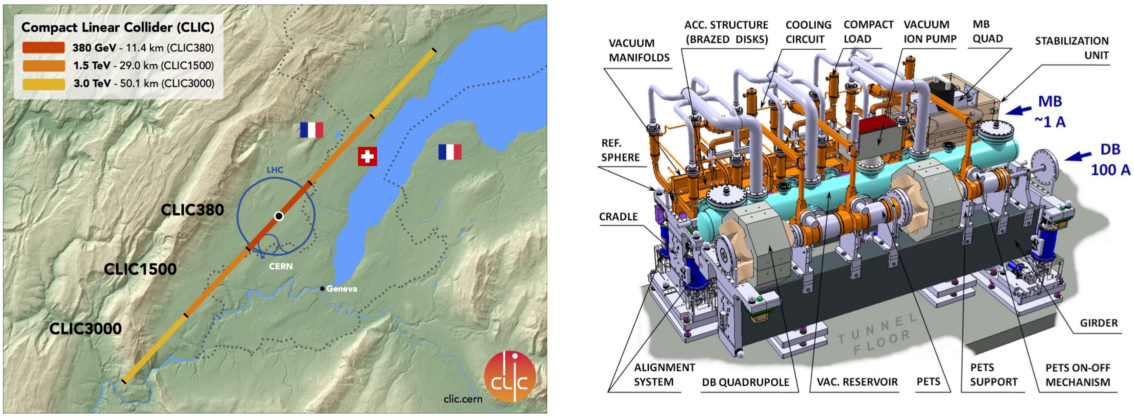

(a) (b)

Figure 1.2: (a) CLIC layout map (*CLIC*, 2017). (b) CLIC module (*Aicheler et al.*, 2012).

proximately 100 m to 150 m below the surface (Figure 1.1). The linacs will consist of about 21 000 two-metre-long modules, which will host hundreds of thousands of components such as quadrupoles and accelerating cavities (Figure 1.2b).

The size, the number of components, the tunnel environmental conditions and the complexity of such accelerators make their design, development, construction and operation a very challenging procedure for the scientific and engineering community. In particular, for the fields of Surveying, Geodesy and Large-Scale Dimensional Metrology the challenge lies in the positioning of the components and the monitoring of the alignment within tight tolerances at the level of a few micrometres.

1.1.1 Alignment tolerance

The *High energy* and the *high luminosity* are two key characteristics of particle accelerators and colliders. Collisions at high centre-of-mass energy increase the discovery potential for Physics beyond the *Standard Model*, while high luminosity provides high event rates that are extremely important for rare physics processes.

Luminosity $\mathcal{L}$ is a measure of the particles interaction probability. It determines the accelerator performance and it is expressed in units of $\mathrm{m^{-2}\,s^{-1}}$.

$$\mathcal{L} \propto \frac{N_{p^+} \cdot N_{p^-}}{4 \cdot \pi \cdot \sigma_x^* \cdot \sigma_y^*} \cdot N_b \cdot f_r \tag{1.1}$$

where

N_{p^+}, N_{p^-}		are the numbers of particles for each bunch.
N_b		is the number of bunches per pulse.
f_r	$[\mathrm{s^{-1}}]$	is the bunch frequency.
σ_x^*, σ_y^*	[m]	are the horizontal and the vertical beam sizes at the interaction point.

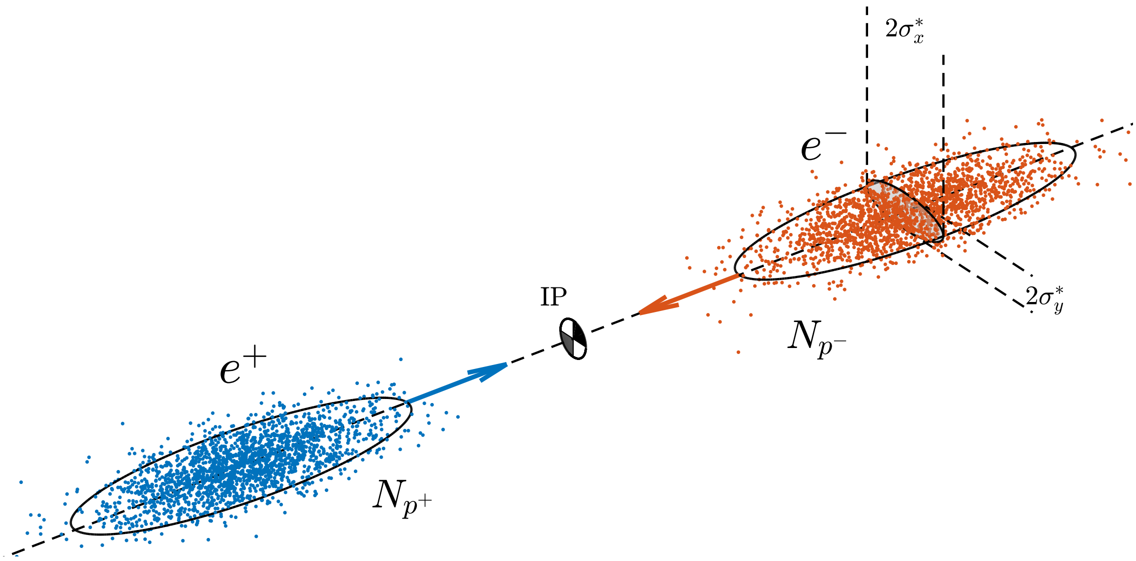

Figure 1.3: Bunches of electrons (e^-) and positrons (e^+) colliding at the interaction point (IP) (remake from *Wille and McFall* (2000)).

According to Equation 1.1, the luminosity is inversely proportional to the beam size in the transverse plane (Figure 1.3) at the interaction point (IP). For the last stage of CLIC the designed beam size at the interaction point has the extremely small values of approximately 40 nm and 1 nm for the σ_x and σ_y, respectively (*Boland et al.*, 2016).

The beam size σ at any point s of the beam can be written in relation to the beam transverse emittance ε (expressed in units of m^2) and to the beta function β.

$$\sigma(s) = \sqrt{\varepsilon \cdot \beta(s)} \tag{1.2}$$

The beta function β —also known as the amplitude function— is the envelope of all particle trajectories and describes the shape of the beam in space at any point of the beam orbit (Figure 1.4a). The beam emittance ε is defined as the area of the beam phase space divided by the constant π (Figure 1.4b). Moving along the *linac*, the phase-space ellipse semi-axes change size and orientation, according to the beta function, while the area of the ellipse, i.e., the emittance, is conserved, according to Liouville's theorem (*Wille and McFall*, 2000). This theorem states that, under the influence of conservative forces, the particle density in phase space, and therefore, the emittance remain constant (*Wiedemann*, 2007).

In practice, the emittance of a beam is not always conserved. It increases when the phase space deviates considerably from an elliptical shape. This happens when there are nonlinearities in the beam guiding system, which cause transverse kicks (*Kleeven et al.*, 1993). For example, when a particle passes through a misaligned quadrupole it experiences a dipole field, which causes a transverse kick. This kick distorts the particle trajectory and results in an emittance growth, which leads to beam losses and a reduced luminosity.

Tightening the alignment tolerance aims at reducing the magnitude of the misalignment, and as a consequence, at mitigating the emittance growth in order to preserve an ultra-small beam size and to increase the luminosity. For future accelerators, such as

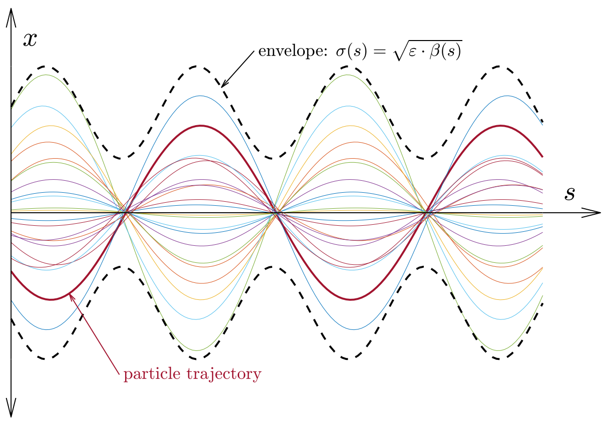

(a)

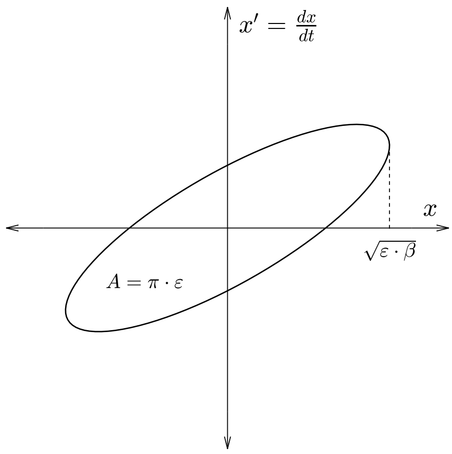

(b)

Figure 1.4: (a) Particle beam envelope function. (b) Particle beam transverse emittance (remake from *Wille and McFall* (2000)).

CLIC, this can be realized with a beam-based alignment, after the precise pre-alignment of the components at the level of 10 µm over a sliding window of 200 m (*Mainaud Durand*, 2004a), and according to the proposed strategy described next.

The required level of precision for CLIC is about an order of magnitude higher than that of the existing colliders. For example, the radial and vertical final pre-alignment (smoothing) tolerance for LHC is at the level of 0.15 mm over a distance of 150 m (*Brüning et al.*, 2004). Eventually, the required high-precision paves the way for research and development in the domains of Large-Scale Dimensional Metrology and Particle Accelerator Alignment.

1.1.2 Alignment strategy

The alignment procedure of a particle accelerator involves various steps in order to accurately place a component in its nominal position and orientation. The main goal is to align the functional axis (e.g., magnetic axis) or the functional centre (e.g., radio frequency cavity centre) of a component with respect to another component or a reference frame.

After years of studies, mainly carried out by the Large-Scale Metrology group at CERN, a proposed alignment strategy for CLIC was included in the CLIC Conceptual Design Report (*Aicheler et al.*, 2012). A non-exhaustive list of references are summarized in *Aicheler et al.* (2012) includes: *Becker et al.* (2003); *Mainaud Durand* (2004a); *Mainaud Durand and Touzé* (2006); *Mainaud Durand et al.* (2010), and in the doctoral dissertation of *Touzé* (2011).

Here, we briefly describe the steps of the pre-alignment process, which takes place in the accelerator tunnel. The step that concerns the fiducialization of the components, which is more relevant to this study, is further analyzed in Section 1.2.

Pre-alignment

Before any attempt for alignment, a geodetic coordinate reference frame should be defined, together with a geoid model and a local 3D Cartesian coordinate system. The CLIC alignment could be based on the existing systems created for the LHC alignment. These are the CERN Geodetic Reference Frame (CGRF), with its related geoid model, and the CERN Coordinate System (CCS) (*Jones*, 2000). Updates of these systems may be needed in order to increase the accuracy in the expanded working area of CLIC. As a consequence, relevant studies have been executed in collaboration with other institutes, e.g., the doctoral study of *Guillaume* (2015), which examines the determination of a precise gravity field in the area of CLIC.

The geodetic reference system is realized by two surveying networks: the surface network and the underground network, which are linked through the access shafts using appropriate techniques (*Mayoud*, 1987; *Hugon*, 2010). The underground network will serve as the initial reference for the installation of the metrological reference frames that are dedicated to the accelerator pre-alignment (Figure 1.5).

The pre-alignment of CLIC will be based on two metrological reference frames.

1. The Metrological Reference Network (MRN) consists of overlapping stretched wires and it is considered to provide a precision of a few micrometres over 200 m. The MRN is installed with respect to the underground geodetic network and it is realized

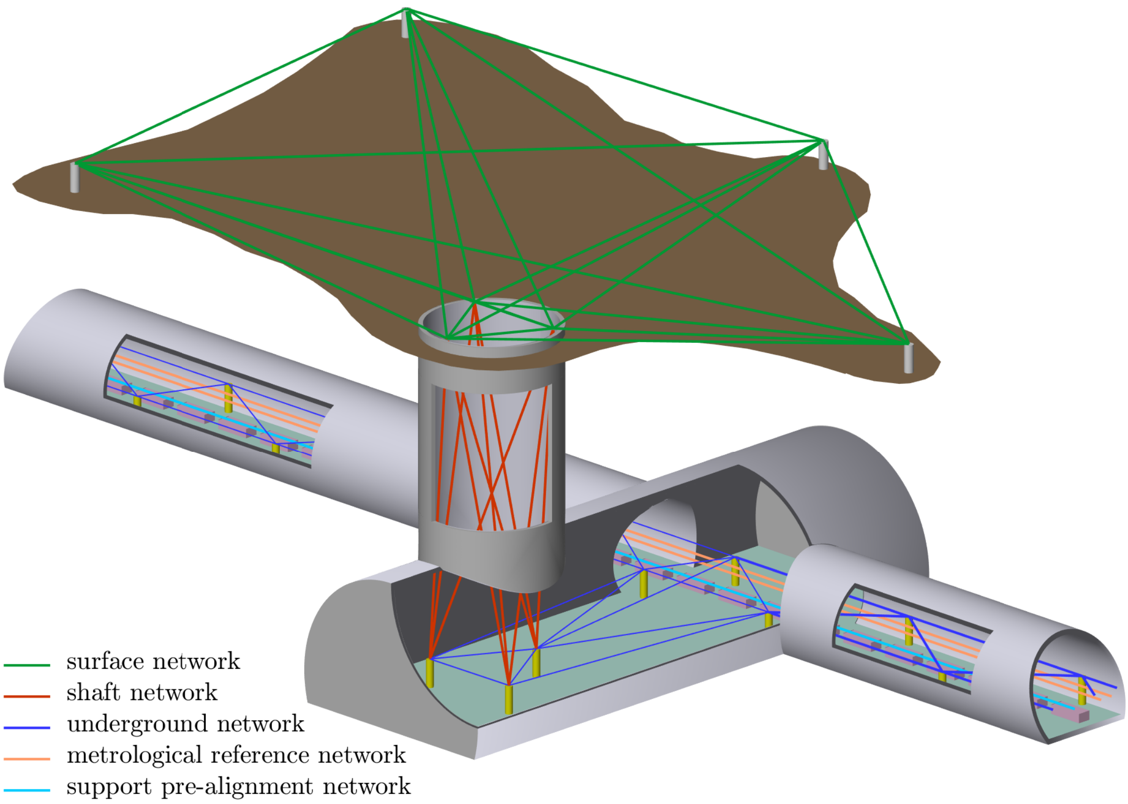

Figure 1.5: Geodetic control of a particle accelerator (remake from *Mayoud* (1987)).

by different types of measuring systems, such as wire positioning systems (WPS), hydrostatic levelling systems (HLS) and inclinometers (for more details see *Becker et al.* (2003) and *Mainaud Durand* (2004b)).

2. The Support Pre-alignment Network (SPN) is based on the stretched wires of the MRN and it is realized by wire positioning system (WPS) sensors. It will be used as a reference frame for the local alignment of the components and it is considered to enable a precision of a few micrometres over a length of 10 m to 15 m.

More details about the MRN and SPN can be found in *Aicheler et al.* (2012).

The pre-alignment of CLIC follows a two-step approach.

1. The initial mechanical pre-alignment with an accuracy of approximately 0.1 mm rms with respect to the MRN.

2. The active pre-alignment, which is only applied to the components with tighter tolerances, such as the Main Beam Quadrupole with pre-alignment precision of 17 µm for a sliding window of 200 m with respect to a straight line in space. The active pre-alignment consists of two recurrent sequential actions: the measurement of the current position of the component and the re-adjustment of the component to its nominal position with the use of actuators.

The precise pre-alignment guarantees that the first beam injected into the accelerator will pass through the components. Subsequently, the Beam Position Monitors (BPM) sense the particle beam and produce signals useful in the next step of the alignment chain, which is the beam-based alignment.

Although the currently proposed technical solution for the CLIC pre-alignment is based on stretched wires observed by WPS sensors, other solutions have been studied as alternatives or supplements to the main solution. Examples are the doctoral study of *Stern* (2016) on the development of a laser-based alignment system (LAMBDA) for CLIC (see also *Budagov et al.* (2014)), and the master study of *van Heijningen* (2012) on the precision improvement of the RASNIK alignment system.

1.2 Magnet fiducialization

As we have already mentioned, in a particle accelerator it is necessary to align the functional axis (or the functional centre) of a component with respect to another component or to a reference frame. In most cases, the functional axis (or centre) of a component is difficult to be materialized or it becomes inaccessible during and after the assembly of the accelerator. To cope with this difficulty, the functional axis (or centre) has to be in advance geometrically linked to accessible, visible or tangible targets located on the external surface of the component. This process is called *fiducialization* and the reference targets are called *fiducials* (Figure 1.6). The fiducialization process usually takes place in a laboratory and not in the installation area.

In the tunnel, during the installation and maintenance of an accelerator, the fiducials are used as reference in order to align a component to its nominal position and orientation. The component is required to be aligned with respect to either a reference frame or a nearby component, without requiring access to the functional axis.

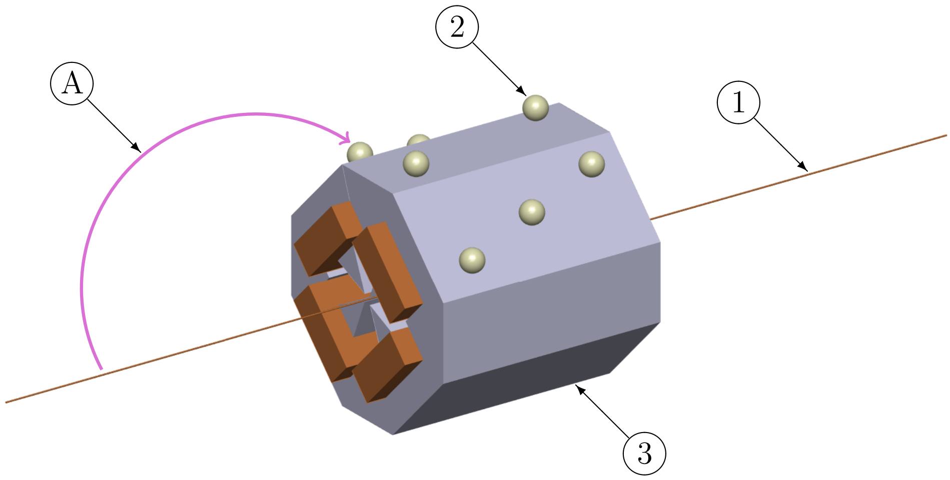

Figure 1.6: Concept of fiducialization. The goal is to establish a geometrical link (A) between the functional axis, materialized by a wire (1), and the fiducial targets (2), mounted on the external surface of a component, e.g., a quadrupole magnet (3).

The fiducialization may become a cost and time efficient process because, although it is time-consuming and requires special equipment, it can be performed for numerous components in parallel. In addition, after the fiducialization, the inaccessible or difficult to determine geometry, such as the magnetic axis, is represented by a few easy-to-access points. Thus, the productivity during the assembly phase of the accelerator can be increased significantly.

Apparently, the fiducialization is an important link in the alignment chain, contributing a considerable amount of the overall error budget. For example, the fiducialization error budget for the Main Beam Quadrupole of CLIC is estimated to be 10 µm (1σ), while the total pre-alignment error budget is estimated to be 17 µm (*Mainaud Durand et al.*, 2011).

High uncertainty or potential errors in the results of the fiducialization will propagate and affect the whole alignment process, no matter how precise the next alignment steps are. Moreover, a potential error in the later steps of the alignment can usually be corrected by the in-situ repetition of a few measurements, while an error in the fiducialization process might require to dismantle, transport and re-fiducialize the component in the laboratory.

Obviously, the geometrical relation between the functional axis and the fiducials may change, subject to mechanical stress and deformations caused by handling (e.g., transportation, lifting, mounting) and environmental factors (e.g., temperature variations). These changes may affect the performance of the accelerator, depending on their magnitude and the capability of the beam-based alignment system to detect them and counteract on them. Therefore, it is necessary to develop a portable fiducialization system in order to perform the fiducialization process in situ.

Without loss of generality, we will focus in the fiducialization of a quadrupole magnet, as this is part of the test bench used in the first case study of this thesis (more details in Chapter 5). The fiducialization process of a quadrupole is divided in two main steps:

(a) the determination of the magnetic axis, using a magnetic measurement technique, and

(b) the establishment of the geometrical link between the magnetic axis and the fiducial points, using a geometrical measurement technique.

The second step is covered by the field of Dimensional Metrology and is relevant to the subject of this thesis.

1.2.1 Magnetic measurement

A number of techniques have been used to define the magnetic axis of a quadrupole. The magnetic axis is defined as the locus of points within its aperture where the magnetic flux density is zero (*Arpaia et al.*, 2015). A review of the rotating coil technique and several stretched wire techniques can be found in *Wolf* (2005). Here, we briefly describe the vibrating wire technique that was further studied and enhanced by *Caiazza* (2017), and used in the PACMAN test bench (*Caiazza et al.*, 2017).

The vibrating wire technique, proposed by *Temnykh* (1997), is the last evolution based on previous stretched wire techniques. This technique employs a monofilament conducting wire that is stretched through the aperture of the magnet and it is fed by alternating current. The wire vibrates due to the *Lorentz* force when it is off the magnetic axis. The high sensitivity of this technique is based on the excitation of the natural resonance of the wire, which enhances the ratio between the magnetic field forces and the displacement (*Wouters et al.*, 2012).

In case of a quadrupole magnet, the position of the magnetic axis is determined as the point where the vibrating wire has the minimum oscillation while it is excited in the first resonance frequency. Correspondingly, the orientation of the axis (pitch and yaw) is determined by exciting the wire in its second resonance frequency. After a scanning procedure, the axis is calculated and the wire is placed back to the axis location and orientation in order to materialize the magnetic axis in space (*Petrone*, 2013).

The sensitivity of the vibrating wire technique is at the sub-micrometre level (*Walckiers*, 2011), while the reproducibility of the magnetic axis is usually reported to be at the level of 1 µm for the position (*Vranković et al.*, 2014), and below the milli-radian level for the orientation (*Wolf*, 2005). Apart from its outstanding accuracy, the technique is very flexible and it can be easily implemented for different types of magnets and aperture sizes (*Wouters et al.*, 2012). Moreover, the portability of the required equipment was demonstrated in the frame of the PACMAN project (*Caiazza et al.*, 2017).

1.2.2 Geometrical measurement

Different technologies and measuring systems have been used for the geometrical measurement of the fiducialization process, such as coordinate measuring machines (CMM), laser trackers, measuring arms, wire positioning systems (WPS), theodolites and interferometers (*Bottura et al.*, 2006; *Griffet*, 2010).

Various techniques related to the geometrical measurement of the fiducialization process are described next. We classify the techniques into three categories:

- the *indirect approach without wire measurements*, where the wire is not observed but its position is induced under assumptions,
- the *indirect approach with wire measurements*, where the wire is observed by sensors different than those observing the fiducials, and
- the *direct approach*, where the wire and the fiducials are observed by the same measuring system.

Indirect approach without wire measurements

In the fiducialization applications with the use of a stretched wire, the wire extremities are mounted on supports that consist of either two tangent ceramic spheres (*Caiazza et al.*, 2017) or a V-notch made by ceramic material (*Jain et al.*, 2008) or metal (*Le Bec*, 2016; *Yu et al.*, 2018).

In this approach, the wire position is not measured, but instead, is geometrically induced under assumptions (Figure 1.7). In brief, the position of the wire is calculated with respect to the wire support under the assumptions that the wire is a perfect cylinder, it has the exact nominal radius, it is not deformed and it touches the tangent spheres or the V-notch in only two points. Before the fiducialization, a calibration measurement geometrically links the wire support to the surveying targets that are rigidly mounted to the support. During the fiducialization process, these targets are linked by measurements with the fiducial points on the magnet.

The standard technique for magnet fiducialization at CERN involves two measuring systems: a coordinate measuring machnine (CMM) and a laser tracker. The CMM measures the surveying targets of the wire support with a tactile probe and the tangent spheres with an optical sensor (camera). Then, a geometrical calculation relates the surveying targets to the theoretical wire position under the aforementioned assumptions (see Figure 5.11a). This process is periodically repeated in order to validate the calibration parameters. During the magnet fiducialization, a laser tracker is used to measure the surveying targets of the wire support and the fiducials of the magnet. After appropriate coordinate transformations the wire axis is calculated with respect to the reference system of the fiducials, as described in (*Petrone*, 2013) and in Section 5.3.3.

Alternatively, the fiducialization with the *indirect approach without wire measurements* can entirely be performed with a CMM, as it is demonstrated in the PACMAN test bench (Section 5.2.1). Such a solution potentially offers a higher accuracy, given the fact that a CMM is typically more precise than a laser tracker. However, this solution is carrying along two important constraints: the lack of portability and limitations in the working volume.

A novel alternative technique based on the trilateration method and a multi-line frequency scanning interferometer (FSI) was also studied in the frame of the PACMAN project (*Kamugasa*, 2018). This technique offers a portable metrology solution with a sub-micrometre accuracy, however, it still follows the *indirect approach without wire measurements.*

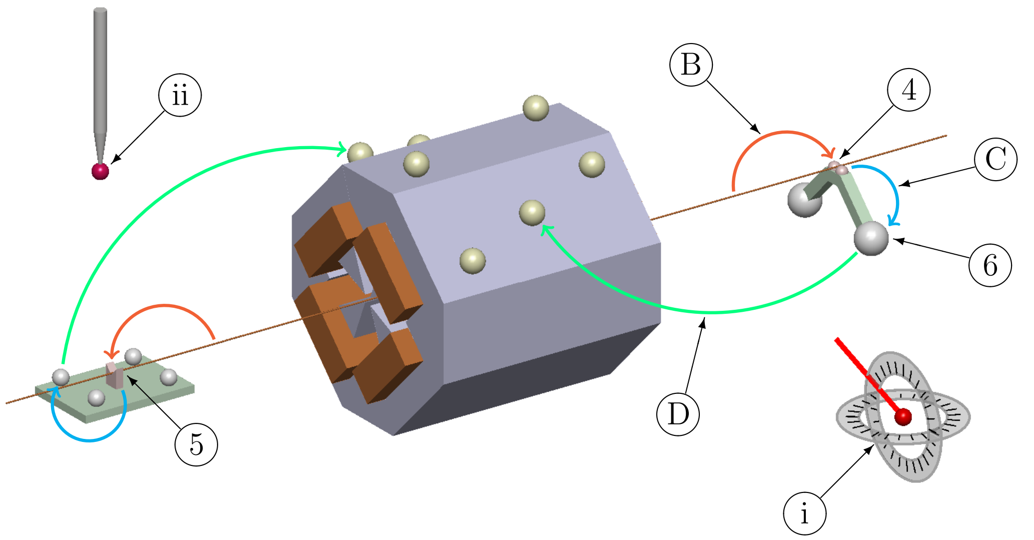

Figure 1.7: Indirect fiducialization without wire measurements. The wire position is induced B (under several assumptions) with respect to its support, which can be either a pair of tangent spheres 4, or a V-notch 5. A calibration measurement C links the wire support to the reference targets 6. Finally, an in-situ measurement D links the reference targets of the wire supports to the fiducial points on the magnet. This measurement is performed either with a laser tracker i or with a touch probe ii (e.g., with a CMM or a measuring arm), depending on the working volume. Arrows in the same color symbolize similar processes.

To summarize, there are three main disadvantages in the *indirect approach without wire measurements* that contribute to the uncertainty of the result:

(a) the induction —under assumptions— of the wire position with respect to the wire supports,

(b) the use of more than one measuring systems, leading to different reference systems that have to be linked with geometrical transformations, and

(c) the asynchronous performance of measurements in different laboratories and under different environmental conditions.

Indirect approach with wire measurements

In this approach, both the wire and the fiducial targets are observed. However, different sensors are employed to measure the wire and the fiducials, which implies the use of different reference systems. Therefore, calibration measurements and coordinate transformations are required in order to complete the fiducialization process. This is the reason for naming it as *indirect approach with wire measurements*.

Figure 1.8 depicts a collection of procedures, technologies and measuring systems that have been presented in the bibliography for this approach.

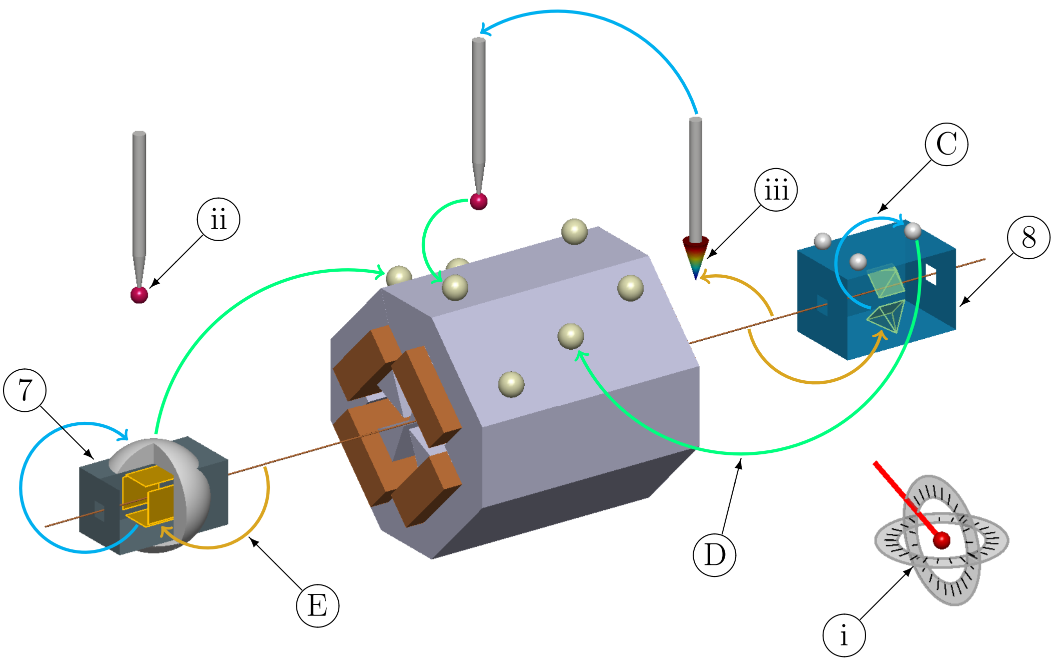

Figure 1.8: Indirect fiducialization with wire measurements. Capacitive 7 or optical 8 wire positioning systems (WPS) directly measure the wire position E. A calibration process C links the sensors with external targets. Finally, an in-situ measurement D (performed either with a laser tracker i, or with a touch probe ii) links the reference targets of the WPS with the fiducial points on the magnet. Alternatively, a con-focal sensor iii and a touch probe, both mounted on a CMM and calibrated in advance, can measure the wire position and the fiducials, respectively. Arrows in the same color symbolize similar processes.

An example of this approach is a novel method proposed at CERN (*Duquenne et al.*, 2014; *Mainaud Durand et al.*, 2014), involving two capacitive wire positioning systems (cWPS) that observe the wire extremities, and a laser tracker that links the WPS device reference points to the fiducials of the magnet.

Zhang et al. (2016) proposes a similar application based on WPS devices embedded in ceramic spheres. The WPS devices directly measure the position of the wire and a CMM measures the position of each sphere with respect to the fiducials of the magnet. In both applications, the WPS devices need to be in advance calibrated in a specialized calibration bench (*Herty et al.*, 2004).

Recently, the Leitz CMM at the Metrology Lab of CERN has been equipped with the PRECITEC LR optical sensor; a non-contact probe based on the con-focal technology. With this sensor, the CMM is able to perform the fiducialization by combining tactile measurement to the fiducials and non-contact measurements to the wire. The combination of these heterogeneous measurements is based on a calibration procedure performed in advance, for both CMM probes. More details about this process are presented in Section 5.3.3.

The use of different measuring systems, which implies different types of observations in different reference systems, could be considered as a disadvantage of the *indirect approach with wire measurements*. The required sequential transformations between different reference systems potentially increase the uncertainty and prevent a rigorous and accurate estimation of the uncertainty of the overall process. In addition, the fact that the calibration process and the fiducialization measurements are not performed at the same time and at the same location potentially results in higher uncertainties due to environmental variations.

Direct approach

In the *direct approach*, the wire and the fiducials of the magnet are measured by the same sensor, in the same reference system, at the same time and location (Figure 1.9).

In this thesis, we propose a method based on triangulation, using image-assisted theodolite systems. According to the *direct approach* at least two theodolites observe both, the fiducials and the wire, and measure horizontal and vertical angles to the targets. The method is further described in Section 1.5, where the advantages and the disadvantages are analyzed.

Here, it is worth mentioning that theodolites have been already used in the past in various fiducialization applications (*Farkhondeh et al.*, 1991). In all cases, the standard triangulation method was applied, i.e., networks with angle observations only to the fidu-

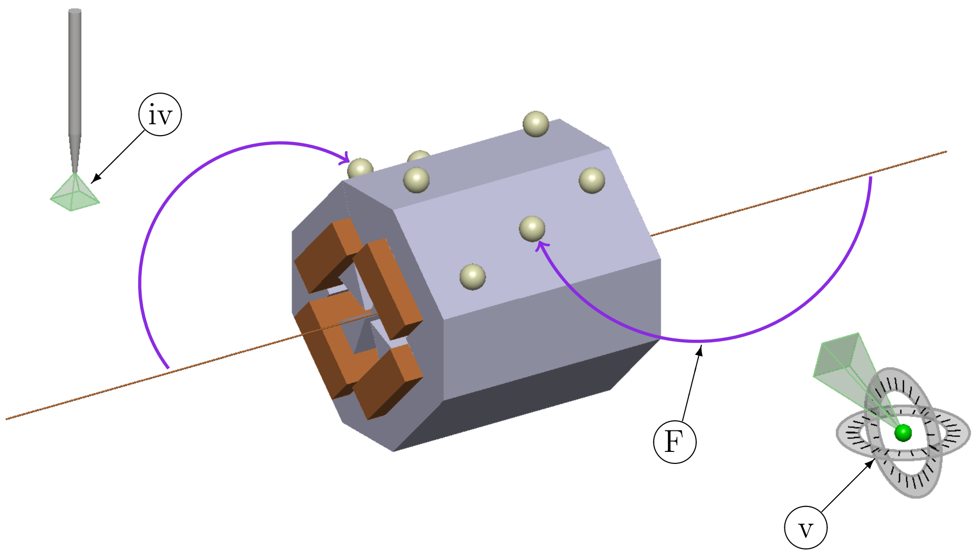

Figure 1.9: Direct fiducialization. The wire and the fiducial points are directly linked (F) with observations performed by a single measuring system, in a single reference system. This approach is based in optical sensors mounted either on a coordinate measuring machine (iv) or on image-assisted theodolite systems (v).

cial points. Those applications performed the fiducialization process in the sense of the *indirect approach without wire measurements.*

A photogrammetric system currently being developed at CERN for accelerator alignment applications (*Behrens et al.*, 2016; *Mergelkuhl et al.*, 2018) can also be used for magnet fiducialization, in the sense of the *direct approach.* Although this system has not been tested yet for fiducialization, it shares a lot of similarities with the proposed triangulation method with theodolites, especially in terms of methodology, working volume and portability.

In addition, at the Brazilian Synchrotron Light Laboratory (LNLS) *Geraldes et al.* (2016) and *Leão et al.* (2017) evaluated the performance of a CCD-based optical sensor mounted on a CMM for direct measurements to the wire and to the fiducials. The limited CMM working volume and the lack of portability remain the two main drawbacks of this solution.

1.3 Triangulation

Triangulation has a long history throughout the centuries. In this thesis, we choose to mention two important scientific achievements of the modern history (18^{th} century) relevant to the use of the triangulation method in the fields of Geodesy and Metrology.

In the years 1735–1744, two expeditions were launched — one in Lapland and the other in Peru — to measure the meridian arcs using the triangulation method. The difference in the lengths of these two arcs confirmed the oblate (flattening at the poles) versus the prolate (elongated at the poles) spheroid shape of the Earth. This measurement put an end to the controversy among the greatest scientists of that period (*Crandall*, 1906).

In the years 1792–1798, Jean-Baptiste Joseph Delambre (1749–1822) and Pierre Méchain (1744–1804) used triangulation to measure the length of the meridian arc of Paris, from Dunkerque to Barcelona. This measurement was used to define the *Metre*, in 1799, as 1/10 000 000 of the half of the Earth's meridian (*Torge and Müller*, 2012).

1.3.1 Principle

In this study, we are interested in the triangulation method as it has been developed and is applied in the field of Surveying and Geodesy, especially employing theodolites as angular measuring instruments.

Triangulation is a well-known method to estimate the unknown position of a *target*, based on horizontal and vertical angle measurements observed from known positions; the *stations.* The angular observations rely on optical measurements, typically in the visible spectrum. The physical model of the method assumes that the observations of one station are all made from a unique, stable point in space, and that the optical paths (rays) to the targets follow straight lines. The mathematical model is based on Euclid's 5^{th} postulate (axiom) that practically leads to the theorem that the sum of the three angles of the triangle is 180° in the Euclidean space.

In Figure 1.10, we see the estimation of the position of a target with the spatial intersection of the optical rays, which form a triangle. This is the simplest form of a triangulation surveying network in the three dimensions. More specifically, two theodolites (see Section 1.4.1) located at the known positions S_i and S_j observe the horizontal angles

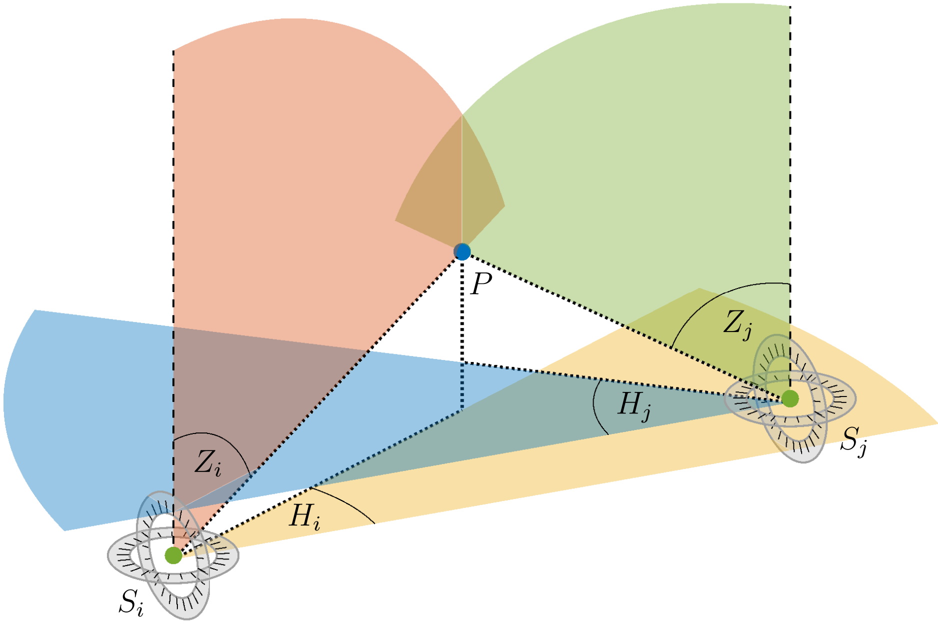

Figure 1.10: The simplest form of a triangulation surveying network in the three dimensions. Two theodolites (S_i, S_j) observe the horizontal angles (H_i, H_j) and zenith angles (Z_i, Z_j) to a point target P.

H_i and H_j and the zenith angles Z_i and Z_j, respectively, to the point target P. The horizontal position of P can be calculated by the horizontal angles, and then the vertical position can be calculated by one of the zenith angles.

The remaining zenith angle that it is not used for the calculation of the 3D coordinates of the point target P is redundant and inconsistent with the result, due to errors in the measurement. In this case, an estimator is required to adjust the observations by estimating the error of each measurement, and to compute the position of the point target using all the available observations. Traditionally, in the fields of Surveying and Geodesy a least-squares estimator is used to adjust the observations. In Chapter 4, the adjustment theory of triangulation surveying networks is presented in more detail.

Eventually, a surveying network offers a large number of redundant observations (in contrast to a trilateration network). For example, in a configuration similar to Figure 1.10, where four theodolites — with known position and orientation — observe five targets, there are 40 observations and 15 unknown coordinates, and therefore, 25 redundant observations or 25 *degrees of freedom*. A large number of degrees of freedom is extremely advantageous in the estimation of the reliability of the observations and in the estimation of the precision of the unknown parameters.

Actually, the triangulation method can precisely define the relative position of the points in a network of angle observations. However, it cannot provide any information about the scale — i.e., the actual size — of the network due to the fact that only angles are observed. This drawback can be resolved with the use of external scale information given either by complementary distance measurements or by coordinate constraints.

1.3.2 Error sources

The triangulation observations are always subject to several systematic errors. Sources of error that are usually taken into account are related to: the instrument (e.g., manufacturing quality, calibration, etc.), the environmental conditions (e.g., temperature, humidity, etc.), the operator (e.g., targeting error due to light conditions, fatigue, etc.), the nature of the measurement (e.g., atmospheric refraction, gravity field, etc.), and various other conditions concerning the configuration (e.g., stability and deformation of the instrument and the tripod, etc.). More detailed lists of the errors that are relevant to the triangulation measurement process, can be found in surveying textbooks such as *Wilson* (1971) and *Ogundare* (2016).

In this study, we include in the functional model, and we therefore estimate, the coefficients of three systematic errors that are relevant to the manufacturing of a theodolite, i.e., the collimation error, the tilting-axis error and the vertical-index error (Section 4.3.1). Moreover, we investigate the stability of an aluminium tripod in the temperature conditions of a metrology room, which is a potential source of error (Sections 5.3.1 and 5.4.1).

The triangulation measurements typically take place in the atmosphere. Hence, although the method assumes straight-line optical paths, it is true that the real optical rays deviate from the straight line as they pass through air masses with different densities, and therefore, different refraction indices. This systematic effect, known as atmospheric refraction, can be modeled and used either to correct the observations, or to augment the triangulation mathematical model.

To measure a triangulation network, the theodolite is installed leveled with respect to the local Earth's gravity field direction in order to be able to measure horizontal and vertical angles. The vertical axis of a modern theodolite can be aligned to the local plumb-line with an accuracy of about 0.1 mgon (or equivalently $1.5\,\mu\mathrm{m\,m}^{-1}$) (*LEICA*, 2002). As a consequence, the triangulation network is always linked to the gravity field, which is advantageous in case of applications where the distinction between the horizontal and vertical direction is important, e.g., in projects involving free water surfaces. Due to the shape of the Earth, the vertical axes of theodolites at different locations are not parallel. To compensate this effect, we use a model of the Earth's shape — or equivalently, a model of the Earth's gravity field — either to correct the observations or to augment the triangulation mathematical model.

Both, the atmospheric refraction and the Earth's curvature have a stronger influence on the height differences, and consequently, the vertical component of the 3D coordinates. Nevertheless, in this study we consider these two sources of errors to be negligible, given the short-range observations of a the micro-triangulation surveying networks presented in Chapters 5 and 6.

1.3.3 Automated micro-triangulation

Micro-triangulation is a specific type of the triangulation method that is applied in small volumes (up to a few metres range) and employs high-precision theodolites. Furthermore, micro-triangulation can achieve a precision at the level of a few micrometres for the network coordinates, under certain conditions and within a limited volume. The precision of the micro-triangulation method is expected to be $5\,\mu\mathrm{m}$ to $15\,\mu\mathrm{m}$ (1σ) in a working volume of 2 m to 5 m, considering the angular precision to be 0.5 arcsec (or approximately 2.4 $\mu m\, m^{-1}$).

There are three factors that contribute to the high precision of the micro-triangulation method, all related to short-range observations:

1. The angular precision of the theodolites, which can be also expressed in $\mu m\, m^{-1}$, indicates that the shorter the distance between a station and a target is, the more precise the estimated coordinates will be.

2. The atmospheric refraction can be considered as negligible for such short distances, depending on the required level of precision.

3. The assumption that the vertical axes of the stations in a small volume are parallel can be considered as valid, always depending on the required level of precision.

Moreover, the continuous development of the theodolites with modern technologies, such as the motorized steering and the automatic targeting, led to the diminution of various error sources. This is due to the capability of modern theodolites to automatically perform observations in a much faster rate and without an observer. Thus, the implementation of the automated micro-triangulation with high-precision robotic theodolites turns into a very attractive method to be used in industrial metrology applications, especially when non-contact measurements are required.

Many commercial metrology systems based on theodolites appeared in the 1990s (*Ingensand and Kyle*, 1992). However, they were gradually abandoned as a result of the increasing use of the laser tracker, which is one of the most recently developed instruments in the field of the large-volume industrial metrology.

In this thesis, we propose the use of the automated micro-triangulation based on specific advantages that this method offers (e.g., the contactless measurements, the automatic targeting, etc.) for particle accelerator components fiducialization and alignment applications (see also Section 1.4.1).

1.4 QDaedalus measuring system

In this thesis, we use the QDaedalus measuring system for the implementation of the micro-triangulation for magnet fiducialization and alignment applications. The key feature of the system is the reversible replacement of the ocular lens (eye-piece) with a CCD camera in an easy and rapid way. QDaedalus is a low-cost upgrade for robotic theodolites (or total stations), consisting of hardware and software components that are described in Sections 1.4.2 and 1.4.3, respectively.

A theodolite that is equipped with an imaging sensor (e.g., QDaedalus) is characterized as an image-assisted theodolite system (IATS) or as a *video-theodolite* (see also Section 1.4.1). In such a system, the image coordinates of a target, which are acquired with a detection algorithm (Section 1.4.4), are transformed to horizontal and vertical angles. This transformation is based on the calibration of the system, briefly described in Section 1.4.5.

The QDaedalus system was designed and developed primarily for astro-geodetic applications by the Geodesy and Geodynamics Lab of the Institute of Geodesy and Photogrammetry at ETH Zurich. During the last decade, the system has been used in a large variety of applications listed in Section 1.4.6.

1.4.1 Image-assisted theodolite systems

A theodolite is an instrument used to measure angles between targets. The modern history of the theodolite starts already in the 18^{th} century (*Crandall*, 1906). A theodolite mainly consists of two graduated circles (for the horizontal and vertical angle measurements), a targeting telescope and a level, which is used to level it with respect to the plumb line. A detailed description of the various parts that compose a theodolite can be found in *Breed et al.* (1971), while different types of theodolites are described in *Wilson* (1971).

An image-assisted theodolite system (IATS) is a combination of a theodolite with an imaging sensor (camera). *Luhmann et al.* (2014) presents the historical development of the *photo-theodolite*, which is dating back to the end of the 19^{th} century. Depending on the implementation, the camera is mounted either co-axially to the theodolite optical axis (*Hauth et al.*, 2012) or in a parallel axis (*Zhu et al.*, 2011). Nowadays, several IATS exist either as commercial products or as research prototypes. An updated list of both categories is presented in the doctoral dissertation of *Wagner* (2017).

The implementation of various modern technologies in the theodolites, such as piezo motors, liquid compensators and digital encoders, makes them very attractive for high-precision applications. These improvements help to perform fast, automated, reliable and high-precision measurements without the need of an observer. Especially the implementation of imaging sensors in the theodolites turns them into a suitable measuring system for a large variety of applications (see Section 1.4.6), mainly due to the following key features:

- **Automation**. The automatic measurement of surveying networks — simultaneously by many instruments — is feasible due to the automatic steering of the instrument and the automatic detection and measurement of a target without the need of an observer. Moreover, the automatic measurement of visible targets is possible without the need of a manual orientation of the targets (e.g., retro-reflective prisms) towards the instrument. The absence of the observer and in general of manual operations during the measurements contributes to a potential improvement of the precision, especially when precision at the level of a fer micrometres is required.

- **Variety of targets**. Automatic measurements can be performed to distant, fragile, hot or cold targets, also enabling the combination of tangible and non-tangible (e.g., printed) surveying targets, physical characteristics of an object (e.g., machined holes), or soft, sensitive and elastic objects that cannot be measured by contact measurements. Moreover, measurement can be performed to targets (or objects) with different geometries (e.g., spheres, crosses, ellipses, lines, corners, etc.), which can be active (e.g., LED), passive (e.g., ceramic spheres) or retro-reflective photogrammetric targets.

- **Versatility of the working environment**. Automatic measurements can be performed in harmful environments for humans, such as extreme temperature or high-level of ionizing radiation. Moreover, measurement can be performed in confined spaces by theodolites that are temporarily or permanently installed on the floor, on the walls or on the ceiling of the laboratory.

In the field of the particle accelerator alignment, a motorized, remotely controlled video-theodolite was already used back in 1967. A Kern DKM3-A theodolite equipped with a camera was used to perform surveying measurements in a high-radiation environment at the Brookhaven National Laboratory in New York (*Hopping and Jacobus*, 1967).

1.4.2 Hardware

The main component of the QDaedalus measuring system is the CCD camera. The original cage of the camera is dismantled and its components are re-assembled in a new cage that enables the theodolite to observe towards the zenith. The shape of the new cage differs, depending on the design of the specific theodolite in use (Figures 1.11a and 1.11b). Other components such as the focusing mechanism and the divergence lens should be added to the system, depending on the theodolite and on the application, in order to automatize and in general to improve the measurement performance.

(a) (b) (c)

Figure 1.11: Theodolites equipped with various QDaedalus system components. (a) A Leica TDA5005 with the CCD camera in the specially designed cage and with the focusing mechanism above. (b) A Leica Nova MS50 with the CCD camera in the specially designed cage and without the focusing mechanism. (c) A Leica Nova TS60 with the additional diverging lens in front of the objective lens (source: Jean-Frederic Fuchs).

A full list of the available components can be found in *Guillaume et al.* (2015) or in *Bürki et al.* (2010) and *Guillaume et al.* (2016a). Here, only the hardware components used for the purposes of this study are presented:

- **Camera**. The camera is the monochrome (sensitivity peak at about 500 nm) CCD sensor *Guppy F-080B*, provided by Allied Vision Technologies. The size of the frame is 1024×786 pixels, with 4.65 µm × 4.65 µm pixel size. The camera uses a Firewire (IEEE 1394a) connection, it can be externally triggered and it can provide up to 30 full frames per second (fps) and up to 60 fps for reduced frames.

- **Focusing mechanism**. The focusing mechanism was developed by *Knoblach* (2009) and it consists of a stepper motor, a conic gearwheel and a rubber toothed belt passing around the focusing knob of the theodolite. The mechanism is mounted on the theodolite, without any modification, and it is used only when the theodolite is not equipped with an internal focusing mechanism. In our case, it was used on the Leica TDA5005 theodolites (Figure 1.11a) for the measurements presented in Chapters 3 and 5.

- **Diverging lens**. A meniscus diverging lens with -4 m focal length should be plugged directly on the objective of the theodolite when the distance to the target exceeds 13 m. The additional lens is used to displace the focal plane by 4 mm towards the image sensor plane. In our case, the diverging lens was used on a Leica Nova TS60 theodolite (Figure 1.11c) for the measurements presented in Chapter 6.

Eventually, the system is operated by a computer, in which the QDaedalus software is installed and the various devices of the QDaedalus system are connected to.

1.4.3 Software

The software of the QDaedalus system has an important role in the measurement configuration, the observation acquisition and the data processing. It has the capability to control the hardware (e.g., the surveying instrument, the camera, the focusing mechanism, etc.) and to receive, store and process the acquired data (e.g., images, angles, time, etc.).

The QDaedalus software is based on open-source technology, it is written in the *C++* programming language and it is developed in the *Qt* development environment. It utilizes the *SQLite* library in order to create and manage SQL databases, and the *OpenCV* library for the digital image processing (*Guillaume et al.*, 2012).

Guillaume et al. (2015) presents the full functionality of the QDaedalus software in detail. Here, we briefly list the workflow with the required steps to be followed in order to configure and perform the measurement of a terrestrial surveying network, which is relevant to this study.

1. Create a new project or open an existing one.
2. Connect the sensors to be used (i.e., the theodolite, the CCD camera and the focusing mechanism).
3. Calibrate the CCD Camera with the use of a fixed, well-defined target.
4. Define the station from which the targets will be observed.
5. Define the target by setting the name, the direction, the suitable detection algorithm and the corresponding user-defined parameter values.
6. Define the measurement plan by selecting the number of observations and the number of repetitions (series) for each target.
7. Export the raw data or the reduced observations in various formats for further processing.

1.4.4 Detection algorithms

The QDaedalus software offers a variety of algorithms developed and implemented for the detection of different types of targets. Each algorithms has specific advantages and disadvantages depending on the characteristics of the target. The first four algorithms of the following list were developed prior to this study (*Guillaume et al.*, 2012), while the last one was developed by *Clerc* (2015), concurrently with this study, and it is also presented in *Guillaume et al.* (2016a).

- **Centre of mass operator** (Figure 1.12a). It is a simple and fast algorithm suitable for real-time applications. It is precise for active targets (e.g., LED). However, it is not suitable for passive or partially obscured targets, which can be considered as an important drawback of the algorithm.

- **Template least-squares matching** (Figure 1.12b). The algorithm is based on a template that should be manually determined in advance. Although the matching is very precise, the observed target should look identical with the template, and therefore, the algorithm cannot be used for precise measurements of targets that are observed from different angles of incidence.

- **Circle detection** (Figure 1.12c). It is used to measure spherical targets, which are always projected as circles on the image plane. The core of the algorithm is a robust least-squares fit of a circle on the edge of the target image. The target can be partially obscured and it should have a good contrast with its background.

- **Ellipse detection** (Figure 1.12d). Correspondingly to the circle detection, the ellipse detection algorithm is used to measure circular targets with a robust least-squares fit of an ellipse on the edge of the target image. It is applicable for photogrammetric targets or any precisely machined hole on a surface.

- **Multi-ellipses detection** (Figure 1.12e). The algorithm performs measurements on images depicting concentric ellipses. It employs multiple robust ellipse fits in the user-defined region of interest and returns the common centre of these ellipses.

(a) (b) (c) (d) (e)

Figure 1.12: Sample images of the target detection algorithms provided by the QDaedalus measuring system: (a) centre of mass operator, (b) template least-squares matching, (c) circle detection, (d) ellipse detection (*Guillaume et al.*, 2012), and (e) multi-ellipses detection (*Clerc*, 2015).

The performance of the circle detection algorithm is examined in Chapter 3. In addition, the circle detection algorithm is used for the validation measurements presented in Chapters 5 and 6.

1.4.5 Model of the optical system

During the measurement of a target, the QDaedalus software extracts the image coordinates of the target (x_t, y_t) with respect to the CCD-plane coordinate system $(\vec{e}_x, \vec{e}_y)$, while it records the readings of the angular encoders of the theodolite, which correspond to the horizontal and zenith angles (H_p, Z_p) of the theodolite principal (or optical) axis (Figure 1.13).

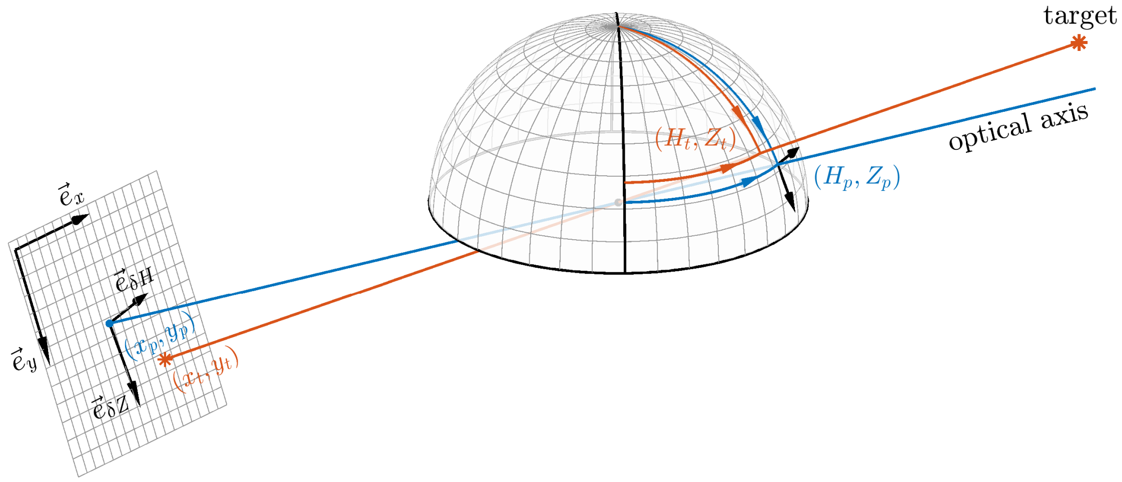

Figure 1.13: Transformation between the CCD space and the theodolite space (remake from *Bürki et al.* (2010)).

The principal point (x_p, y_p) is defined as the intersection of the principal axis with the CCD plane. This is the origin of an intermediate coordinate system that is oriented according to the tangents $(\vec{e}_{\delta H}, \vec{e}_{\delta Z})$ of the meridian and the parallel circles of the topocentric system. The relation between the CCD space and this intermediate system can be described by an affine transformation.

The direction of the target in the theodolite space, expressed with the horizontal and the zenith angles (H_t, Z_t), can be computed as

$$H_t = H_p - \arctan\Big(\frac{1}{\sin Z_p} \cdot \tan\big(a_{11} \cdot (x_t - x_p) + a_{12} \cdot (y_t - y_p)\big)\Big) \tag{1.3}$$

$$Z_t = Z_p - a_{21} \cdot (x_t - x_p) + a_{22} \cdot (y_t - y_p) \tag{1.4}$$

where

H_t, Z_t	are the horizontal and the zenith angles of the target.
x_t, y_t	are the image coordinates of the target image (in pixels).
H_p, Z_p	are the horizontal and the zenith angles of the principal point.
x_p, y_p	are the image coordinates of the principal point (in pixels).
a_{ij}	are the rotation and the scaling parameters of the affine transformation.

The parameters x_p, y_p, a_{11}, a_{12}, a_{21}, and a_{22} are estimated prior to the measurement with a calibration process that is described in *Bürki et al.* (2010) or *Guillaume et al.* (2015).

1.4.6 Applications

Despite the brief description of the QDaedalus system in this introduction, it becomes clear that QDaedadus is a versatile system regarding its hardware and software components, and its collection of target detection algorithms. For that reason, the QDaedalus system is a suitable solution for a large variety of applications and it has been successfully used for:

- **Astro-geodetic measurements**. The estimation of the deflection of the vertical (DoV) with a $0.1-0.2$ arcsec precision, by accumulating $20-30$ min of stellar observations (*Tóth and Völgyesi*, 2016; *Hauk et al.*, 2017).
- **Refraction coefficient studies**. The investigation of the fluctuation of the refraction coefficient, under various conditions, based on simultaneous reciprocal vertical angle measurements (*Hirt et al.*, 2010; *Frangez et al.*, 2017).
- **Large-volume industrial metrology**. Experimental evaluation measurements in the field of particle accelerator component alignment have demonstrated an accuracy at the level of 10 µm for the 3D coordinates of micro-triangulation networks, compared with results obtained with either a laser tracker or a coordinate measuring machine (CMM) (*Schmid et al.*, 2010; *Griffet*, 2012; *Guillaume et al.*, 2012).
- **Real-time deformation and vibration analysis**. The production of the 3D position time series, with sub-millimetre precision, of highly kinematic objects, owing to the capability of synchronizing several QDaedalus measuring systems in high-frequency observation acquisition (*Charalampous et al.*, 2015; *Hübscher et al.*, 2017).
- **Aircraft tracking**. The observation of the 3D trajectories of passenger aircrafts that are flying at about 5 km distance, with a precision of $1-2$ m, by angular measurements from at least two theodolites that are synchronized up to 20 Hz (*Nüssli and Salzgeber*, 2015; *Guillaume et al.*, 2016b; *Neff*, 2016).

1.5 Thesis overview

The present study is part of the *Particle Accelerator Components' Metrology and Alignment to the Nanometre scale* (PACMAN) research project (*PACMAN@CERN*, 2018).

The scientific goal of PACMAN is to propose, develop and validate an alternative reliable solution for the fiducialization process of CLIC, combining state-of-the-art technologies in the aforementioned scientific domains. The main achievements of the PACMAN project are summarized in *Mainaud Durand et al.* (2017).

1.5.1 Motivation

Future particle accelerators demand a high-precision alignment —at the level of a few micrometres— in order to maintain high luminosity, which provides high event rates that are extremely important for rare physics processes. High luminosity is ensured by preserving a small beam size at the interaction point —at the level of a few nanometres— and a low beam transverse emittance. The misalignment of the accelerator components causes unintentional kicks to the beam, which result in an emittance growth. Tighter alignment tolerances aim at reducing the magnitude of the misalignment, and therefore, at increasing the luminosity of future particle accelerators.

The alignment procedure involves various steps in order to accurately place an accelerator component in the nominal position and orientation. Fiducialization is the first and the most important step in the alignment procedure, contributing a considerable amount to the total alignment error budget. A high uncertainty or potential errors in the result of the fiducialization will be propagated and will affect the whole alignment chain, no matter how precise the next alignment steps will be.

The fiducialization process is divided into the magnetic and the geometrical measurements. The vibrating wire technique, based on a stretched wire, is widely used at CERN for the magnetic measurement, while an *indirect approach without wire measurements* is used for the geometrical link between the functional axis and the fiducial targets of the component (e.g., a quadrupole magnet).

The *indirect approaches with or without wire measurements* are usually time consuming with a low level automation and portability, and they are based on several measuring systems, employed at different times and locations. As a consequence, uncertainties and potential errors are accumulated. Moreover, the indirect approaches are not efficient for the fiducialization of tens of thousands of components, which is required in large particle accelerators such as CLIC.

For the fields of Surveying, Geodesy and Large-Scale Dimensional Metrology the challenge lies in the development of new technologies, methods and measuring systems capable of achieving the required precision, following the constraints imposed by the nature and the magnitude of the application.

1.5.2 Aim

The PACMAN project aims to propose an alternative solution for the fiducialization process of future accelerators. In this framework, the present study aims to develop, validate, and evaluate the precision of a metrology solution based on the automated micro-triangulation method and on image-assisted theodolite systems that can directly observe the fiducials and the stretched wire.

The system is required to be portable, remotely-controlled and capable of performing fast, accurate, contactless, automated measurements. A potential implementation of the proposed solution is presented in (Figure 1.14), where at least two theodolites create a micro-triangulation surveying network with angle observations to the fiducials and to the stretched wire. The proposed solution could also be used for alignment applications of particle accelerator components, in which stretched-wires are used as reference (*Quesnel et al.*, 2008).

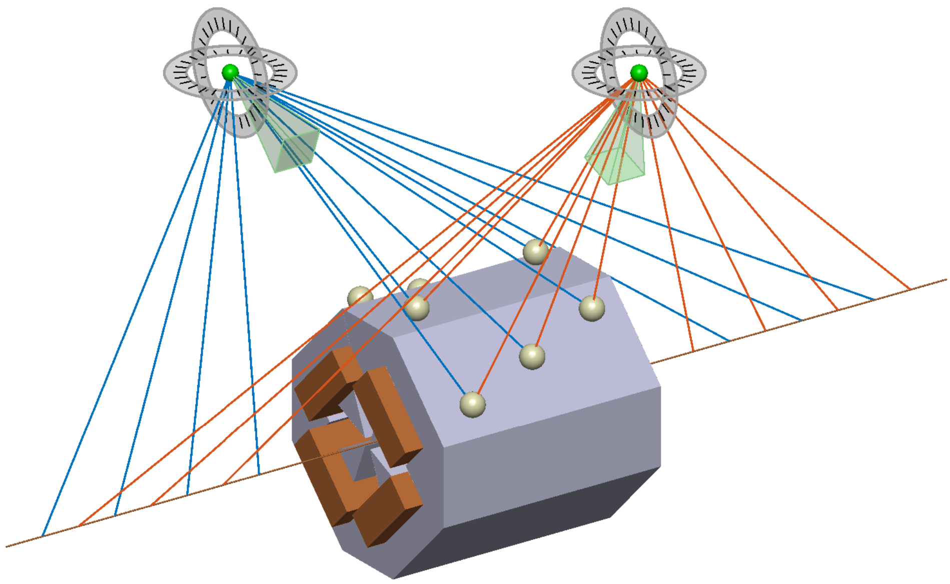

Figure 1.14: Conceptual design of the micro-triangulation method for a magnet fiducialization application. Theodolites equipped with the QDaedalus system are located around the component to be fiducialized. A micro-triangulation surveying network is created by the angle observations to the fiducials and to the stretched wire. The micro-triangulation network consists of horizontal and zenith angle observations to discrete targets (the fiducials) and to non-discrete points on the stretched wire.

1.5.3 Problem statement

The QDaedalus measuring system has been evaluated in the past for standard micro-triangulation networks, demonstrating very promising results (*Guillaume et al.*, 2012). The successful achievement of the aim of this study imposes the adaptation of both the micro-triangulation method and the QDaedalus system. The proposed methodology would be able to perform and analyze angle observations to the stretched wire, which is used as a standard tool for both, the fiducialization and the alignment procedures at CERN.

The proposed *micro-triangulation method with targets and stretched wires* goes beyond the standard method by also integrating angle observations to one or more wires into a standard surveying network. The particularity is that there are no distinguishable points on a wire, especially in the case that the wire has a uniform surface (Figure 1.14). Therefore, it is impossible to observe the same point from two or more stations, or even worse, in the two faces of the theodolite. Consequently, arbitrarily selected points on the wire are observed only once. To solve such networks, new angle observation equations and constraints should be integrated into the solution, according to a model that corresponds to the shape of the wire (e.g., straight line, parabola, hyperbolic cosine, etc.).

As a consequence, although the commercial surveying or geodetic software can adjust standard micro-triangulation networks that consist of points (instrument stations and targets), it is not possible to solve a network that contains observations to objects (e.g., a line, a catenary, etc.). To tackle this problem, we developed a software that can adjust integrated surveying networks, based on the least-squares estimation theory.

1.5.4 Objectives

The work required to successfully accomplish the aim of this study is divided into several objectives that basically correspond to the chapters of the present thesis.

The development and implementation of an image-processing algorithm to detect and measure the position of a stretched wire in the image is very important in order to achieve a high-level automation during the surveying network measurement. In **Chapter 2**, we analyze the developed wire detection algorithm and we describe in detail its implementation and integration into the QDaedalus software.

To ensure the precision and the robustness of the wire detection algorithm, in **Chapter 3**, we experimentally evaluated the influence that various parameters and conditions may have on the result of the wire measurement. In addition, the evaluation was expanded to the circle detection algorithm, which is used to measure the fiducial points.

Chapter 4 is dedicated to the formulation of the expanded mathematical model that integrates angle observations to objects, such as lines and catenaries, into a standard triangulation surveying network. Moreover, we describe various statistical tools used for the analysis of the reliability of the observations and the analysis of the precision of the unknown parameters and their product magnitudes.

The first experimental validation of the novel micro-triangulation method for magnet fiducialization took place in a metrology room, where the PACMAN test bench was installed. **Chapter 5** presents the results of several test measurements performed to evaluate the precision of the proposed methodology and the instrumentation, in the given laboratory conditions and in comparison to a coordinate measuring machine (CMM).

To examine the feasibility and the efficiency of the proposed method in the special environmental conditions and space limitations of the Large Hadron Collider (LHC) tunnel, we performed a second test measurement campaign, described in **Chapter 6**. As a result, we evaluated the precision of the proposed methodology for alignment applications and the agreement with the ecartometry, which is the standard alignment method used at the LHC tunnel.

Finally, in **Chapter 7**, we summarize the aims and the achievements of this study, and we discuss potential future developments of software and hardware tools that will facilitate the application of the proposed methodology and potentially increase its precision.

Chapter 2

Stretched-wire detection algorithm

In this chapter, we analyze the developed wire detection algorithm that is used to precisely measure the position and the orientation of the wire axis, in the image space. In Section 2.1, we introduce the concept of the wire detection and measurement, and we define the associated tasks. We also examine the wire as a physical object and the wire as it is depicted in an image. In Section 2.2, we review relevant wire detection applications and we establish that a detection that is based on the edges of the wire in the image is the most suitable method for our application. The developed wire detection algorithm is presented in Section 2.3. Finally, we describe in detail the implementation of the algorithm and its integration to the existing QDaedalus software in Section 2.4, before we highlight the most important concluding remarks in Section 2.5.

2.1 Introduction

As mentioned in Section 1.4, the QDaedalus measuring system will be used in this study to perform the automated micro-triangulation measurements for magnet fiducialization and alignment applications. During the fiducialization process, two detection algorithms will be used to automatize the acquisition of the angle observations to the fiducial points and to the stretched wire.

For the reference targets on the magnet (fiducials), which are materialized by ceramic spherical targets, we will use the *circle detection* algorithm. This algorithm is already implemented in the existing QDaedalus software (Section 1.4.4).

For the measurement of the stretched wire, we develop and integrate into the QDaedalus software a *wire detection* algorithm . The wire detection algorithm is able to work independently and cooperatively with any other detection algorithm provided by the software.

2.1.1 Objective

The objective is to develop a stretched-wire detection algorithm, dedicated to extract the image coordinates (in pixels) of a point that belongs to the wire axis (Figure 2.1). The pair of coordinates is then transformed into precise horizontal and zenith angle observations. More information about the transformation and its calibration process can be found in Section 1.4.5 or in *Bürki et al.* (2010). The precision of the wire position in the image space should be at the level of 0.1 pixels, or better, considering the corresponding precision of the theodolite angle measurements, which is approximately 2.4 $\mu m\,m^{-1}$, according to the manufacturer.

The orientation of the wire with respect to the 2D image coordinate system is also extracted but not used in the current implementation. This information could be valuable for further use, e.g., for a software tool that could be used to automatically steer the theodolite in order to follow the wire axis and measure points in given angular intervals.

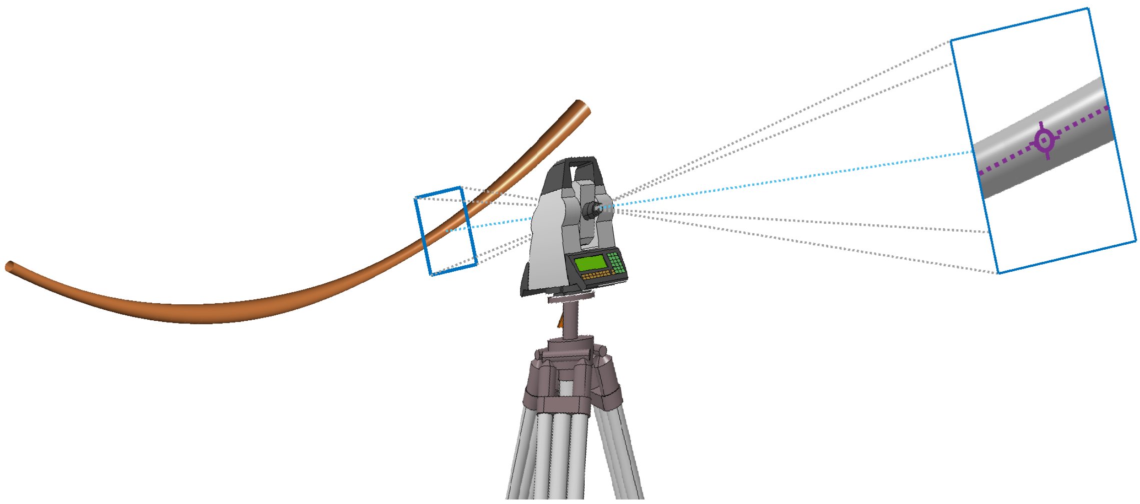

Figure 2.1: Concept of the streched-wire measurement with an image-assisted theodolite for micro-triangulation measurements.

2.1.2 Tasks

The development of the new algorithm can be divided into two tasks:

- The **design**, which has to satisfy several requirements relevant to: the nature of the measurement, the measuring system, the environmental conditions, the wire as a physical object (Section 2.1.3), and finally, the characteristics and the quality of the wire image (Section 2.1.4).
- The **implementation**, which has to be compatible with the QDaedalus software. This means to respect and comply with the constraints imposed by the structure of the existing software, and concurrently, to exploit the software infrastructure, such as the methods, the libraries and the graphical user interface in the best possible way.

2.1.3 The wire as a physical object

A monofilament Copper-Beryllium (CuBe) wire is used in the PACMAN test bench for the magnet fiducialization (Section 5.2.1). Here, we describe the geometrical features of the wire that are relevant to the image of the wire, as it is acquired by the specific optical system.

Size

The diameter of the wire is one of the factors that affect its visibility. In general, the visibility of the wire is a function of the diameter, the magnification of the theodolite telescope, the resolution of the imaging sensor, and the distance to the camera. For the PACMAN project, the diameter of the wire is chosen to be 100 µm with a specified manufacturer tolerance of $\pm 10\,\%$. This makes the wire width to be $3-5$ pixels for distances of 4 m to 2 m, respectively.

Form

The theoretical form of the wire is cylindrical. However, the longitudinal diameter variation ($\pm 10\,\%$) — due to the wire-drawing process — results in a shape that can be conceived as sequential truncated cones (conical frustums). This variation is expected to have extremely small-scale structures with respect to the wire length (Figure 2.1). As a result, the wire edges on the image will appear as converging or diverging straight lines. This phenomenon cannot be distinguished from that caused by the perspective view, owing to the angle of incidence between the camera and the wire axis.

Shape

For the fiducialization process the wire is mechanically stretched. The shape of the stretched-wire can be described as a hyperbolic cosine (catenary), under the assumption that only two forces act on the wire: the tension of the stretching-device and the gravity. The sagitta due to the gravity is about 10 µm to 20 µm for approximately 1 m long wire of this specific type and for the given applied tension. Nevertheless, the part of the wire depicted in an image (approximately 1.5 cm for a distance of 1 m to 2 m between the wire and the camera) can be considered as a straight line due to the narrow field of view (approximately 0.8° × 1.1°) of the theodolite optical system.

Surface

The surface of the wire is smooth, uniform and highly-reflective. This results in a gradual variation of the pixel intensity that enables the edge detection to successfully detect the edges between the wire and the background, given an adequate contrast and proper user-defined parameter values.

2.1.4 The image of the wire

To better understand the requirements that the algorithm has to fulfill, we examine the features and the quality of the image, and later, the geometrical characteristics of the depicted wire. Figure 2.2 shows a set of images captured by the QDaedalus measuring system mounted on a Leica TDA5005 theodolite. The five images are taken from different theodolite stations observing a wire at about 2 m distance.

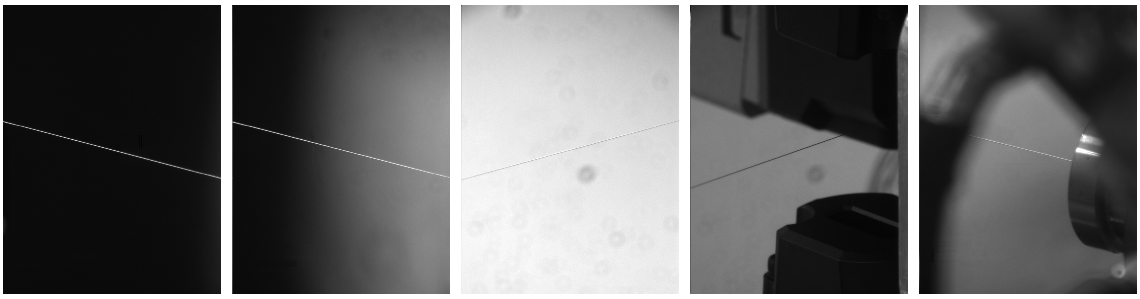

(a) (b) (c) (d) (e)

Figure 2.2: A representative set of images of a Copper-Beryllium wire (⌀100 µm) captured by the QDaedalus measuring system mounted on a Leica TDA5005 theodolite.

Image quality

In Figure 2.2, we notice that the resolution of the images is high enough to depict such a thin wire in the working volume of a few metres. The wire can easily be distinguished in the image, while it appears sharp and in good contrast with the background. Moreover, the images do not appear to be particularly noisy. Here, we focus in some general features of the wire images with regard to the laboratory conditions of the PACMAN test bench.

- **Illumination**
  The laboratory ceiling lights were the only available source of illumination for the micro-triangulation measurements in the metrology room. Neither a flashing light coaxial to the camera was used nor any other additional illuminating system. In Figure 2.2a, the wire appears to be directly illuminated, while in Figure 2.2d, the wire appears in the shadow of the surrounding objects.

Moreover, the light bodies are unevenly distributed and they are lacking diffusers. This causes spatial variations of the wire illumination and direct reflections of the light bulbs on the wire, depending on the angle of incidence (Figure 2.2c). In general, poor light conditions usually demand higher gain or ISO values on the sensor, which results in an increase of the image noise.

- **Image background**
  The background of the wire consists of various objects. These objects have different colors, they are in various distances from the wire, and they appear under different illumination. This results in a large variety of image background intensities, from very dark (Figure 2.2a) to very bright (Figure 2.2c). Occasionally, the wire appears in front of a gradient image background (Figure 2.2b).

  The image foreground and background usually appear blurred (Figure 2.2e) when the wire is in focus due to the shallow depth of field, which is estimated to be a few millimetres for distances of about 2 m to 4 m. In addition, the wire is hanging in the air a few decimetres away from the surrounding objects, and therefore, the shadow of the wire in the image background is not visible. A shadow of the wire would potentially appear as a second false wire, parallel to the real one.

- **Dust particles**
  The laboratory is designed for metrology measurements but it is not classified as a clean room. Therefore, during the fiducialization process, the wire attracts dust particles and fibers, floating in the laboratory. Due to the magnification of the theodolite telescope, these tiny bodies are visible in the image of the wire. Special care should be taken in the detection algorithm to prevent biases in the estimation of the wire axis due to such objects.

Geometrical characteristics of the depicted wire

The geometrical characteristics of the depicted wire (Figure 2.2) that are relevant to the detection procedure and have to be taken into consideration for the development of the wire detection algorithm are listed below.

- **Position**
  The wire always passes through the center of the image, owing to the functionality of the QDaedalus software. This is always recommended in order to mitigate the lens distortion effects.

- **Orientation**
  The wire appears in various orientations with respect to the image coordinate system. Theoretically, the wire can appear in the strictly horizontal or vertical orientation. For that reason, we should develop the wire detection algorithm to be resilient to numerical issues related to the orientation of a straight line.

- **Length**
  As mentioned earlier, the length of the wire depicted in the image is approximately 1.5 cm horizontally and 2.0 cm vertically for a distance of 1 m to 2 m. The depicted part of the wire is considered as a straight line, despite the catenary shape of the

entire wire. The wire can be obscured by other objects (see Figures 2.2d and 2.2e), and therefore, the user should be able to choose the part of the wire to be used for the detection and measurement.

- **Width**
  The thickness of the depicted wire is $3-5$ pixels for a distance of 4 m to 2 m, respectively. This depends on the camera resolution, the optical system of the theodolite, the diameter of the wire, and the distance between the camera and the wire. In fact, the wire occupies an extremely small portion of the area of the image. For this reason, it would be preferable to focus the detection algorithm on a part of the image (region of interest) in order to increase the speed of the detection.

- **Perspective view**
  Although the wire depicted in Figure 2.2 was stretched approximately horizontally, it appears in a perspective view due to the angle of incidence between the camera axis and the wire axis. In this case, the algorithm should be able to compute the wire axis, which bisects the two edge lines that are not parallel, but they converge (or diverge).

To summarize, we have to deal with a wire that is typically depicted in the centre of the image, it is easily distinguishable from the background, usually with sharp edges, and it appears in an arbitrary orientation as a straight line with a width of a few pixels.

2.2 Wire detection in computer vision

The term *computer vision* usually refers to the methods, algorithms and applications that are relevant to the extraction of spatial information from images. The field of the computer vision resembles the human optical and neural system, which is able to collect and analyze information by observing features such as shape, texture, color, shade, luminosity, parallax, etc.

Each person perceives information in a more-or-less different way, depending on the ability to receive the signal, the sensitivity to a particular signal, the interest in a special piece of information, etc. Correspondingly, there is a large variety of methods and techniques in the field of computer vision that are proposed to solve each particular problem, from very simple and intuitive to very complex and sophisticated.

2.2.1 Stretched-wire detection applications

There are several applications relevant to the detection of a wire or a cable through imaging techniques. Here, we choose to focus on applications that share two important characteristics with our application; they detect hanging (stretched) wires and they are based on optical images.

Power cable detection and mapping applications

The overhead electric power lines are the most common example of stretched wires (cables). These cables, being suspended by towers or poles, are following the catenary shape due to the Earth's gravity field.

There is a great interest in the *detection* and *mapping* of the power cables, mainly for two safety reasons: a) to avoid collisions by low altitude aerial vehicles like helicopters and unmanned aerial vehicles (UAV) (*Sanders-Reed et al.*, 2009), and b) to avoid explosive arc flashes (*Ishikawa et al.*, 2009) by establishing clearance with the ground, plantation, buildings or heavy machines.

The *airborne collision avoidance systems* can be categorised in image-based (passive) detection (*Nixon and Loveland*, 2005) and in radar-based (active) detection (*Silverman*, 1986), according to the employed technology. Various image-based detection applications are described in *Song and Li* (2014), *Fu and Lu* (2011), *Huang et al.* (2015), *Candamo and Goldgof* (2008) and *Candamo et al.* (2009).

The *power cable mapping applications* aim to measure the position of the wires with respect to the surrounding natural and built environment. These applications are mainly based on mobile mapping systems (*Ishikawa et al.*, 2009; *Chan et al.*, 2013) or on airborne light detection and ranging (LIDAR) systems (*McLaughlin*, 2006; *Jwa et al.*, 2009). Such applications fit the catenary shape to 3D point clouds acquired with ranging techniques in order to determine the position and orientation of the hanging wires.

The aforementioned applications share similar characteristics with the application of the present study, as well as they demonstrate some important differences:

- The image-based detection applications use either color, or black-and-white optical images acquired from low-altitude flights, while in our application we use only black-and-white images.

- Although the optical systems, the diameter of the wires, and the distances between the camera and the wire are completely different for each of these applications, the combination of those factors usually causes the wire to be depicted in about $2-5$ pixels.

- The processing steps of the various image-based detection applications are quite similar. These steps can be summarized into: a) noise reduction, b) edge-point detection, and c) line-segment detection and validation through morphological characteristics like straightness, parallelism, separation distance, etc. In our application, although we follow the second and third step, by extracting the edge points and then fitting straight lines through those points, we do not use smoothing filters for the noise reduction.

- The image-based detection applications for collision avoidance aim at a very fast detection (approximately 10 ms to 100 ms) and at small false alarm ratio (number of false detections), while there is no interest in a precise localization of the wire in the image. In our application, we also target to a very fast calculation (less than 50 ms), however, we are interested in measuring the position of the wire in the image with a sub-pixel precision.

- Due to the narrow field of view, in our application the wire appears as a straight line, while in the airborne collision avoidance systems the wire usually appears to be curved, following the catenary shape.

Particle accelerator alignment applications

During the last 10 years, the Large Scale Metrology (SU) group at CERN has been involved in many studies related to the detection and measurement of stretched wires. The most relevant methods to our study are the optical wire position system (oWPS) and the close-range photogrammetry due to the fact that they are based on optical images.

The oWPS mainly consists of two cameras, which are taking pictures of the same section of a stretched wire from two different directions, and an infrared flashing LED light. The wire axis is defined as the intersection of two planes. More details about the hardware of the oWPS and its wire detection techniques can be found in *Bestmann et al.* (2010).

The photogrammetric application for wire measurements, currently tested at CERN for non-metallic wires, is based on a commercial software. The software offers two different algorithms (*centerline* and *edge*) that work with the first and second derivatives of the intensity profile, respectively. Both algorithms need starting points to be manually selected into two of the images in order to initiate the wire detection and measurement process. The lack of automation and the fact that the source code of the algorithms is not open are considered to be the main drawbacks of this measuring system (*Behrens et al.*, 2016).

According to *Behrens et al.* (2016), practical tests demonstrated that the *centerline* method is more suitable for thin wires, whereas the *edge* method is considered to be more robust and to provide more satisfying results. This remark is in accordance with the result of the simulation in Section 2.2.2.

Regarding the image of the wire, the photogrammetric approach is closer to our application, especially in terms of volume and methodology. The width of the wire in the image is about $3-5$ pixels for a distance of 2 m to 1 m, respectively, when the wire diameter is 0.3 mm. However, the depicted wire does not appear as a straight line due to the wide field of view and the optical distortion. On the contrary, for the oWPS, the wire is depicted as a straight line with a width of approximately 250 pixels when a 0.3 mm diameter wire is observed from about 75 mm range.

2.2.2 Problem statement

According to the applications described in Section 2.2.1, there are three different methods to detect a wire: a) by estimating the brightest point of the wire, b) by relying on the wire edges, and c) by best fitting a Gaussian curve to the intensity profile (*Flesia et al.*, 2014). In our application we do not intend to use coaxial to the camera flash light for the measurements of the PACMAN project. In this case, the only source of illumination will be the ceiling lights of the laboratory, and therefore, it is worth examining the variation of the intensity profile of the depicted wire with respect to the angle of incidence between the light rays and the optical axis of the camera.

Thus, we simulated in MATLAB® a configuration that consists of a cylinder in the color of copper, which represents the wire, a camera view and five light sources placed in various angles of incident with respect to the camera optical axis. In Figure 2.3a, we see the position of the lights (yellow spheres) and the camera, all laying in a plane that is perpendicular to the cylinder axis. The angle of incidence ϑ varies from 0° to 80° in intervals of 20°. Using the simulated camera view, we created a set of photo-realistic images, each time technically illuminating the cylinder from a different angle of incidence

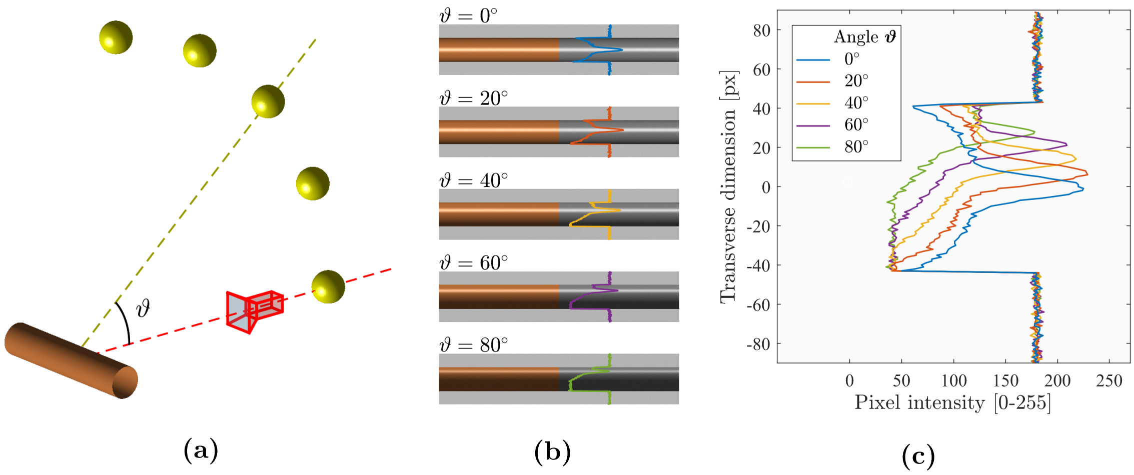

Figure 2.3: (a) Simulation configuration of the wire, the camera and the lights. (b) Photo-realistic images and the transversal pixel intensity of the wire for each angle ϑ. (c) Superimposition of the intensity profiles for each angle ϑ.

ϑ. In Figure 2.3b, we see the five photo-realistic images in color and in black-and-white, and the mean transverse profile of the pixel intensities.

In the superimposition of the profiles (Figure 2.3c), we observe that the edges remain in a stable position, independently of the illumination angle of incidence, while the brightest point is changing position with respect to the wire axis. Therefore, in our application, where the light sources are stable and the wire is observed from many arbitrarily distributed cameras, we expect to get a more consisted result by relying on the edges of the wire image rather than on the points with the highest intensity.

2.2.3 Edge detection

In computer vision, an *edge* is defined as an abrupt change in the intensity between two neighboring pixels. The goal of an edge detection algorithm is to return a binary image, in which a nonzero value denotes the presence of an edge in the initial (raw) image.

A grey-scale digital image is a discrete function $f : \mathbb{Z}^2 \rightarrow \mathbb{Z}$ that can be represented by a 2D array $\mathcal{I}_{n\times m}$, where n is the number of rows and m the number of columns, or the width and the height of the image, respectively. Each cell of the array (or pixel of the image) $\mathcal{I}$ has the intensity value $\rho_{x,y}$,

$$\rho_{x,y} = \mathcal{I}(x, y) \tag{2.1}$$

where

$x \quad \in \{0, 1, \ldots, n\}.$

$y \quad \in \{0, 1 \ldots, m\}.$

$\rho_{x,y} \quad \in \{0, 1, \ldots, 2^k - 1\}.$

$k \quad$ is the number of bits of the imaging sensor.

For the imaging sensor utilized in our application, n is equal to 1024, m is equal to 684 and k is equal to eight, therefore, the pixel intensity can get a value in the range $[0, 255]$.

An edge can be detected using the first or second derivative of the image intensity. In the field of image processing the derivatives can be simplified and expressed as differences of adjacent pixel values (*Luhmann et al.*, 2014). For example, in the direction x the differences are:

$$\begin{aligned}\frac{\partial \mathcal{I}(x,y)}{\partial x} &= \mathcal{I}(x+1) - \mathcal{I}(x) \\ \frac{\partial^2 \mathcal{I}(x,y)}{\partial x^2} &= \mathcal{I}(x+1) - 2 \cdot \mathcal{I}(x) + \mathcal{I}(x-1)\end{aligned} \tag{2.2}$$

Image filtering is one of the most important techniques in the image processing. In general, the filtering process replaces the pixel value with a new value that is a function of the neighboring pixels. Filters can be categorized as *smoothing* or *sharpening*. Smoothing (or low-pass) filters are based on averaging the neighboring pixels and they are useful for image blurring and noise reduction. On the contrary, sharpening (or high-pass) filters are used to highlight changes in the intensity of the image by subtracting the values of neighboring pixels.

Sharpening filters (or operators) such as Prewitt, Sobel, Roberts and Lagrangian of Gaussian (LoG) can be considered as simple and intuitive tools for edge detection (*Sinha*, 2012; *Sonka et al.*, 2014), while the Canny edge detector (*Gonzalez and Woods*, 2008) can be categorized as a complex algorithm.

2.3 Description of the algorithm

In this section, we describe the developed wire detection algorithm. For visualization purposes, we created an artificial image (Figure 2.4) in order to demonstrate the functionality of the algorithm. The artificial image includes the basic characteristics that the wire detection algorithm is required to deal with. In the raw image, the wire appears in a perspective view and it is placed in an arbitrary position and orientation. Moreover, dust particles and fibers were added on the surface of the wire, and dark shadows were also added in the background. Finally, the image was contaminated with random (Gaussian) noise.

Region of interest calculation

The algorithm starts with the calculation of the region of interest (ROI) $\mathcal{R}$ that is used to isolate the part of the wire to be measured, and at the same time, to expedite the edge detection process.

Let $\bar{\mathbf{p}}^{\mathcal{I}}$ be the centre point of the image $\mathcal{I}$ with coordinates ($\bar{x}^{\mathcal{I}}$, $\bar{y}^{\mathcal{I}}$), which are calculated as

$$\bar{x}^{\mathcal{I}} = \mathrm{nint}\left(\frac{m}{2}\right), \qquad \bar{y}^{\mathcal{I}} = \mathrm{nint}\left(\frac{n}{2}\right) \tag{2.3}$$

where m is the width and n is the height of the image.

Let also $\bar{\mathbf{p}}^{\mathcal{R}}$ be the centre point of $\mathcal{R}$, where w and h are the width and the height of the definition of the ROI, respectively. Obviously, four parameters are required to define the position and the size of the ROI in the image. In order to reduce the required user-defined

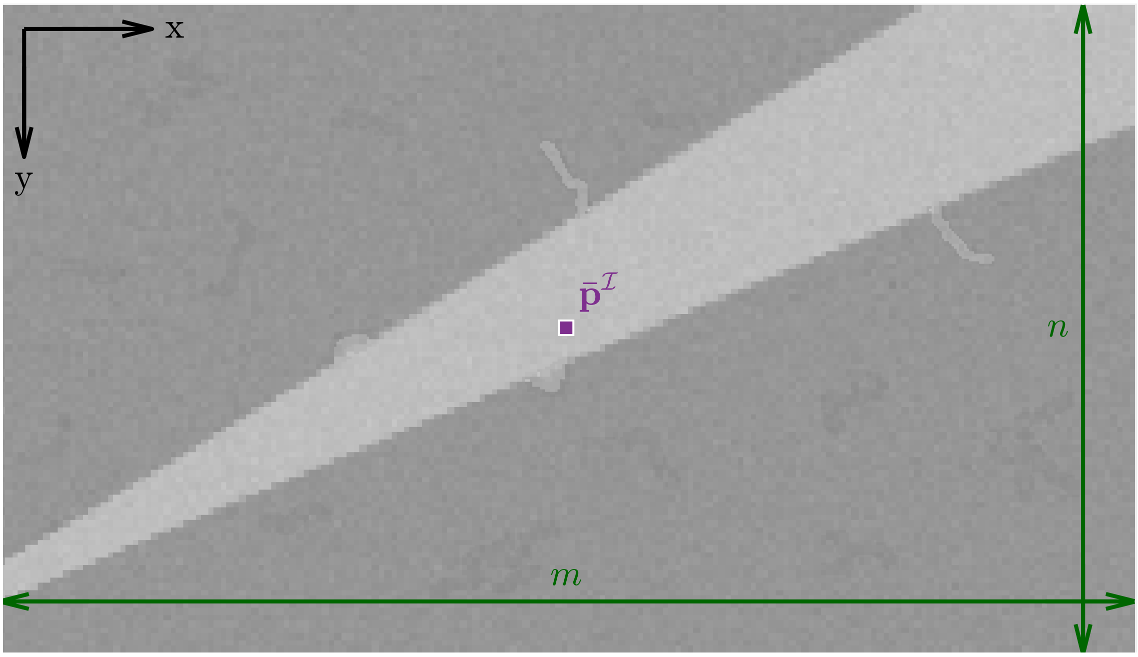

Figure 2.4: Artificial raw image with its coordinate system and its dimensions.

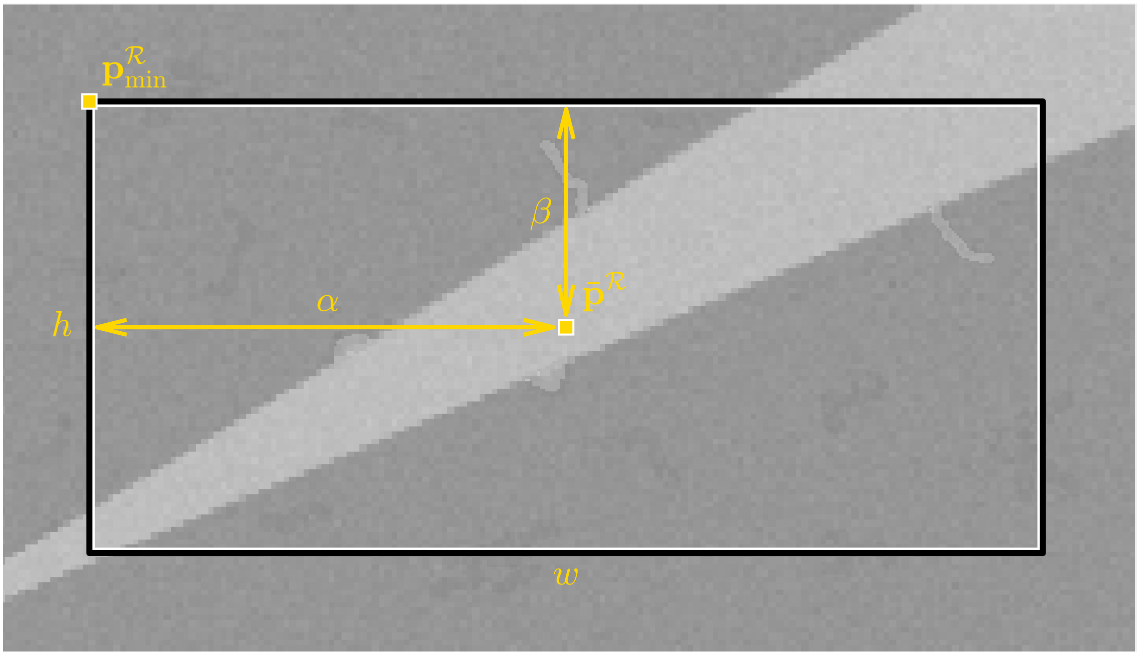

Figure 2.5: Region of interest (ROI).

parameters for the region $\mathcal{R}$, we use the constraint $\bar{\mathbf{p}}^{\mathcal{R}} \equiv \bar{\mathbf{p}}^{\mathcal{I}}$ aiming at placing the ROI in the centre of the image. As a result, only two user-defined parameters are required for the definition of the region $\mathcal{R}$: the half-width α and the half-height β (see Figure 2.5).

To apply the ROI, the library in use requires to input four parameters: the top-left corner $\mathbf{p}^{\mathcal{R}}_{\text{min}}$ with coordinates $(x^{\mathcal{R}}_{\text{min}},\ y^{\mathcal{R}}_{\text{min}})$, the width w and the height h of the ROI. These four parameters are calculated as

$$\begin{aligned} x^{\mathcal{R}}_{\text{min}} &= \bar{x}^{\mathcal{I}} - \alpha, \qquad & w &= 2 \cdot \alpha \\ y^{\mathcal{R}}_{\text{min}} &= \bar{y}^{\mathcal{I}} - \beta, \qquad & h &= 2 \cdot \beta \end{aligned} \tag{2.4}$$

Canny edge detection

The region of interest $\mathcal{R}_{h \times w} \subseteq \mathcal{I}_{n \times m}$ is the area where the edge detection is applied. The edge detection returns a binary image, in which the non-zero pixels are the detected edge points (Figure 2.6). The vectors $\mathbf{x}$ and $\mathbf{y}$ contain the coordinates of the N detected edge points.

$$\underset{N,1}{\mathbf{x}} = \begin{bmatrix} x_1 & x_2 & \dots & x_N \end{bmatrix}^{\mathsf{T}}, \qquad \underset{N,1}{\mathbf{y}} = \begin{bmatrix} y_1 & y_2 & \dots & y_N \end{bmatrix}^{\mathsf{T}} \tag{2.5}$$

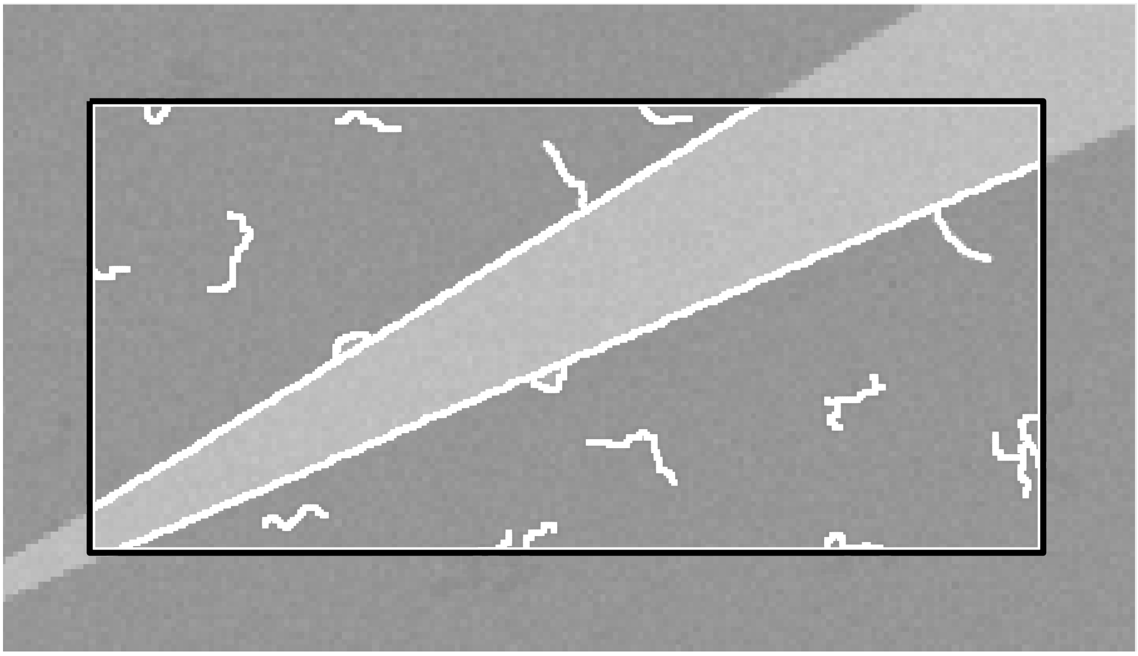

Figure 2.6: Detected edge points (in white color) in the ROI.

Course line fit

Four different 2D lines are computed in different stages of the wire detection algorithm. In general, for a 2D line L, the parametric form is:

$$\mathbf{p}^L_i = \mathbf{p}^L + \mathbf{v}^L \cdot t^L_i \tag{2.6}$$

where

$\mathbf{p}_i^L(x_i^L, y_i^L)$	is an arbitrary point i on the line L.
$\mathbf{p}^L(x^L, y^L)$	is the reference point of the line L.
$\mathbf{v}^L(v_\mathrm{x}^L, v_\mathrm{y}^L)$	is the unit direction vector of the line L.
t_i^L	is the scalar parameter of the arbitrary point i $\left(t_i^L \in \mathbb{R}\right)$.

The benefit of the parametric form is that Equation 2.6 remains valid independently of the line orientation with respect to the coordinate system.

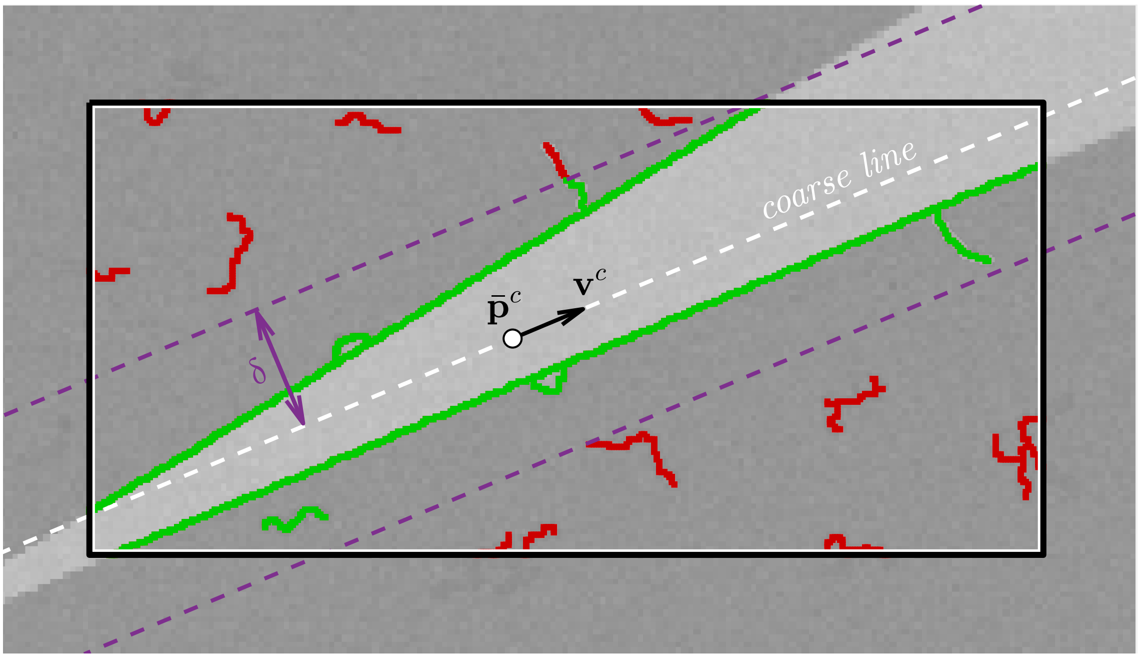

Figure 2.7: The *coarse line* (in white color) is calculated using the edge points (in green color) that are within the maximum permissible interval for the residuals (in purple color). The edge points that are rejected as outliers are depicted in red color.

Initially, the algorithm fits a line to all N detected edge points $(\mathbf{x}, \mathbf{y})$. This line does not precisely represent the axis of the depicted wire, however, it is a good approximation, and as a sequence, we name it *coarse line* (Figure 2.7). The calculation of the *coarse line* c starts with the centroid point $\bar{\mathbf{p}}^c(\bar{x}^c, \bar{y}^c)$,

$$\bar{x}^c = \frac{1}{N} \cdot \sum_{i=1}^{N} x_i, \qquad \bar{y}^c = \frac{1}{N} \cdot \sum_{i=1}^{N} y_i \tag{2.7}$$

The unit direction vector $\mathbf{v}^c$ of the *coarse line* is obtained by the eigendecomposition of the 2×2 covariance matrix $\mathbf{C}$ of the N edge point coordinates (x_i, y_i),

$$\mathbf{C} = \frac{1}{N-1} \cdot \sum_{i=1}^{N} \begin{bmatrix} (x_i - \bar{x}^c)^2 & (x_i - \bar{x}^c) \cdot (y_i - \bar{y}^c) \\ (x_i - \bar{x}^c) \cdot (y_i - \bar{y}^c) & (y_i - \bar{y}^c)^2 \end{bmatrix} \tag{2.8}$$

Here, we divide by the factor $N-1$ because the true mean value of the coordinates is not known in advance. The matrix $\mathbf{C}$ is symmetric and positive semi-definitive, therefore, it can be decomposed to its eigenvalues and eigenvectors.

$$\mathbf{C} = \mathbf{U} \cdot \mathbf{\Lambda} \cdot \mathbf{U}^{\mathrm{T}} = \begin{bmatrix} \mathbf{v}_0 & \mathbf{v}_1 \end{bmatrix} \cdot \begin{bmatrix} \lambda_0 & 0 \\ 0 & \lambda_1 \end{bmatrix} \cdot \begin{bmatrix} \mathbf{v}_0^{\mathrm{T}} \\ \mathbf{v}_1^{\mathrm{T}} \end{bmatrix} \tag{2.9}$$

where

$\mathbf{v}_0$ is the unit direction vector of the *coarse line* ($\mathbf{v}^c$).

$\mathbf{v}_1$ is the unit vector that is perpendicular to the *coarse line* ($\mathbf{v}^c_\perp$).

$\lambda_0,\ \lambda_1$ are the eigenvalues of $\mathbf{C}$.

For the outlier detection, we need to compute the residuals of the fit, i.e., the distance between each point and the best-fit line. Firstly, we compute the vector $\mathbf{u}_i$ between the centroid $\bar{\mathbf{p}}^c$ and each point $(x_i,\ y_i)$, as depicted in Figure 2.8,

$$\mathbf{u}_i = \begin{bmatrix} x_i - \bar{x}^c \\ y_i - \bar{y}^c \end{bmatrix} \tag{2.10}$$

and then, we compute the distances d_i as dot-products between the vectors $\mathbf{u}_i$ and the unit vector $\mathbf{v}^c_\perp$, which is perpendicular to the *coarse line*.

$$d_i = \mathbf{u}_i \cdot \mathbf{v}^c_\perp \tag{2.11}$$

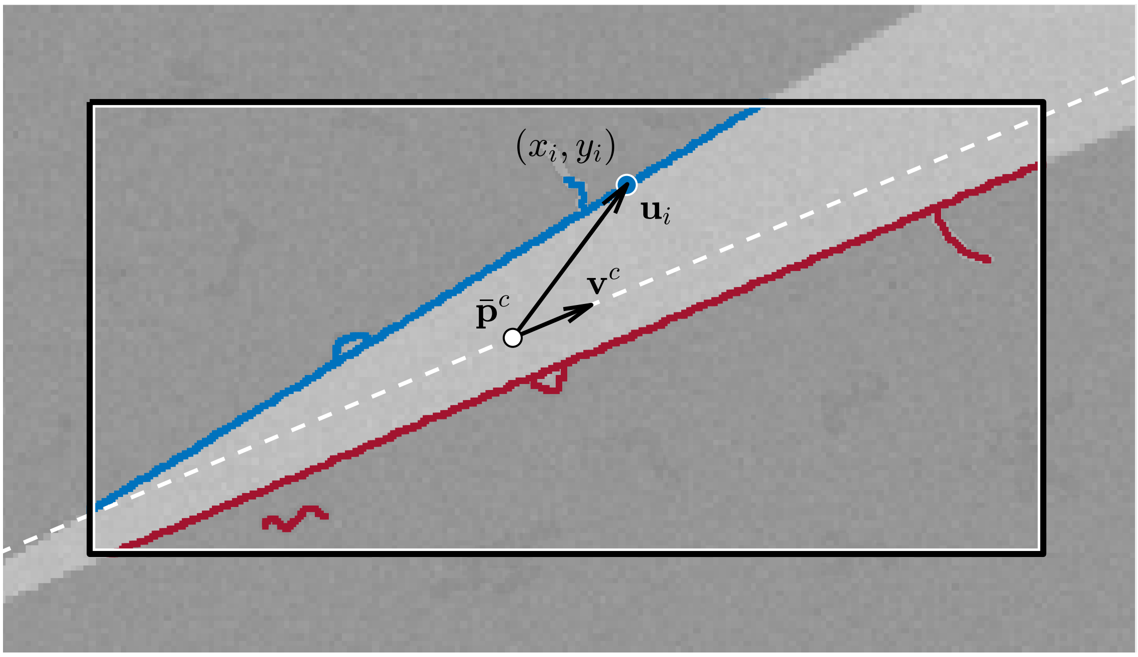

Figure 2.8: The edge points are split into the *positive group* (in blue color) and into the *negative group* (in red color) for further processing.

At this stage, we introduce the two criteria that are used for the outlier detection:

$$\max \mathbf{d} < \delta, \qquad N \geq N_{\min} \tag{2.12}$$

where

- $\mathbf{d}$ is the vector of the distances d_i (Equation 2.11), which are the absolute values of the residuals.
- δ is the maximum permissible residual (user-defined).
- N is the number of edge points that participate in the line fit.
- $N_{\min}$ is the minimum permissible number of points participating in the line fit (user-defined).

Typically, the algorithm iterates through Equations 2.7 − 2.12 before we get the final robust solution for the *coarse line* $(\bar{\mathbf{p}}^c, \mathbf{v}^c)$ and the remaining edge points $(\mathbf{x}', \mathbf{y}')$, which are depicted in green color in Figure 2.7.

Positive and negative line fit

The next step of the wire detection algorithm is to fit a line in each edge of the depicted part of the wire. To do so, we firstly separate into two groups the edge points $(\mathbf{x}', \mathbf{y}')$ that participated in the *coarse line* fit. The separation is according to the *coarse line* and, technically, it is based on the sign of the quantity K_i, which is computed for each edge

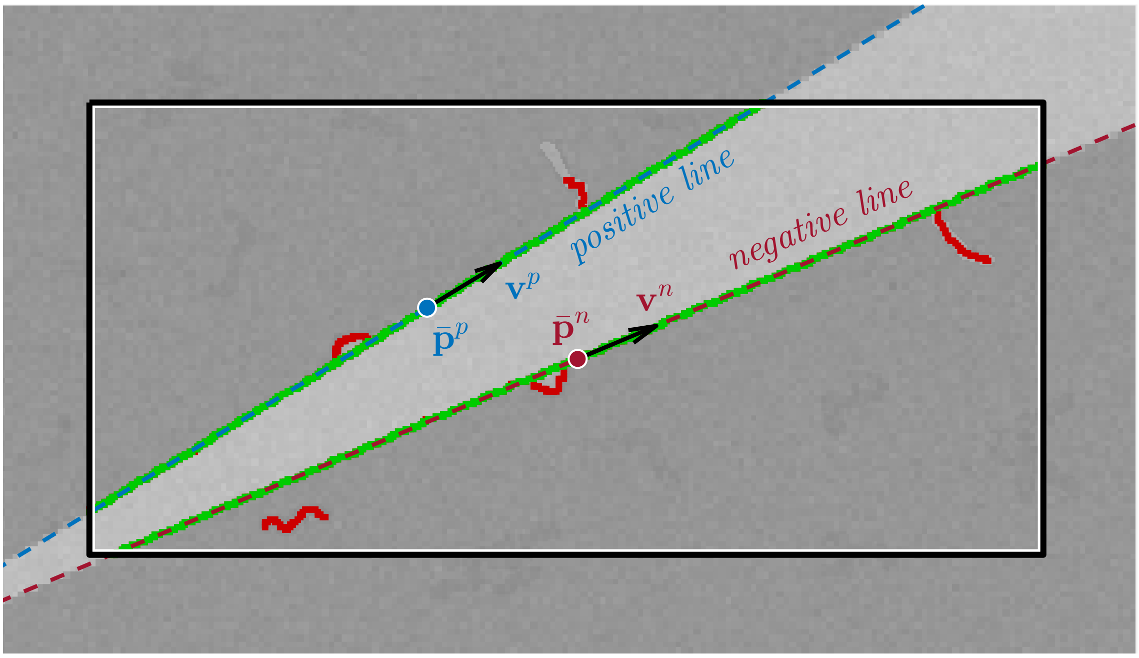

Figure 2.9: The robust best fit *positive line* (in blue color) and *negative line* (in red color), as well as the edge points that participated in the solution (in green color) and the edge points that were rejected as outliers (in red color).

point as

$$K_i = u_{i\mathrm{x}} \cdot v^c_{\mathrm{y}} - u_{i\mathrm{y}} \cdot v^c_{\mathrm{x}} \tag{2.13}$$

Equation 2.13 describes the non-zero part of the cross-product of the vectors $\mathbf{v}^c$ and $\mathbf{u}_i$ (Figure 2.8), given that the two vectors are supplemented by a third dimension coefficient that is equal to zero. The quantity K_i can be considered as the third and the only non-zero coefficient of the vector that is perpendicular to the image plane, or as the sine of the angle between the two vectors.

In our case, we are interested in the sign of the quantity K_i. If K_i is positive, the edge point is listed in the *positive group*, otherwise, if K_i is negative, the edge point is listed in the *negative group* (Figure 2.8).

The algorithm continues with the robust fit of the *positive line* p and the *negative line* n, using the edge points of the *positive group* and the *negative group*, respectively. The process is identical with that already described for the *coarse line*, with the only difference to be that the parameter δ of Equation 2.12 is, in this case, by default set to one pixel.

The robust fit algorithm returns the position and the unit direction vector for the *positive line* $(\bar{\mathbf{p}}^p, \mathbf{v}^p)$ and the respective values for the *negative line* $(\bar{\mathbf{p}}^n, \mathbf{v}^n)$. Figure 2.9 depicts the *positive line* and the *negative line*, as well as the edge points that participated in each line fit (in green color) and the points that were rejected as outliers (in red color).

Wire axis line calculation

The last part of the algorithm concerns the calculation of the line that represents the depicted wire axis, which we call *fine line*. The *fine line* f is computed as the bisector of the *positive line* and the *negative line*, i.e., the locus of the points that keep equal distance from the two lines. Initially, we compute the unit direction vector $\mathbf{v}^f$,

$$\mathbf{v}^f = \frac{\mathbf{v}^p + \mathbf{v}^n}{|\mathbf{v}^p + \mathbf{v}^n|} \tag{2.14}$$

At this stage, any arbitrarily selected point in the image space could be used to start the computation of the exact position of the *fine line* and later, any arbitrarily selected point that belong to the *fine line* could be returned by the algorithm as the final measured point on the wire axis. Our selection is to pick up the point $\mathbf{p}^f(x^f,\ y^f)$ of the *fine line* that is the closest to the centroid point $\bar{\mathbf{p}}^c(\bar{x}^c,\ \bar{y}^c)$ of the *coarse line*.

For this reason we proceed in computing the intersection points $\mathbf{p}^p_{\mathrm{int}}(x^p_{\mathrm{int}},\ y^p_{\mathrm{int}})$ and $\mathbf{p}^n_{\mathrm{int}}(x^n_{\mathrm{int}},\ y^n_{\mathrm{int}})$ of the *positive line* and the *negative line*, respectively, with the line that is perpendicular to the bisector line and passes through the *coarse line* centroid $\bar{\mathbf{p}}^c$.

Following the notation of Figure 2.10, the coordinates of the positive intersection point $\mathbf{p}^p_{\mathrm{int}}$ can be written as

$$x^p_{\mathrm{int}} = \bar{x}^p + v^p_{\mathrm{x}} \cdot t^p, \quad y^p_{\mathrm{int}} = \bar{y}^p + v^p_{\mathrm{y}} \cdot t^p \tag{2.15}$$

or as

$$x^p_{\mathrm{int}} = \bar{x}^c + v^c_{\mathrm{x}\perp} \cdot t^c, \quad y^p_{\mathrm{int}} = \bar{y}^c + v^c_{\mathrm{y}\perp} \cdot t^c \tag{2.16}$$

Solving for either t^p or t^c, we calculate the coordinates of the intersection point $\mathbf{p}^p_{\mathrm{int}}$. The same process is followed for the negative intersection point $\mathbf{p}^n_{\mathrm{int}}$.

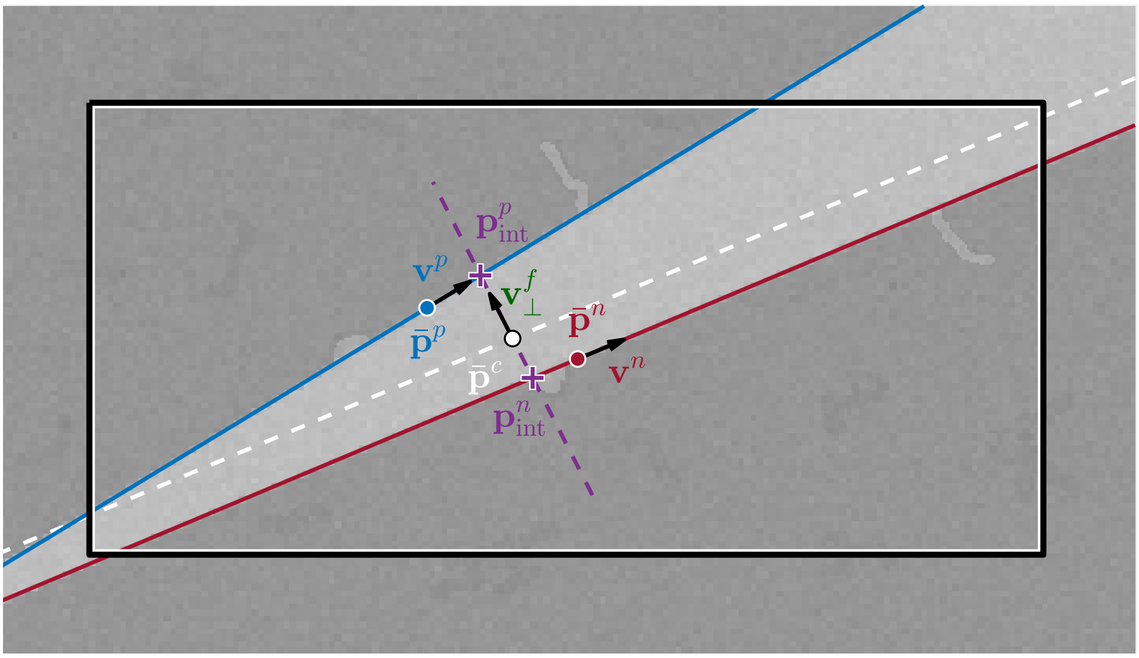

Figure 2.10: The intersection points $\mathbf{p}^p_{\mathrm{int}}$ and $\mathbf{p}^n_{\mathrm{int}}$ of the *positive line* and the *negative line*, respectively, with the line (in purple color) that is perpendicular to the bisector of the positive and the negative lines ($\mathbf{v}^{\mathbf{f}}_\perp$) and passes through the *coarse line* centroid $\bar{\mathbf{p}}^c$.

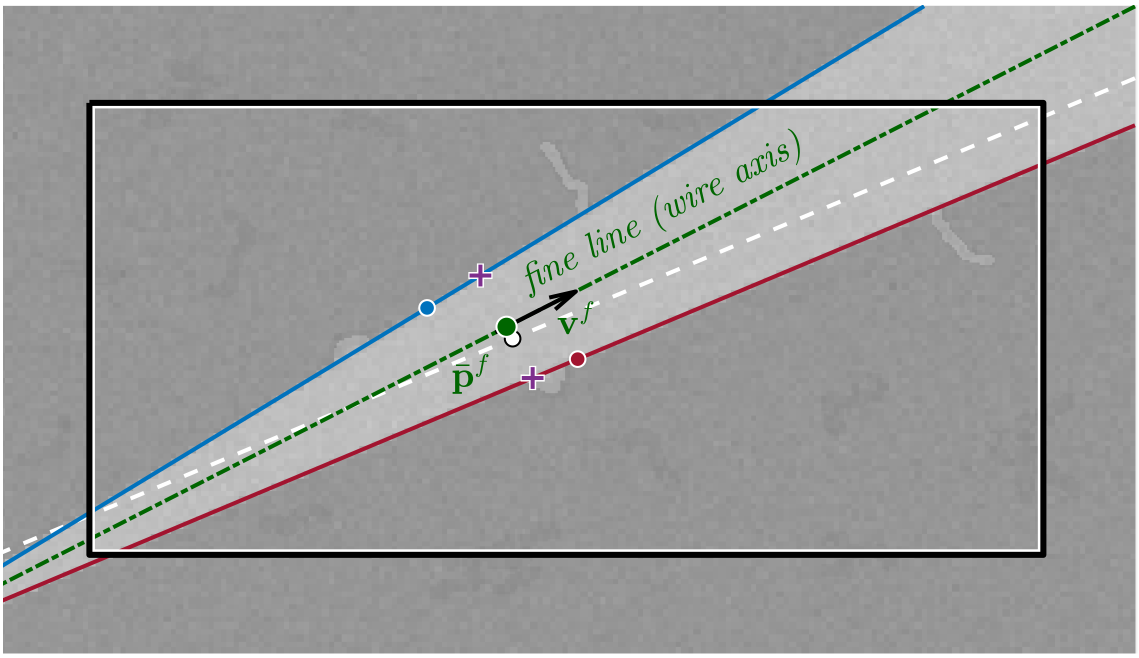

Figure 2.11: The reference point $\mathbf{p}^f$ and the unit direction vector $\mathbf{v}^f$ of the *fine line.*

Finally, the point $\mathbf{p}^f$ is computed as

$$x^f = \frac{x^p_{\text{int}} + x^n_{\text{int}}}{2}, \qquad y^f = \frac{y^p_{\text{int}} + y^n_{\text{int}}}{2} \tag{2.17}$$

The point $\mathbf{p}^f$ is the final outcome of the wire detection algorithm that is considered to be on the axis of the wire (Figure 2.11). These coordinates are later transformed to horizontal and zenith angles (see Section 1.4.5).

2.4 Implementation of the algorithm

In this section, we describe the implementation of the developed wire detection algorithm. We present the measurement procedure of the QDaedalus software and the interaction between the QDaedalus software and the new algorithm. The data structures and the functions of the algorithm are described in detail with reference to the source code, which can be found in Appendix A.

2.4.1 The QDaedalus software environment

The QDaedalus software executes the procedure presented in the flowchart in Figure 2.12 in order to obtain an angle measurement. For each measurement, there are several interactions between the software and the hardware. Firstly, the software steers the theodolite to the target and drives the focusing mechanism to the appropriate position. Then, it

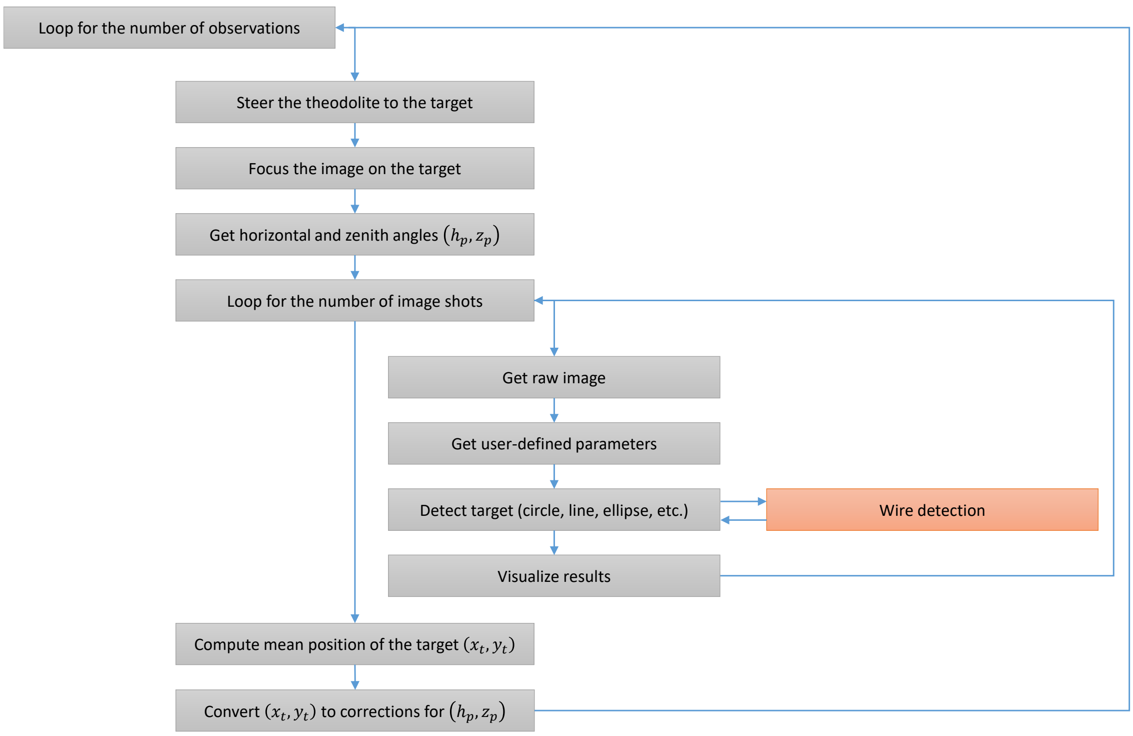

Figure 2.12: Flowchart of the QDaedalus measurement procedure.

records the readings of the horizontal and zenith angles that correspond to the theodolite optical axis, and captures as many images as the user has selected. For each camera shot, the software passes the raw image and the user-defined parameters to the selected target detection algorithm, in our case to the wire detection algorithm. After the image processing, the detection algorithm returns the image coordinates of the target and some more information that is used for the visualization of the result.

When all the shots are processed, the software calculates the robust mean of the image coordinates that were extracted from the shots. The criterion for the robust mean is a user-defined threshold of the standard deviation of the sample. Finally, the mean coordinates are transformed into horizontal and vertical angle measurements, according to Equations 1.3 and 1.4 in Section 1.4.5.

Software-related requirements

The software-related requirements that are listed below had to be fulfilled in order to facilitate the integration of the new detection algorithm and to avoid any redesign and restructure of other parts of the existing QDaedalus software. Therefore, these requirements were imposed by the structure and the specifications of the existing QDaedalus software. The challenge in this case was to respect the requirements without any downgrade effect on the functionality and performance of the new algorithm. Finally, the algorithm was successfully designed to conform and cooperate with the existing QDaedalus software workflow.

- **Programming language**
  The algorithm had to be developed with the technique of procedural programming, using the *C++* programming language.

- **Development environment**
  The *Qt* integrated development environment (IDE) had to be used for the development of the algorithm.

- **Functions structure**
  The new functions should have similar interfaces as the existing detection algorithms in order to enable an efficient input and output data transfer and to facilitate the maintenance of the software in the future.

- **Open source libraries**
  The existing detection algorithms of the QDaedalus software, as well as the wire detection algorithm, use the *OpenCV* (Open Source Computer Vision) library.

- **Edge detection algorithm**
  The Canny edge detection algorithm, as implemented in *OpenCV*, was extensively used in the existing detection algorithms of the QDaedalus software, and therefore, it was also selected for the wire detection algorithm.

- **User interface**
  The existing detection algorithms were based on five user-defined parameters, different for each algorithm. These parameters are used to tune the detection algorithm

with respect to the given conditions and to improve its performance. This restriction was an additional constraint for the development of the wire detection algorithm.

- **Execution time**
  The algorithm should run in less than 10 ms (100 Hz) in a modern architecture portable computer. This is in compliance with the frame rate of modern cameras, which can easily provide 100 fps (frames per second).

2.4.2 Data structure declaration and function prototyping

Three data structures and two functions were used to handle the wire detection process. Here, we present in detail the data structures with the encapsulated variables and the interface prototyping of the functions, i.e., the input and output variables and data structures.

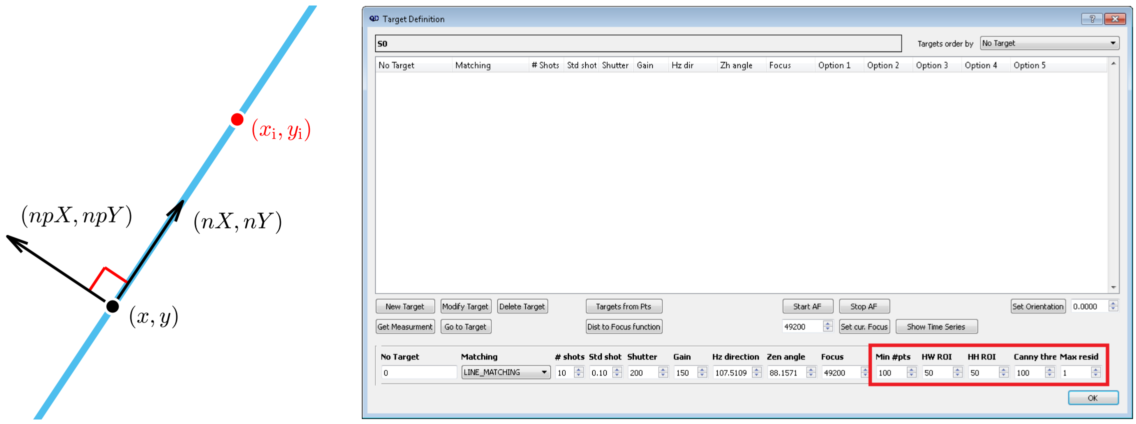

(a) (b)

Figure 2.13: (a) The six elements of the `parametric2DLine` data structure, in black color. (b) The panel of the user-defined parameters (red frame) as appears in the QDaedalus *Target Definition* window.

- **Data structure: `parametric2DLine`**
  Due to the fact that the algorithm mainly deals with straight lines in the 2D image domain it is rather useful to define a data structure that describes a line in two dimensions (Equation 2.6). The `parametric2DLine` data structure (Appendix A.1, lines 3 – 12) contains the coordinates of a point (x, y) that belongs to the line, the coefficients of a unit vector (nX, nY) that is parallel to the line, and the coefficients of a unit vector (npX, npY) that is perpendicular to the line (Figure 2.13a).

- **Data structure: `userParameters`**
  The `userParameters` data structure contains the five user-defined parameters of the wire detection algorithm, i.e., `minEdgePnts`, `halfWidthROI`, `halfHeightROI`, `maxResidual` and `cannyThreshold`. The description of the parameters can be found in Appendix A.1 (lines 14 – 22). Figure 2.13b shows the QDaedalus interface window used during the target definition and the particular panel of the user-defined parameters.

- **Data structure:** `wireDetectionData`
  The `wireDetectionData` data structure (Appendix A.1, lines 24 – 35) is used to store the computed lines. It consists of four `parametric2DLine` data structures that are used for the *coarse line*, the *positive line*, the *negative line*, and the *fine line* (Figure 2.11). It also contains the number of points that are finally used to fit each line and the calculated width of the depicted wire in pixels.

- **Function:** `wireDetection`
  The `wireDetection` function is the core of the algorithm. The function gets the raw image of the wire and the user-defined parameters as input, and returns the `wireDetectionData` data structure and an image with the Canny edge points for visualization purposes (Figure 2.16). The prototyping of the function is given in Appendix A.1 (lines 42 – 46).

- **Function:** `robustFit2DLine`
  The `robustFit2DLine` function is used to robustly fit a 2D line. It is called three times within the `wireDetection` function and each time it gets as input the two relevant user-defined parameters (`minEdgePnts` and `maxResidual`) and the corresponding edge point coordinates. After the robust fit, the function returns a `parametric2DLine` data structure and the coordinates of the points that were finally used to fit the line (not those that were rejected). The prototyping of the function is listed in Appendix A.1 (lines 48 – 59).

2.4.3 The `wireDetection` function implementation

In this Section, we describe in detail the `wireDetection` function workflow (Figure 2.14). For each step, we provide a reference to the source code in Appendix A, as it is implemented in our application.

Variable declaration

All the variables and data structures are declared in the beginning of the function. A detailed description can be found in Appendix A.2 (lines 5 – 51). The variables are declared in the same order as they are used.

Region of interest (ROI) calculation

The ROI is defined as an *OpenCV* rectangle (`CvRect`) in order to facilitate the use of the *OpenCV* function `cvSetImageROI` for the image masking. The `CvRect` data structure contains four integer parameters, which are described in Equation 2.4. The source code for the ROI calculation can be found in Appendix A.2 (lines 54 – 66).

Canny edge detection

The *Canny edge detection* is used in the majority of the QDaedalus detection algorithms, as well as in the wire detection algorithm, and it is applied with the *OpenCV* built-in function `cvCanny`. Initially, we create a new image to accommodate the edges by cloning the attributes from the raw image and then we apply the ROI mask to both of them.

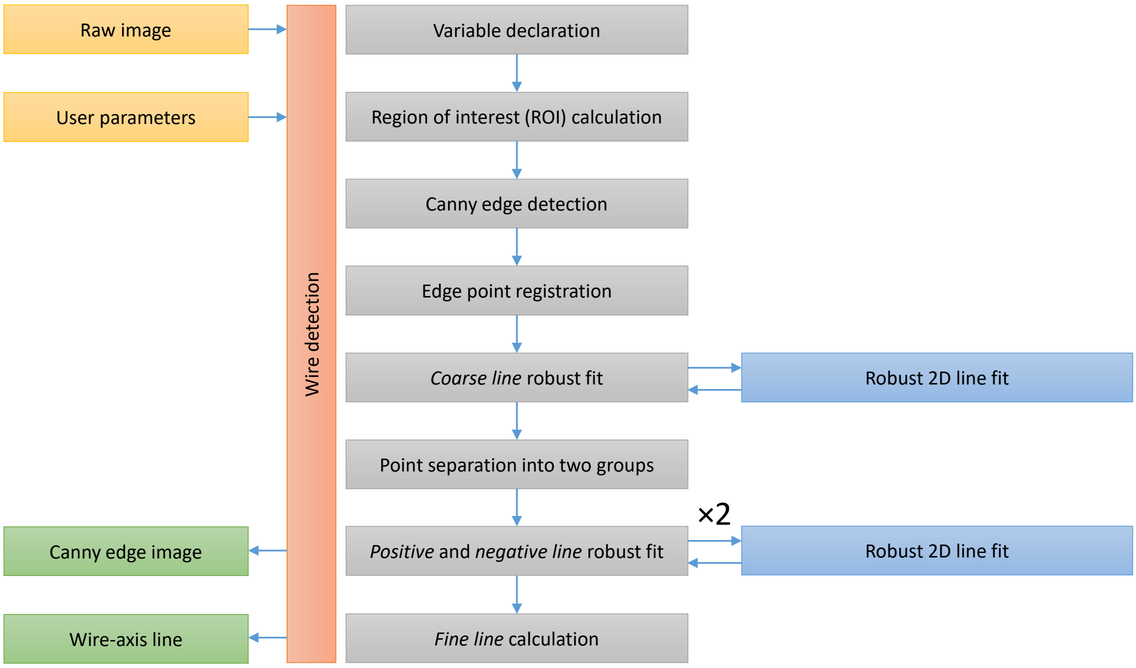

Figure 2.14: Flowchart of the `wireDetection` function. It consists of the input data (in yellow color), the output data (in green color), the steps of the algorithm (in gray color), and the three calls of the `robustFit2DLine` function (in blue color).

Afterwards, we apply the `cvCanny` function, which gets five arguments. These arguments are the raw image, the edge image (for output), the two thresholds for the hysteresis procedure (the first is user-defined and the second is set to be 1/3 of the first), and the size of the Sobel operator, which is set by default to be 3×3. This block of source code (Appendix A.2, lines 69 – 88) ends with the deletion of the ROI mask from both images and the return of the binary image of the Canny edge points for visualization purposes.

Edge point registration

The output of the Canny edge detection is a binary image. Pixels with intensity equal to one (or 255) correspond to the detected edge points, while the rest of the pixel values are equal to zero. To get a list of the edge points, we scan the user-defined ROI with a double loop and we register the pixel coordinates (Equation 2.5) in two vectors (`initX`, `initY`). The source code can be found in Appendix A.2 (lines 91 – 115).

Coarse line robust fit

To robustly fit 2D lines we have developed the `robustFit2DLine` function, described in detail in Section 2.4.4. The user can control the iterative process with two parameters: the minimum permissible number of the edge points (`minEdgePnts`) and the maximum permissible residual (`maxResidual`), both required for the robust line fit (see Equation 2.12). The source code can be found in Appendix A.2 (lines 118 – 138).

In Figure 2.7, we see that the `maxResidual` parameter is used to define an interval, in which the edge points should lay in. To properly set this value, avoiding to reject a large number of edge points, we should consider the estimated width of the wire in pixels, which is shown in the sample image (Figure 2.16c).

The user-defined value for the `maxResidual` parameter is only utilized for the robust fit of the *coarse line*, while for the precise robust fit of the *positive line* and the *negative line* the `maxResidual` parameter value is by default set to 1 pixel.

Point separation into two groups

After the robust fit of the *coarse line* the remaining edge points are separated into two groups. If the result of Equation 2.13 is evaluated to be greater than zero, the edge point is listed in the *positive group*, otherwise the edge point is listed in the *negative group* (Appendix A.2, lines 141 – 161).

Positive and negative line robust fit

The `robustFit2DLine` function is called twice in order to fit a line in each group of the edge points (*positive* and *negative*).

The value of the `minEdgePnts` parameter is crucial for the robust fit of the *positive line* and the *negative line*. It should be set to be less than the half of the total number of the edge points due to the fact that each edge of the depicted wire typically has about half of the total number of edge points.

The value for the maximum permissible residual (`maxResidual`) has to be preset at this stage due to the fact that the user-defined parameters are restricted to five. For our application, in which we are interested in a precise fit, we set the maximum permissible residual to the lowest acceptable value, which is 1 pixel (Appendix A.2, lines 164 – 207).

Fine line calculation

The calculation of the *fine line*, which is considered to be the representation of the wire axis, is the last step of the algorithm. It is calculated as the bisector of the *positive* and the *negative* edge lines. The orientation (unit vector) and the position of the *fine line* are computed according to Equations 2.14 and 2.17, respectively. The relevant source code can be found in Appendix A.2 (lines 210 – 310).

As mentioned, the outcome of the wire detection algorithm is a pair of image coordinates that correspond to a specific target, i.e., a point on the depicted wire axis. These coordinates are later transformed to horizontal and vertical angles (see Section 1.4.5).

2.4.4 The `robustFit2DLine` function implementation

The `robustFit2DLine` function is developed to fit a 2D line, following an iterative process with outlier detection and rejection criteria (Equation 2.12). The function gets five arguments; three as input data and two as output data (Figure 2.15). The input data consist of two user-defined parameters, i.e., the minimum permissible number of points remaining in the line fit and the maximum permissible residual, as well as the image coordinates of the edge points. The output data consist of a `parametric2DLine` data

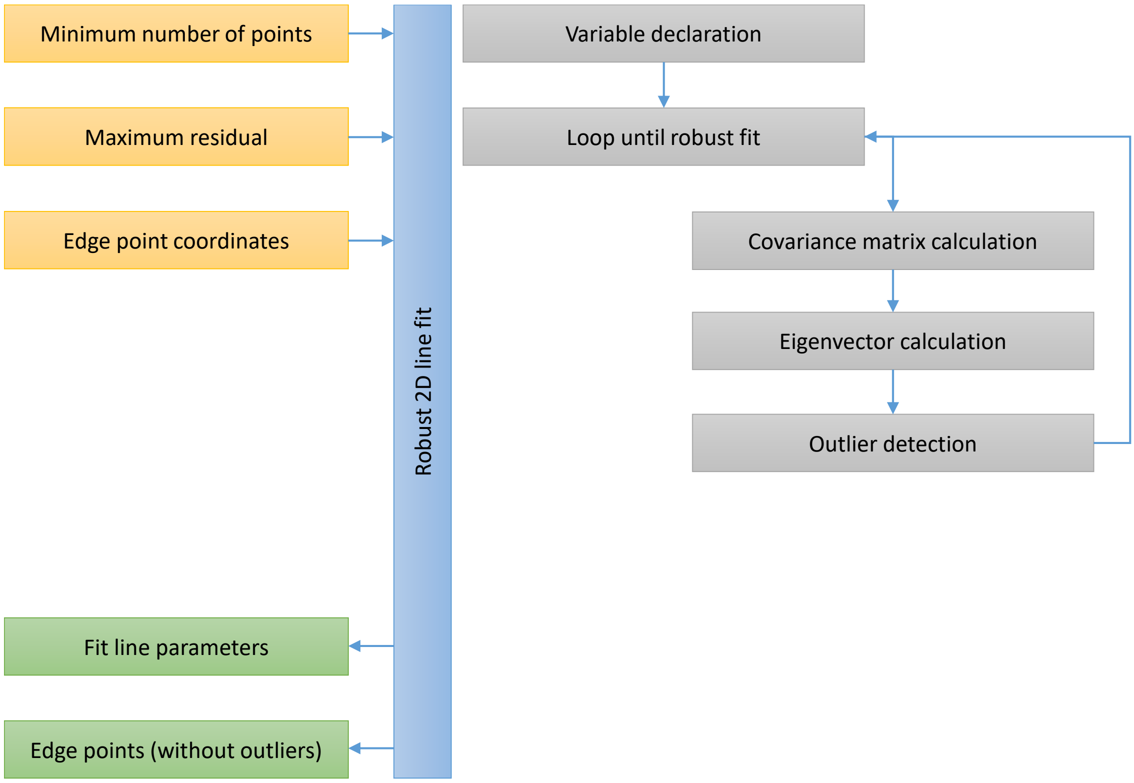

Figure 2.15: Flowchart of the `robustFit2DLine` function. It consists of the input data (in yellow color), the output data (in green color) and the steps of the algorithm (in gray color).

structure, which contains the best-fit line, and the image coordinates of the edge points that finally participated in the solution.

The principal component analysis (PCA) is employed to obtain the position and the orientation of the best-fit line. This technique is selected because it is easily implemented and rapidly executed during the runtime. After the initial fit, the residuals — distances of the points to the line — are compared with the user-defined `maxResidual` value. In case there are residuals that exceed the threshold, the edge point that corresponds to the largest residual is removed and a new fit is re-computed.

The robust fit is successful if there is no residual above the maximum residual threshold and if the number of points participating in the fit is larger than the user-defined `minEdgePnts` value. In case the robust fit is not successful, the wire detection stops and the QDaedalus software takes command.

Variable declaration

All the variables and data structures are declared in the beginning of the function. A detailed description can be found in Appendix A.3 (lines 5 – 29). The variables are declared in the same order as they are used.

Covariance matrix calculation

The covariance matrix of the edge point coordinates is calculated with Equation 2.8. The source code can be found in Appendix A.3 (lines 36 – 65).

Eigenvector calculation

The eigenvalue decomposition is applied using the *OpenCV* built-in function `cvEigenVV`. According to Equation 2.9, the function returns a 2×2 matrix that contains the unit vector in the direction of the best-fit line and the perpendicular vector. The source code can be found in Appendix A.3 (lines 68 – 83).

Outlier detection

The outlier detection is performed after each line fit. The residuals are computed and compared to the `maxResidual` value. If there are more than one residual that exceed the threshold, then only the edge point that corresponds to the largest residual is removed and the fitting algorithm is repeated. The source code can be found in Appendix A.3 (lines 86 – 122).

2.4.5 Visualization

The QDaedalus software provides to the user a visualization of the target detection process both, during the target definition and during the measurement. The visualization assists the user to define the values for certain parameters and to realize problems that might occur during the detection.

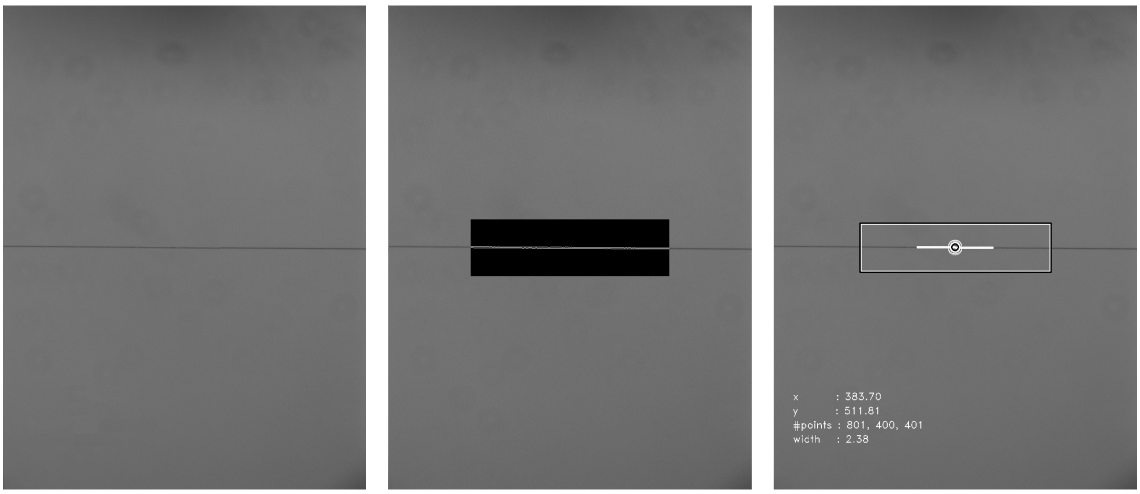

(a) (b) (c)

Figure 2.16: (a) Typical raw image of the wire. (b) Result of the Canny edge detection inside the ROI. (c) Visualization of various results of the algorithm with graphic elements and numerical values.

In the *Target Definition* window, the software initially displays the raw image captured by the camera (Figure 2.16a). When a detection algorithm is selected, the software superimposes the result of the detection on the raw image (Figure 2.16c). In particular for the wire detection, the software also shows the edge points that are detected by the Canny edge detector inside the ROI (Figure 2.16b).

In Figure 2.16c, we see the ROI, the axis of the *fine line* and the reference point on the axis of the *fine line*, which is the actual measurement. The *positive line*, the *negative line*, and their centroid points are also shown to the user, however, they can be distinguished only if the wire is wide enough.

On the bottom-left part of the image we also see the output coordinates (x, y) in pixels, the total number of edge points, the number of the remaining edge points in the *positive group* and in the *negative group*, and the measured width of the wire in the detection region, also given in pixels.

2.5 Concluding remarks

In this chapter, we described the development of a stretched-wire detection algorithm that aims to automatize the micro-triangulation measurements for fiducialization and alignment applications. Based on sample images, on simulations and on the relevant literature, we concluded that an edge-detection based algorithm is expected to be more robust compared to a brightest-point based algorithm, particularly, when no special light is used (e.g., flashing light) that is coaxial to the camera axis.

Before the wire detection algorithm design, it was valuable to examine the geometrical characteristics of the wire, both as a physical object and as it is depicted in the image that is produced by the combination of the optical system and the camera. According to the sample images, the wire is depicted as a straight line, although a stretched wire follows the catenary shape when suspended. Moreover, we observe that the images have enough resolution and high quality to depict a wire of 100 µm diameter, when observed from a distance of at least 4 m.

The new algorithm is based on the Canny edge detector, on a robust best-line fit and on geometrical calculations to precisely measure the position and orientation of the wire in the image coordinate system. The qualitative and quantitative performance of the new algorithm are evaluated in Chapter 3, in which we experimentally examine the precision of the algorithm in terms of repeatability, and its robustness against various user-defined parameter values and environmental conditions.

The implementation of the new algorithm respects all the software-related requirements that were set in order to successfully integrate the algorithm into the QDaedalus software. The wire detection algorithm is able to work independently and in cooperation with the existing QDaedalus detection algorithms. The successful accomplishment of this task enables the automatic angle measurements to a wire. This is a very important step towards the utilization of the micro-triangulation method for fiducialization and alignment applications of particle accelerator components.

Chapter 3

Experimental evaluation of the wire detection and the circle detection algorithms

In this chapter, we experimentally evaluate the performance of the wire detection and the circle detection algorithms following the methodology described in Section 3.2. A qualitative evaluation of the wire detection algorithm is presented in Section 3.3. In Section 3.4, we discuss the influence that various parameters have on the result of the wire detection algorithm measurement, while in Section 3.5, we focus on the experimental evaluation of the circle detection algorithm. Recommendations for the good practice on how to use the algorithms, and proposals for further development of the acquisition software are discussed in Section 3.6, followed by the concluding remarks in Section 3.7.

3.1 Introduction

The primary objective of the test measurements presented in this chapter is to evaluate the performance of the *wire detection algorithm* under laboratory conditions. The wire detection algorithm was developed as part of this thesis (see Chapter 2) to be used in measuring a micro-triangulation network for magnet fiducialization and alignment applications.

Such a network consists of an approximately horizontally stretched wire, some targets on the magnet and theodolites distributed around the magnet. In such a configuration, the wire forms various angles of incidence with the optical axes of the theodolites, thus, it usually appears inclined in the images. Moreover, the wire is projected in front of various background gray-scale colors.

To ascertain that the new wire detection algorithm will be able to perform the micro-triangulation network measurements under the aforementioned conditions, we conducted a qualitative evaluation by executing a set of different tests. These tests focus only on the capability of the algorithm to perform measurements and not on the precision of these measurements.

In addition, the quantitative evaluation of the wire detection algorithm aims to estimate the influence of various user-defined parameters or ambient conditions on the result of the measurement. A potential influence is expected to appear as difference in the dispersion (indication of precision) or bias (indication of accuracy) in the measurement result. Throughout these measurements, either we keep the conditions stable and change values of one parameter or we keep the parameter values stable and change the environmental conditions.

In this chapter, we do not attempt to estimate the angular precision of the QDaedalus measuring system. The reason is that the measurements of this chapter concern a specific direction in space, thus, the configuration does not comply with that proposed by the relevant *ISO 17123-3* (2001). Instead, we perform statistical tests for the estimated variance of each parameter value against the variance provided by the theodolite manufacturer, aiming to discover whether the detection algorithm reduces the precision of the angle observations.

Apart from the *wire detection algorithm*, for the micro-triangulation measurements we also use the *circle detection algorithm*, which was developed prior to and independently of this study (see also Section 1.4.4). Hence, the secondary objective of this chapter is the performance evaluation of the circle detection algorithm under similar conditions as in the case of the wire detection algorithm.

The test measurements described in this chapter can be easily acquired due to the high-level automation of the measuring system, with the most time-consuming part to be the installation of the measuring system and its configuration. To ensure the reproducibility of the results, we repeated these measurements many times at different locations and different time periods. Here, we present and discuss a representative sample of the acquired measurements, given the fact that the results of the different measurement campaigns were consistent.

3.2 Methodology

3.2.1 Location and time

The test measurements presented in this chapter took place at CERN, in the building 375/T1-A03, on the weekend of February 25 – 26, 2017. This place is part of the experimental hall used to host the Intersecting Storage Rings (ISR) back in 70s – 80s, while in 2017 it was used for magnetic measurements. The building is covered by soil and it has a massive concrete floor, resulting in both, temperature stability and vibration isolation, especially during the weekends, when there is no activity in the building or around it. It is worth mentioning that the ISR began operation in 1971 and ran until 1984, holding the luminosity record for hadron colliders until 2004. Moreover, on January 27, 1971, two beams of protons collided in the ISR for the first time (*ISR@CERN*, 2018).

3.2.2 Instruments and configuration

A QDaedalus measuring system (see Section 1.4) mounted on a Leica TDA5005 theodolite was used for the test measurements. The QDaedalus system consisted of the CCD camera and the focusing mechanism, while the additional divergence lens was not used, since the distances between the instrument and the targets were less that 13 m.

The TDA5005 was mounted on a Leica MST36 carbon-fiber tripod (Figure 3.2a ①). The optical axis of the TDA5005 was at about 1.15 m above the ground. The parts of the configuration were installed a few days before the measurements in order to be well acclimatized. Moreover, both, the QDaedalus and the TDA5005 were connected to a power converter in order to stay switched-on for the entire measurement period.

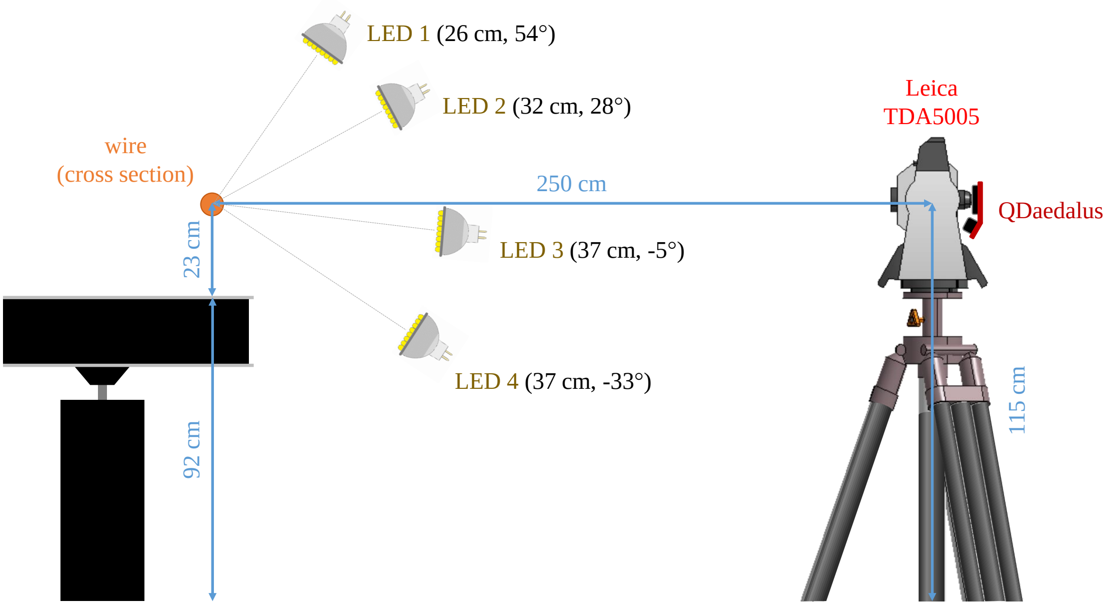

Figure 3.1: Test measurement configuration (not to scale).

Two data loggers HygroLog HL20, by Rotronic AG, were used to record the temperature variation during the test measurements. According to the manufacturer, this specific model has an accuracy of 0.2 °C at 23 °C. One of the temperature sensors was placed under the tripod, approximately 50 cm above the floor level (Figure 3.2a 2), while the second was placed close to the targets on the optical table (Figure 3.2a 3). The log interval was set to 15 s for both sensors.

A piece of monofilament Copper-Beryllium wire (⌀100 µm) was used as target for the wire detection algorithm. The wire was stretched horizontally, perpendicularly to the optical axis of the theodolite and at the same height with it, i.e., approximately 23 cm above the optical table surface (Figure 3.1). Each extremity of the wire was supported by a pair of tangent ceramic spheres (⌀8 mm). The wire was stretched by the force of an

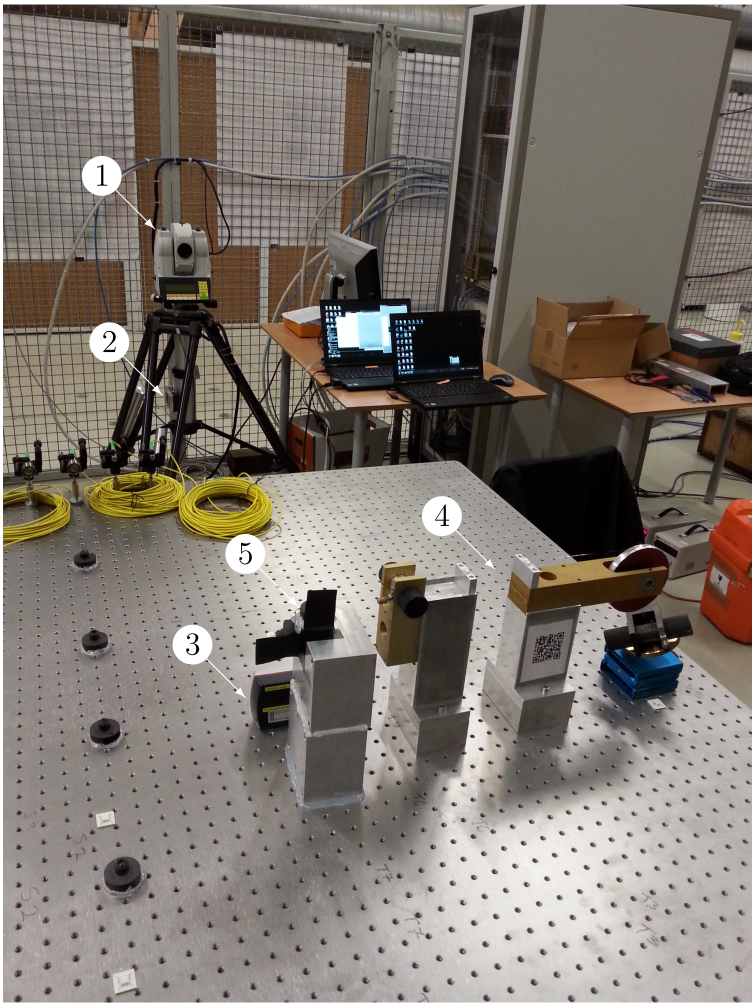

(a)

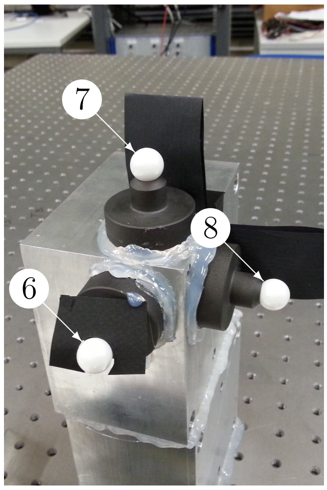

(b)

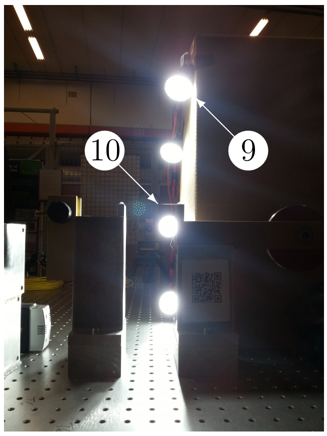

(c)

Figure 3.2: (a) Test measurement configuration, (b) Ceramic spherical targets, (c) LED lamps were used to illuminate the wire.

approximately 700 g suspended mass, and the hanging length of the wire was about 8.5 cm (Figure 3.2a ④).

Ceramic spheres of 12.7 mm (0.5 inch) diameter were used as targets for the circle detection algorithm. The ceramic targets were mounted on aluminium supports with magnetic force, and then, the supports were glued with hot glue on aluminium blocks. Subsequently, the aluminium blocks were also glued with hot glue on the optical table (Figure 3.2a ⑤). To increase the stability of the setup, special care was taken to ensure that the surfaces of all the components were in contact, without layers of glue in between. Three targets were used with their supports being placed in specific directions (Figure 3.2b):

- the *Front* target (Figure 3.2b ⑥) was oriented towards the theodolite (aligned to the optical axis and horizontal),
- the *Up* target (Figure 3.2b ⑦) was oriented towards the ceiling (perpendicular to the optical axis and vertical), and
- the *Side* target (Figure 3.2b ⑧) was perpendicular to the other two (i.e., perpendicular to the optical axis and horizontal).

The wire and the spherical targets were placed on an optical table at a distance of 2.5 m away from the theodolite and approximately at the same height with it (Figure 3.1).

Finally, four LED lights (Figure 3.2c ⑨), a black sheet of paper and a white sheet of paper were used for the investigation of the influence of the light conditions and the background intensity on the wire measurements. The main characteristics of the LED lights are: 5 W power consumption, 6500 K color temperature, 450 lm luminosity and 120° diffusion angle. The lights were placed around the wire (Figure 3.2c ⑩) in a distance of about 30 cm and in various directions (Figure 3.1). A detailed description of the scenario of these experiments is given in Section 3.4.4.

3.2.3 Temperature and light conditions

We consider two main ambient factors that may affect the measurements; the temperature variation and the light conditions. The temperature variation can affect the internal geometry of the measuring system, the relative position of the theodolite and the target, as well as the optical path. The light conditions are expected to influence the result of the measurements, given the fact that the observations are based on passive optical images.

As we mentioned earlier, the building is covered by soil and is expected to demonstrate stable temperature conditions. To quantify the level of stability, we recorded the air temperature in two positions (close to the targets and close to the theodolite) during the test measurements. Figure 3.3 depicts the temperature variation for the two sensors. Each point of the time series is calculated as the average of 40 recorded values, i.e., one point for every 10 min. The graph shows an extremely small temperature variation that stays within 0.15 °C during the weekend. We can also notice the high level of agreement between the two sensors.

Although this variation can be considered negligible for such measurements, we used a carbon-fiber tripod for the theodolite and an optical table for the targets in order to diminish the influence of any abrupt temperature variation. Moreover, we left the equipment

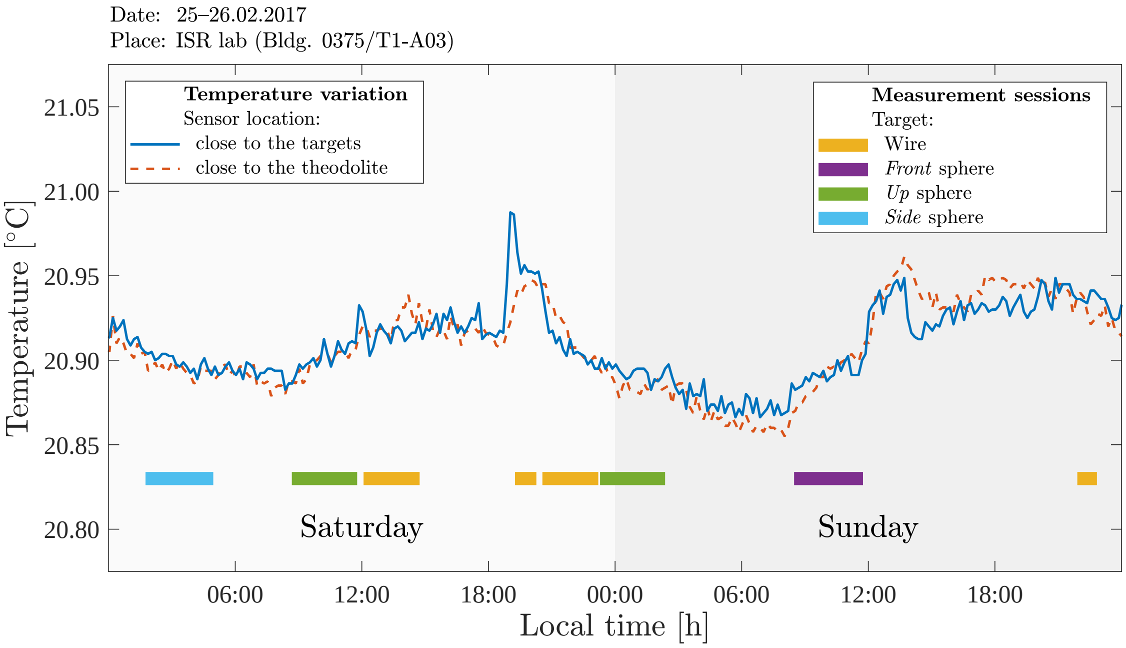

Figure 3.3: Temperature variation in the ISR lab during the measurement campaign.

to acclimatize in the experimental area for a few days and we warmed up the measuring systems (theodolite and CCD camera) for at least a day before the measurement campaign.

Regarding the light conditions, these are created only by the artificial light emitted from the ceiling light bodies, which are located about 8 m above the floor. The experimental hall can also be switched to emergency lights resulting in a much darker room that enabled test measurements with additional directional light sources (Figure 3.2c).

3.2.4 Observations and data processing

For each parameter P under examination — either this is a user-defined parameter or an ambient condition — several values p_k were selected for testing, with $k \in \{1, 2, \dots, M\}$. For each value p_k, several measurements x_i were acquired, with $i \in \{1, 2, \dots, n_k\}$.

Each measurement consists of a *horizontal direction* and a *zenith angle* observation, measured in the two faces of the theodolite. The reduced values for each measurement are calculated using the double-face observations:

$$H_i = \frac{H_i^I + (H_i^{II} - \pi)}{2} \tag{3.1}$$

$$Z_i = \frac{Z_i^I + (2\pi - H_i^{II})}{2} \tag{3.2}$$

where

H_i is the reduced observation of the horizontal direction (or the horizontal angle between an arbitrary direction and a target) measured along the horizontal circle of the theodolite.

H_i^I, H_i^{II} are the horizontal directions measured in the *face I* (or *left face*) and the *face II* (or *right face*) telescope positions of the theodolite, respectively.

Z_i is the reduced observation of the zenith angle (or the vertical angle between the zenith of the observer and a target) measured along the vertical circle of the theodolite.

Z_i^I, Z_i^{II} are the zenith angles measured in the *face I* (or *left face*) and the *face II* (or *right face*) telescope positions of the theodolite, respectively.

In the following graphs, instead of the zenith angle Z_i — which is the theodolite reading — we chose to use the complementary *altitude* or *elevation angle* E_i in order to facilitate the reader with the sense of the up and down directions. The elevation angle is the vertical angular distance between the local horizon and a target, which is computed as

$$E_i = \frac{\pi}{2} - Z_i \tag{3.3}$$

Moreover, we use the µrad (or µm m^{-1}) unit, which is more intuitive than the gon or grad units that are typically utilized by surveyors and geodesists.

The statistical sample $\mathcal{S}$ consists of the total number of measurements x_i, with $i \in \{1, 2, \ldots, N\}$, where

$$N = \sum_{k=1}^{M} n_k \tag{3.4}$$

The sample mean $\bar{x}_{\mathcal{S}}$ is computed for the set $\mathcal{S}$:

$$\bar{x}_{\mathcal{S}} = \frac{1}{N} \cdot \sum_{i=1}^{N} x_i, \quad x_i \in \mathcal{S} \tag{3.5}$$

In addition, for each parameter value p_k we consider a subset $\mathcal{P}_k \subseteq \mathcal{S}$. For the n_k number of elements of the subset $\mathcal{P}_k$ we compute the sample mean $\bar{x}_{\mathcal{P}_k}$ and the sample variance $s^2_{\mathcal{P}_k}$:

$$\bar{x}_{\mathcal{P}_k} = \frac{1}{n_k} \cdot \sum_{i=1}^{n_k} x_i, \quad x_i \in \mathcal{P}_k \tag{3.6}$$

$$s^2_{\mathcal{P}_k} = \frac{1}{n_k - 1} \cdot \sum_{i=1}^{n_k} (x_i - \bar{x}_{\mathcal{S}})^2, \quad x_i \in \mathcal{P}_k \tag{3.7}$$

as well as the variance of the mean value $s^2_{\bar{x}_{\mathcal{P}_k}}$:

$$s^2_{\bar{x}_{\mathcal{P}_k}} = \frac{s^2_{\mathcal{P}_k}}{n_k} \tag{3.8}$$

For a better and consistent visualization in the graphs to follow, we refer the reduced angle observations x_i to the sample mean $\bar{x}_{\mathcal{S}}$ by plotting the respective residuals r_i:

$$r_i = x_i - \bar{x}_{\mathcal{S}}, \quad x_i \in \mathcal{S} \tag{3.9}$$

where the mean of the residuals $\bar{r}_{\mathcal{S}}$ is zero by definition:

$$\bar{r}_{\mathcal{S}} = \frac{1}{N} \cdot \sum_{i=1}^{N} r_i \equiv 0 \tag{3.10}$$

Correspondingly to Equations 3.6 and 3.7, the mean of the residuals for each parameter value p_k is

$$\bar{r}_{\mathcal{P}_k} = \bar{x}_{\mathcal{P}_k} - \bar{x}_{\mathcal{S}} \tag{3.11}$$

and the variance $s^2_{\bar{r}_{\mathcal{P}_k}}$ of the mean value $\bar{r}_{\mathcal{P}_k}$ is

$$s^2_{\bar{r}_{\mathcal{P}_k}} = s^2_{\bar{x}_{\mathcal{P}_k}} \tag{3.12}$$

The quantities presented in this section are used to define confidence intervals and to perform statistical tests according to the formulation given in Appendix B, in which the corresponding values for each parameter under examination are also listed.

3.3 Qualitative evaluation of the wire detection algorithm

The qualitative evaluation aims to validate the ability of the algorithm to detect the Copper-Beryllium wire in different cases as they are summarized in the following list:

- **Angle of incidence**: In Figure 3.4a, the wire is perpendicular to the optical axis of the theodolite (0° angle of incidence), while in Figure 3.4b, the wire forms a 30° angle with the optical axis (60° angle of incidence). In Figure 3.4b, the wire appears as a double cone due to the shallow depth of field of the optical system, thus, only the central part of the wire is in focus.
- **Background**: Figures 3.4a, 3.4c and 3.4d show the tests of the algorithm in a large range of gray background intensities, from a very dark to a very bright. The background intensity has an influence on the result of the measurement as we will demonstrate in Section 3.4.4.
- **Focus**: Figure 3.4a depicts the wire in focus. However, in Figure 3.4e, the image is focused in front of the wire, and in Figure 3.4f, the image is focused behind the wire. In Section 3.4.2, we demonstrate that a slightly improper focus has no influence on the result of the measurement.
- **Orientation**: In Figures 3.4a, 3.4g and 3.4h, we see the wire being horizontal, vertical and in about 45° inclination with respect to the image. In all the cases the wire remains perpendicular to the optical axis.

Sample images for each case are presented in Figure 3.4. For these tests, the wire was placed at a distance of about 2.5 m from the theodolite, which is estimated to be the average distance for the micro-triangulation network measurements discussed in Chapter 5.

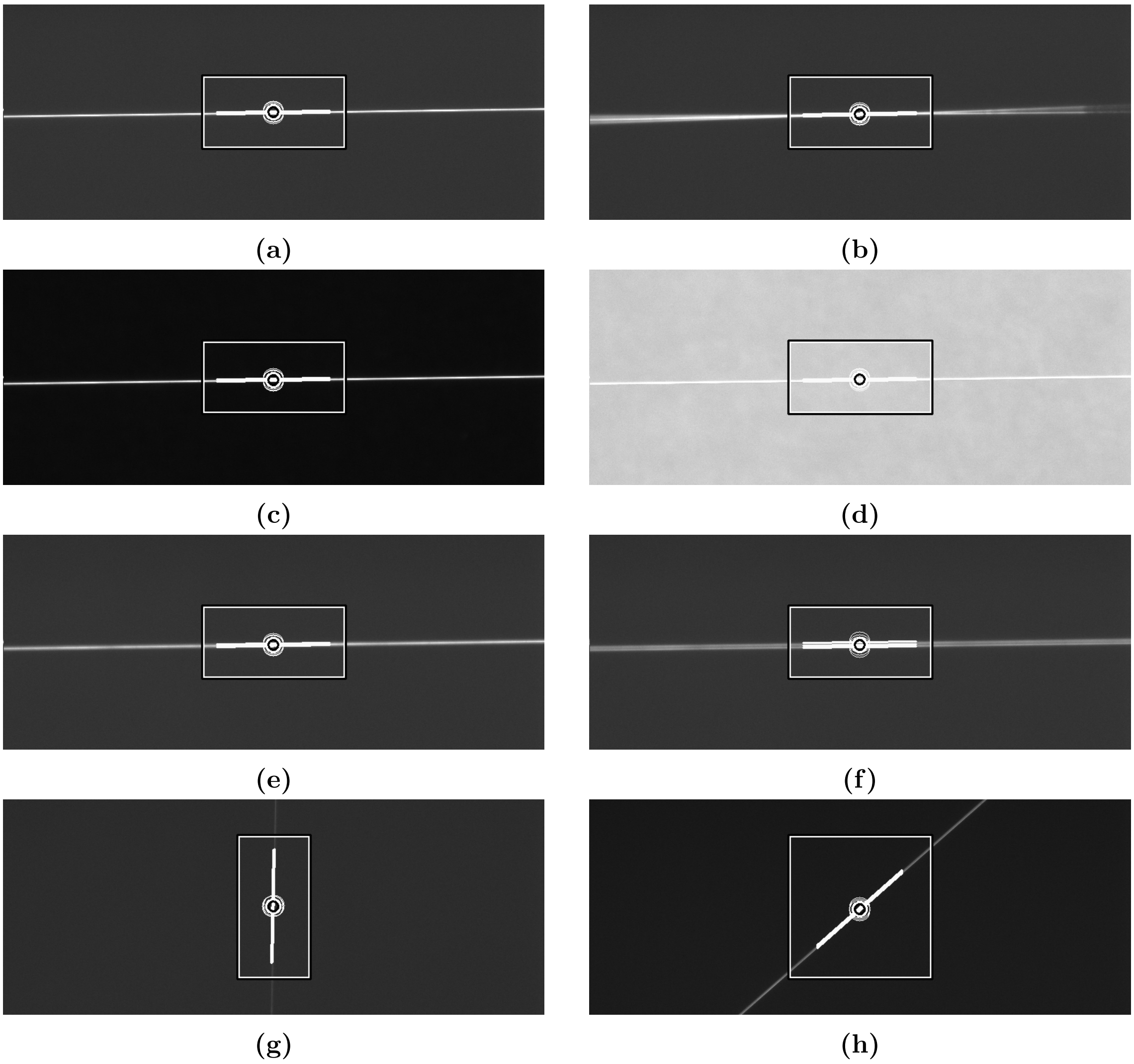

Figure 3.4: Sample images illustrating different conditions for the wire detection algorithm on a Copper-Beryllium wire: (a) wire on a gray background, in focus, horizontal and perpendicular to the optical axis, (b) wire in a 60° angle of incidence with the optical axis, (c) wire on a dark background, (d) wire on a bright background, (e) focus in front of the wire, (f) focus behind the wire, (g) vertical wire, (h) a 45° inclined wire.

In each image of Figure 3.4, we notice a circle and a line inside the rectangular region of interest. The line represents the estimated wire axis in the image, while the circle represents a point on the axis, which is the expected result of the algorithm. Therefore, we ensure that the developed wire detection algorithm is able to acquire measurements in all the aforementioned cases. After the successful qualitative evaluation, we are confident that the wire detection algorithm can be used in micro-triangulation measurements for magnet fiducialization and alignment applications.

3.4 Performance evaluation of the wire detection

The parameters under examination are categorized in different groups according to their nature. For example, the used-defined parameters *Shutter*, *Gain* and *Focus* change the appearance of the acquired image, so they are categorized as *image parameters*, while the *environmental conditions* are related to changes in the ambient light condition and the background intensity.

For each experiment we tested several parameter values, starting always from the same set of reference values. The range of the values for each experiment were chosen in such a way that the detection should be successful for the vast majority of the measurements. Extreme values that are not probable to be selected under normal laboratory conditions were also included. In Table C.1, we see the reference parameter values for the wire detection, arranged in the same sequence and with the same name as they appear in the QDaedalus software interface.

Supporting material relevant to the test measurements of the wire detection algorithm, such as sample images and tables of parameter values, are presented in Appendix C.

For the wire detection algorithm, we present only the elevation angles. The horizontal angles demonstrate a large dispersion that cannot be used for the current evaluation. This behavior is expected, due to the fact that there is no distinct point on the wire to be used as a target for the horizontal angle measurement. Therefore, in order to isolate the targeting ambiguity in the horizontal angles, we chose to observe a horizontal wire from a position in the perpendicular direction to the wire axis, and at the same height with it (Figure 3.1).

Each of the following graphs illustrates the measurement series of the parameters under examination. The X-axis represents the local time in hours and the Y-axis represents the residuals of the elevation angle with respect to the corresponding sample mean (Equation 3.9), expressed in µrad.

Each color represents a different parameter value. For each parameter value, the mean of the residuals (Equation 3.11) is depicted with a horizontal black line that extents over the sample. The vertical black line represents the confidence interval for a 95 % confidence level, according to Equation B.4. In the background, we see the $\pm 1\sigma$, $\pm 2\sigma$ and $\pm 3\sigma$ confidence intervals with respect to the manufacturer σ, according to Equations B.2 and B.3.

3.4.1 Acquisition parameters

Two user-defined parameters are categorized as acquisition parameters: the number of camera shots (*# shots* parameter), and the maximum permissible standard deviation (*Std shot* parameter), expressed in pixels. The first parameter indicates the number of the shots to be averaged in order to get one set of image coordinates for a target. The second parameter is the upper threshold of the standard deviation of the image coordinates acquired from each shot. If the standard deviation of the sample is over the user-defined threshold, then the measurement with the larger residual is rejected, following an iterative process.

For the *# shots* parameter we chose the values: 3, 5 and 10 shots, keeping the rest of the parameters the same, while for the *Std shot* parameter we chose the values 0.05, 0.10

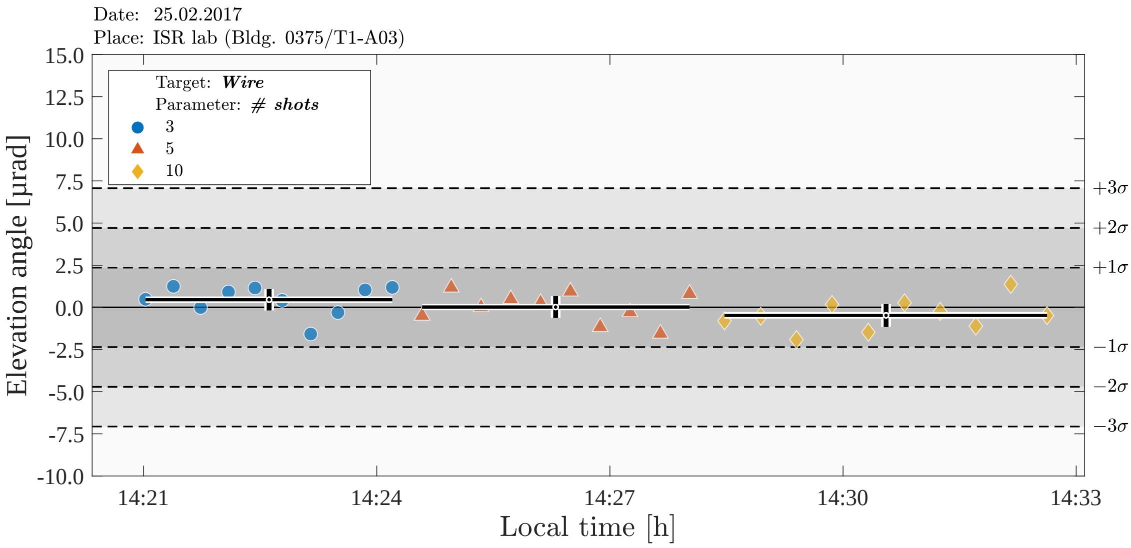

Figure 3.5: Scatter of the elevation angle to the wire for different values of the *# shots* parameter.

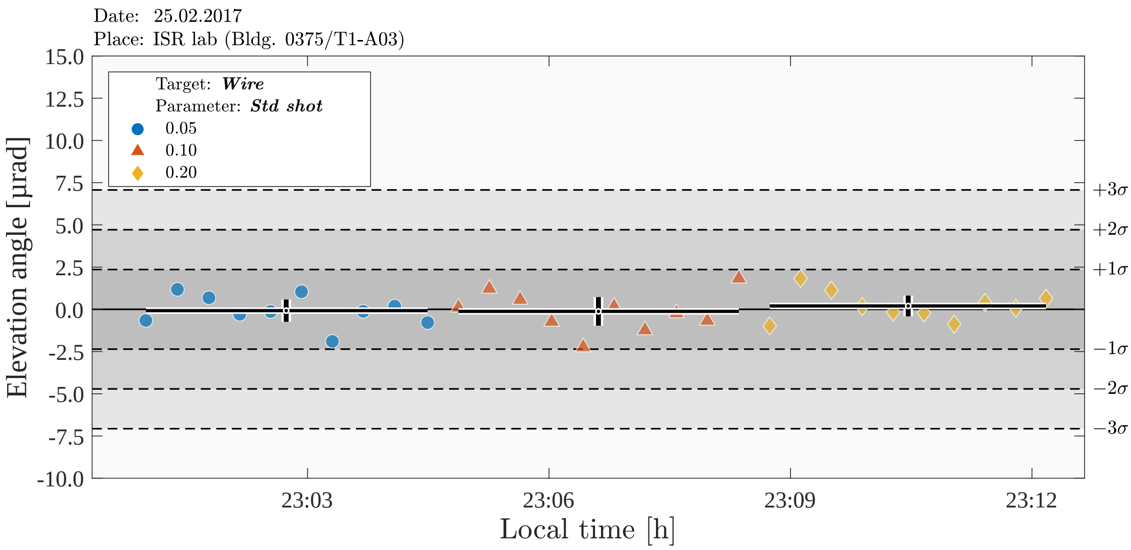

Figure 3.6: Scatter of the elevation angle to the wire for different values of the *Std shot* parameter.

and 0.20 pixels. The full set of the parameter values for these two experiments are given in Tables C.2 and C.3. A typical image of the wire, corresponding to these parameters, is shown in Figure C.1.

In Figures 3.5 and 3.6, we notice that neither of these two parameters significantly affects the result of the measurement in terms of precision and accuracy. More specifically, for both parameters the results of the statistical tests, presented in Tables B.1 and B.2, suggest that the variance $s^2_{\mathcal{P}_k}$ for each parameter value p_k is statistically smaller than the variable σ^2 for a 95 % confidence level, as well as that there is no significant bias between the mean values $\bar{r}_{\mathcal{P}_k}$ for a 99 % confidence level.

3.4.2 Image parameters

The exposure time or shutter speed (*Shutter* parameter), the CCD sensor gain (*Gain* parameter) and the number of steps of the focusing mechanism (*Focus* parameter) are categorized as image parameters, because these parameters affect the appearance of the raw image. For each parameter we select seven different values. More precisely:

- For the *Shutter* parameter, we select the values from 210 ms to 390 ms, in intervals of 30 ms (Figure 3.7). The full set of the parameter values is shown in Table C.4, while in Figure C.2 we see sample images for each value.
- For the *Gain* parameter, we select the values from 110 to 290, in intervals of 30 (Figure 3.8). Table C.5 contains the parameter values and Figure C.3 illustrates the corresponding sample images.
- For the *Focus* parameter, we select the values from 108 000 to 108 600 steps, in intervals of 100 steps (Figure 3.9). The focus parameter values (Table C.6) correspond to the number of steps for the stepper motor that controls the focusing knob of the theodolite. These specific values are selected in order to set the optical system from focusing in front of the wire up to focusing behind the wire, as depicted in Figure C.4.

Figures 3.7, 3.8 and 3.9 correspond to the experiments for the *Shutter*, *Gain* and *Focus* parameters, respectively. In all three graphs we do not observe any significant effect on the result of the measurement while switching among the different parameter values.

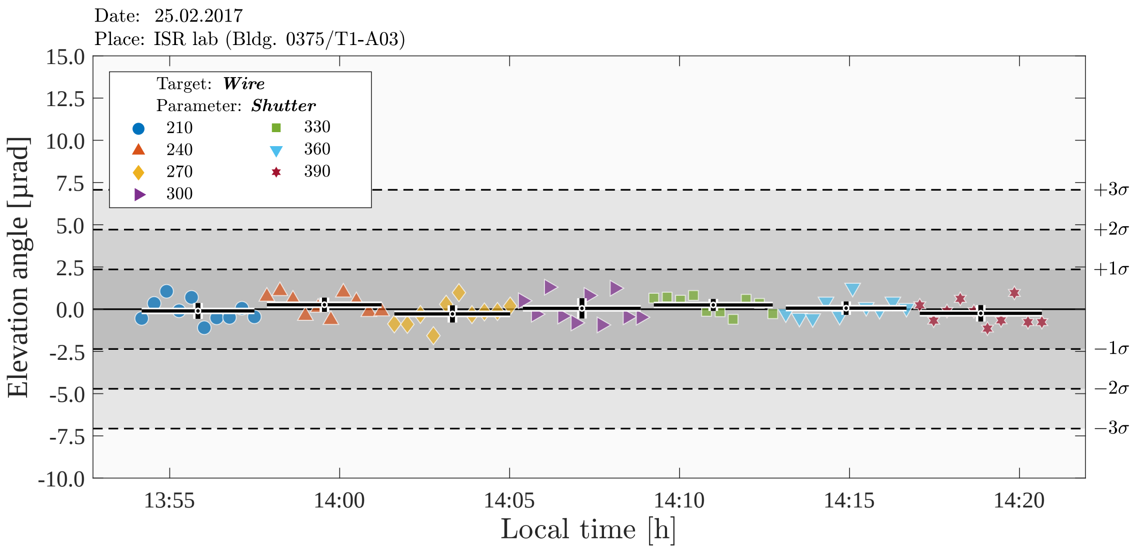

Figure 3.7: Scatter of the elevation angle to the wire for different values of the *Shutter* parameter.

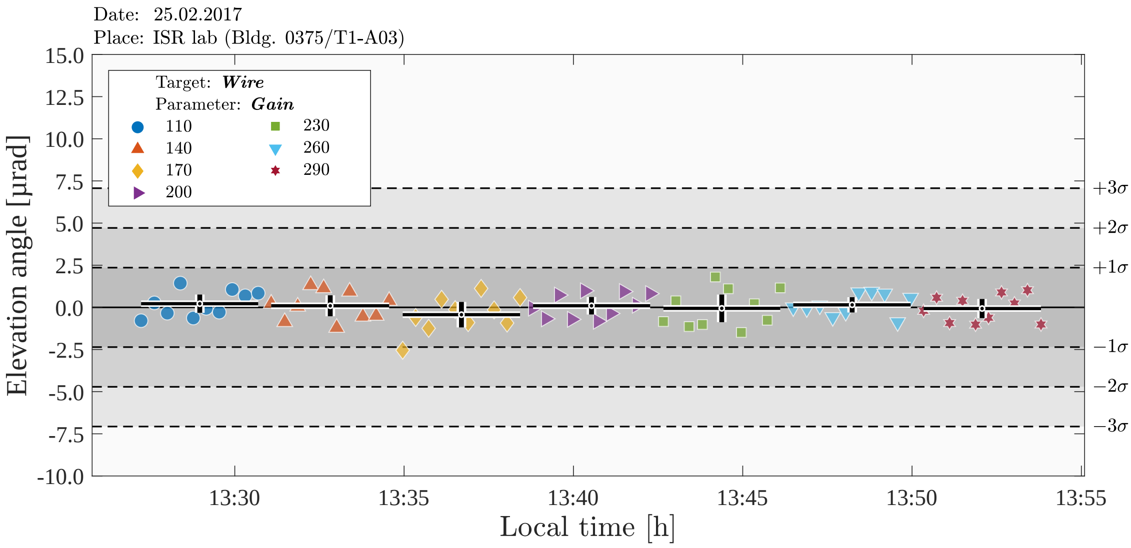

Figure 3.8: Scatter of the elevation angle to the wire for different values of the *Gain* parameter.

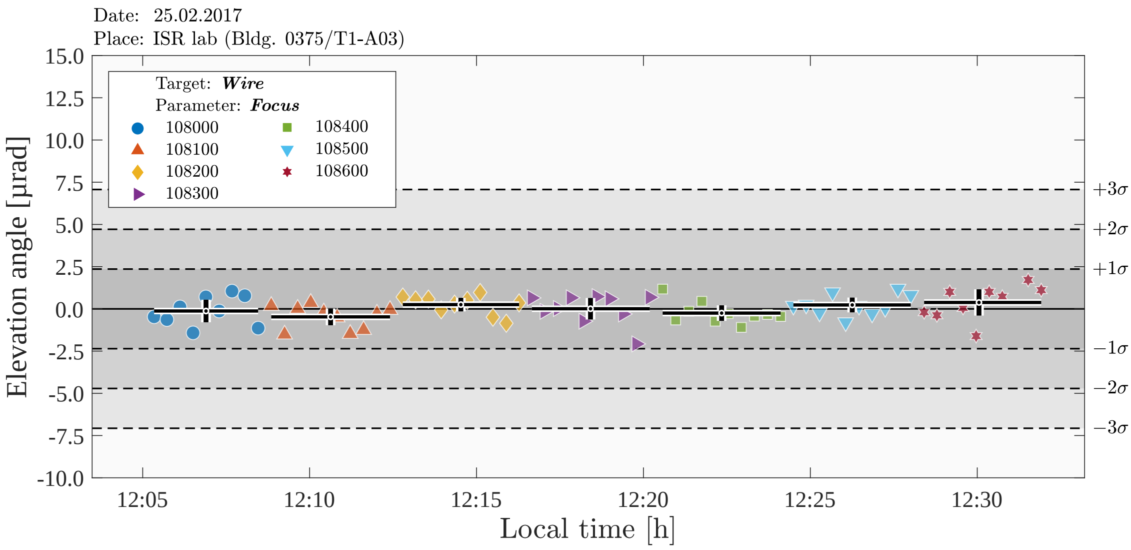

Figure 3.9: Scatter of the elevation angle to the wire for different values of the *Focus* parameter.

According to the results of the statistical tests (Tables B.3, B.4 and B.5), the variance for each parameter value is statistically smaller than σ^2 for a 95 % confidence level, while there are no significant biases for a 99 % confidence level.

3.4.3 Detection parameters

This section concerns two parameters that are relevant to the detection algorithm: the half-width of the region of interest window (*HW ROI* parameter), which determines the part of the depicted wire that is taken into consideration for the measurement, and the Canny edge detection threshold (*Canny thres* parameter), which defines the sensitivity of the edge detection, therefore, it is related to the contrast between the target and the background. More analytically:

- For the *HW ROI* parameter, we select the values from 50 to 350 pixels, in intervals of 50 pixels (Figure 3.10). This range corresponds from a very small region of interest up to a window that contains the whole length of the wire depicted in the image (Figure C.5). For each value, it is necessary to also tune the user-defined parameter *Min #pts*, which is the minimum permissible number of the edge points that participate in the line fit (for more details see Section 2.4.3). Table C.7 presents the full set of the parameter values.

- For the *Canny thres* parameter, we select the pixel intensities from 60 to 180, in intervals of 20 (Figure 3.11). These values correspond to the difference in the intensities of adjacent pixels that will be considered as edge. The full set of the parameter values for this experiment are given in Table C.8, while in Figure C.6, we present the Canny edge image in the region of interest for all the cases.

As we notice in Figures 3.10 and 3.11, there is no significant impact on the result of the measurement for both parameters. The statistical tests in Tables B.6 and B.7 also suggest that the variance for every parameter value is statistically smaller than σ^2 for a 95 % confidence level, and that the mean values $\bar{r}_{\mathcal{P}_k}$ of the parameter values do not demonstrate any bias for a 99 % confidence level.

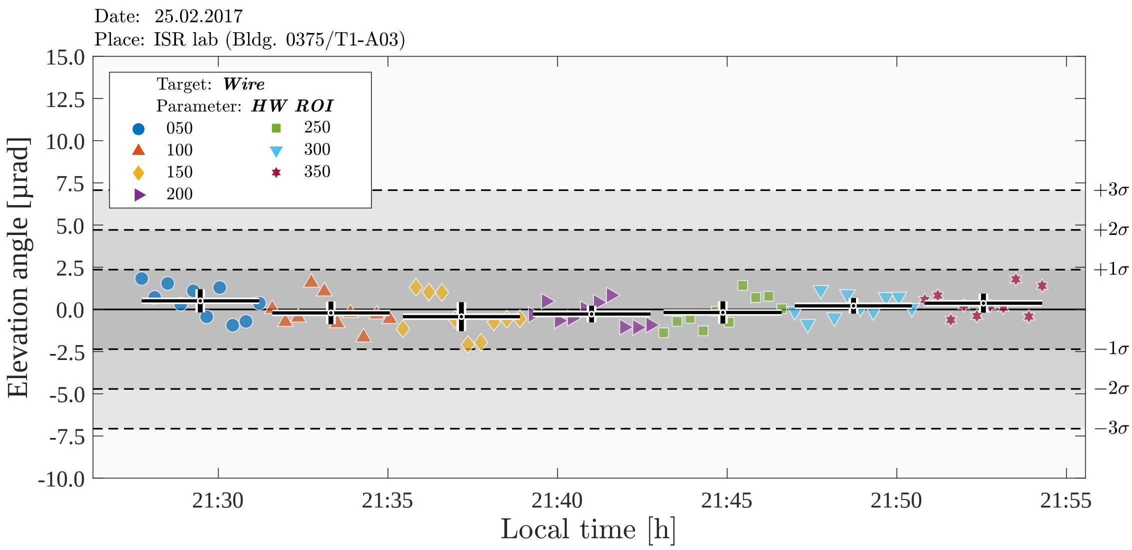

Figure 3.10: Scatter of the elevation angle to the wire for different values of the *HW ROI* parameter.

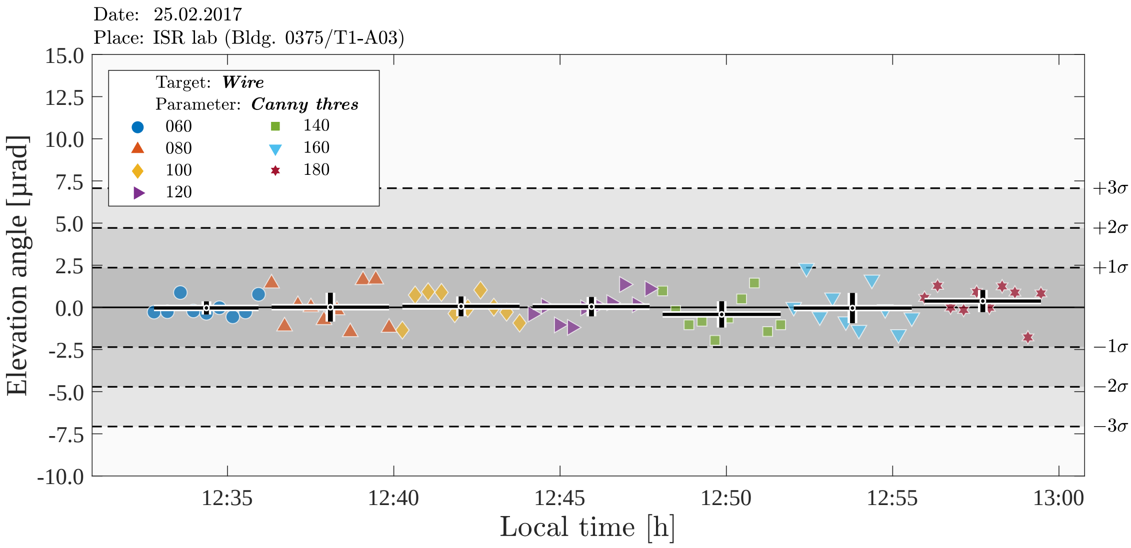

Figure 3.11: Scatter of the elevation angle to the wire for different values of the *Canny thres* parameter.

3.4.4 Environmental conditions

In this section, we evaluate the performance of the wire detection algorithm under different *Background* intensities and *Light* conditions. For these experiments, the user-defined parameter values mostly remain the same (Tables C.9 and C.10). Only a few small changes were required for the *Light* conditions experiment in order to improve the detection of the wire.

Background intensity. Except from the usual grey color background generated by the objects that are out of focus and far behind the wire, we created a much darker and a much brighter background. This was achieved by using pieces of black and white paper located a few centimetres behind the wire. The sample images of these three cases are shown in Figure C.7. During the measurement, the background was carefully swapped a few times, avoiding to cause any vibration to the setup.

In Figure 3.12, we observe that the scatter in each case is not affected, while there is an obvious bias caused by different background intensities. This observation is verified by the statistical tests shown in Table B.8. The wire consistently appears to be measured higher in case it is in front of the black background. This is caused by the fact that the shadow of the wire cannot be distinguished from the black background, so the wire appears thinner and therefore its axis is displaced upwards.

Light condition. We created seven cases (Figure C.8) to examine this parameter. In the first case, only the ceiling lights of the laboratory were switched on. In the second case, the hall was illuminated only by the security lights, which results in a low illumination in the hall. In the next four cases, while only the security lights were switched on, we switched on one LED light each time (Figure 3.2a). In the last case, we switched on all the LED lights simultaneously (see Figure 3.2c), while still keeping switched on only the security lights of the laboratory.

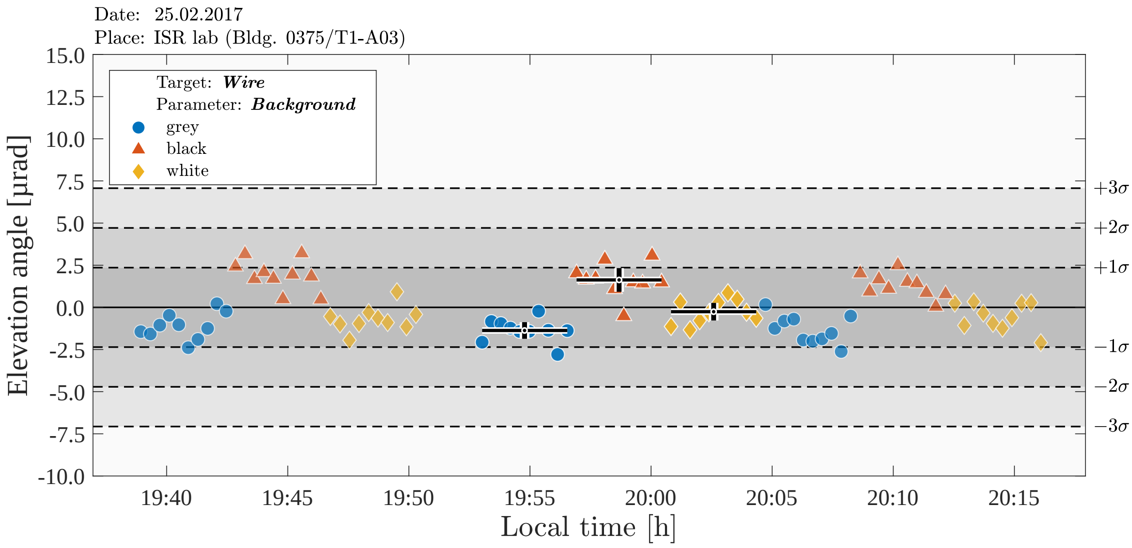

Figure 3.12: Scatter of the elevation angle to the wire for different *Background* intensities.

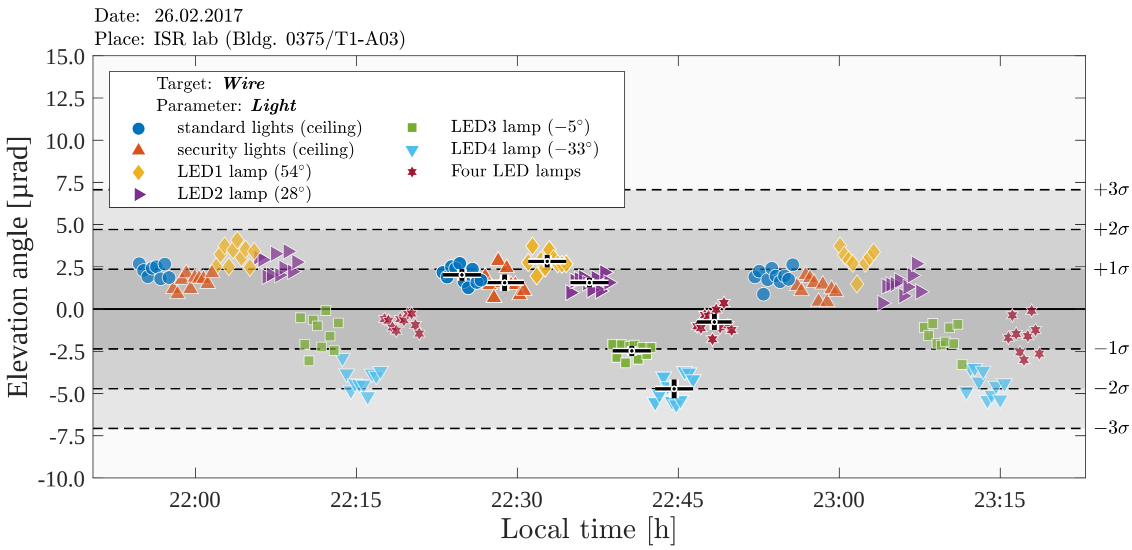

Figure 3.13: Scatter of the elevation angle to the wire for different *Light* conditions.

In Figure 3.13, we observe that although the variance of each set does not significantly change (see also the result of the statistical tests in Table B.9), there are biases between the mean values for the different light conditions. It is clear that the measurements for the first four cases are more consistent, compared to the rest of the cases. This can be linked to the fact that in the first four cases the light source is above the wire, despite the different intensities and distances between the light sources and the wire.

This effect is similar to that observed in the *Background* experiment. When the wire is illuminated from above, a shadow is created at the bottom part of the wire, causing the wire axis to appear in a higher position.

From these two experiments we conclude that the ambient conditions, i.e., the illumination of the target and the background intensity, affect the value of a measurement but not its variance. Such a behavior is expected, given the fact that the observation is based on passive optical measurements that are susceptible to light and contrast variations.

3.4.5 Session and campaign summary

The experiments concerning the various used-defined parameters were executed sequentially in a session of measurements. In Figure 3.14, the measurements of one *Session* are shown together. Moreover, in order to confirm the results, we repeated the measurement sessions for several times. In Figure 3.15, a *Campaign* of two sequential sessions is summarized.

In both figures, we observe a high stability of the setup for about 12 h. Drifts that are very small with respect to the level of precision are noticeable, most probably caused by the temperature variation. It is also noticeable that the wire detection algorithm provides an excellent robustness against different values of the user-defined parameters. The mean of the standard deviation values ($s_{\mathcal{P}_k}$) for the 41 sets of the zenith angle measurements to the wire (Tables B.1 – B.7) is 0.79 µrad, which is approximately three times better than the precision specified by the manufacturer of the theodolite (approximately 2.4 µrad).

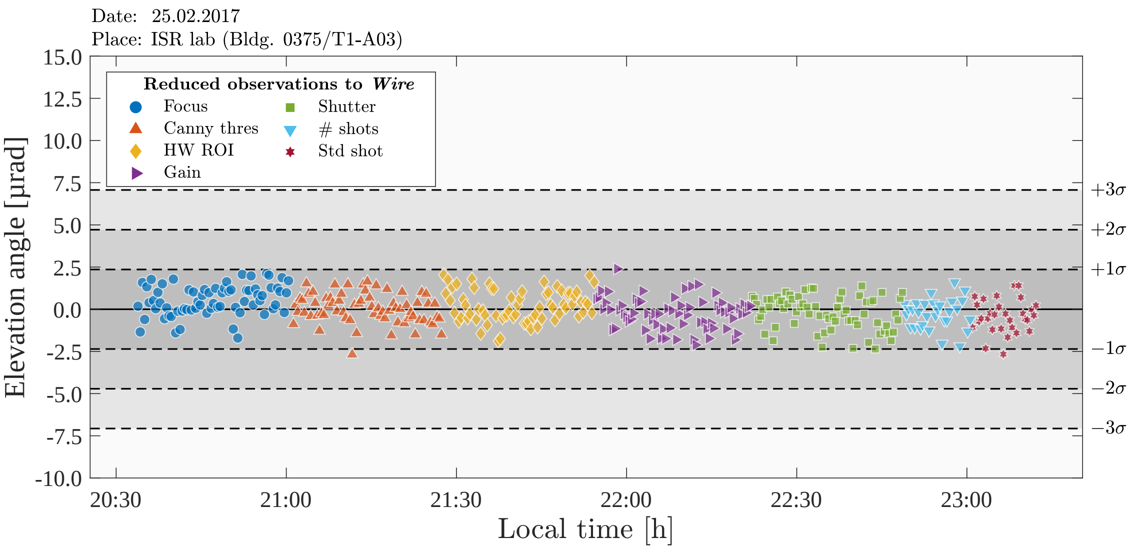

Figure 3.14: Scatter of the elevation angle to the wire for a measurement *Session* that consists of the subgroups of measurements for all user-defined parameters under examination.

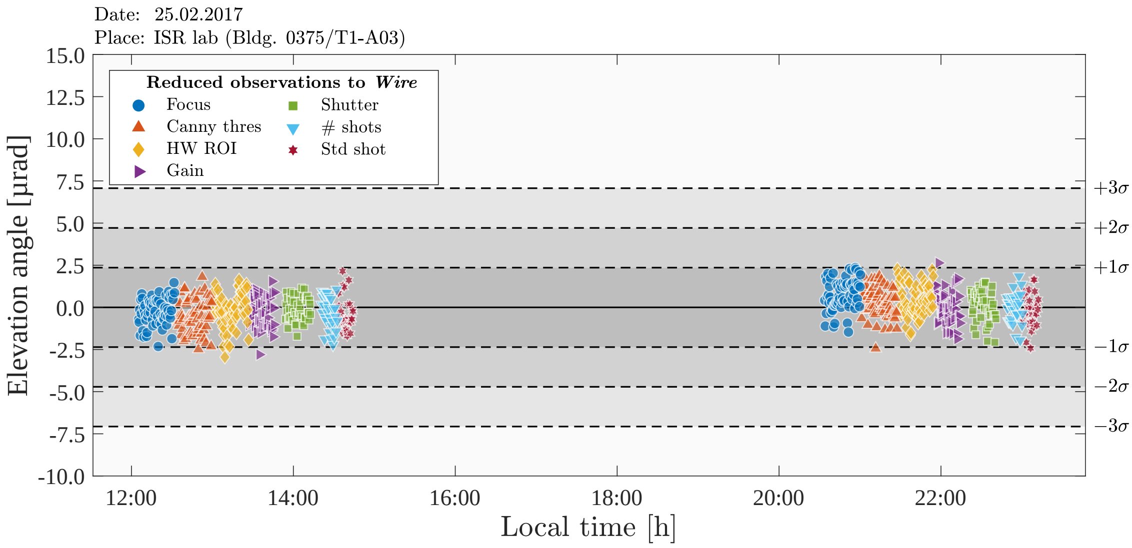

Figure 3.15: Scatter of the elevation angle to the wire for a measurement *Campaign* that consists of two sequential sessions.

3.5 Performance evaluation of the circle detection

The experiments for the circle detection algorithm are designed and executed in the same way as for the wire detection algorithm. Although the circle detection algorithm was not developed in the frame of this study, we decided to proceed to these experiments due to the fact that this algorithm will be used for the test measurements of the micro-triangulation for magnet fiducialization and alignment applications.

The experiments are categorized in three groups, following the same criteria as for the wire detection parameters. Compared to Section 3.4, there are identical experiments (i.e., for the parameters *# shots*, *Std shot*, *Shutter*, *Gain*, *Focus* and *Canny thres*), omitted experiments (i.e., for the parameters *HW ROI*, *Background* and *Light*), and new experiments (i.e., for the parameters *Hz direction* and *Zen angle*).

For the evaluation of the circle detection algorithm, we used three spherical targets that have different orientation with respect to the theodolite. The three targets are described in Sections 3.2.2 and they are shown in Figure 3.2b. Due to the fact that the acquired results are practically identical for the three targets, we choose to present representative samples for all the parameters. Figure D.1 illustrates sample images of the *Front*, *Side* and *Up* target, and Tables D.1, D.2 and D.3 contain the corresponding reference parameter values.

Supporting material relevant to the test measurements of the circle detection algorithm, such as sample images and tables of parameter values, are presented in Appendix D.

3.5.1 Acquisition parameters

Similar to the wire detection algorithm results, there is no significant effect of the acquisition parameters *# shots* and *Std shot* on the variance of the horizontal and elevation angle measurements (Figures 3.16 and 3.17). Moreover, there is no significant bias for

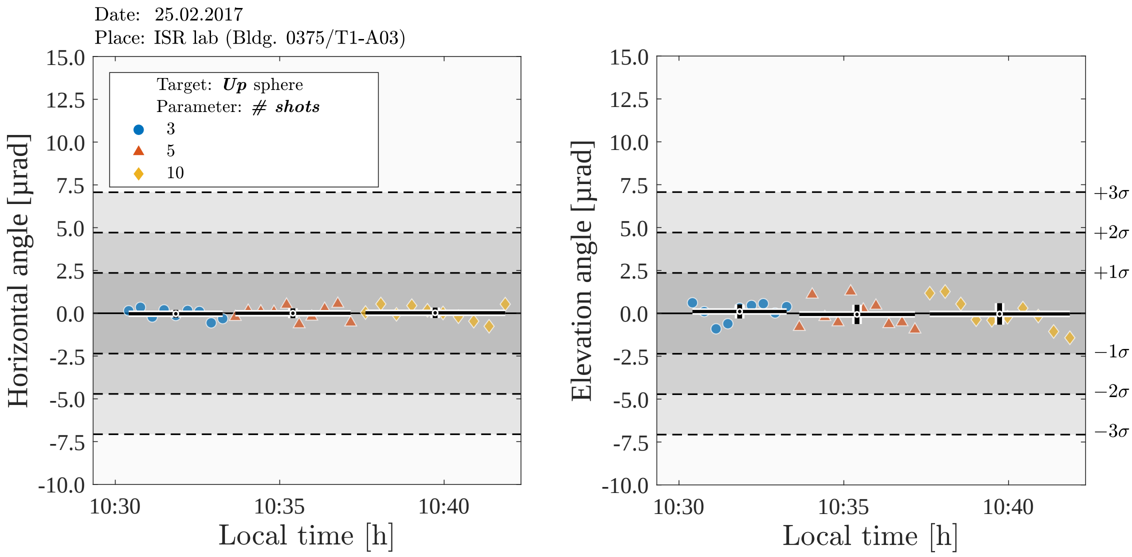

Figure 3.16: Scatter of the horizontal and elevation angles to the *Up* spherical target for different values of the # *shots* parameter.

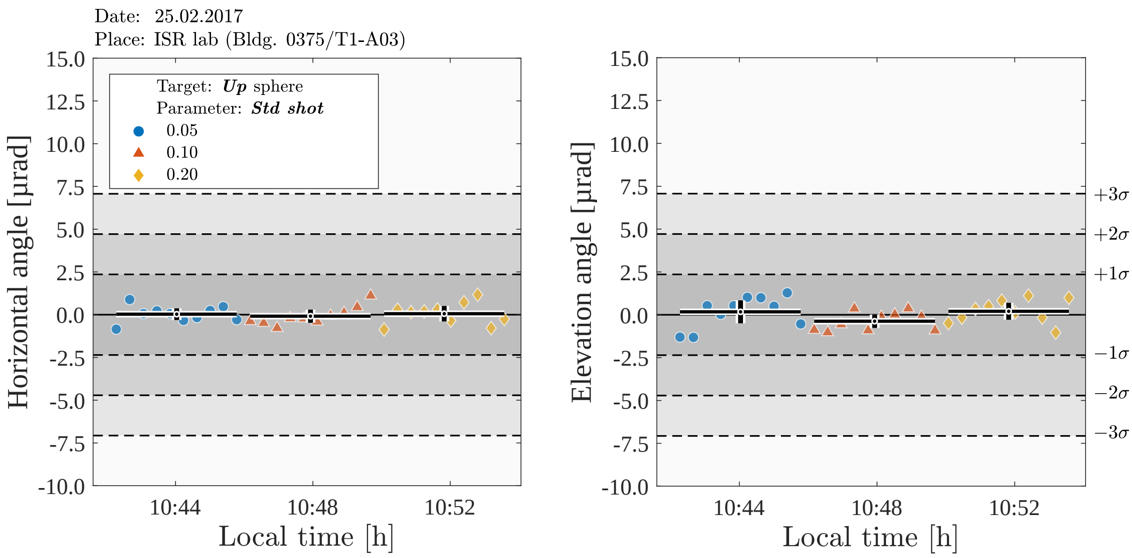

Figure 3.17: Scatter of the horizontal and elevation angles to the *Up* spherical target for different values of the *Std shot* parameter.

the horizontal angle, according to the results of the statistical tests given in Tables B.10 and B.12, and for the elevation angle (Tables B.11 and B.13). The complete set of the parameter values for the two experiments of this category, concerning the *Up* target, can be found in Tables D.4 and D.5.

3.5.2 Image parameters

The influence of the exposure time (*Shutter* parameter), the CCD sensor gain (*Gain* parameter) and the number of steps of the focusing mechanism (*Focus* parameter) on the wire detection algorithm were already examined and analyzed in Section 3.4.2. Similar test measurements were also performed for the circle detection algorithm. In Figures D.2, D.3 and D.4, we present sample images for each parameter value, while in Tables D.6, D.7 and D.8, the full sets of the parameter values are listed for the *Up*, *Side* and *Front* targets, respectively.

The statistical tests for the variances of the *Shutter* parameter values (Tables B.14 and B.15) suggest that there is no significant influence on the scatter for both, the horizontal and the elevation angles. This is also valid for the horizontal and the elevation angles of the *Gain* parameter values (Tables B.16 and B.17, respectively), as well as for the *Focus* parameters values (Tables B.18 and B.19).

In Figures 3.18, 3.19 and 3.20, we notice that the different parameter values of all three parameters do not significantly affect the mean values of the horizontal angle samples. However, the statistical tests presented in Table B.14 reveal that there is a statistical bias for the last parameter value of the *Shutter* parameter for a 99 % confidence level.

The most interesting result is the obvious bias of the elevation angle towards larger values when the target becomes brighter in the image, either by increasing the exposure time (*Shutter* parameter) or by increasing the CCD sensor gain value (*Gain* parameter).

In this group, we examine two additional parameters that are relevant with the position of the circular target on the image. These parameters correspond to the apparent horizontal position (*Hz direction* parameter) and the apparent vertical position (*Zen angle* parameter) of the target in the image. In more details:

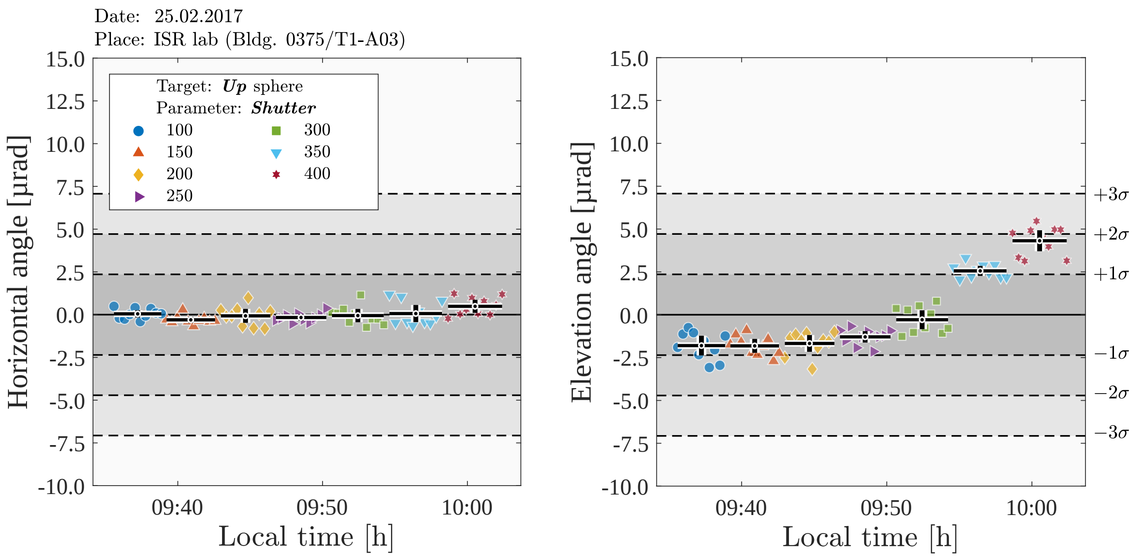

Figure 3.18: Scatter of the horizontal and elevation angles to the *Up* spherical target for different values of the *Shutter* parameter.

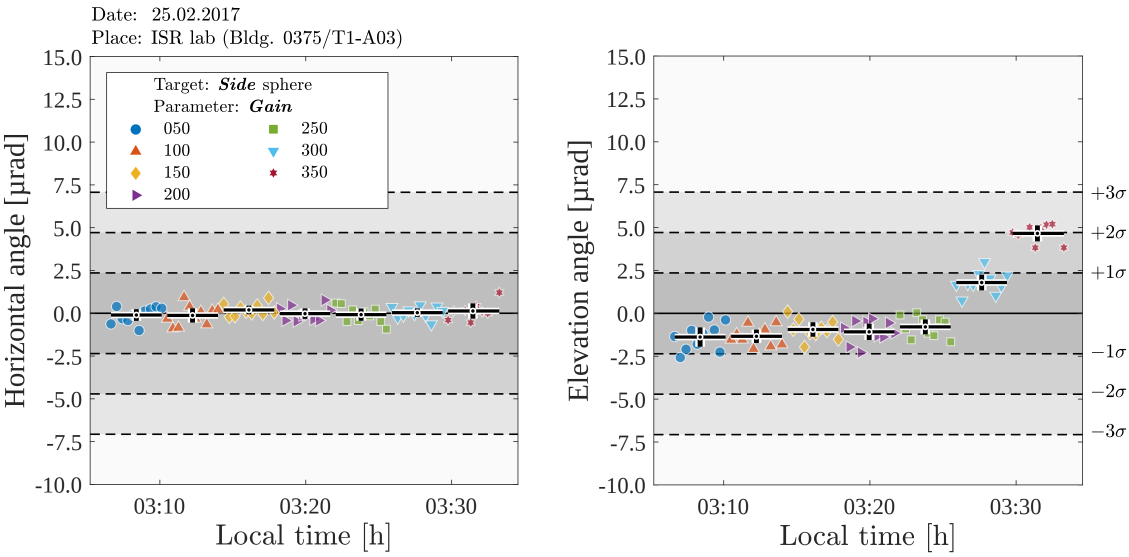

Figure 3.19: Scatter of the horizontal and elevation angles to the *Side* spherical target for different values of the *Gain* parameter.

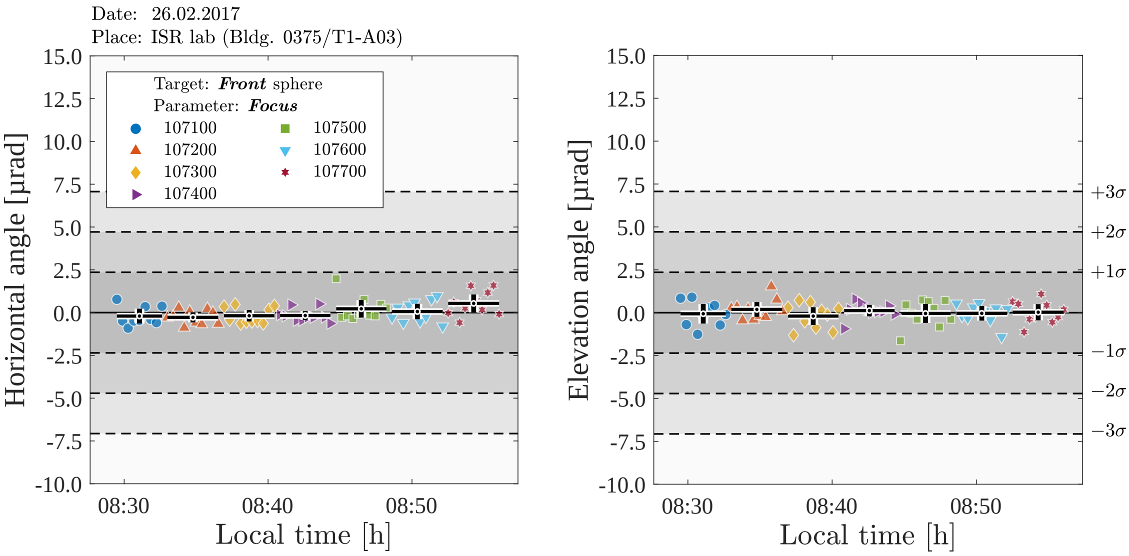

Figure 3.20: Scatter of the horizontal and elevation angles to the *Front* spherical target for different values of the *Focus* parameter.

- For the *Hz direction* parameter experiment, we set seven different values (Table D.9) in the QDaedalus software by changing each time only the horizontal angle of the theodolite (Figure D.5).
- For the *Zen angle* parameter experiment, we also set seven different values (Table D.10) in the QDaedalus software, this time, by changing only the zenith angle of the theodolite (Figure D.6).

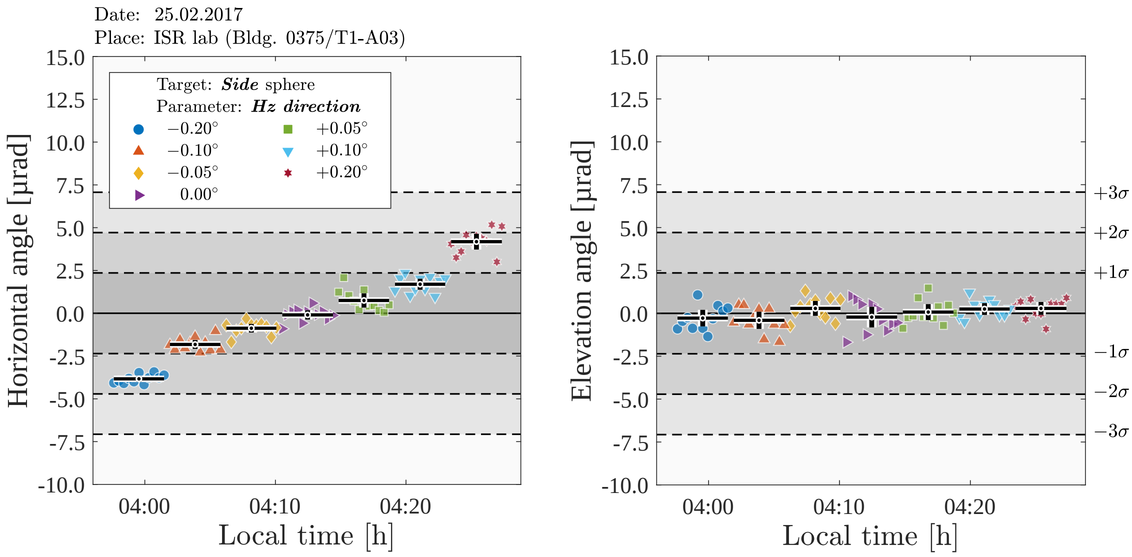

Figure 3.21: Scatter of the horizontal and elevation angles to the *Side* spherical target for different values of the *Hz direction* parameter.

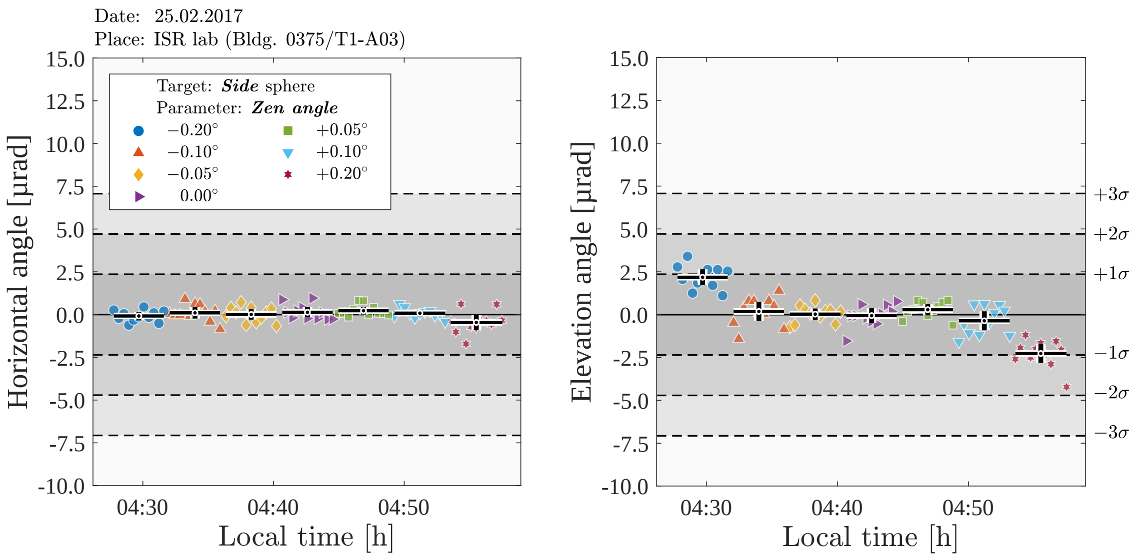

Figure 3.22: Scatter of the horizontal and elevation angles to the *Side* spherical target for different values of the *Zen angle* parameter.

In Figure 3.21, we observe that for the *Hz direction* parameter there is a significant bias only in the horizontal angle measurements, while the elevation angle appears to be stable. As the target apparently moves from left ($-0.20°$) to right ($0.20°$), the observed horizontal angle increases. According to Table B.20, different *Hz direction* parameter values do not significantly affect the variance of the horizontal angle samples but they only cause biases between the mean values. On the contrary, for the samples of the elevation angle the variances and the mean values remain unaffected by the horizontal position of the target in the image (see Table B.21).

For the *Zen angle* parameter (Figure 3.22), the statistical tests show that different parameter values do not affect neither the variance nor the mean of the horizontal angle measurements (Table B.22). The variance of the elevation angle is also not affected (Table B.23), however, statistical biases appear when the target is located towards the edges of the image (at $-0.20°$ and $+0.20°$).

The source of the biases that is related to the position of the target in the image seems to be a part of the lens distortion effect that is not absorbed by the calibration process (see Section 1.4.5).

3.5.3 Detection parameter

The Canny edge detection threshold (*Canny thres* parameter) is the only parameter that is relevant to the detection algorithm and that has been chosen to be examined for the influence it may have on the result of the circle detection algorithm. The rest of the detection parameters, described in *Guillaume et al.* (2015), are related to the size and the quality of the target, and therefore, it is pointless to test different values to a specific target. The *Canny thres* parameter is already explained in Section 3.4.3.

In Figure 3.23, we see that in the range of the values from 80 to 200, in intervals of 20, there is no significant influence on the result of the measurement. This finding is in accordance to the statistical tests presented in Table B.24 for the horizontal angles, and in Table B.25 for the elevation angles. Sample edge images for the *Front* target and the full set of the parameter values can be found in Figure D.7 and in Table D.11, respectively.

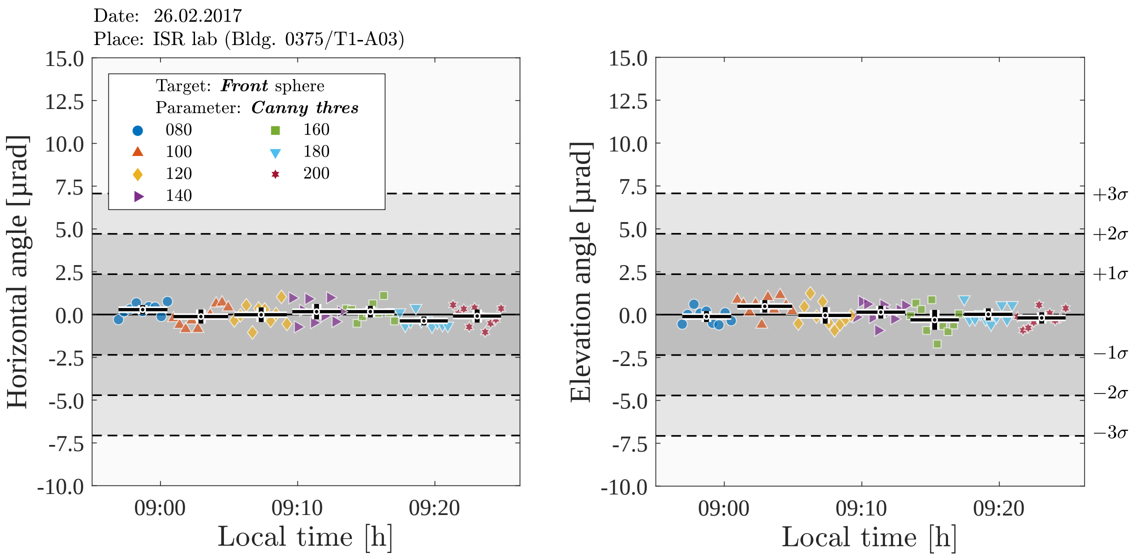

Figure 3.23: Scatter of the horizontal and elevation angles to the *Front* spherical target for different values of the *Canny thres* parameter.

3.5.4 Session and campaign summary

As described in Section 3.4.5, the sequential experiments are considered to be a *Session* of measurements. In Figure 3.24, we see a session of measurements for the *Side* target. Concerning the performance of the circle detection algorithm, we can easily notice three problematic parameters: the *Hz direction* parameter for the horizontal angle, and the *Shutter*, *Gain* and *Zen angle* parameters for the elevation angle.

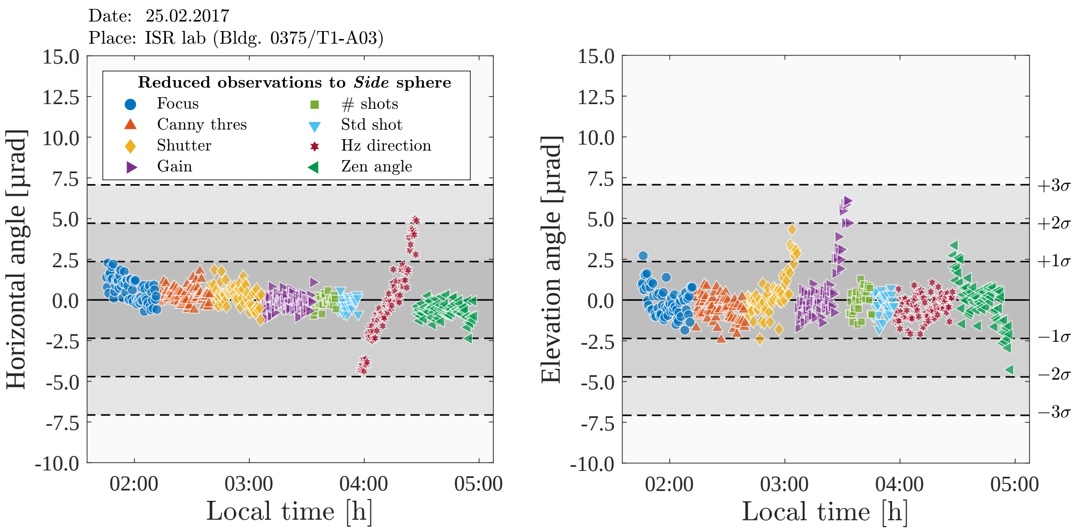

Figure 3.24: Scatter of the horizontal and elevation angles to the *Side* spherical target. A measurement *Session* consists of the subgroups of measurements that correspond to all user-defined parameters under examination.

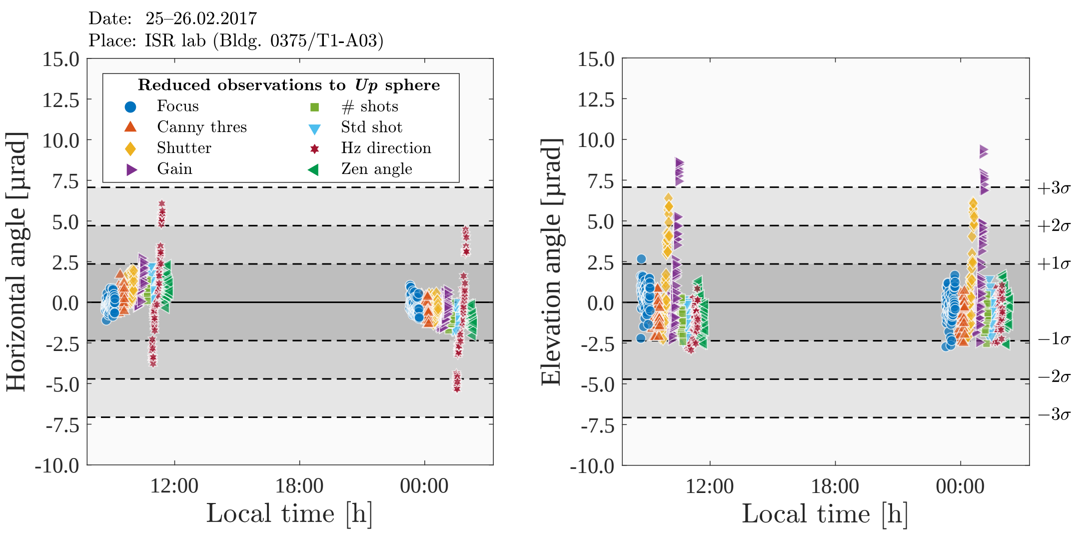

Figure 3.25: Scatter of the horizontal and elevation angles to the *Up* spherical target. A measurement *Campaign* consists of two sequential sessions.

The mean of the standard deviation values ($s_{\mathcal{P}_k}$) for the 48 sets of the horizontal angle measurements to the *Front*, *Up* and *Side* targets (Tables B.10, B.12, B.14, B.16, B.18, B.20, B.22 and B.24) is 0.47 µrad. The respective value for the zenith angle measurements (Tables B.11, B.13, B.15, B.17, B.19, B.21, B.23 and B.25) is 0.65 µrad. These experimental values for the standard deviation are approximately four to five times better than the precision specified by the manufacturer of the theodolite (approximately 2.4 µrad).

In order to confirm the results, we repeated the measurement sessions several times. Figure 3.25 depicts the measurements of a *Campaign*, which consists of two sequential sessions for the *Up* target. Apart from the repeatability of the results, we also observe the high stability of the setup, as we have already seen for the wire measurements. The drift of the measurement over a time period of several hours is expected, given the temperature variation of the experimental hall, illustrated in Figure 3.3.

3.6 Recommendations

Following the results obtained by numerous test measurements, such as those described in this chapter, as well as the experience acquired by measuring several micro-triangulation networks in more realistic conditions —described in the following chapters— we recommend good practices on how to manually select suitable parameter values with respect to the current implementation of the QDaedalus hardware and software. Moreover, we propose developments in the QDaedalus system that aim to increase the level of automation in the selection of various currently manually defined parameters, and potentially, to improve the accuracy and the robustness of the measurements.

Acquisition parameters

A fast acquisition combined with the adequate redundancy can be achieved with 3 to 5 shots (*# shots* parameter), assuming a very stable target. For the *Std shot* parameter the optimal value is 0.10 pixels in order to achieve a precision for the sample that is compatible with the angular precision of the theodolite, as described in *Bürki et al.* (2010).

The development of an algorithm that takes into consideration a user-defined minimum and maximum number of shots and the required standard deviation of the sample will increase the efficiency of the data acquisition in terms of speed and precision, by optimizing the number of the acquired shots.

Image parameters

For the micro-triangulation network measurements, a high shutter speed (low exposure time) is recommended in order to expedite the measurement process. The CCD sensor gain is recommended to remain low in order to avoid additional noise in the image. By selecting small values for the *Shutter* and *Gain* parameters, we also avoid potential biases on the measurements. Obviously, it is always better to keep as well as possible the image in focus.

An automatic selection of the *Shutter* and *Gain* parameters can be achieved with image processing techniques, e.g., by measuring the contrast between the target and the background, and at the same time, by measuring the noise level of the image. Moreover, a passive auto-focus function can easily be employed to ensure a fast and precise focus on the target.

To avoid biases caused by a non-centered target, it is required to always set the target in the center of the image. With the current software implementation, the centering of the target takes place during the target configuration process and not during the measurements. Although the current implementation of the semi-automatic targeting is adequate for objects that remain stable during the measurement, the development and implementation of an algorithm being able to perform an automatic centering just before each angle measurement is proposed.

Detection parameters

The size of the region of interest (ROI) is recommended to be as large as required to contain only the part of the wire that is in focus (due to the angle of incidence and to the shallow depth of field only a part of the depicted wire is in focus, as explained in Sections 2.1.4 and 3.3). Moreover, the size of the ROI should be suitably selected in order to avoid objects that obscure parts of the wire. For the Canny edge detection threshold, extremely small values (e.g., less than 30) should be strictly avoided because this may result in a large number of artifact edge points, which will significantly increase the processing time.

Environmental conditions

As it is demonstrated by the results of the evaluation, the ambient light conditions play a significant role in passive optical measurements. The illumination conditions and the background intensity usually vary significantly in a micro-triangulation network due to different lines-of-sight and shadows, caused by the complexity of the configuration.

Illumination that is coaxial to the theodolite optical axis is expected to mitigate these biases. In case an illumination device is mounted on the theodolite telescope, additional studies have to be conducted to ensure that the theodolite performance and functionality will not be affected by the additional weight, the cables and the thermal load. In our case, this solution was not an option as it was not in the scope of this study to develop such an illumination system.

3.7 Concluding remarks

The test measurements described in this chapter are dedicated to the experimental evaluation of the wire detection and the circle detection algorithms. As long as the QDaedalus measuring system is based in passive optical imaging, the target detection is susceptible to the ambient light conditions. Therefore, additional task-specific test measurements, relevant to the nature of a project, might be required. With regard to the present study, the tests measurements were repeated many times in different locations and configurations, in which consistent results were obtained. A set of representative results were presented in this chapter.

The evaluation results can be divided into three parts. The first part is the qualitative evaluation of the wire detection algorithm, including a group of tests concerning the capability of the algorithm to perform measurements in various configurations. The successful qualitative evaluation leads to the conclusion that the developed wire detection algorithm fulfills the requirements imposed by the nature of the micro-triangulation networks, and therefore, it can be used to measure micro-triangulation networks with stretched wires.

The latter two parts of the results are relevant to the quantitative performance evaluation of the two detection algorithms. Here, we investigated the potential effects of various user-defined parameters and environmental conditions on the variance and on the measured value of the angle observations, under specific conditions and with specific targets.

The results for both, the wire detection and the circle detection algorithms, consistently demonstrate that the variance of the measurements is not affected by changes in the parameter values. Moreover, the statistical tests for the variance, for a range of user-defined parameter values against the variance provided by the theodolite manufacturer, suggest that both detection algorithms do not reduce the theodolite precision. The results clearly show that the variance of the measurement samples acquired by the QDaedalus measuring system is statistically smaller than the specified angular precision of the theodolite for a 95 % confidence level.

The experimental evaluation of the wire detection algorithm and the circle detection algorithm demonstrated high-precision angle measurements. The standard deviation values obtained in different experiments for measurement sets of nine or ten measurements and for double-face measurements in one direction in space are between 0.25 µrad to 1.25 µrad. The horizontal angles acquired by the circle detection algorithm show the smaller values, while the larger values belong to the vertical angles of the wire detection algorithms.

The higher standard deviation values for the vertical angle measurements of the wire detection do not necessarily indicate less precise measurements due to the fact that the spread of these measurements on the wire axis depends on the angle of incidence between the wire axis and the optical axis of the theodolite. In general, the results are considered as satisfying, given the fact that the standard deviation values are on average approximately five times better than the angular precision of the employed theodolite. These results are also very promising for the precision that such a measuring system could reach in surveying networks with optimal geometry configuration, measured under stable environmental conditions.

Statistical tests were also performed for the bias between measurements that are acquired with different parameter values. The wire detection algorithm appears to be very robust against changes in the user-defined parameter values, while the measurements are influenced by different environmental conditions, such as the background intensity and the light conditions. On the contrary, the measurements of the circle detection algorithm are susceptible to changes in the image brightness as it is regulated by the exposure time and the sensor gain parameters. Moreover, the eccentric position of the target in the image could cause a bias, however, this situation can be easily avoided by a careful configuration of the parameters that are relevant to the horizontal and the vertical angles to the target.

Chapter 4

Triangulation network adjustment with targets, straight lines and catenaries

In this chapter, we describe the method we apply for the adjustment of a triangulation network that contains horizontal and zenith angle observations to targets, straight lines and catenaries. In Section 4.1, we introduce the necessity to develop a new functional model that also describes the horizontal and vertical angle observations to the wire. The least-squares adjustment is based on the parametric model with constraints between parameters, as described in Sections 4.2. The functional model is presented in Section 4.3, the stochastic model in Section 4.4, and the constraints required to solve the system of equations in Section 4.5. In Section 4.6, we describe the indicators used in this study to evaluate the reliability of the functional and stochastic models, while the indicators used to analyze the precision of the solution are discussed in Section 4.7. Finally, concluding remarks can be found in Section 4.8.

4.1 Introduction

A triangulation network is a very common type of surveying networks, especially used in the elder years when the distance measurements were extremely laborious. In a *standard triangulation network* the points represent either instrument positions or targets and the observations consist of horizontal and zenith angles. A typical approach to adjust the observations of a triangulation network is the least-squares adjustment that can be executed by a plethora of available software.

The *triangulation method with targets and stretched wires* goes beyond the standard method by integrating angle observations to one or more stretched wires into the network. The observations to the wire are horizontal and zenith angles that are assumed to be measured to the axis of the wire. The particularity is that there are no distinguishable points on a wire, especially when the wire has a uniform surface. Therefore, it is impossible to observe the same point from two or more stations, or even worse, in the two faces of the theodolite. Moreover, distance observations cannot be performed due to the fact that the wire is so thin that it cannot reflect a usual optical measuring beam.

As a result of the non-corresponding points on the wire, it is impossible to directly compute coordinates for the observed points on the wire following the standard network adjustment. There are various applications that reconstruct the geometry of power lines, in which point coordinates are fitted to the catenary model (*McLaughlin*, 2006; *Jwa et al.*, 2009; *Chan et al.*, 2013; *Hatibovic*, 2014). However, this solution is not suitable for our problem. Instead, we have to develop a methodology to reconstruct the stretched wire position and orientation in space according to a model (e.g., straight line, catenary, etc.), directly using the angle observations.

Assuming the simplest form of such a network — i.e., consisting of two instrument stations, several targets and a stretched wire forming a straight line — , an intuitive three-steps approach could be followed in order to reconstruct the wire in space. Firstly, a standard network adjustment could be performed using only the observations to the targets in order to estimate the instrument positions. Subsequently, a mean plane could be estimated using the coordinates of the instrument positions and the observations to the wire. Finally, the straight line parameters of the wire could be computed by intersecting the two planes corresponding to the two instrument stations.

This three-step methodology can be easily and directly applied without any effort spent on a software development, however, it has numerous disadvantages. Firstly, it does not include all the observations into one common adjustment. Secondly, it cannot be expanded to other wire models such as the catenary, unless more complicated algorithms are developed to estimate higher-order surfaces and their intersection is space. Moreover, in case of more instrument positions, a more complicated approach has to be developed in order to compute the intersection of multiple planes or surfaces. Lastly, the reliability and the precision of the result cannot be directly and rigorously estimated due to the lack of a global functional and stochastic model.

In order to overcome the aforementioned disadvantages and to achieve a precise, rigorous and reliable solution, we choose to follow the well-established least-squares adjustment methodology and to develop a new functional model for the observations to the wire. To formulate the new observation equations for the horizontal and zenith angles to the stretched wire, we integrate the straight line or the catenary parametric equations into the standard observation equations used in surveying. This approach is based on the adaptation of a method developed in the past, related to a 3D line reconstruction with photogrammetric observations (*Mulawa and Mikhail*, 1988; *Guelch*, 1995; *Zielinski*, 1993), for surveying (horizontal and zenith) angle observations.

The most important advantages of the proposed one-step methodology are the following.

- The methodology benefits from the least-squares analysis, which enables the full control of the systematic errors and the gross errors.
- It is similar to the standard surveying methodology, which is based on observation equations and analysis tools that are familiar to a surveying engineer.
- It is expandable to various wire models (e.g., parabola, circle, etc.) and natural processes (e.g. Earth's curvature, atmospheric refraction, etc.).
- The estimated parameters are accompanied with a full variance-covariance matrix, which allows the rigorous estimation of the uncertainty of any derived quantity.
- A large number of instrument positions, targets and stretched wires in different shapes can be included in a surveying network adjustment and be processed simultaneously, given the software and hardware performance.

The main disadvantage of this approach is the necessity for the development of a sophisticated software that is able to handle the different types of observations, unknown parameters and constraints. In addition, the methodology definitely inherits from the triangulation method the lack of scale, and thus, this has to be treated accordingly.

The theory and the mathematical formulation for various aspects of the least-squares adjustment theory can be found in classic and modern bibliography. An indicative list of the books used in this chapter includes *Mikhail and Ackermann* (1976), *Mikhail and Gracie* (1981), *Dermanis* (1986), *Dermanis* (1987), *Teunissen* (2000), *Teunissen* (2006), *Ghilani* (2010), *Luhmann et al.* (2014), *Ogundare* (2016) and the lecture notes of *Guillaume* (2018).

4.2 Least-squares adjustment

A surveying network can be represented by a *functional model*, which is a list of equations $\mathbf{f}$ that link the true values of the n observed quantities $\mathbf{l}$ (e.g., angles) to the true values of the m parameters $\mathbf{x}$ that are selected to describe the network (e.g., coordinates).

$$\mathbf{f}\big(\mathbf{l},\ \mathbf{x}\big) = \mathbf{0} \tag{4.1}$$

where

$$\underset{n,1}{\mathbf{l}} = \begin{bmatrix} l_1 & l_2 & \dots & l_n \end{bmatrix}^{\mathsf{T}} \tag{4.2}$$

$$\underset{m,1}{\mathbf{x}} = \begin{bmatrix} x_1 & x_2 & \dots & x_m \end{bmatrix}^{\mathsf{T}} \tag{4.3}$$

In general, a functional model is built by taking into account several assumptions, mainly originated from the measurement environment in relation with the nature of the observations, the attributes of the observing instruments and the observed objects, as well as the objectives of the application.

4.2.1 Gauss-Markov model

If the n observations $\mathbf{l}$ can be written as functions of the m selected parameters $\mathbf{x}$, the functional model is called *parametric model* or *Gauss-Markov model*, and it can be expressed as

$$\mathbf{l} = \mathbf{f}(\mathbf{x}) \tag{4.4}$$

The exact equations of the functional model for a standard triangulation network and for a triangulation network with observations to straight lines and to catenaries are presented in Section 4.3.

There are surveying networks (e.g., leveling networks), where the system of equations described in Equation 4.4 is linear and it can be written as

$$\underset{n,1}{\mathbf{l}} = \underset{n,m}{\mathbf{A}} \cdot \underset{m,1}{\mathbf{x}} + \underset{n,1}{\mathbf{b}} \tag{4.5}$$

where $\mathbf{A}$ consists of the coefficients of the parameters $\mathbf{x}$, and $\mathbf{b}$ is a vector of constant values.

However, for other geodetic networks, such as a triangulation network, the system of equations is not linear. Such systems of equations have to be linearized in order to be solved as linear systems. In this case, the equations are expanded in *Taylor series*, in the vicinity of the solution.

$$\mathbf{l} = \mathbf{f}(\mathbf{x}^0) + \left.\frac{\partial \mathbf{f}(\mathbf{x})}{\partial \mathbf{x}}\right|_{\mathbf{x}^0} \cdot (\mathbf{x} - \mathbf{x}^0) + \text{higher order derivatives} \tag{4.6}$$

or, in matrix notation (neglecting the higher order derivatives), we can write

$$\underset{n,1}{\mathbf{l}} - \underset{n,1}{\mathbf{l}^0} = \underset{n,m}{\mathbf{A}} \cdot (\underset{m,1}{\mathbf{x}} - \underset{m,1}{\mathbf{x}^0}) \tag{4.7}$$

where

$\mathbf{x}^0$ is the vector of the approximate values of the parameters $\mathbf{x}$.

$\mathbf{l}^0$ is the vector of the the system of equations (Equation 4.4), evaluated at $\mathbf{x} = \mathbf{x}^0$.

$\mathbf{A}$ is the *Jacobian matrix*, i.e., the matrix of the first-order partial derivatives of the system of equations (Equation 4.4) with respect to the parameters $\mathbf{x}$, evaluated at $\mathbf{x} = \mathbf{x}^0$,

$$\underset{n,m}{\mathbf{A}} = \begin{bmatrix} \left.\frac{\partial f_1(\mathbf{x})}{\partial x_1}\right|_{\mathbf{x}^0} & \left.\frac{\partial f_1(\mathbf{x})}{\partial x_2}\right|_{\mathbf{x}^0} & \cdots & \left.\frac{\partial f_1(\mathbf{x})}{\partial x_m}\right|_{\mathbf{x}^0} \\ \left.\frac{\partial f_2(\mathbf{x})}{\partial x_1}\right|_{\mathbf{x}^0} & \left.\frac{\partial f_2(\mathbf{x})}{\partial x_2}\right|_{\mathbf{x}^0} & \cdots & \left.\frac{\partial f_2(\mathbf{x})}{\partial x_m}\right|_{\mathbf{x}^0} \\ \vdots & \vdots & \ddots & \vdots \\ \left.\frac{\partial f_n(\mathbf{x})}{\partial x_1}\right|_{\mathbf{x}^0} & \left.\frac{\partial f_n(\mathbf{x})}{\partial x_2}\right|_{\mathbf{x}^0} & \cdots & \left.\frac{\partial f_n(\mathbf{x})}{\partial x_m}\right|_{\mathbf{x}^0} \end{bmatrix} \tag{4.8}$$

Given the fact that the observations are always susceptible to errors, the true unknown observation can be written as

$$\mathbf{l} = \tilde{\mathbf{l}} + \mathbf{v} \tag{4.9}$$

where

$\tilde{\mathbf{l}}$ is the vector of the numerical result of the observations.

$\mathbf{v}$ is the vector of the true unknown values of the observation errors.

Substituting Equation 4.9 into Equation 4.7, we obtain the following linearized system of equations:

$$\underset{n,1}{\delta\mathbf{l}} + \underset{n,1}{\mathbf{v}} = \underset{n,m}{\mathbf{A}} \cdot \underset{m,1}{\delta\mathbf{x}} \tag{4.10}$$

where

$$\delta\mathbf{l} = \tilde{\mathbf{l}} - \mathbf{l}^0 \tag{4.11}$$

and

$$\delta\mathbf{x} = \mathbf{x} - \mathbf{x}^0 \tag{4.12}$$

In the system of equations described in Equation 4.10, the number of the equations n is always smaller than the total number of the unknowns $(n+m)$, considering as unknowns the m parameters $\mathbf{x}$ and the n observation errors $\mathbf{v}$. Therefore, the system is underdetermined and there exist an infinite number of solutions.

The errors occurring during the observations are usually categorized into random or stochastic errors, systematic errors, and gross errors or mistakes. In this stage, we assume that the potential gross errors have been detected and eliminated and that the systematic errors have been either mitigated by the applied measurement technique or introduced as parameters in the functional model. Therefore, we consider that the vector $\mathbf{v}$ only contains random errors. Under this assumption, we search for the solution that follows the *least-squares criterion*, which is also the *maximum likelihood criterion*, where the sum of the squares of the estimated observation errors (or residuals) $\hat{\mathbf{v}}$ are minimum:

$$\hat{\mathbf{v}}^\mathsf{T} \cdot \hat{\mathbf{v}} \rightarrow \min \tag{4.13}$$

or, in the case of weighted least squares,

$$\hat{\mathbf{v}}^\mathsf{T} \cdot \mathbf{P} \cdot \hat{\mathbf{v}} \rightarrow \min \tag{4.14}$$

where the matrix $\mathbf{P}$ is given according to the stochastic model, as described in Section 4.4.

It can be proven that the unique solution of the system on equations described in Equation 4.10, according to the criterion of Equation 4.14, is

$$\delta\hat{\mathbf{x}} = \left(\mathbf{A}^\mathsf{T} \cdot \mathbf{P} \cdot \mathbf{A}\right)^{-1} \cdot \mathbf{A}^\mathsf{T} \cdot \mathbf{P} \cdot \delta\mathbf{l} \tag{4.15}$$

also written as

$$\delta\hat{\mathbf{x}} = \mathbf{N}^{-1} \cdot \mathbf{u} \tag{4.16}$$

where

$\mathbf{N}$ is the normal equation matrix.

$\mathbf{u}$ is the absolute term (*Luhmann et al.*, 2014).

4.2.2 Parametric model with constraints between parameters

The normal equation matrix $\mathbf{N}$ of a usual geodetic network does not have full rank, and therefore, it cannot be inverted as required in Equation 4.16. The rank of a square matrix is the number of linearly independent rows or columns of the matrix. The *rank defect* (or *rank deficiency*) of the matrix $\mathbf{N}$ is the difference between the dimension of the square matrix and its rank.

One of the techniques to overcome this issue is to provide additional information in the form of equality equations that only contain the parameters $\mathbf{x}$ or a subset of them. These equations are the constraints of the solution and they should be at least equal in number to the rank defect of the network. More details about the rank defect and the constraints of a triangulation network are discussed in Section 4.5.

A system of equations with a number s of constrains can be written as

$$\mathbf{c}(\mathbf{x}) = \mathbf{0} \tag{4.17}$$

Thus, the full system of equations for the network becomes

$$\begin{aligned} \mathbf{l} &= \mathbf{f}(\mathbf{x}) \\ \mathbf{c}(\mathbf{x}) &= \mathbf{0} \end{aligned} \tag{4.18}$$

and if required, it can be linearized.

$$\begin{aligned} \mathbf{l} &= \mathbf{f}(\mathbf{x}^0) + \left.\frac{\partial \mathbf{f}(\mathbf{x})}{\partial \mathbf{x}}\right|_{\mathbf{x}^0} \cdot (\mathbf{x} - \mathbf{x}^0) + \text{higher order derivatives} \\ \mathbf{0} &= \mathbf{c}(\mathbf{x}^0) + \left.\frac{\partial \mathbf{c}(\mathbf{x})}{\partial \mathbf{x}}\right|_{\mathbf{x}^0} \cdot (\mathbf{x} - \mathbf{x}^0) + \text{higher order derivatives} \end{aligned} \tag{4.19}$$

or, in matrix notation and with neglecting the higher order derivatives, we can write

$$\begin{aligned} \underset{n,1}{\delta\mathbf{l}} + \underset{n,1}{\mathbf{v}} &= \underset{n,m}{\mathbf{A}} \cdot \underset{m,1}{\delta\mathbf{x}} \\ \underset{s,1}{\mathbf{t}} &= \underset{s,m}{\mathbf{C}} \cdot \underset{m,1}{\delta\mathbf{x}} \end{aligned} \tag{4.20}$$

where

$$\mathbf{t} = -\mathbf{c}(\mathbf{x}^0) \tag{4.21}$$

and

$$\underset{s,m}{\mathbf{C}} = \begin{bmatrix} \left.\frac{\partial c_1(\mathbf{x})}{\partial x_1}\right|_{\mathbf{x}^0} & \left.\frac{\partial c_1(\mathbf{x})}{\partial x_2}\right|_{\mathbf{x}^0} & \cdots & \left.\frac{\partial c_1(\mathbf{x})}{\partial x_m}\right|_{\mathbf{x}^0} \\ \left.\frac{\partial c_2(\mathbf{x})}{\partial x_1}\right|_{\mathbf{x}^0} & \left.\frac{\partial c_2(\mathbf{x})}{\partial x_2}\right|_{\mathbf{x}^0} & \cdots & \left.\frac{\partial c_2(\mathbf{x})}{\partial x_m}\right|_{\mathbf{x}^0} \\ \vdots & \vdots & \ddots & \vdots \\ \left.\frac{\partial c_s(\mathbf{x})}{\partial x_1}\right|_{\mathbf{x}^0} & \left.\frac{\partial c_s(\mathbf{x})}{\partial x_2}\right|_{\mathbf{x}^0} & \cdots & \left.\frac{\partial c_s(\mathbf{x})}{\partial x_m}\right|_{\mathbf{x}^0} \end{bmatrix} \tag{4.22}$$

It has been shown (e.g., in *Luhmann et al.* (2014) and *Guillaume* (2018)) that this system of equations can be solved as

$$\begin{bmatrix} \underset{m,1}{\delta\hat{\mathbf{x}}} \\ \underset{s,1}{\mathbf{k}} \end{bmatrix} = \begin{bmatrix} \underset{m,m}{\mathbf{A}^\top \cdot \mathbf{P} \cdot \mathbf{A}} & \underset{m,s}{\mathbf{C}^\top} \\ \underset{s,m}{\mathbf{C}} & \underset{s,s}{\mathbf{0}} \end{bmatrix}^{-1} \cdot \begin{bmatrix} \underset{m,1}{\mathbf{A}^\top \cdot \mathbf{P} \cdot \delta\mathbf{l}} \\ \underset{s,1}{\mathbf{t}} \end{bmatrix} \tag{4.23}$$

where $\mathbf{k}$ is the vector of the Lagrangian multipliers.

Since the block matrix has now full rank, it is invertible. After the inversion, the new block matrix can be re-partitioned, so that Equation 4.23 can be written as

$$\begin{bmatrix} \underset{m,1}{\delta\hat{\mathbf{x}}} \\ \underset{s,1}{\mathbf{k}} \end{bmatrix} = \begin{bmatrix} \underset{m,m}{\mathbf{Q}_{11}} & \underset{m,s}{\mathbf{Q}_{12}} \\ \underset{s,m}{\mathbf{Q}_{21}} & \underset{s,s}{\mathbf{Q}_{22}} \end{bmatrix} \cdot \begin{bmatrix} \underset{m,1}{\mathbf{A}^\top \cdot \mathbf{P} \cdot \delta\mathbf{l}} \\ \underset{s,1}{\mathbf{t}} \end{bmatrix} \tag{4.24}$$

and consequently, the solution is

$$\delta\hat{\mathbf{x}} = \mathbf{Q}_{11} \cdot \mathbf{A}^\top \cdot \mathbf{P} \cdot \delta\mathbf{l} + \mathbf{Q}_{12} \cdot \mathbf{t} \tag{4.25}$$

After the estimation of $\delta\hat{\mathbf{x}}$, we are able to compute the estimation $\hat{\mathbf{x}}$ of the parameters $\mathbf{x}$, the estimated residuals $\hat{\mathbf{v}}$ and the adjusted observations $\hat{\mathbf{l}}$:

$$\begin{aligned} \hat{\mathbf{x}} &= \mathbf{x}^0 + \delta\hat{\mathbf{x}} \\ \hat{\mathbf{l}} &= \mathbf{A} \cdot \hat{\mathbf{x}} \\ \hat{\mathbf{v}} &= \hat{\mathbf{l}} - \tilde{\mathbf{l}} \end{aligned} \tag{4.26}$$

as well as their variance-covariance matrices:

$$\begin{aligned} \hat{\mathbf{C}}_{\hat{\mathbf{x}}\hat{\mathbf{x}}} &= \hat{\sigma}_0^2 \cdot \mathbf{Q}_{\mathbf{xx}} = \hat{\sigma}_0^2 \cdot \mathbf{Q}_{11} \\ \hat{\mathbf{C}}_{\hat{\mathbf{l}}\hat{\mathbf{l}}} &= \hat{\sigma}_0^2 \cdot \mathbf{Q}_{\mathbf{ll}} = \hat{\sigma}_0^2 \cdot \mathbf{A} \cdot \mathbf{Q}_{11} \cdot \mathbf{A}^\top \\ \hat{\mathbf{C}}_{\hat{\mathbf{v}}\hat{\mathbf{v}}} &= \hat{\sigma}_0^2 \cdot \mathbf{Q}_{\mathbf{vv}} = \hat{\sigma}_0^2 \cdot \left(\mathbf{P}^{-1} - \mathbf{A} \cdot \mathbf{Q}_{11} \cdot \mathbf{A}^\top\right) \end{aligned} \tag{4.27}$$

where $\hat{\sigma}_0^2$ is the *a posteriori* estimated variance of the unit weight:

$$\hat{\sigma}_0^2 = \frac{\hat{\mathbf{v}}^\top \cdot \mathbf{P} \cdot \hat{\mathbf{v}}}{r} \tag{4.28}$$

and r is the *redundancy number* or the *degrees of freedom* of the network, computed as

$$r = n - m + s \tag{4.29}$$

4.3 Functional model

A functional model can be expressed as a parametric model when the observation equations can be written in the form:

$$\tilde{l} = f(x_1,\ x_2,\ \ldots) - v \tag{4.30}$$

where the numerical result $\tilde{l}$ of an observation is located on one side of the equation, and the mathematical expression of the parameters is located on the other side.

In this study, we have four types of observations, which are the horizontal angle and the vertical angle to a target and to a point on the stretched wire axis, respectively. Firstly, we describe the two observation equations for the horizontal angle and the vertical angle to a target, starting with a simple model, in which an observation is assumed to be a straight ray in a Euclidean space. Subsequently, we augment the model with the three major systematic errors of a theodolite, which inversely affect the value of each face observation of the theodolite.

To obtain the observation equations in the case where a stretched wire is observed, we substitute the target coordinates according to the parametric equations of a straight line or of a catenary (hyperbolic cosine).

The functional model applied for this study does not take into account the Earth's curvature and the atmospheric refraction. The reason is that this study was meant to focus on small volumes of a few metres and to be used in a metrology room with controlled conditions, thus, the aforementioned effects were considered negligible for the required level of precision.

4.3.1 Observation equations for point targets

In a topocentric Cartesian coordinate system (Figure 4.1), with the Z-axis being parallel to the local vertical direction, the horizontal angle observation from an instrument station i to a point target j is written as

$$\tilde{H}_{ij} = \tan^{-1}\left(\frac{\mathrm{d}x_{ij}}{\mathrm{d}y_{ij}}\right) - \omega_i - v \tag{4.31}$$

where ω_i is the angle between the zero indication of the horizontal circle and the Y-axis. The respective zenith angle observation is written as

$$\tilde{Z}_{ij} = \tan^{-1}\left(\frac{s_{ij}}{\mathrm{d}z_{ij}}\right) - v \tag{4.32}$$

where

$$\begin{aligned} \mathrm{d}x_{ij} &= x_j - x_i \\ \mathrm{d}y_{ij} &= y_j - y_i \\ \mathrm{d}z_{ij} &= z_j - z_i \end{aligned} \tag{4.33}$$

and s_{ij} is the horizontal distance between the station and the target:

$$s_{ij} = \sqrt{\mathrm{d}x_{ij}^2 + \mathrm{d}y_{ij}^2} \tag{4.34}$$

In a standard surveying network the angles are observed in both faces of the theodolite, however, usually only the reduced observations (Equations 3.1 and 3.2) are used for the adjustment. The observations of each face contain several systematic errors, among others those coming from the imperfect construction of the instrument. These errors are

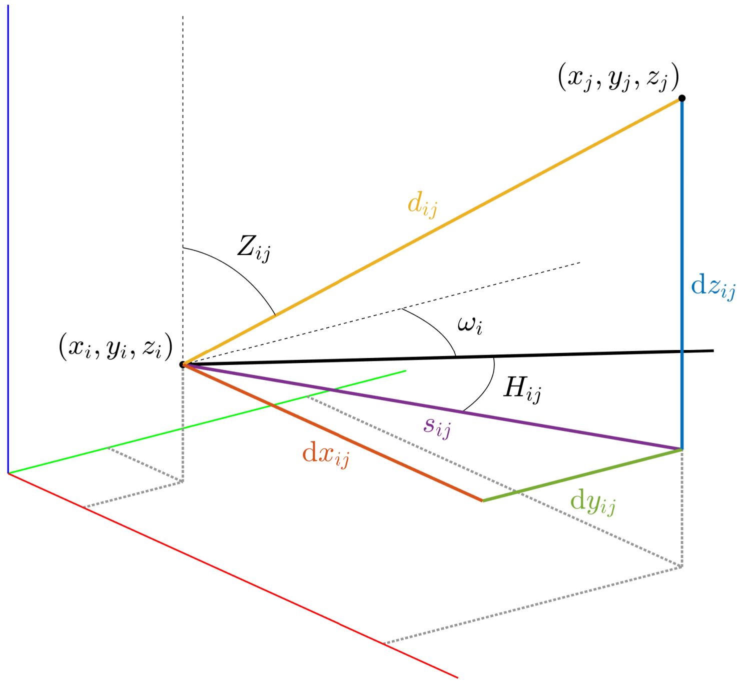

Figure 4.1: The horizontal angle H_{ij} and the zenith angle Z_{ij} in a topocentric Cartesian coordinate system.

considered to affect the observations of the two faces by the same amount but with the opposite sign, under the assumption that the same target is observed. By combining the two faces in one reduced observation the systematic errors of the instrument are practically eliminated.

Due to the fact that it is impossible to define a specific point on the stretched wire and measure it in both faces, the adjustment is performed with the raw observations of both faces. For this study, the three major systematic errors of a theodolite are taken into account, i.e., the collimation error e^c and the tilting-axis error e^t for the horizontal angles, and the vertical-index error e^v for the zenith angles (Figure 4.2). In order to estimate these systematic errors, the following corrections should be added to the functional model, for each observation and with the right sign:

$$K_{ij}^c = \frac{e_i^c}{\sin(Z_{ij})} \tag{4.35}$$

$$K_{ij}^t = \frac{e_i^t}{\tan(Z_{ij})} \tag{4.36}$$

$$K_{ij}^v = e_i^v \tag{4.37}$$

The values of these systematic error coefficients e^c, e^t, e^v are subject to change each time the instrument is calibrated. In practice, we perform a calibration each time an instrument is installed and initialized as a new station. Moreover, for an *image-assisted*

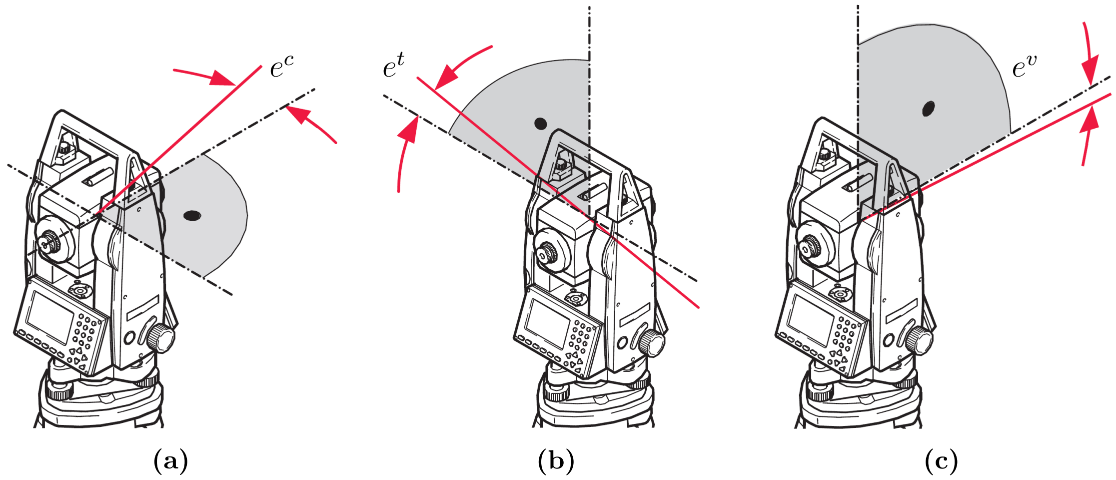

Figure 4.2: (a) Collimation error. (b) Tilting-axis error. (b) Vertical-index error. (source: *Zeiske* (2004)).

theodolite system the error coefficients are also changing after each camera calibration. For that reason, we prefer to add a new set of error coefficients e_i^c, e_i^t, e_i^v for each station i.

More details about the nature and the formulation of these errors can be found in almost every modern surveying textbook (e.g., in *Ogundare* (2016)).

To express the corrections K^c and K^t only in terms of the parameters $\mathbf{x}$, we need to substitute the zenith angle Z_{ij} in Equation 4.35 with

$$Z_{ij} = \sin^{-1}\left(\frac{s_{ij}}{d_{ij}}\right) \tag{4.38}$$

where

$$d_{ij} = \sqrt{\mathrm{d}x_{ij}^2 + \mathrm{d}y_{ij}^2 + \mathrm{d}z_{ij}^2} \tag{4.39}$$

and the zenith angle Z_{ij} in Equation 4.36 with Equation 4.32. After the substitution, we obtain the following expressions:

$$K_{ij}^c = e_i^c \cdot \frac{d_{ij}}{s_{ij}} \tag{4.40}$$

$$K_{ij}^t = e_i^t \cdot \frac{\mathrm{d}z_{ij}}{s_{ij}} \tag{4.41}$$

Consequently, the horizontal angle observation equations for each face become

$$\begin{aligned} \tilde{H}_{ij}^I &= \tan^{-1}\left(\frac{\mathrm{d}x_{ij}}{\mathrm{d}y_{ij}}\right) - e_i^c \cdot \frac{d_{ij}}{s_{ij}} - e_i^t \cdot \frac{\mathrm{d}z_{ij}}{s_{ij}} - \omega_i - v \\ \tilde{H}_{ij}^{II} &= \tan^{-1}\left(\frac{\mathrm{d}x_{ij}}{\mathrm{d}y_{ij}}\right) + e_i^c \cdot \frac{d_{ij}}{s_{ij}} + e_i^t \cdot \frac{\mathrm{d}z_{ij}}{s_{ij}} - \omega_i - v \end{aligned} \tag{4.42}$$

Correspondingly, by adding the correction K^v (Equation 4.37) to each face of the zenith angle observation equation, we get

$$\begin{aligned}\tilde{Z}_{ij}^{I} &= \tan^{-1}\left(\frac{s_{ij}}{\mathrm{d}z_{ij}}\right) - e_i^v - v \\ \tilde{Z}_{ij}^{II} &= \tan^{-1}\left(\frac{s_{ij}}{\mathrm{d}z_{ij}}\right) + e_i^v - v\end{aligned} \tag{4.43}$$

Up to this point, we have described the observation equations of the horizontal and the zenith angles measured from a theodolite station i to a target j, and for each face, by including the major systematic errors of a theodolite. Next, we formulate the corresponding observation equations for the case where a point is observed on the axis of a stretched wire.

4.3.2 Observation equations for straight lines

The straight line parametric equations are widely used for a line reconstruction in photogrammetry (e.g., in *Mulawa and Mikhail* (1988), *Zielinski* (1993) and *Guelch* (1995)). The parametric equations describe a straight line in space, independently of its orientation. This is rather useful in the case of a vertical line, where the explicit form cannot be used. The parametric straight line equations for the coordinates of a point p that belongs to a straight line in three dimension are

$$\begin{aligned}x_p &= x_0 + u_x \cdot t_p \\ y_p &= y_0 + u_y \cdot t_p \\ z_p &= z_0 + u_z \cdot t_p\end{aligned} \tag{4.44}$$

where, according to Figure 4.3a,

x_p, y_p, z_p	are the coordinates of an arbitrary point p on the line.
x_0, y_0, z_0	are the coordinates of a fixed reference point on the line.
u_x, u_y, u_z	are the coefficients of the direction vector of the line.
t_p	is the scalar parameter of the vector between the reference point and the point p.

By substituting the coordinate differences (Equation 4.33) into Equations 4.42 and 4.43 with the following expressions:

$$\begin{aligned}\mathrm{d}x_{ip} &= x_0 + u_x \cdot t_p - x_i \\ \mathrm{d}y_{ip} &= y_0 + u_y \cdot t_p - y_i \\ \mathrm{d}z_{ip} &= z_0 + u_z \cdot t_p - z_i\end{aligned} \tag{4.45}$$

we obtain the observation equations of the horizontal and the zenith angles, measured from a theodolite station i to a point p on a straight line.

4.3.3 Observation equations for catenaries

In this study, we deal with lightweight stretched wires that are suspended from the two extremities with high tension in an approximately horizontal orientation. In this case, modeling the wire as a straight line is a good approximation but not adequate for the required level of precision. A much better model for such a stretched wire is the catenary (or hyperbolic cosine) shape. A catenary has a U-shape that is formed when an elastic thin string with homogeneous linear density rests in equilibrium under the forces of a suspension tension and the gravitational force.

For the catenary, we also chose to work with the parametric equations in the three dimensional space in order to have a consistent notation and a similar approach as with the straight line. This is very helpful in terms of computer programming because some parts of the code can be used for both models of the wire.

In fact, the catenary shape defines a vertical plane. Therefore, for the horizontal coordinates the catenary parametric equations are identical with those of the straight line. However, the vertical component is different, and therefore, we use a catenary equation that is parameterized according to (*Chan and Lichti*, 2011).

$$\begin{aligned} x_p &= x_0 + u_x \cdot t_p \\ y_p &= y_0 + u_y \cdot t_p \\ z_p &= a + c \cdot \cosh\left(\frac{t_p - b}{c}\right) - c \end{aligned} \tag{4.46}$$

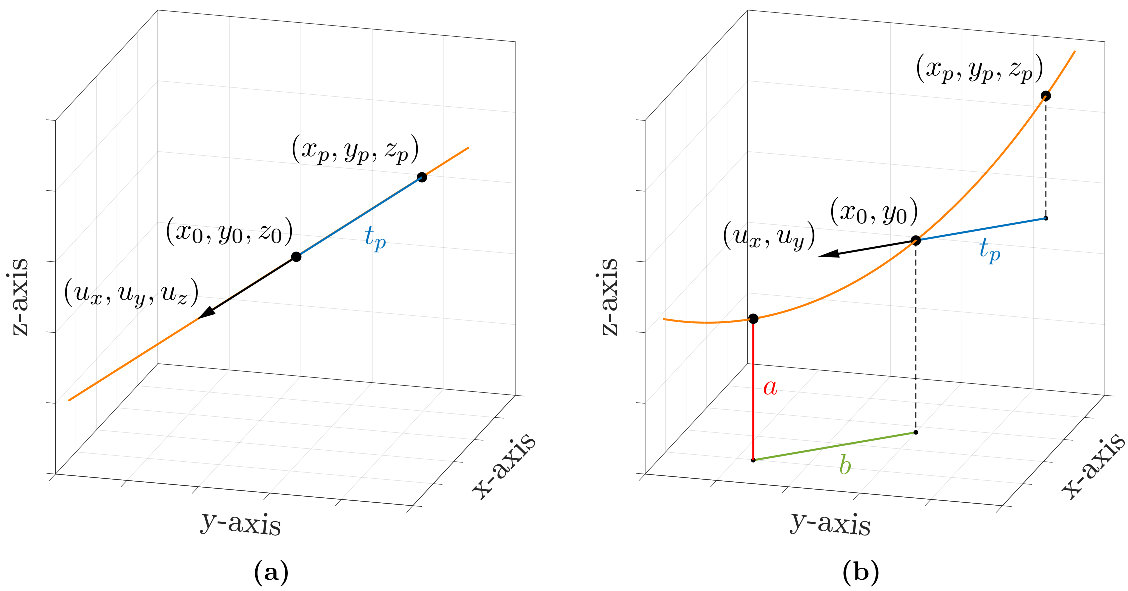

Figure 4.3: (a) Straight-line parameters. (b) Catenary parameters.

where, according to Figure 4.3b,

x_p, y_p, z_p	are the coordinates of an arbitrary point p on the catenary.
x_0, y_0	are the coordinates of a fixed reference point on the catenary.
u_x, u_y	are the coefficients of the horizontal direction vector of the catenary.
a	is the height of the vertex (lowest point of the catenary) with respect to the local coordinate system.
b	is the horizontal distance between the vertex and the reference point (x_0, y_0).
c	is the form parameter of the catenary shape (in units of length).
t_p	is the length scale parameter of the horizontal vector between the reference point and the point p.

By substituting the coordinate differences (Equation 4.33) into Equations 4.42 and 4.43 with the following expressions:

$$\begin{aligned} \mathrm{d}x_{ip} &= x_0 + u_x \cdot t_p - x_i \\ \mathrm{d}y_{ip} &= y_0 + u_y \cdot t_p - y_i \\ \mathrm{d}z_{ip} &= a + c \cdot \cosh\left(\frac{t_p - b}{c}\right) - c - z_i \end{aligned} \tag{4.47}$$

we obtain the observation equations of the horizontal and the zenith angles, measured from a theodolite station i to a point p on a catenary.

4.4 Stochastic model

A stochastic model describes the probabilistic (or stochastic) behavior of observations. An observation is considered to be a random variable due to the variability of the results obtained when the observation is repeated under practically identical conditions. The stochastic behavior of a random variable is totally described by a probability density function (PDF). The selection of a proper stochastic model leads to a more accurate evaluation of the applied functional model and to a more reliable outlier detection.

Geodetic observations, such as the angles we use in this study, are assumed to be random variables, following the *Gaussian* (or *normal*) distribution. A normally distributed observation $\tilde{l}_i$ is uniquely characterized by the first two moments, i.e., the mean (or expected value) $\check{l}_i$ and the variance σ_i^2:

$$\tilde{l}_i \sim \mathcal{N}(\check{l}_i,\, \sigma_i^2) \tag{4.48}$$

The stochastic model of the random vector $\tilde{\mathbf{l}}$, which is a set of n observations $\tilde{l}_i$ (Equation 4.2), is expressed as

$$\tilde{\mathbf{l}} \sim \mathcal{N}(\check{\mathbf{l}},\, \mathbf{C_{ll}}) \tag{4.49}$$

where $\check{\mathbf{l}}$ is the vector of the expected values of the observations and $\mathbf{C_{ll}}$ is the variance-covariance matrix of the observation vector $\tilde{\mathbf{l}}$.

The variance-covariance matrix $\mathbf{C_{ll}}$ is square, symmetric, and positive-definite (all diagonal elements are positive).

$$\underset{n,n}{\mathbf{C_{ll}}} = \begin{bmatrix} \sigma_1^2 & \rho_{12}\sigma_1\sigma_2 & \dots & \rho_{1n}\sigma_1\sigma_n \\ \rho_{21}\sigma_2\sigma_1 & \sigma_2^2 & \dots & \rho_{2n}\sigma_2\sigma_n \\ \vdots & \vdots & \ddots & \vdots \\ \rho_{n1}\sigma_n\sigma_1 & \rho_{n2}\sigma_n\sigma_2 & \dots & \sigma_n^2 \end{bmatrix} \tag{4.50}$$

where

ρ_{ij} is the correlation coefficient between $\tilde{l}_i$ and $\tilde{l}_j$, for $i \neq j$, with $-1 \leq \rho_{ij} \leq 1$.

σ_i^2 is the variance of the observation $\tilde{l}_i$.

$\rho_{ij}\sigma_i\sigma_j$ is the covariance between the observations $\tilde{l}_i$ and $\tilde{l}_j$.

The cofactor matrix $\mathbf{Q_{ll}}$ is obtained by introducing the multiplication factor σ_0^2, which is known as *reference variable.*

$$\mathbf{Q_{ll}} = \frac{1}{\sigma_0^2}\mathbf{C_{ll}} \tag{4.51}$$

The weight matrix $\mathbf{P_{ll}}$, which is required for the adjustment, is the inverse of the cofactor matrix.

$$\mathbf{P_{ll}} = \mathbf{Q_{ll}}^{-1} \tag{4.52}$$

The weight of an observation practically indicates the probability of its value to occur, or how trustful a value is.

The geodetic observations are usually assumed to be uncorrelated and statistically independent. As a result, the correlation coefficient ρ is equal to zero, and therefore, the weight matrix is diagonal.

$$\underset{n,n}{\mathbf{P_{ll}}} = \begin{bmatrix} \frac{\sigma_0^2}{\sigma_1^2} & 0 & \dots & 0 \\ 0 & \frac{\sigma_0^2}{\sigma_2^2} & \dots & 0 \\ \vdots & \vdots & \ddots & \vdots \\ 0 & 0 & \dots & \frac{\sigma_0^2}{\sigma_n^2} \end{bmatrix} \tag{4.53}$$

The reference variance σ_0^2 is also known as *variance of the unit weight*, given the fact that the weight p_i of an observation will be equal to unity when the reference variance is equal to the variance σ_i^2 of an observation.

$$p_i = \frac{\sigma_0^2}{\sigma_i^2} = 1 \tag{4.54}$$

When this is valid for all the observations of the network, then the weight matrix $\mathbf{P}$ becomes the identity matrix $\mathbf{I}$.

The *a priori* value for an observation variance σ_i^2 is usually a combination of the variances of various factors that affect the measurement process. Observations performed under the same conditions, with the same instrument, from the same observer, and with the same equipment (e.g., same targets) are usually considered to have equal variance. Although there is no observer in the case of the automated triangulation, the variances of two observations might be different owing to the performance of the target detection algorithm that replaces the observer.

In this study, we set a different *a priori* variance to each group of observations, depending on the type of observation (horizontal or zenith angle), and on the type of the observed point (target or wire). The values of the *a priori* variance for each group of observations are rectified during the adjustment, according to the *a posteriori* variance components of each group of observations (see Section 4.6.2).

4.5 Constraints

As mentioned in Section 4.2.2, the normal equation matrix $\mathbf{N}$ (Equation 4.16) has a rank defect, and therefore, it cannot be inverted. In a standard triangulation network, the rank defect is caused only by the fact that the observations do not contain enough information about the datum definition. In such cases, the rank defect is equal to the *datum defect*. However, there are cases such as the triangulation network with wire observations — which we examine in the present study — where the datum defect is only a part of the total rank defect of $\mathbf{N}$, while the other part is due to the use of more parameters than those required to describe the natural system.

The missing information that causes the *datum defect* is related to the definition of the reference system, or the *network datum* (e.g., position, orientation and scale). For this reason, additional information concerning the datum has to be introduced either in the form of constraints or by adding specific types of observations. The number and the type of the necessary constraints depends on the nature of the network (e.g., 1D, 2D, etc.) and on the type of the observations (e.g., angles, distances, etc.).

If the number of constraints is equal to the datum defect, and only if the constraints contain the missing datum information, we get a *minimum constraint* network solution. The minimum constraint solution is preferable for the analysis of the quality of the observations, as it is not affected by the potential inconsistencies of the datum coordinates, therefore, it does not deform the observations. It is clear that a set of minimum constraints is not unique. Each set of constraints defines a different datum and as a result the solution is different for $\hat{\mathbf{x}}$ and $\hat{\mathbf{C}}_{\hat{\mathbf{x}}\hat{\mathbf{x}}}$, while $\hat{\mathbf{v}}$, $\hat{\mathbf{C}}_{\hat{\mathbf{v}}\hat{\mathbf{v}}}$, $\hat{\mathbf{l}}$ and $\hat{\mathbf{C}}_{\hat{\mathbf{l}}\hat{\mathbf{l}}}$ always remain invariant.

A particular form of minimal constraints are the *inner constraints*, which are applied when the network is not required to be attached to a specific reference system. The solution has the following properties:

$$\mathrm{tr}\big(\mathbf{Q}_{\hat{\mathbf{x}}_k\hat{\mathbf{x}}_k}\big) \rightarrow \min \tag{4.55}$$

and

$$\delta\hat{\mathbf{x}}_k{}^{\mathsf{T}} \cdot \delta\hat{\mathbf{x}}_k \rightarrow \min \tag{4.56}$$

and it is called *free network* solution with *partial trace minimization* when $\mathbf{x}_k$ is a subset of the parameters $\mathbf{x}$, or *free network* solution with *full trace minimization*, when $\mathbf{x}_k$ is the full set of the parameters $\mathbf{x}$.

In this study, we apply a set of partial trace minimization constraints, in the form of similarity constraints, in order to overcome the datum defect (Section 4.5.1), and a pair of *minimum constraints* for each wire in order to overcome the part of the rank defect caused by the selected parameterization of the stretched wire model (Section 4.5.2).

4.5.1 Datum constraints

A geodetic network can be considered as an object with seven degrees of freedom with respect to a coordinate system (it is free to move in three directions, to rotate around three axes and to change size according to a scaling factor). Different types of observations constrain different types of degrees of freedom, depending on their nature. For example, a distance measurement constrains the scale of the network, an azimuth measurement constrains the horizontal orientation and a zenith angle measurement constrains the direction of the horizontal plane.

A standard 3D triangulation network that includes only horizontal and zenith angles has five degrees of freedom. Three degrees of freedom are related to the position in the three dimensions, one to the horizontal orientation, and one to the scale. Therefore, five datum constraints are required. In this study, we decided to constrain the solution to a group of k reference points of the network.

The similarity constraint equations in this case are

$$c_1 : \sum_{i=1}^{k} \left(x_i - x_i^0\right) = 0 \tag{4.57}$$

which fixes the X-axis position of the network at the average value of the X-axis coordinates of the k reference points,

$$c_2 : \sum_{i=1}^{k} \left(y_i - y_i^0\right) = 0 \tag{4.58}$$

which fixes the Y-axis position of the network at the average value of the Y-axis coordinates of the k reference points,

$$c_3 : \sum_{i=1}^{k} \left(z_i - z_i^0\right) = 0 \tag{4.59}$$

which fixes the Z-axis position of the network at the average value of the Z-axis coordinates of the k reference points,

$$c_4 : \sum_{i=1}^{k} \left(y_i^0 \cdot \left(x_i - x_i^0\right) - x_i^0 \cdot \left(y_i - y_i^0\right)\right) = 0 \tag{4.60}$$

which fixes the rotation of the network at the average bearing between the centroid and the k reference points, and

$$c_5 : \sum_{i=1}^{k} \left(x_i^0 \cdot \left(x_i - x_i^0\right) + y_i^0 \cdot \left(y_i - y_i^0\right) + z_i^0 \cdot \left(z_i - z_i^0\right)\right) = 0 \tag{4.61}$$

which fixes the scale of the network at the average distance between the centroid and the k reference points. A full description of the seven inner constraint equations for a datum definition can be found in *Tan* (2005).

According to Equation 4.22, a constraint matrix contains the first-order partial derivatives of the constraint equations with respect to the parameters $\mathbf{x}$. The part of the constraint matrix that corresponds to a selected point i is

$$\underset{5,3}{\mathbf{G}_i} = \begin{bmatrix} 1 & 0 & 0 \\ 0 & 1 & 0 \\ 0 & 0 & 1 \\ y_i^0 & -x_i^0 & 0 \\ x_i^0 & y_i^0 & z_i^0 \end{bmatrix} \tag{4.62}$$

The elements of the matrix $\mathbf{G}_i$ can also be extracted by the Helmert 3D transformation equations (*Ghilani*, 2010; *Teunissen*, 2006; *Guillaume*, 2018), so they are also called *Helmert constraints* or *Helmert conditions*.

The constraint matrix $\mathbf{C}_D$, which is related to the datum defect, is created by putting the matrices $\mathbf{G}_i$ at the right place, following the order of the parameters $\mathbf{x}$, and by filling the remaining elements with zero values:

$$\underset{5,m}{\mathbf{C}_D} = \begin{bmatrix} \cdots & \underset{5,3}{\mathbf{G}_1} & \cdots & \underset{5,3}{\mathbf{G}_2} & \cdots \end{bmatrix} \tag{4.63}$$

with

$$\operatorname{rank}\big(\mathbf{C}_D\big) = 5 \tag{4.64}$$

4.5.2 Wire constraints

Straight line

A straight line in the three dimensional space can be described by four independent parameters (*Hartley and Zisserman*, 2004). The parameterization that we apply in this study uses six parameters (x_0, y_0, z_0, u_x, u_y, u_z), and therefore, two constraints have to be added to the adjustment.

The first equation constrains the vector components (u_x, u_y, u_z) to form a unit vector,

$$c_6 : |u| = 1 \tag{4.65}$$

which can be written in the form of Equation 4.17 as

$$c_6 : \sqrt{u_x^2 + u_y^2 + u_z^2} - 1 = 0 \tag{4.66}$$

The second constraint equation is used to fix the position of the reference point (x_0, y_0, z_0) of the straight line. In *Zielinski* (1993) the reference point is constrained to be the closest to the origin of the coordinate system. The disadvantage of this solution is that the parameters t_p in Equation 4.44 may become very large when the angle observations to the wire are far from the origin of the coordinate system, thus, this solution may cause numerical problems.

In this study, we select a constraint equation that brings the reference point (x_0, y_0, z_0) into the centre of the N observations to each observed straight line W, thus, it minimizes the values of the N_W parameters t_p:

$$c_7 : \sum_{p=1}^{N_W} t_p = 0 \tag{4.67}$$

The constraint matrix for each observed straight line W is created by placing the first-order partial derivatives of the constraint equations c_6 and c_7 according to the order of the parameters $\mathbf{x}$, and by filling the remaining elements with zero values:

$$\underset{2,m}{\mathbf{C}_W} = \begin{bmatrix} \cdots & \dfrac{u_x}{|u|} & \dfrac{u_y}{|u|} & \dfrac{u_z}{|u|} & 0 & 0 & \cdots & 0 & \cdots \\ \cdots & 0 & 0 & 0 & 1 & 1 & \cdots & 1 & \cdots \end{bmatrix} \tag{4.68}$$

Catenary

For the catenary, we also need two constraint equations. The first equation is similar to c_6 (Equations 4.66), with the only difference that it is written only for the two components (u_x, u_y) of the horizontal vector $\mathbf{u}$:

$$c_8 : \sqrt{u_x^2 + u_y^2} - 1 = 0 \tag{4.69}$$

The second equation is exactly the same as c_7 and it is used to relocate the reference point of the catenary into the centre of the observations, instead of being the lowest point (vertex) of the catenary.

4.5.3 Constraint matrix

The full constraint matrix used in the adjustment is the combination of the submatrix $\mathbf{C}_D$ (Equation 4.63) for the datum constraints, and submatrices $\mathbf{C}_{W\,i}$ (Equation 4.68) for the wire constraints:

$$\underset{5+2\cdot q,m}{\mathbf{C}} = \begin{bmatrix} \underset{5,m}{\mathbf{C}_D} \\ \underset{2,m}{\mathbf{C}_{W\,1}} \\ \underset{2,m}{\mathbf{C}_{W\,2}} \\ \vdots \\ \underset{2,m}{\mathbf{C}_{W\,q}} \end{bmatrix} \tag{4.70}$$

with

$$\operatorname{rank}(\mathbf{C}) = 5 + 2 \cdot q \tag{4.71}$$

where q is the number of the stretched wires (straight lines or/and catenaries) that are included in the network.

4.6 Analysis of reliability

The reliability of the results depends on the accuracy of the functional and the stochastic models, and represents the proximity of the employed models to the true physical model of the measurements. To quantify the reliability of the results, we compute indicators and perform statistical tests.

In this study, we select to perform the statistical tests for the estimated reference variance and for the estimated variance components of different groups of observations, given the fact that we consider groups of observations with different uncertainties. Moreover, we evaluate the reliability of each observation by computing the local reliability indicator.

Finally, seeking to diminish the impact of potential gross errors on the results, we apply an iteratively reweighted least-squares adjustment, based on the standard residuals of the observations. This approach replaces the standard data snooping technique for the detection of gross errors.

4.6.1 Statistical test for the estimated variance

The statistical test for the estimated variance — also known as *global test* — is usually the first test conducted after the adjustment. This test concerns the comparison between the *a priori* reference variance σ_0^2 and the *a posteriori* estimated value of the reference variance $\hat{\sigma}_0^2$. The null hypothesis H_0 assumes that the two values are statistically equal, while the alternative hypothesis H_a assumes that they are not equal:

$$\mathrm{H}_0: \ \sigma_0^2 = \hat{\sigma}_0^2, \qquad \mathrm{H}_\mathrm{a}: \ \sigma_0^2 \neq \hat{\sigma}_0^2 \tag{4.72}$$

The null hypothesis H_0 is accepted when the following two-tailed test is successful, with respect to the χ^2 distribution:

$$\chi_r^{2\ (1-\alpha/2)} \leq \frac{r \cdot \hat{\sigma}_0^2}{\sigma_0^2} \leq \chi_r^{2\ (\alpha/2)} \tag{4.73}$$

or equivalently, with respect to the *Fischer* distribution:

$$F_{r,\infty}^{(1-\alpha/2)} \leq \frac{\hat{\sigma}_0^2}{\sigma_0^2} \leq F_{r,\infty}^{(\alpha/2)} \tag{4.74}$$

where r is the number of the degrees of freedom of the network and α is the significance level of the test.

The significance level α is the probability to reject H_0 when it is in fact true (also known as type I error). This probability is usually selected according to the application requirements. By increasing the value of α, the statistical test becomes stricter. This is due to the fact that the probability to reject a true H_0 is getting higher, while the probability to accept a wrong H_0 (type II error) is getting lower.

The global test is suitable to reveal whether there are problems on either the functional or the stochastic model. However, it cannot indicate the exact source of the problem. When the global statistical test fails, other indicators should be examined and more statistical tests should be performed. An indicative list of reasons that may result in a global test failure can be found in *Guillaume* (2018), and they can be summarized as:

- One or more observations might be influenced by gross errors.
- The functional model might not be correct (e.g., it may omit one or more systematic effects).
- Systematic errors may have influenced the observations (e.g., reductions to the observations have not been applied).
- The *a priori* covariance matrix of the observations might not be realistic.
- The observations might not be Gaussian random variables.

4.6.2 Statistical test for the estimated variance components

The *a posteriori* estimated reference variance $\hat{\sigma}_0^2$ is a valuable indicator for the precision of the whole network, especially when the observations have comparable levels of precision. In case that a network consists of different types of observations or of observations with different levels of precision, the variance component indicators can be used. For each group G of observations with homogeneous precision, the estimated variance component $\hat{\sigma}_G^2$ is computed as

$$\hat{\sigma}_G^2 = \frac{\hat{\mathbf{v}}_G^{\mathsf{T}} \cdot \mathbf{P}_G \cdot \hat{\mathbf{v}}_G}{r_G} \tag{4.75}$$

where r_G is the partial redundancy of this particular group of observations:

$$r_G = \mathrm{tr}\big(\mathbf{Q_{vv}} \cdot \mathbf{Q_{ll}}^{-1}\big) \tag{4.76}$$

The statistical hypothesis test for the estimated variance component of each group G of observations is identical to Equation 4.73. However, in this case the null hypothesis H_0 and the alternative hypothesis H_a are formulated as

$$\mathrm{H}_0: \ \sigma_0^2 = \hat{\sigma}_G^2, \qquad \mathrm{H}_\mathrm{a}: \ \sigma_0^2 \neq \hat{\sigma}_G^2 \tag{4.77}$$

If the following two-tailed test is successful, then the null hypothesis H_0 is accepted.

$$\chi^{2\,(1-\alpha/2)}_{r_G} \leq \frac{r_G \cdot \hat{\sigma}_G^2}{\sigma_0^2} \leq \chi^{2\,(\alpha/2)}_{r_G} \tag{4.78}$$

As previously mentioned, when the global test fails, the source of the problem cannot be precisely revealed. In such a case, the statistical test of the estimated variance component of a group of observations can be proven to be a useful indicator to the specific group of observations that is potentially problematic.

In practice, the ratio

$$\frac{\hat{\sigma}_G^2}{\sigma_0^2} \tag{4.79}$$

can be used as a scale factor in order to update the *a priori* variance values for each group of observations, aiming to obtain more representative values. Eventually, after a few repetitions of the adjustment, and by updating the *a priori* variance values, Equation 4.79 tends to the unit value.

4.6.3 Local reliability

The *local reliability* indicator quantifies how well an observation can be controlled in a network, and hence, how reliable a particular observation is. At the same time, the local reliability quantifies the redundancy of an observation in a network. For that reason it is also called *partial redundancy.* The local reliability z_i of an observation i can take values between 0 and 1, and it is computed as

$$z_i = \frac{q_{v_i v_i}}{q_{l_i l_i}} \tag{4.80}$$

where

$q_{l_i l_i}$ is the *a priori* variance of the observation i, or the diagonal element of the cofactor matrix $\mathbf{Q_{ll}}$ (Equation 4.27), and

$q_{v_i v_i}$ is the variance of the residual i, or the diagonal element of the cofactor matrix $\mathbf{Q_{vv}}$ (Equation 4.27).

There are two advantages of the z_i indicator: a) it is an invariant magnitude, and thus, it does not depend on the selection of the reference system, and b) it can be calculated before any observation is performed, therefore, it is a useful tool at the stage of a network design.

The observations can be categorized with respect to their local reliability value as:

$$\begin{aligned} 0 \leq z_i < 0.25 &\quad \text{poorly controlled} \\ 0.25 \leq z_i < 0.75 &\quad \text{enough controlled} \\ 0.75 \leq z_i < 1 &\quad \text{well controlled} \end{aligned} \tag{4.81}$$

In general, if a part of a network demonstrates small z_i values, it might be required to add observations, aiming to reinforce the network. On the contrary, observations could be reduced in case the z_i values in an area of the network are high enough.

A matrix $\mathbf{Z}$ of the local reliabilities of all the observations (also known as *redundancy matrix*) can also be computed with a matrix multiplication,

$$\mathbf{Z} = \mathbf{Q_{vv}} \cdot \mathbf{Q_{ll}}^{-1} \tag{4.82}$$

The sum of the z_i values of all observations (i.e., the trace of the matrix $\mathbf{Z}$) is equal to the degrees of freedom of the whole network.

$$\operatorname{tr}(\mathbf{Z}) = \sum_{i=1}^{n} z_i = r \tag{4.83}$$

In terms of computing, this is a very useful attribute to be used as a crosscheck calculation in the algorithm.

4.6.4 Statistical test for gross errors

The contamination of the observations with gross errors cannot be excluded, even if most of the observations in the field of surveying and geodesy are currently automatically acquired.

Gross errors have an impact on the network solution, and therefore, it is a good practice to detect the gross errors and eliminate their influence on the network adjustment.

The observations that contain gross errors are usually called *outliers* (or *blunders*). For surveying observations, the most common technique to detect outliers is called *data snooping*. Although it is intuitive to consider that observations with large residuals most probably contain gross errors, this is not true due to the fact that a large residual can be the result of the unfavorable geometry of the network configuration or of an incomplete functional model. For that reason, the data snooping is usually done with the statistical test of the *standard residual* (or *normalized residual*) $\hat{w}_i$ of the observation i.

$$\hat{w}_i = \frac{\hat{v}_i}{\sigma_0 \cdot \sqrt{q_{v_i v_i}}} \tag{4.84}$$

The null hypothesis H_0 of this statistical test suggests that the observation does not contain a gross error, while the alternative hypothesis H_a suggests that the observation does contain a gross error. The standard residual $\hat{w}_i$ follows the *normal* distribution (*Teunissen*, 2006; *Lehmann*, 2013), therefore, the null hypothesis H_0 is accepted if

$$|\hat{w}_i| \leq \mathrm{z}^{\alpha/2} \tag{4.85}$$

and the alternative hypothesis H_a is accepted if

$$|\hat{w}_i| > \mathrm{z}^{\alpha/2} \tag{4.86}$$

where

$\mathrm{z}^{\alpha/2}$ is the percentage point of the *Gaussian* (or *normal*) distribution.

α is the significance level.

In a typical data snooping approach only one observation should be removed before the repetition of the adjustment. Typically, the observation with the largest standard residual value that fails the statistical test is removed. A variation of this approach proposes to assign a very small weight to the outlier observation instead of completely removing that observation. This approach is more favorable in terms of software programming as it mitigates the influence of the outlier to the network adjustment, while it preserves the sizes of the matrices for each iteration.

Iteratively reweighted adjustment

In this study, we prefer to apply an *iteratively reweighted adjustment*. The first step in the application of an *iteratively reweighted adjustment* (or *robust adjustment*) is the selection of a *loss function* (or *cost function*). Many loss functions have been proposed in the bibliography, in which the residual $\hat{v}$ is the input parameter (*Hartley and Zisserman*, 2004). A very common loss function, used in photogrammetric projects (*Molnár*, 2010), is the Huber loss function $\rho_{\text{Huber}}(\hat{v})$.

$$\rho_{\text{Huber}}(\hat{v}) = \begin{cases} \dfrac{1}{2} \cdot \hat{v}^2 & \text{for } |\hat{v}| \leq c \\ c \cdot |\hat{v}| - \dfrac{1}{2} \cdot c^2 & \text{for } |\hat{v}| > c \end{cases} \tag{4.87}$$

According to *Holland and Welsch* (1977), the Huber weight function $p_{\text{Huber}}(\hat{v})$ is:

$$p_{\text{Huber}}(\hat{v}) = \begin{cases} 1 & \text{for } |\hat{v}| \leq c \\ \dfrac{c}{|\hat{v}|} & \text{for } |\hat{v}| > c \end{cases} \tag{4.88}$$

Given the fact that the residual is not the best indicator of whether or not an observation contains a gross error, in this study we implement the Biber weight function $p_{\text{Biber}}(\hat{w})$ (Figure 4.4). This is a modified Huber function, in which the standard residual $\hat{w}_i$ is used instead of the residual $\hat{v}_i$ (*Guillaume*, 2018)

$$p_{\text{Biber}}(\hat{w}) = \begin{cases} 1 & \text{for } |\hat{w}| \leq c \\ \dfrac{c}{|\hat{w}|} & \text{for } |\hat{w}| > c \end{cases} \tag{4.89}$$

where the factor c is substituted by the percentage point $\mathrm{z}^{\alpha/2}$ of the *normal* distribution. In this study, we use the value 1.96 that corresponds to the 95 % of the *normal* distribution.

Finally, for each next iteration $k+1$, the new weight p_i^{k+1} of each observation i is calculated by multiplying the initial weight of a particular observation p_i^0 with the corre-

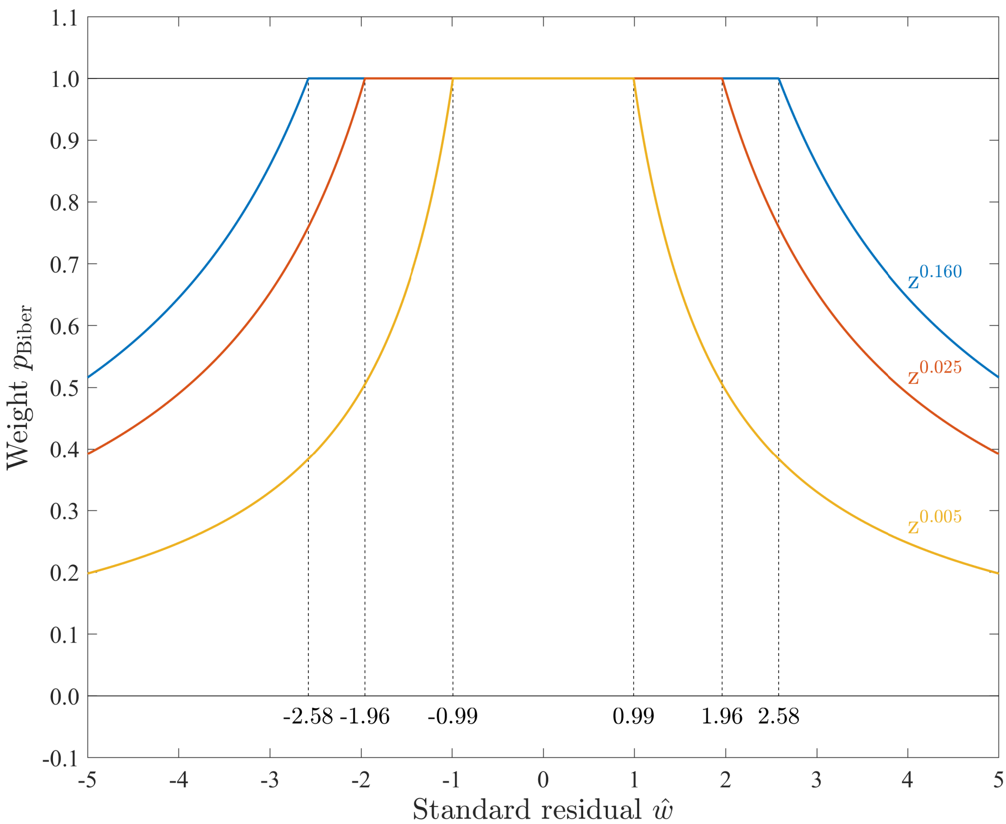

Figure 4.4: Biber weight function for 0.32, 0.05 and 0.01 significance level α, which correspond to 68 %, 95 % and 99 % of the *normal* distribution.

sponding weight $p^k_{\text{Biber},i}$, which is calculated according to Equation 4.89 with the standard residuals $\hat{w}^k_i$ of the current iteration k.

$$p_i^{k+1} = p^k_{\text{Biber},i} \cdot p_i^0 \tag{4.90}$$

4.7 Analysis of precision

The vector of the estimated parameters $\hat{\mathbf{x}}$ and its variance-covariance matrix $\hat{\mathbf{C}}_{\hat{\mathbf{x}}\hat{\mathbf{x}}}$ are two important results of the least-squares adjustment (Equations 4.26 and 4.27).

The variance-covariance matrix $\hat{\mathbf{C}}_{\hat{\mathbf{x}}\hat{\mathbf{x}}}$ contains all the information concerning the precision of $\hat{\mathbf{x}}$. Usually, $\hat{\mathbf{C}}_{\hat{\mathbf{x}}\hat{\mathbf{x}}}$ has a very large size because it refers to a multi-dimensional space, which is difficult to visualize or even to conceive. Therefore, it is better to reduce the analysis of the precision into one or two dimensions, and rarely into three dimensions. In one dimension, the precision of a single parameter is expressed with its *confidence interval*. The confidence interval is the range of an one-dimensional probability density function — centered in the estimated parameter value — that corresponds to a specific *probability* (or *confidence level*). Similarly, in two dimensions, the precision of a pair of parameters (e.g., the horizontal coordinates of a point) is expressed with a *confidence ellipse*, which is the area of a two-dimensional probability density function that corresponds to a specific probability.

4.7.1 Precision indicators in one dimension

A very common precision indicator for a parameter $\hat{x}_i$ of the functional model (e.g., a coordinate) is the standard deviation $\hat{\sigma}_{\hat{x}_i}$, which is expressed in the same units as the parameter itself,

$$\hat{\sigma}_{\hat{x}_i} = \sqrt{\hat{c}_{\hat{x}_i\hat{x}_i}} = \hat{\sigma}_0 \cdot \sqrt{q_{x_i x_i}} \tag{4.91}$$

The confidence interval $\mathcal{I}_{\hat{x}_i}$ represents a range of values around the estimated parameter $\hat{x}_i$, according to a given probability expressed as a confidence level $1-\alpha$.

$$\mathcal{I}_{\hat{x}_i} = \left[\, -k^{(1-\alpha)} \cdot \hat{\sigma}_{\hat{x}_i},\, +k^{(1-\alpha)} \cdot \hat{\sigma}_{\hat{x}_i} \right] \tag{4.92}$$

where the factor k is calculated from the *Student's t* distribution:

$$k^{(1-\alpha)} = t_r^{(\alpha/2)} \tag{4.93}$$

and α is the significance level.

Due to the fact that $\hat{\mathbf{x}}$ is an estimation with r degrees of freedom (Equation 4.29), it is no more a multivariate Gaussian random vector. Instead, it follows the *Student's t* distribution. When $r \to \infty$, the *Student's t* distribution converges to the *Gaussian* distribution. In the case of a triangulation network, which usually has a large number of degrees of freedom, the factor k can be computed by either the percentile of the *Gaussian* distribution z or the percentile of the χ^2 distribution for one degree of freedom.

$$k^{(1-\alpha)} = \mathrm{z}^{(\alpha/2)} = \sqrt{\chi_1^{2(\alpha)}} \tag{4.94}$$

In this study, we usually refer to a 95 % confidence level, for which the value of k is equal to 1.96.

After the adjustment, it may be required to compute a quantity that is not observed but it is a known function of a set of the parameters $\mathbf{x}$. In this case, we should also estimate the standard deviation and the confidence interval of this quantity. The computation is performed according to the *law of uncertainty (or error) propagation*, applied to the relevant elements of the variance-covariance matrix $\hat{\mathbf{C}}_{\hat{\mathbf{x}}\hat{\mathbf{x}}}$.

For a system of equations

$$\mathbf{y} = \mathbf{f}(\mathbf{x}) \tag{4.95}$$

the general form of the uncertainty propagation can be expressed in matrix notation as

$$\mathbf{C}_{\mathbf{yy}} = \frac{\partial \mathbf{f}}{\partial \mathbf{x}} \cdot \mathbf{C}_{\mathbf{xx}} \cdot \left(\frac{\partial \mathbf{f}}{\partial \mathbf{x}}\right)^{\mathsf{T}} \tag{4.96}$$

For example, in this study we are interested to compute the distance between a reference target and the stretched wire in two or three dimensions. In the three dimensions, the equation of the distance between a reference target (fiducial) f and its orthogonal projection to the wire p is:

$$d_{pf} = \sqrt{(x_p - x_f)^2 + (y_p - y_f)^2 + (z_p - z_f)^2} \tag{4.97}$$

where the coordinates of the orthogonal projection p are calculated from the estimated parameters of the wire and for a given t_p, according to Equation 4.44 when the stretched wire is modeled as a straight line. In this case, Equation 4.97 is written as

$$d_{pf} = \sqrt{(x_0 + u_x \cdot t_p - x_f)^2 + (y_0 + u_y \cdot t_p - y_f)^2 + (z_0 + u_z \cdot t_p - z_f)^2} \tag{4.98}$$

The standard deviation is calculated according to the law of uncertainty propagation,

$$\hat{\sigma}_{d_{pf}} = \sqrt{\mathbf{F} \cdot \hat{\mathbf{C}}_{\hat{\mathbf{x}}\hat{\mathbf{x}}_{pf}} \cdot \mathbf{F}^{\mathsf{T}}} \tag{4.99}$$

where

$$\underset{1,9}{\mathbf{F}} = \begin{bmatrix} \dfrac{\partial d_{pf}}{\partial x_f} & \dfrac{\partial d_{pf}}{\partial y_f} & \dfrac{\partial d_{pf}}{\partial z_f} & \dfrac{\partial d_{pf}}{\partial x_0} & \dfrac{\partial d_{pf}}{\partial y_0} & \dfrac{\partial d_{pf}}{\partial z_0} & \dfrac{\partial d_{pf}}{\partial u_x} & \dfrac{\partial d_{pf}}{\partial u_y} & \dfrac{\partial d_{pf}}{\partial u_z} \end{bmatrix} \tag{4.100}$$

is the 1×9 matrix of the first-order partial derivatives of the distance d_{pf} with respect to the point coordinates parameters (x_f, y_f, z_f) and the wire (straight line) parameters (x_0, y_0, z_0, u_x, u_y, u_z), and

$$\underset{9,9}{\hat{\mathbf{C}}_{\hat{\mathbf{x}}\hat{\mathbf{x}}_{pf}}} = \begin{bmatrix} \hat{\sigma}^2_{x_f} & \hat{\sigma}_{x_f y_f} & \hat{\sigma}_{x_f z_f} & \hat{\sigma}_{x_f x_0} & \hat{\sigma}_{x_f y_0} & \hat{\sigma}_{x_f z_0} & \hat{\sigma}_{x_f u_x} & \hat{\sigma}_{x_f u_y} & \hat{\sigma}_{x_f u_z} \\ & \hat{\sigma}^2_{y_f} & \hat{\sigma}_{y_f z_f} & \hat{\sigma}_{y_f x_0} & \hat{\sigma}_{y_f y_0} & \hat{\sigma}_{y_f z_0} & \hat{\sigma}_{y_f u_x} & \hat{\sigma}_{y_f u_y} & \hat{\sigma}_{y_f u_z} \\ & & \hat{\sigma}^2_{z_f} & \hat{\sigma}_{z_f x_0} & \hat{\sigma}_{z_f y_0} & \hat{\sigma}_{z_f z_0} & \hat{\sigma}_{z_f u_x} & \hat{\sigma}_{z_f u_y} & \hat{\sigma}_{z_f u_z} \\ & & & \hat{\sigma}^2_{x_0} & \hat{\sigma}_{x_0 y_0} & \hat{\sigma}_{x_0 z_0} & \hat{\sigma}_{x_0 u_x} & \hat{\sigma}_{x_0 u_y} & \hat{\sigma}_{x_0 u_z} \\ & & & & \hat{\sigma}^2_{y_0} & \hat{\sigma}_{y_0 z_0} & \hat{\sigma}_{y_0 u_x} & \hat{\sigma}_{y_0 u_y} & \hat{\sigma}_{y_0 u_z} \\ & & & & & \hat{\sigma}^2_{z_0} & \hat{\sigma}_{z_0 u_x} & \hat{\sigma}_{z_0 u_y} & \hat{\sigma}_{z_0 u_z} \\ & & \text{Symmetric} & & & & \hat{\sigma}^2_{u_x} & \hat{\sigma}_{u_x u_y} & \hat{\sigma}_{u_x u_z} \\ & & & & & & & \hat{\sigma}^2_{u_y} & \hat{\sigma}_{u_y u_z} \\ & & & & & & & & \hat{\sigma}^2_{u_z} \end{bmatrix} \tag{4.101}$$

is a 9×9 submatrix of the variance-covariance matrix $\hat{\mathbf{C}}_{\hat{\mathbf{x}}\hat{\mathbf{x}}}$ that contains the variances and covariances of the relevant parameters.

4.7.2 Precision indicators in two dimensions

A very common indicator of precision in two dimensions is the confidence ellipse. The ellipse takes into account not only the variance of each parameter but also their covariance. Although an ellipse can be calculated for every pair of the parameters $\hat{\mathbf{x}}$, it is mostly used to describe the precision of the estimated position of a point in two dimensions. In this case, the ellipse is graphically centered to the point location, which makes it more intuitive. Although, the most frequent case is to compute and visualize the ellipse in the horizontal plane, it is obvious that we could do the same with the other two planes that are parallel to the axes of the coordinate system.

To compute a confidence ellipse, we select the elements of the variance-covariance matrix $\hat{\mathbf{C}}_{\hat{\mathbf{x}}\hat{\mathbf{x}}}$ that correspond to the relevant coordinates. For example, for the ellipse of a point p in the horizontal plane the variance-covariance matrix is

$$\underset{2,2}{\hat{\mathbf{C}}_{\hat{\mathbf{x}}\hat{\mathbf{x}}_p}} = \begin{bmatrix} \hat{\sigma}^2_{x_p} & \hat{\sigma}_{x_p y_p} \\ \hat{\sigma}_{y_p x_p} & \hat{\sigma}^2_{y_p} \end{bmatrix} \tag{4.102}$$

The variance-covariance matrix $\hat{\mathbf{C}}_{\hat{\mathbf{x}}\hat{\mathbf{x}}_p}$ is symmetric, thus, it can be analyzed in its eigenvectors and eigenvalues following the eigenvalue decomposition:

$$\hat{\mathbf{C}}_{\hat{\mathbf{x}}\hat{\mathbf{x}}_p} = \mathbf{U} \cdot \mathbf{\Lambda} \cdot \mathbf{U}^\mathsf{T} = \begin{bmatrix} u_{x_1} & u_{x_2} \\ u_{y_1} & u_{y_2} \end{bmatrix} \cdot \begin{bmatrix} \lambda_1 & 0 \\ 0 & \lambda_2 \end{bmatrix} \cdot \begin{bmatrix} u_{x_1} & u_{y_1} \\ u_{x_2} & u_{y_2} \end{bmatrix} \tag{4.103}$$

where

U contains the linearly independent and perpendicular to each other unit vectors of the two axes of the ellipse, and

Λ contains the eigenvalues, which represent the magnitudes of the corresponding eigenvectors.

Therefore, the semi-axes of the confidence ellipse are:

$$\begin{aligned} \mathbf{a} &= k^{(1-\alpha)} \cdot \sqrt{\lambda_1} \cdot \begin{bmatrix} u_{x_1} & u_{y_1} \end{bmatrix}^\mathsf{T} \\ \mathbf{b} &= k^{(1-\alpha)} \cdot \sqrt{\lambda_2} \cdot \begin{bmatrix} u_{x_2} & u_{y_2} \end{bmatrix}^\mathsf{T} \end{aligned} \tag{4.104}$$

where the factor k is calculated according to the percentile of the *Fischer* distribution:

$$k^{(1-\alpha)} = \sqrt{2 \cdot F^{(\alpha)}_{2,r}} \tag{4.105}$$

or, when the number of the degrees of freedom is very large (theoretically when $r \to \infty$), the factor k can be calculated according to the percentile of the χ^2 distribution for two degrees of freedom:

$$k^{(1-\alpha)} = \sqrt{\chi_2^{2(\alpha)}} \tag{4.106}$$

In this study, we usually refer to a 95 % confidence level, for which the value of k equals to 2.45.

It is obvious that an error ellipse can be calculated for any defined point on the wire. To define a point p on a wire w, a value has to be assigned to the parameter t_p (see Equations 4.44 or 4.46). A new covariance matrix $\hat{\mathbf{C}}_{\hat{\mathbf{x}}\hat{\mathbf{x}}_p}$ is calculated according to the law of uncertainty propagation,

$$\hat{\mathbf{C}}_{\hat{\mathbf{x}}\hat{\mathbf{x}}_p} = \sqrt{\mathbf{F} \cdot \hat{\mathbf{C}}_{\hat{\mathbf{x}}\hat{\mathbf{x}}_w} \cdot \mathbf{F}^{\mathsf{T}}} \tag{4.107}$$

where, in the case of an horizontal ellipse,

$$\underset{2,4}{\mathbf{F}} = \begin{bmatrix} \dfrac{\partial x_p}{\partial x_0} & \dfrac{\partial x_p}{\partial y_0} & \dfrac{\partial x_p}{\partial u_x} & \dfrac{\partial x_p}{\partial u_y} \\ \dfrac{\partial y_p}{\partial x_0} & \dfrac{\partial y_p}{\partial y_0} & \dfrac{\partial y_p}{\partial u_x} & \dfrac{\partial y_p}{\partial u_y} \end{bmatrix} \tag{4.108}$$

is the 2×4 matrix of the first-order partial derivatives of the defined point coordinates (x_p, y_p) with respect to the wire (e.g., straight line) parameters (x_0, y_0, u_x, u_y), and

$$\underset{4,4}{\hat{\mathbf{C}}_{\hat{\mathbf{x}}\hat{\mathbf{x}}_w}} = \begin{bmatrix} \hat{\sigma}^2_{x_0} & \hat{\sigma}_{x_0 y_0} & \hat{\sigma}_{x_0 u_x} & \hat{\sigma}_{x_0 u_y} \\ & \hat{\sigma}^2_{y_0} & \hat{\sigma}_{y_0 u_x} & \hat{\sigma}_{y_0 u_y} \\ & & \hat{\sigma}^2_{u_x} & \hat{\sigma}_{u_x u_y} \\ \text{Sym.} & & & \hat{\sigma}^2_{u_y} \end{bmatrix} \tag{4.109}$$

is a 4×4 submatrix of the covariance matrix $\hat{\mathbf{C}}_{\hat{\mathbf{x}}\hat{\mathbf{x}}}$ that contains the variances and covariances of the wire parameters —when it is modeled as a straight line— only for the horizontal plane.

Subsequently, the new covariance matrix $\hat{\mathbf{C}}_{\hat{\mathbf{x}}\hat{\mathbf{x}}_p}$ is analyzed according to Equation 4.103 in order to compute the semi-axes of the ellipse, as it is previously described.

4.8 Concluding remarks

The angle observations to a stretched wire are performed to non-corresponding points, therefore, they cannot be processed by a typical surveying software. To overcome this difficulty, we developed a new functional model for these observations, and subsequently, a new software to process the integrated triangulation networks.

The standard least-squares adjustment is applied using the parametric —or Gauss-Markov— model with constraints. The new observation equations for the horizontal and zenith angles are formulated for each of the double-face measurements of the theodolite. The three main systematic errors of a theodolite, i.e., the collimation, the tilting-axis and the vertical-index errors are also included in the functional model.

The stretched wire is modeled as a straight line or as a catenary by integrating the corresponding parametric equations in the three dimensions into the observation equations. Due to the selected parameterization, more constraints should be added in the system of equations for each stretched wire, in addition to the standard datum constraints that are required in a triangulation network.

The analysis of the functional and the stochastic model reliability is performed with standard tools. In order to mitigate the influence of potential gross errors to the solution, we apply an iteratively reweighted adjustment scheme, instead of the standard data snooping technique. A weight function based on the standard residuals of the observations is applied for the observation reweighting.

Finally, the precision indicators in one and two dimensions that are used in this study are identical with those used in a standard surveying network. The law of uncertainty propagation is formulated for the uncertainty estimation of quantities that are functions of the estimated parameters, such as the distance between a target and a stretched wire.

Chapter 5

Validation of micro-triangulation for fiducialization applications in a metrology room

In this chapter, we examine the feasibility and the performance of the micro-triangulation method with direct wire observations for fiducialization applications of particle accelerator components. An overview of the test measurement configuration is given in Section 5.1. A detailed description of the test bench and the employed instrumentation can be found in Section 5.2, while in Section 5.3 we present the data processing methodology for each set of data. The results presented in Section 5.4 indicate that the fiducialization of a quadrupole magnet can be achieved with an accuracy of approximately 10 µm rms, in comparison to a high-precision coordinate measuring machine, following the proposed micro-triangulation method. The most important aspects of the outcome of this test measurement are summarize in Section 5.5.

5.1 Introduction

The fiducialization process of a quadrupole magnet is divided into two parts. In the first part, magnetic measurements are carried out in order to define the position and orientation of the magnetic axis. In the second part, the magnetic axis is geometrically linked to the reference targets (fiducials), which are located on the surface of the magnet. This study is related to the second part of the fiducialization process, i.e., the establishment of a geometrical link between the magnetic axis and the fiducials.

Several methods have been used — while others are under development — to perform the fiducialization of a quadrupole magnet. At CERN, the standard methodology for the fiducialization process includes: a) the vibrating-wire technique, for the magnetic measurement (Section 1.2.1), and b) a combination of measurements acquired with a coordinate measuring machine (CMM) and a laser tracker, for the geometrical measurement (Section 1.2.2).

In this chapter, we aim at validating, for the first time, a metrology solution for magnet fiducialization applications that is based on direct angle observations to the stretched wire. The proposed solution combines the *automated micro-triangulation* method (Section 1.3.3) with the use of *image-assisted theodolite systems* (Section 1.4.1). Moreover, we aim at

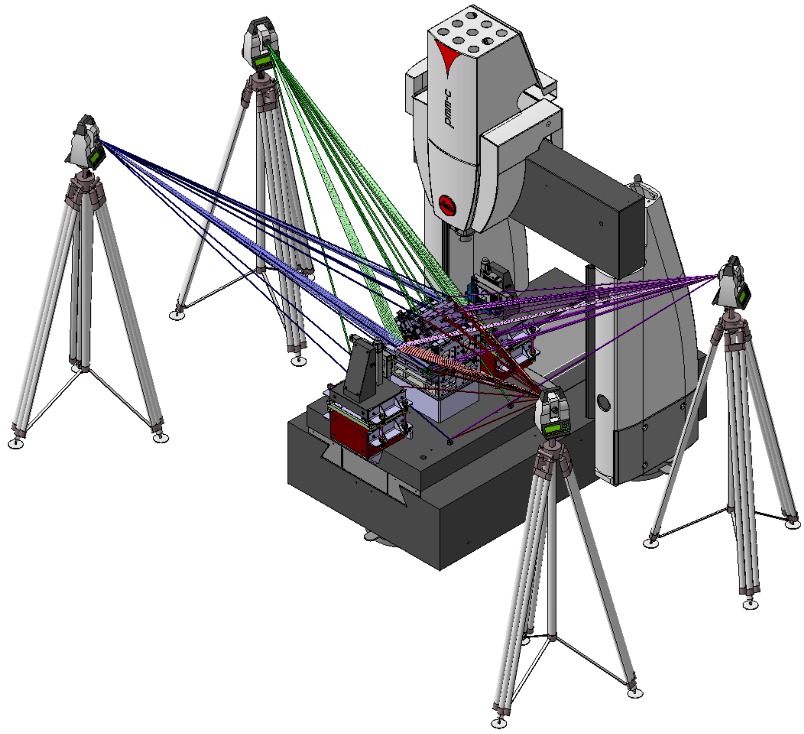

Figure 5.1: Conceptual design of the configuration in the metrology room. The test bench is placed on a coordinate measuring machine and is surrounded by four theodolites equipped with the QDaedalus system. Angle observations to the targets and to the wire are depicted in different colors, according to the observing theodolite (Source: François Nicolas Morel, CERN).

evaluating the accuracy of the proposed methodology with respect to one of the most accurate coordinate measuring machines on the market, under specific conditions and constraints.

In parallel to our main objectives, we investigate the effects that temperature variations in the metrology room have on the stability of the tripod of the theodolite, depending on its height and material.

A test bench called Final PACMAN Alignment Bench (FPAB) was installed in a metrology room at CERN. The development of various parts of the bench and the installation of the test bench in the metrology room was part of the PACMAN project (Section 1.5). The FPAB bench enabled numerous test measurements, as part of several doctoral studies, by employing various measuring devices (*Mainaud Durand et al.*, 2017).

The bench was available for measurements during three specific measurement campaigns: from July 20 to July 31, 2016 (*1st campaign*), from November 12 to December 11, 2016 (*2nd campaign*), and from March 25 to April 7, 2017 (*3rd campaign*). Measurements concerning the objectives of this chapter were repeatedly performed during the three campaigns in order to ensure the validity of the results. Here, we present the results of an indicative and representative part of the measurements.

The general configuration of the test bench for the three campaigns is presented in Figure 5.1. The CMM was located in the central area of the metrology room and the FPAB bench (described in Section 5.2.1) was installed on the CMM table. Four theodolites were placed around the CMM in suitable positions, taking into account the lines-of-sight to the targets, the confined space of the room, and the restrictions imposed by the existence of equipment related to other measurements that were taking place synchronously.

The analysis revealed that the temperature variations in the metrology room significantly affect the position of the theodolites, demonstrating that the vertical displacement variation of the theodolite position may have an amplitude up to 18 µm with an approximate period of 40 min, for a fully extended aluminium tripod.

Despite the unfavorable conditions of the measurement (i.e., temperature variations, poor light conditions and non-optimal network configuration), the micro-triangulation method provided results with a mean expanded uncertainty of approximately 5 µm to 7 µm for a 95 % confidence level for the reconstruction of the wire position in the lateral and the vertical directions. The achieved precision is comparable to the precision of both the standard and the novel fiducialization methods at CERN, as described in Section 1.2.2, which are estimated to offer 4 µm standard deviation (*Duquenne et al.*, 2014; *Mainaud Durand et al.*, 2014).

In addition, the mean expanded uncertainty of the offsets between the wire and the fiducials, as computed by the micro-triangulation measurements, was estimated at approximately 10 µm for a 95 % confidence level. The comparison with the offsets computed by the CMM measurements resulted in a mean accuracy of approximately 10 µm, as expressed in terms of the root-mean-square of the differences.

Preliminary results of the measurements presented in this chapter can also be found in *Vlachakis et al.* (2016) and *Caiazza et al.* (2017).

5.2 Equipment

5.2.1 Test bench

In this section, we describe the parts of the Final PACMAN Alignment Bench (FPAB) that are relevant to the micro-triangulation measurements, as presented in Figure 5.2. The FPAB is also described in detail in *Caiazza et al.* (2017).

Quadrupole magnet

One of the main components of the FPAB bench is the prototype Main Beam Quadrupole (MBQ) of Type 1 of the CLIC project (*Vorozhtsov and Modena*, 2011). The magnet, which is 420 mm long, was placed in an aluminium frame that encloses the stabilization and the nano-positioning systems of the MBQ (*Artoos et al.*, 2013). The frame was standing on

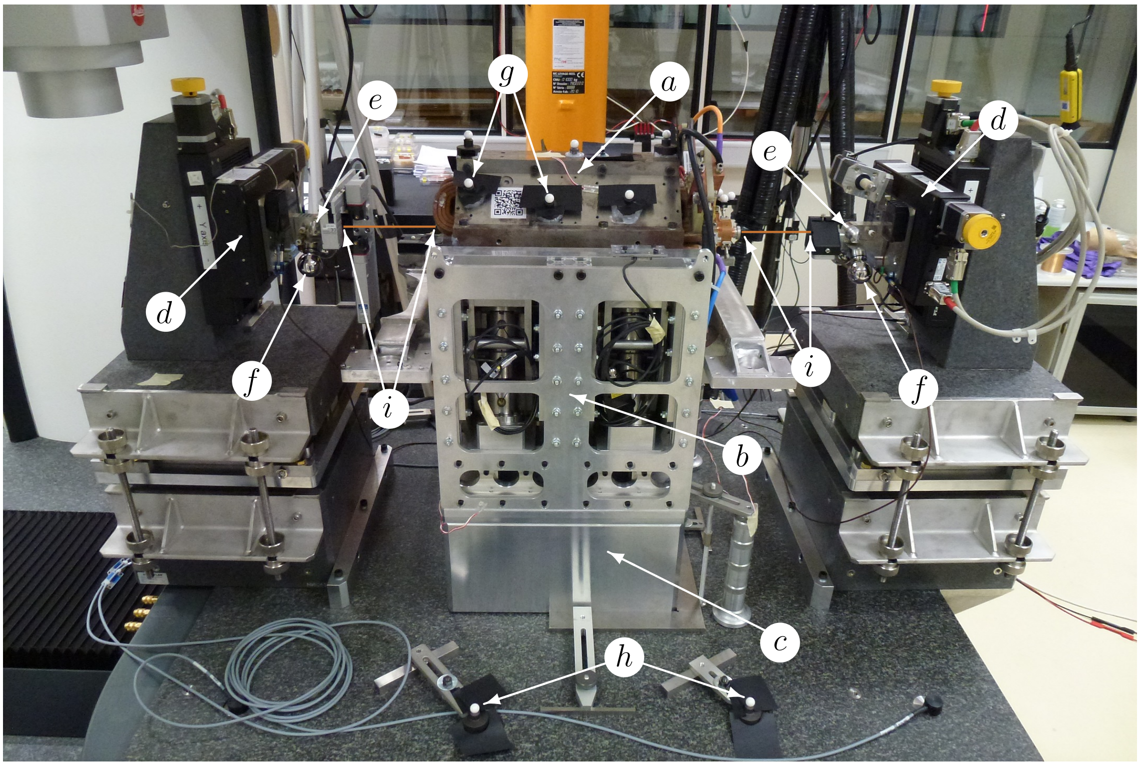

Figure 5.2: Final PACMAN Alignment Bench in the metrology room. The quadrupole magnet *a* is placed in the aluminium frame of the stabilization and the nano-positioning systems *b*, which is standing on an aluminium block *c*. Each stretched-wire support system is equipped with two displacement stages *d*, a pair of tangent spheres *e* to support the wire extremities, and two reference spheres *f*. Ceramic spheres are used as fiducial points on the surface of the magnet *g* and as additional targets of the triangulation network on the CMM table *h*. The stretched wire is passing through the magnet aperture, therefore, it is visible only for about 10 cm on each side of the magnet *i*.

an aluminium block, which only served to bring the aperture of the magnet to the correct height, i.e., within the working area of the stretched-wire displacement stages.

Stretched-wire support system

On each side of the magnet, a pair of perpendicular displacement stages is used to move the wire in the aperture of the magnet during the magnetic measurement. On each horizontal displacement stage, a pair of tangent ceramic spheres with 1 mm diameter is used to support the wire. The wire rests tangential to both spheres (Figure 5.11a). In addition, two reference spheres with 38.1 mm (1.5 inch) diameter are rigidly connected with the tangent spheres. These spheres are used as reference for the computation of the theoretical position of the wire suspension points (see Section 5.3.3).

Fiducial targets

White ceramic spheres were used as fiducial targets that are made by Zirconium dioxide (ZrO_2), with 12.7 mm diameter and 1 µm sphericity (Grade 40, *ISO 3290-1* (2001)). The spheres were attached by magnetic force to aluminium supports, and subsequently, the supports were mounted to the magnet or to the granite table with hot glue.

Wire

The magnetic axis was materialized by a monofilament wire made by *Beryllium Copper Alloy 25* (also coded as *UNS C17200* or *CDA 172*). During the *1st campaign* a wire of 125 µm diameter was used, while for the *2nd* and the *3rd campaign* the diameter of the wire was 100 µm. For the three campaigns, the length of the suspending wire was about 860 mm. More details concerning the physical characteristics of the wire can be found in *Sanz et al.* (2015).

5.2.2 Metrology room

Temperature variations

The measurements presented in this chapter were performed in the metrology room of the EN-MME group (Engineering Department - Mechanical and Materials Engineering) at CERN. The metrology room is classified as CLASS 1, according to VDE/VDI 2627 standard. It operates at a reference temperature of 20 °C, with temporal temperature gradients of $0.2\,\mathrm{K\,h^{-1}}$ and $0.4\,\mathrm{K\,d^{-1}}$, and a spatial temperature gradient of $0.1\,\mathrm{K\,m^{-1}}$.

Four temperature sensors are used to control the room temperature. All the sensors are mounted on the CMM; three on the CMM granite table and one on the bridge. In Figure 5.3, we present a sample of the recordings of the sensors that belongs to the *2nd campaign* (November 2016) and it has a 3.5 h duration and a sampling rate of 1 Hz. The variation profile shows a fast drop of the temperature to the lowest point, due to the air-conditioning system, followed by a slower rise up of the temperature to the highest point. In Figure 5.3, we also see the time series of the mean of the four sensors, which is smoothed by a low-pass filter, specifically, a moving average of three sequential values.

According to this sample, the mean value of all sensors is 19.98 °C, the amplitude of the temperature variation is about 0.3 °C over 3.5 h, and the period is approximately 39 min.

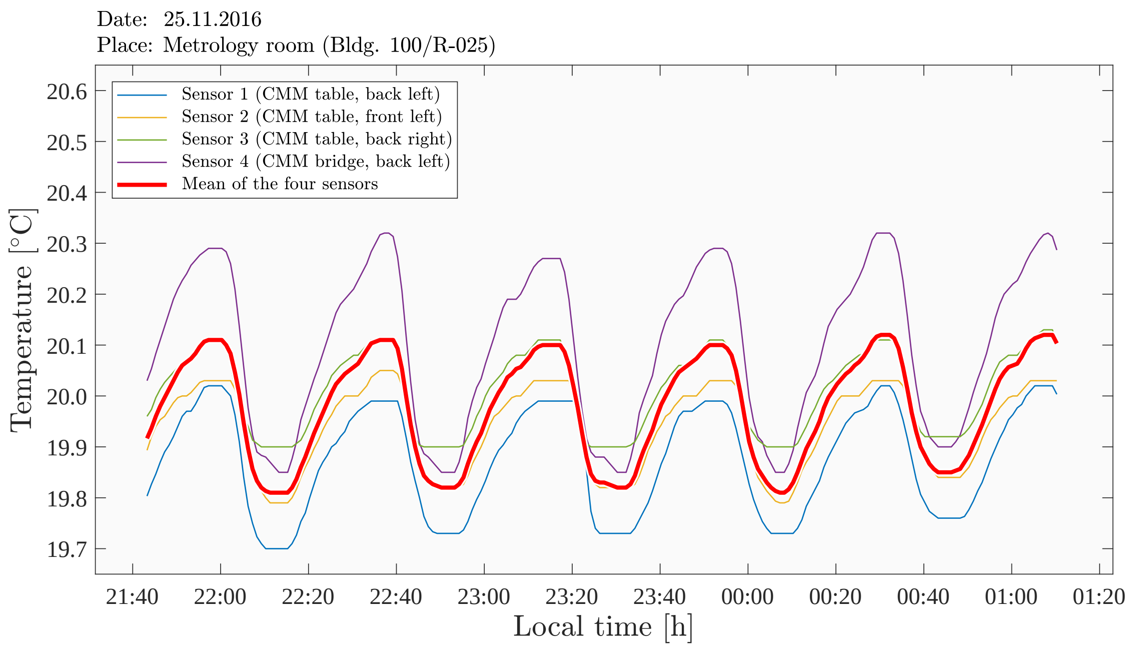

Figure 5.3: Sample of the recordings of the temperature sensors in the metrology room and the time series of the mean value of the four sensors.

These values indicate that the metrology room operates according to the specifications. During the measurement campaigns, we observed small differences in the period and the profile of the temperature variation, possibly related to the difference between the room temperature and the external temperature, which seems to affects the operation of the air-conditioning system.

Space

The metrology room measures $32\,\mathrm{m}^2$ ($5.3\,\mathrm{m} \times 6.2\,\mathrm{m}$), and apart from the CMM, the room is equipped with three office desks, a granite table, a tool box and a crane. During the PACMAN measurement campaigns, more equipment related to the actual test bench was installed in the room. In addition, space was reserved by the CMM operator in order to prepare and execute the CMM measurements.

The aforementioned space constraints, in combination with the high position of the magnet — about 1.6 m from the floor to the top of the magnet — caused difficulties in the selection of the positions for the theodolites. As a result, a non-optimal geometrical configuration of the surveying network was realized. More details about the exact configuration can be found in Section 5.3.4.

Light conditions

The illumination of the metrology room is entirely based on artificial light, which is produced by a few light bodies without diffusers, mounted on the ceiling. The room does not have any window to the natural daylight in order to achieve better insulation.

The low luminosity of the light bodies and the lack of diffusers (Figure 5.7) result in dark shadows on the lower part of the white ceramic spheres and bright reflections on the upper part (see sample images in Appendix F). Moreover, objects such as the CMM bridge and the crane boom partially obscured some light bodies, creating different light conditions for the different points of view of the theodolites.

Although pieces of black paper were placed behind the targets in order to increase the contrast between the white targets and the background (Figure 5.2), the proper selection of the user-defined detection parameters remained to be a challenging task, aiming at optimizing for short duration acquisition of the measurements and for high-precision target detection.

5.2.3 Coordinate measuring machine (CMM)

The Leitz PMM-C Infinity coordinate measuring machine performed measurements during the PACMAN measurement campaigns. These measurements were used as reference for the comparison with the results of the micro-triangulation method.

The Leitz PMM-C Infinity is equipped with the LSP-S4 probe head and a moving granite table, which offers a maximum load capacity of 750 kg. The working volume of the CMM is 1200 mm × 1000 mm × 700 mm. The CMM is installed on three vibration dumpers (Figure 5.9a).

The manufacturer specifies that the maximum permissible error for length measurements ($\mathrm{MPE_E}$) is 0.3 µm + 1 µm m^{-1} (*HEXAGON*, 2011), according to *ISO 10360-2* (2001), over a temperature range from 19 °C to 21 °C. The specified accuracy should be valid anywhere in the measuring volume for specific styli and without extensions.

Tactile probes

The Leitz PMM-C Infinity performed tactile measurements to spherical targets with a variety of probes depending on the accessibility of the targets. The tactile probes were assembled by various styli, extensions, angular joints and cubes (Figure 5.4). All probes were assembled and calibrated before each measurement and they were available on the automatic probe changer rack for fast exchange during the measurement.

Optical probes

Three different optical probes of the PRECITEC LR optical sensor were used for the contactless measurement of points on the wire (Figure 5.5). The measurement principle of the PRECITEC LR optical sensor is based on the chromatic aberration of a white-light beam. The beam is focused on a surface and the distance between the sensor and the target results from the peak frequency of the reflected light (*HEXAGON*, 2015).

According to the manufacturer, the measurement range is 100 µm, the measuring distance is about 6.5 mm, and the spot diameter is about 1.4 µm. Moreover, the offset between a tactile probe and the PRECITEC LR optical sensor should be less than 1 µm, according to the manufacturer. The sensor can measure only in 0° and 90° beam directions (Figure 5.5).

Details on the procedure of the stretched-wire contactless measurements are given in Section 5.3.3.

Figure 5.4: Images of the tactile probes used for the PACMAN measurement campaigns, depending on the accessibility of the targets. The probes consist of various styli, extensions, angular joints and cubes. (Source: Didier Glaude and Cyril Haerinck, CERN).

Figure 5.5: Images of the PRECITEC LR optical sensor probes used for the stretched-wire measurement of the PACMAN test bench. (Source: Didier Glaude and Cyril Haerinck, CERN).

5.2.4 Surveying equipment

Theodolite

Four Leica TDA5005 were used for the validation measurements presented in this chapter. According to the manufacturer specifications, the angular accuracy of the TDA5005 is 0.15 mgon for 1σ, with respect to *ISO 17123-3* (2001), which is approximately equal to 2.4 µrad or 2.4 µm m^{-1}. Moreover, the accuracy of the realization of the vertical direction is 0.1 mgon (*LEICA*, 2002).

QDaedalus

Each TDA5005 theodolite was equipped with the CCD camera and the focusing mechanism of the QDaedalus measuring system. The diverging lens was not used on the objective lens of the theodolite due to the fact that the range of the measurements did not exceed 13 m. More details about the hardware of the QDaedalus system can be found in Section 1.4.2.

Each theodolite and the corresponding QDaedalus system were connected to a separate power converter, located outside the metrology room, in order to stay switched-on for the whole measurement campaign. Four laptops were also placed outside the metrology room; one for each system. Each laptop is connected with a 9 m Firewire (IEEE 1394a) extension cable (3 pieces $\times$ 3 m) to the corresponding CCD camera and with two 10 m USB extension cables (2 pieces $\times$ 5 m) to the theodolite and to the focusing mechanism. The laptops were connected to the power grid and to the internet network with an Ethernet cable, enabling remote measurements.

Tripods

Four Leica AT21 aluminium tripods were used for the majority of the measurements presented in this chapter. A Leica MST36 carbon-fiber tripod was also used for a test measurement concerning the behavior of the tripod with regard to the temperature variations of the metrology room (Section 5.3.1).

In an attempt to mitigate the effects of the temperature variations, a customized insulation was applied to two of the Leica AT21 aluminium tripods during the *2nd campaign*. The insulation consisted of a rubber sheet layer of about 20 mm thickness, covered by overlapping layers of insulating tape.

The insulation was applied to the fully extended legs (Figure 5.6a) and to the central column, up to the fixation ring (Figure 5.6b), assuming that the rest of the column can freely expand downwards without affecting the rest of the tripod. Special care was taken to completely cover the aluminium tubes around the joints (Figure 5.6c) and the feet (Figure 5.6d). Although this solution is cost effective, it is very laborious — especially due to the double aluminium tubes in the upper part of the legs — and time consuming, requiring almost a working day for each tripod.

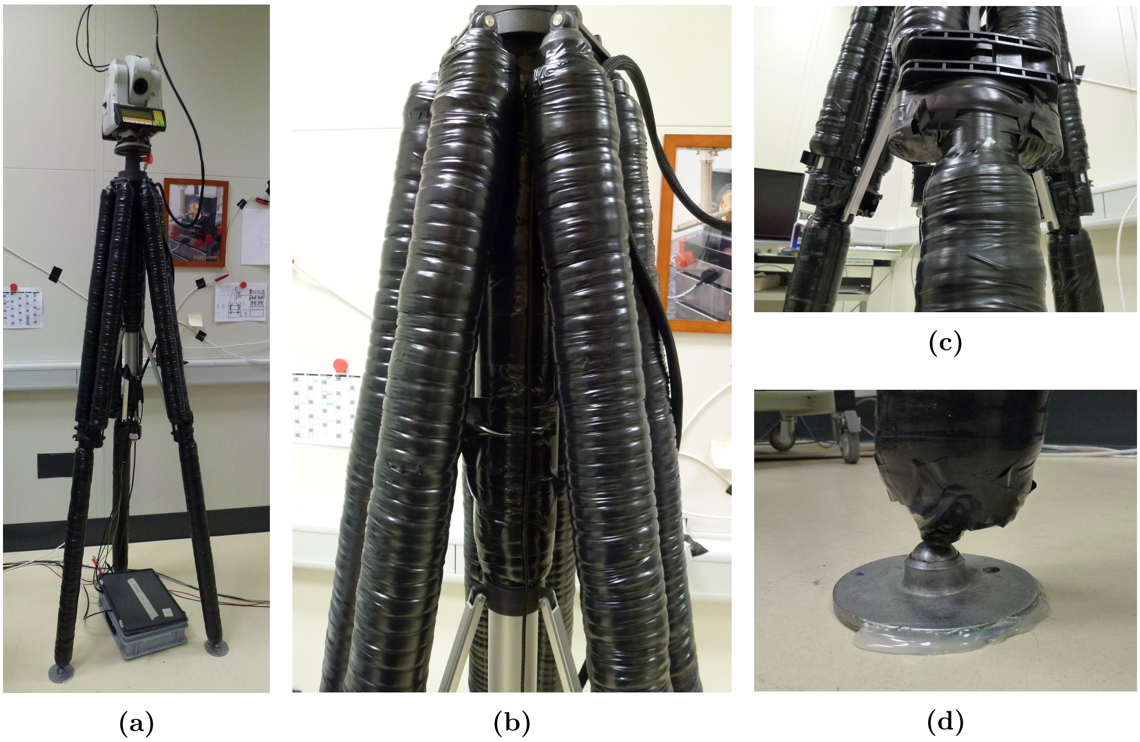

Figure 5.6: Details of the insulation applied to a Leica AT21 aluminium tripod.

5.3 Methodology

5.3.1 Tripod stability measurements

During the *1st campaign* in the metrology room, a test measurement over a few hours — executed in order to ensure the smooth operation of the four QDaedalus systems — revealed a periodic variation of the angle observations.

The configuration consisted of four theodolites mounted on Leica AT21 aluminium tripods, at about 2.3 m instrument height, and a ceramic spherical target on the top of the quadrupole magnet (Figure 5.7). The telescopic legs of the tripods were fully extended but they were not fully deployed (Figure 5.6a). The theodolites were continuously observing the horizontal and the zenith angles to the target, in both faces.

The variation in the measured angles appeared to have a similar frequency to the temperature variation of the metrology room. However, no further analysis was possible due to the fact that we did not manage to retrieve the corresponding temperature recordings on time. Unfortunately, the temperature recordings remain available to the operator of the air-conditioning system for only a few days, before they get overwritten.

During the *2nd campaign*, we repeated the same measurements in order to carefully examine the effect that the temperature variation might have on the tripod stability. The configuration was similar to that of the *1st campaign*, with the difference that two of the tripods were insulated as described in Section 5.2.4, and shown in Figure 5.8.

Two additional measurements with different configurations took place during the *2nd campaign*. In the first measurement, two theodolites were installed on the floor of the

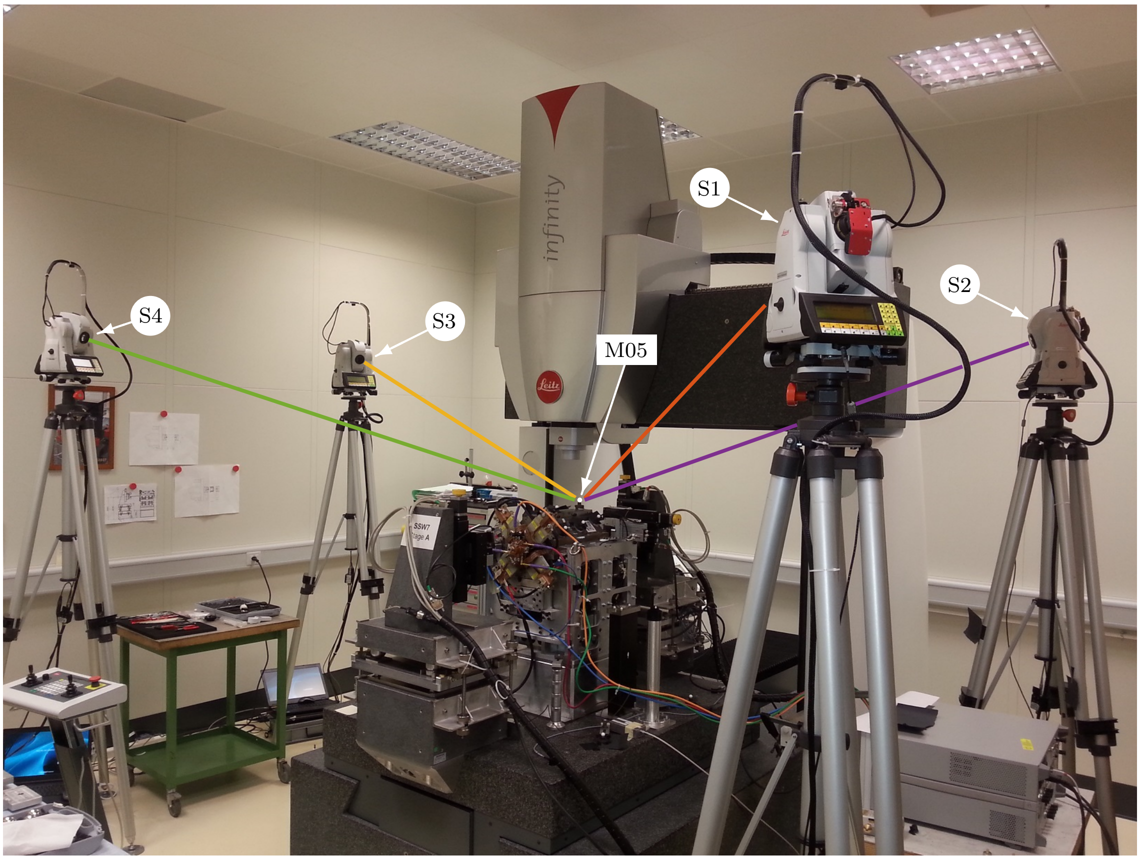

Figure 5.7: Measurement configuration in the metrology room during the *1st campaign*. Four theodolites were observing the target M05 located on the top of the quadrupole magnet.

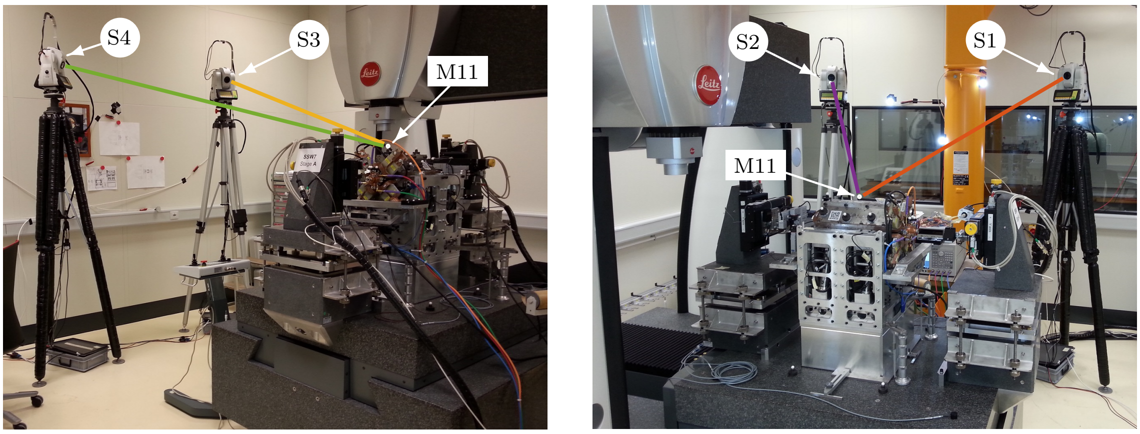

(a) (b)

Figure 5.8: Measurement configuration in the metrology room during the *2nd campaign*. Four theodolites were observing the target M11 located on the top of the magnet. The tripods of the theodolites S1 and S4 were insulated.

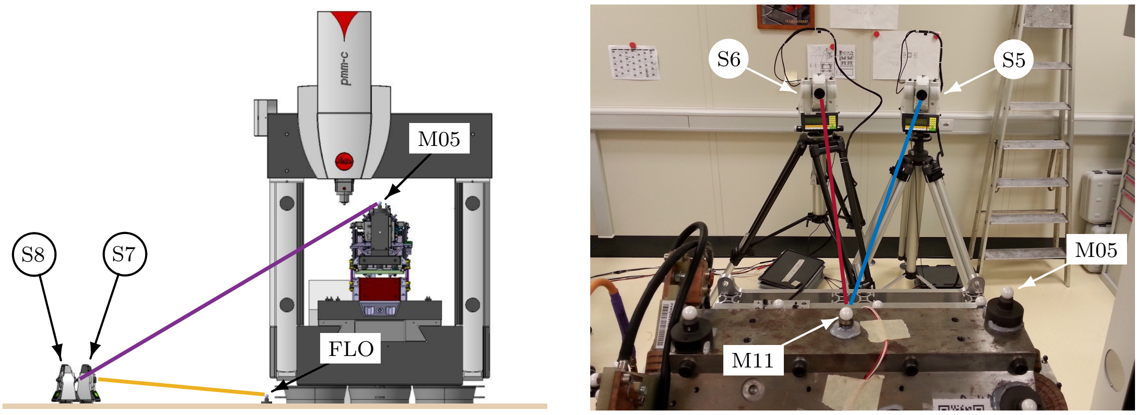

(a) (b)

Figure 5.9: Measurement configuration in the metrology room during the *2nd campaign*. (a) Two theodolites were installed on the floor. Theodolite S7 was observing the target M05, while theodolite S8 was observing the target FLO on the floor. (b) One theodolite (S5) was mounted on a Leica AT21 aluminium tripod, while the other (S6) was mounted on a Leica MST36 carbon-fiber tripod, both were observing the target M11.

metrology room; one was observing a target on the floor, while the other was observing a target on the top of the quadrupole (Figure 5.9a). In the second measurement, two theodolites were simultaneously observing a target on the top of the quadrupole. One theodolite was mounted on a Leica AT21 aluminium tripod and the other on a Leica MST36 carbon-fiber tripod, both at about 1.4 m instrument height (Figure 5.9b).

The data processing is identical to what has already been described in Section 3.2.4. To summarize, a time series is created for each theodolite with the reduced observations of the horizontal angle H and the zenith angle Z. For the reduced measurement i in a total of n measurements, we compute:

$$H_i = \frac{H_i^I + (H_i^{II} - \pi)}{2} \tag{5.1}$$

and

$$Z_i = \frac{Z_i^I + (2\pi - Z_i^{II})}{2} \tag{5.2}$$

where (H_i^I, Z_i^I) and (H_i^{II}, H_i^{II}) are the observations with the theodolite telescope in the *face I* (*left face*) and *face II* (*right face*) position, respectively.

Subsequently, for each time series we compute the mean value $\bar{x}$,

$$\bar{x} = \frac{1}{n} \cdot \sum_{i=1}^{n} x_i \tag{5.3}$$

where x represents either the horizontal angle H or the zenith angle Z.

Finally, we compute the time series of the residuals r_i as

$$r_i = x_i - \bar{x} \tag{5.4}$$

We choose to plot the *elevation angle* (Equation 3.3) as it is more intuitive concerning the up and down directions. The elevation angle is complementary to the zenith angle and measures the angular distance from the horizon to the target, along the local vertical circle. Moreover, we convert the angles to µrad or $\mu m\, m^{-1}$ units.

A simulation was also performed to verify the cause of the angle variation. For the simulation, we made the simplistic assumption that the theodolite is mounted on a vertical tube, which is made of the same material (i.e., aluminium) and it has the same height as the tripod. Moreover, we assumed that the target position remains invariant.

Firstly, the height variation δh_i of the theodolite is computed as the length variation of the tube at a given time T_i,

$$\delta h_i = (T_i - T_0) \cdot \alpha \cdot L_0 \tag{5.5}$$

where

- T_i is the temperature at a given time t_i.
- T_0 is the reference temperature at the time t_0.
- α is the linear thermal expansion coefficient for the given material.
- L_0 is the reference length of the tube at the time t_0.

Secondly, the elevation angle E_i at a given time t_i, is computed as

$$E_i = \tan^{-1}\left(\frac{h_{targ} - (h_{theod} + \delta h_i)}{d}\right) \tag{5.6}$$

where

- h_{targ} is the invariant (according to the assumption) height of the target.
- h_{theod} is the reference instrument height of the theodolite at the time t_0.
- δh_i is the height variation of the theodolite.
- d is the invariant (according to the assumption) horizontal distance between the theodolite and the target.

Finally, the behavior of the simulated elevation angle is compared with the observed elevation angle (see Section 5.4.1).

5.3.2 Magnetic measurements

As already mentioned, the vibrating-wire technique was used for the magnetic measurements of the PACMAN project, mainly to determine the position and the orientation in space of the magnetic axis of the quadrupole magnet. Another output of the magnetic measurements, which is interesting for this study, is the value of the first resonance frequency f_1 of the vibrating wire.

The form factor c describes the catenary shape of a stretched wire (Equation 4.46). The form factor is directly estimated by the least-squares adjustment of the micro-triangulation network as described in Chapter 4. Moreover, it can also be precisely calculated as function of the resonance frequency f_1, and therefore, it can be used for comparison with the micro-triangulation results.

According to *Hatibovic* (2014), if the suspension points of the stretched wire are at the same height, the sagitta s of the wire can be expressed as

$$s = 2 \cdot c \cdot \sinh^2\left(\frac{L}{4 \cdot c}\right) \tag{5.7}$$

where

L is the horizontal distance between the suspension points of the wire.

c is the form factor of the catenary shape in units of length.

Eventually, the assumption that the suspension points are at the same height is a very good approximation for the PACMAN test bench configuration, given the fact that the height difference between the suspension points does not exceed the value of 0.25 mm for the three measurement campaigns (Figures 5.27a and 5.39a).

For the PACMAN test bench configuration, the argument of the hyperbolic sine in Equation 5.7 is evaluated to be in the order of $2 \cdot 10^{-5}$ to $5 \cdot 10^{-5}$ due to the small length and the high tension applied to the stretched wire. Therefore, given that $\sinh(x) \to x$, when $x \to 0$, the sagitta s can be approximated by the expression:

$$s = \frac{L^2}{8 \cdot c} \tag{5.8}$$

On the other hand, according to *Wolf* (2005), under the assumption that the suspension points of the stretched-wire are at the same height, the sagitta s of the wire can be expressed as

$$s = \frac{g}{32 \cdot f_1^2} \tag{5.9}$$

where

f_1 is the first resonance frequency of the vibrating wire.

g is the gravity acceleration (typical value: $9.81\,\mathrm{m/sec^2}$).

Combining Equations 5.8 and 5.9, a precise value for the catenaty form factor c can be computed as

$$c = \frac{4 \cdot f_1^2 \cdot L^2}{g} \tag{5.10}$$

5.3.3 CMM measurements

During the PACMAN measurement campaigns, the coordinate measuring machine executed tactile measurements to the spherical targets, and contactless measurements to the wire. The measurements were performed by Didier Glaude and Cyril Haerinck, members of the Metrology Laboratory at CERN. The results of the CMM measurements were used as a reference for the evaluation of the quality of the micro-triangulation measurements.

Three different pieces of information provided by the CMM measurements are relevant to the analysis of this chapter:

(a) the coordinates of the targets that were used as reference for the precision evaluation of the micro-triangulation network,

(b) the tactile measurements of the reference targets of the wire stages that were used to deduce the theoretical position of the suspension points of the stretched wire, and

(c) the optical measurements of the CMM to the wire that were used to estimate the position and the shape of the stretched wire.

Next, we describe how each different piece of information is acquired and processed in order to get the results that we are interested in.

Tactile measurements to the spherical targets

The CMM performed several tactile measurements on the surface of each spherical target (Figure 5.10). The measurements were well distributed on the accessible part of the spherical surface (Figure 5.10c). The results of this measurement process are the coordinates of the center and the radius of the sphere, estimated by a least-squares fit. The 3D coordinates of the targets are referred to the CMM coordinate system. Unfortunately, in our case no information was provided about the precision of the result or the goodness of the fit.

In this study, we used the CMM coordinates of the targets for two purposes. Initially, a part of these coordinates is used to constrain the datum of the triangulation network, mainly providing a very accurate scale to the triangulation network. After the triangulation network analysis, the CMM coordinates were used as reference for the evaluation of the estimated target coordinates, and the wire position and orientation.

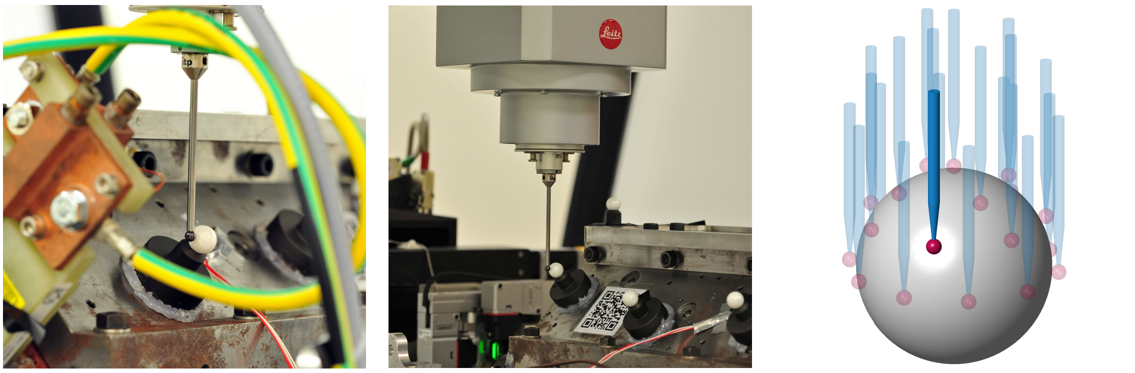

(a) (b) (c)

Figure 5.10: CMM tactile measurements. (a, b) Tactile probes performing measurements of the spherical targets. (c) The tactile measurements were well distributed on the accessible part of the target surface.

Computation of the stretched-wire suspension points

The calibration of the wire stages is required in order to define the relative position of the wire axis with respect to the tangible reference targets. The core structure of the wire stage is depicted in Figure 5.11a. According to the calibration process, a CMM measures the two reference spheres with a tactile probe and the two tangent support spheres with an imaging sensor. Subsequently, a circle with the diameter of the wire is graphically positioned to be tangent to the image of the support spheres. For each stage, a local coordinate system (CS^{CAL}) is set to be parallel to the plane defined by three points, namely, the centers of the two reference spheres and the center of the circle. The origin of the coordinate system is placed at the center of the circle, while the X-axis is set to be parallel to the straight line defined by the centers of the reference spheres (Figure 5.11a).

According to the standard fiducialization process, after the completion of the magnetic measurements, the stretched wire is placed at the position of the estimated magnetic axis. Subsequently, the reference spheres of the wire stages and the fiducial points are measured with a laser tracker, or in our case, with the CMM and their coordinates are obtained in the CMM coordinate system (CS^{CMM}). In Figure 5.11b, we notice that in general the axis connecting the two reference spheres is misaligned with respect to the CS^{CMM} by an angle φ around the Z-axis (X-Y plane) and by an angle ϑ around the X-axis (Y-Z plane).

To extract the position of the wire axis in the CS^{CMM}, the solution would have been to perform a $7-$parameter 3D Helmert transformation from the CS^{CAL} to the CS^{CMM}, if the stages were equipped with at least three non-coplanar spheres. Since there are only two spheres available, only six parameters of the 3D transformation can be estimated, while the last one (the rotation around the axis connecting the two spheres) should be constrained. In this study, we constrain this rotation to zero, which means that the computed point of the wire axis is constrained to belong to the vertical plane that passes through the reference spheres.

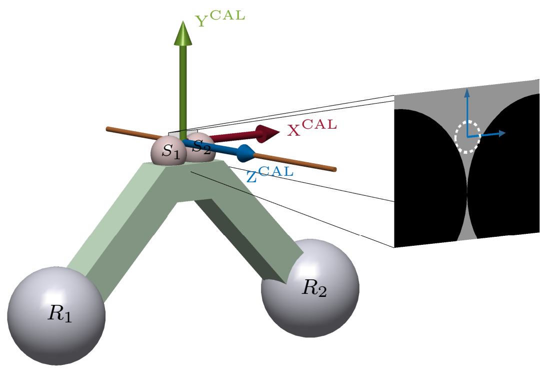

(a)

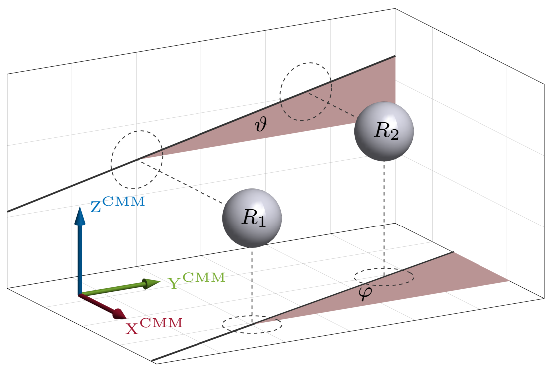

(b)

Figure 5.11: Calibration process of the wire stage. (a) The stretched wire is assumed to be tangent to the support spheres S_1 and S_2. A circle with the nominal diameter of the wire is graphically positioned to be tangent to the image of the support spheres. (b) The axis connecting the reference spheres R_1 and R_2 is typically misaligned with respect to the CMM coordinate system.

Optical measurements to the stretched wire

The optical probes of the PRECITEC LR optical sensor were used to measure points on the stretched-wire in the CMM coordinate system. Initially, for each point, a plane parallel to the CMM coordinate system was selected. This plane was also assumed to be perpendicular to the wire axis. Therefore, three coplanar measurements on the surface of the wire are adequate to define a circle that is perpendicular to the wire (Figure 5.12c). The vertical optical probe measured a point on the top of the wire and the two horizontal optical probes measured one point on each side of the wire (Figures 5.12a and 5.12b).

The center and the radius of each circle were computed from the three measured points. Finally, the 3D coordinates of each point on the wire axis were obtained by combining the 2D coordinates of the circle center (lateral and vertical positions) and the position of the selected plane that is perpendicular to the wire (longitudinal position).

For the *1st* and the *2nd* campaigns of measurements, only two points on the wire axis were measured with this method. These points were located on the accessible part of the stretched wire on each side of the magnet. During the *3rd campaign*, a micro-triangulation test measurement was performed without the magnet. In that case, 29 points were measured with this method, evenly distributed along the wire.

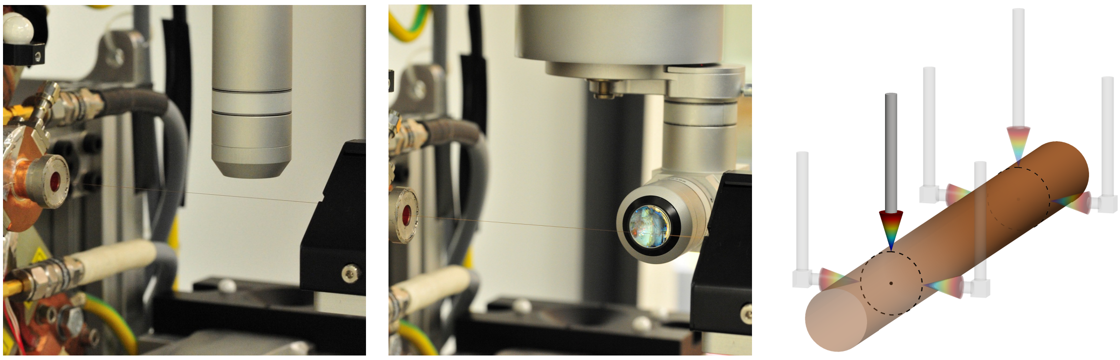

(a) (b) (c)

Figure 5.12: Direct wire measurement with the PRECITEC LR optical sensor. a) The vertical probe measuring a point on the top of the wire. b) The horizontal probe measuring a point on each side of the wire. c) The wire axis was defined as the center of the circle, computed from the three coplanar measurements on the surface of the wire.

5.3.4 Micro-triangulation measurements

The micro-triangulation measurement procedure for the quadrupole fiducialization in the metrology room mainly consists of three steps. The first step includes the installation of the equipment inside and outside the metrology room, as described in Section 5.2.4. The installation used to take place at the same time with the installation of the test bench and it was followed by a check of the smooth operation of all parts.

As soon as the test bench was in place, we were proceeding to the second step, which was the configuration of the detection parameters for each instrument. As an example, Appendices E and F contain the full set of the parameter values used for the network measured on April 7, 2017, during the *3rd campaign*. By the end of the configuration process, a test measurement used to take place in order to verify the validity of the parameters.

The last step was the acquisition of the observations that were used for this study. The micro-triangulation network used to be measured immediately after the CMM measurement, which was following the magnetic measurement. For each network many series of angle measurements were performed, depending on the time availability. Each series of angle measurements used to last for about 8 min to 15 min, depending on the number of the measured points and on the values of some specific user-defined parameters, such as the shutter speed, the number of shots and the number of angle measurements per point.

In this chapter two indicative networks are analyzed. The first network is part of the *2nd campaign*, measured on November 25, 2016, while the second network is part of the *3rd campaign*, measured on April 7, 2017. For simplicity, from now on we will call the first network *161125 network* and the second one *170407 network*.

A detailed description of the two networks and the significant elements of the least-squares adjustment follows.

Description of the *161125 network*

The *161125 network* consists of nine fiducial points mounted on the surface of the magnet, four targets mounted on the CMM table, a stretched wire passing through the aperture of the magnet and four theodolites. The targets and the wire are described in Section 5.2.1. The length of the wire is 0.857 m, the height difference of the suspension points is 0.21 mm and the sagitta is approximately 12 µm. The configuration of the network is presented in Figure 5.13.

- **Functional model.** The applied functional model is described in detail in Section 4.3. It is an expanded model, including three systematic errors for each theodolite and each series of measurements, and the catenary parameters of the stretched wire. The functional model is based on a topocentric coordinate system and does not include corrections for the Earth's curvature or the atmospheric refraction.

- **Observations.** The total number of observations is 1814. The horizontal and zenith angles of four sequential series of angle measurements are included in the adjustment. The total acquisition time for the four series is about 40 min, which is selected to correspond to the period of the temperature variation (see Section 5.4.1 and Figure 5.16). The observations are divided into 920 observations for the *left face* and 894 observations for the *right face* of the theodolite. This difference is due to the fact that a few wire observations used to systematically fail in the *right face* telescope position. They can also be divided into 907 horizontal angles and 907 zenith angles, of which 566 observations were made to the targets and 1248 observations to the wire.

- **Unknowns.** The total number of unknown parameters is 782. According to the applied functional model, for each instrument position and for each series of measurements seven unknown parameters are added (three coordinates, the orientation and three theodolite systematic errors). The total number of the theodolite-related parameters is 112, the unknown coordinates of the targets are 69, and there are also 631 unknowns concerning the wire. Seven of the wire-related unknowns are used to describe the position, orientation and shape of the centenary, while the rest are the parameters t_p of the parametric catenary model (see Equation 4.46).

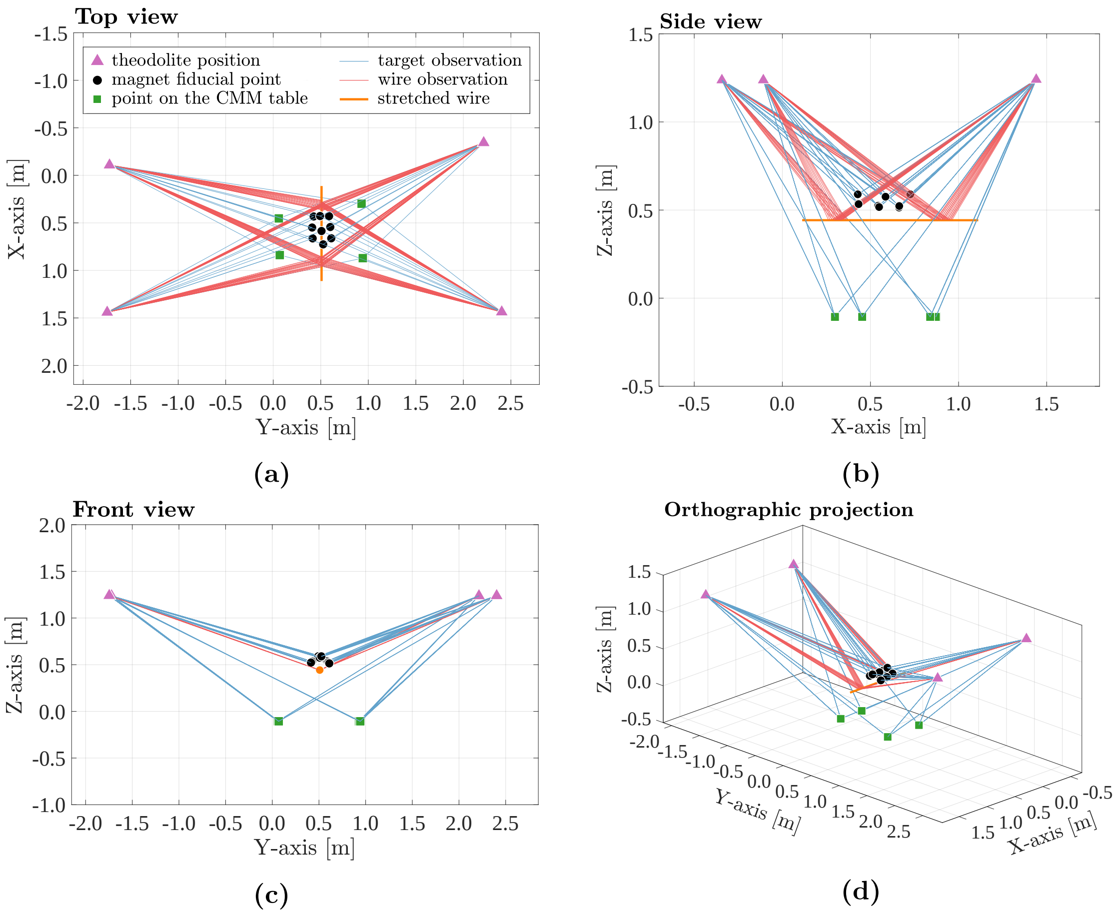

Figure 5.13: Configuration of the *161125 network*. The network consists of 13 targets (nine on the magnet and four on the CMM table), four theodolite positions, and an approximately horizontally stretched wire. The network occupies a volume of $1.8\,\mathrm{m} \times 4.2\,\mathrm{m} \times 1.3\,\mathrm{m}$. The height of all the theodolites is approximately 2.3 m from the floor, while the minimum and the maximum range of the angle observations are 1.8 m and 3.2 m, respectively.

- **Constraints.** The rank defect of the normal equation matrix is equal to seven, therefore, an equal number of constraints was added. In order to perform a partial trace minimization adjustment, the 27 coordinates of the nine fiducial points were used to create five Helmert conditions (Section 4.5.1). Two more constraints were added for the wire, as described in Section 4.5.2.

Description of the *170407 network*

The configuration of the *170407 network* is similar to that of the *161125 network*, however, there are some differences. Firstly, the magnet was removed. Therefore, there were no fiducial points, and the wire was visible over the whole suspending length. Secondly, two more targets were added on the CMM table, and lastly, less tension was applied to the stretched wire, resulting in an approximate sagitta of 21 µm. The configuration of the network is presented in Figure 5.14.

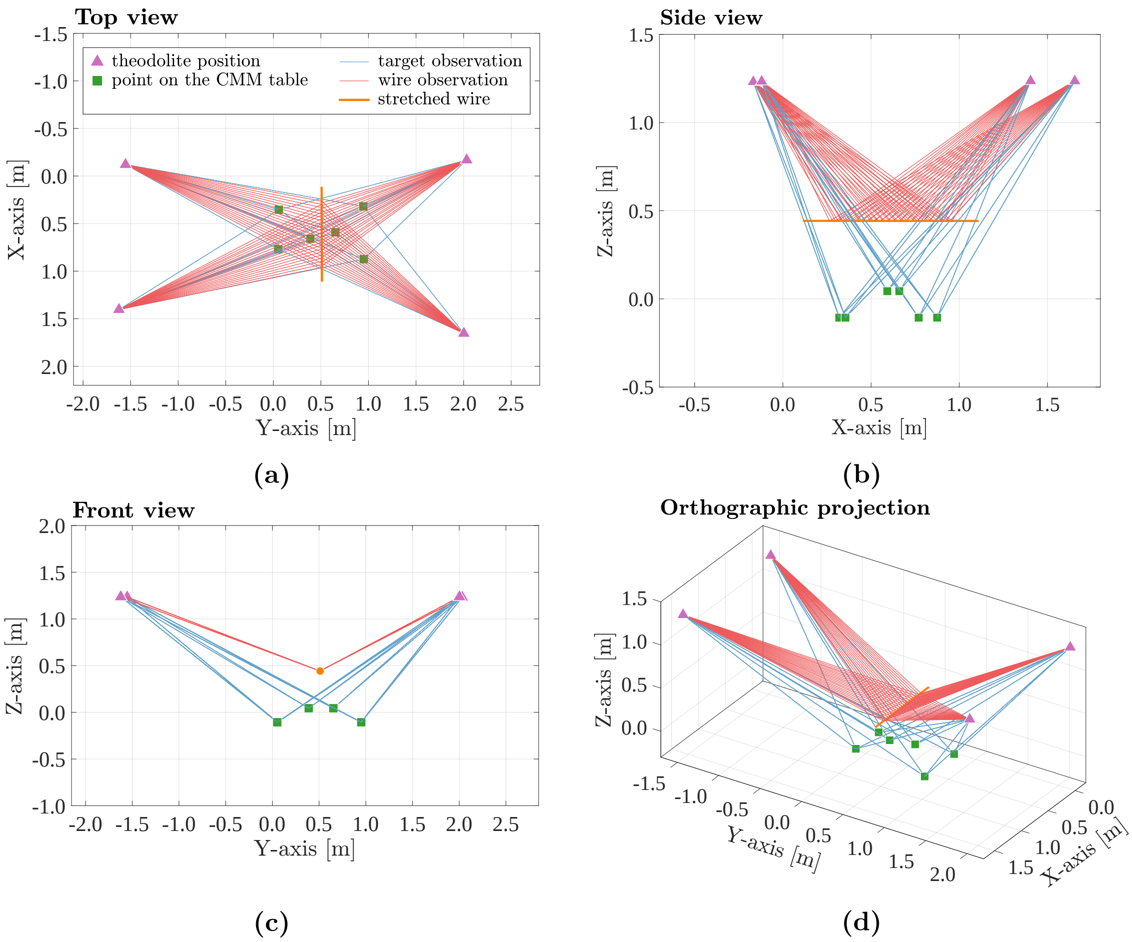

Figure 5.14: Configuration of the *170407 network*. The network consists of six targets on the CMM table, four theodolite positions, and an approximately horizontally stretched wire. It occupies a volume of 1.8 m × 3.7 m × 1.3 m, and the theodolites are installed approximately 2.3 m above the floor. The minimum and the maximum range of the angle observations are 1.8 m and 3.2 m, respectively.

- **Functional model.** The functional model applied to this network is exactly the same as in the *161125 network*.

- **Observations.** Three sequential series of angle measurements were included in the adjustment, with a total acquisition time of about 40 min. The set of the 2512 observations is divided into 1272 observations for the *left face* and 1240 observations for the *right face* of the theodolite. There are 1256 horizontal angles and 1256 zenith angles, of which 600 observations were made to the targets and 1912 observations to the wire.

- **Unknowns.** The total number of unknown parameters is 1065, divided into: 84 parameters related to the theodolites (position, orientation, systematic errors), 18 unknown coordinates of the targets and 963 unknown parameters that concern the wire.

- **Constraints.** The constraints introduced to the network are similar to those introduced to the *161125 network* except that in this case the Helmert conditions are calculated with the 18 coordinates of the six targets mounted on the CMM table.

5.3.5 Accuracy evaluation

The results of this chapter are focusing on three comparisons. The comparisons aim to evaluate the accuracy of a micro-triangulation network for magnet fiducialization that it measured with the described instrumentation and in the described environmental conditions. The reference for these comparisons are the CMM measurements that are considered to be about an order of magnitude more accurate than the micro-triangulation measurements.

Fiducial point coordinates comparison

For each of the two case studies that are analyzed in the present chapter, the coordinates are expressed in two different coordinate systems; the CMM coordinate system and the triangulation coordinate system. The two systems have neither an equal scale, nor the same centroid, due to fact that the triangulation network datum was constrained to a part of the CMM coordinates. Moreover, the two coordinate systems are not parallel, therefore, before the comparison we applied a 7-parameter 3D Helmert transformation. We selected to transform the CMM coordinates to the triangulation coordinates in order to preserve the local vertical direction of the triangulation network.

For each case study, the transformation parameters were estimated by using all the available common targets.

Stretched-wire position and shape comparison

For each case study, seven wire-related parameters are estimated from the network adjustment. These parameters are used to reconstruct the catenary-shaped wire in the 3D space, which we call the *micro-triangulation wire*, for simplicity. This estimation of the wire position and shape (curvature) is going to be compared with the other two estimations obtained from of the CMM measurements. Depending on which data we use for the reconstruction, we will call them the *indirect wire* and the *direct wire*.

For the *indirect wire* the following algorithm is executed. Firstly, we apply the aforementioned transformation to the coordinates of the wire-stages reference targets measured by the CMM. Secondly, the suspension points of the wire are computed according to the method described in Section 5.3.3. Subsequently, the form factor of the catenary shape is estimated by the resonance frequency of the wire, according to Section 5.3.2. Lastly, the coordinates of the suspension points and the form factor are used in Equation 4.46 in order to reconstruct the catenary shape of the wire in space.

The calculation of the *direct wire* parameters is different for the two case studies. In the case of the *161125 network*, in which only two points are available, we followed the same algorithm as for the *indirect wire*. The only difference is that the coordinates of the two directly measured points were used instead of the two computed suspension points. On the contrary, in the case of the *170407 network*, in which 29 points have been directly measured, we followed a different approach in order to calculate the *direct wire*. After the coordinate transformation of the 29 points directly measured by the CMM on the wire, we proceeded to a least-squares fit of the catenary equation in order to estimate the appropriate parameters.

Given the parameters of each of the estimated wires, we can compare the relative position of the catenaries and their shape, as expressed by the form factor.

Fiducial points to stretched-wire offset comparison

An important output of the fiducialization process is the offsets (distances) between the fiducial points and the functional axis of the particle accelerator component (e.g., the magnetic axis in case of a quadrupole magnet). The offsets represent the geometry of the fiducials and the stretched wire, independently of the coordinate system in use.

To obtain the offsets either from the CMM measurements or from the network of the micro-triangulation measurements, we firstly compute the projection of each fiducial point onto the corresponding wire, and subsequently, we compute the distance between the projection point and the fiducial (see also Figure 6.6b). Actually, we can compute and compare the horizontal offsets, the vertical offset and the offsets in the 3D space.

In addition, for the micro-triangulation network the full covariance matrix of the estimated parameters is available, therefore, we are able to rigorously estimate the uncertainty of any product magnitude; in this case the offsets. In Section 4.7.1, we describe in detail the uncertainty estimation for the 3D offset.

5.4 Results

5.4.1 Tripod stability

In this section, we discuss the results of the angle measurement time series concerning the stability of the theodolite position under the environmental conditions of the metrology room. More specifically, in each of the following four figures we superimpose the measurements of the theodolites that are simultaneously monitoring one or more targets, depending on the configuration. The time series are smoothed by a low-pass filter, i.e., a moving average of three sequential values. In Sections 5.3.1, we described in detail the various configurations and the data processing methodology.

First measurement

In Figure 5.15, we see the superimposition of the angle measurements of four theodolites observing a spherical target located on the top of the magnet. The measurements took place during the *1st campaign* and the configuration is depicted in Figure 5.7. The sample has a duration of 2 h 16 min, sampling one double-face measurement every 25 s. For each

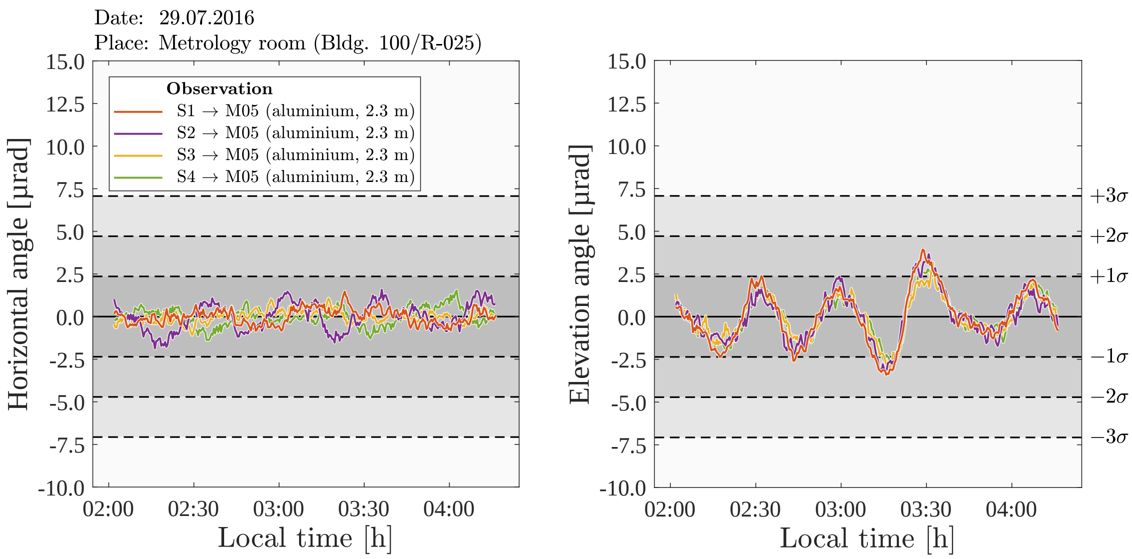

Figure 5.15: Horizontal and elevation angle variations of four theodolites observing a spherical target. The theodolites were installed on aluminium tripods at approximately 2.3 m instrument height.

time series, we observe a periodic behavior with a period of approximately 29 min that reflects the periodic temperature variation in the room during the measurement.

In Figure 5.15, we observe that the horizontal angle variations are incoherent for the four theodolites, while the elevation angle variations are coherent. The period is similar to the temperature variation in the metrology room, thus, we assume that the angle variations are related to the thermal expansion. However, due to the lack of the corresponding temperature recordings, we could not draw a clear conclusion, therefore, we decided to further investigate the cause of this variation during the next measurement campaign.

Second measurement

A similar measurement took place during the *2nd campaign*. This experiment has two important differences with respect to the first measurement: a) the air-conditioning system had been in maintenance a few weeks before the measurement, and b) two of the aluminium tripods were insulated with rubber sheets (Figure 5.8). In Figure 5.16, we see a 2 h sample of the time series, sampling one double-face measurement every 28 s.

The largest range of the horizontal angle variation is observed for the theodolite S2 (on aluminium tripod), which is equal to 4.9 µrad, and corresponds to a horizontal displacement of about 10 µm. The theodolite S3 (on aluminium tripod) demonstrates the largest range of the elevation angle variation, which is equal to 6.9 µrad, and corresponds to a vertical displacement of approximately 18 µm. The corresponding values for the theodolite S1 (on insulated tripod) are significantly smaller, i.e., 4.8 µrad and 11 µm, respectively.

A simulation was performed for the effect of the temperature variation on the elevation angle, specifically, from the theodolite S3 to the target M11. The exact formulation of the simulation is presented in Section 5.3.1.

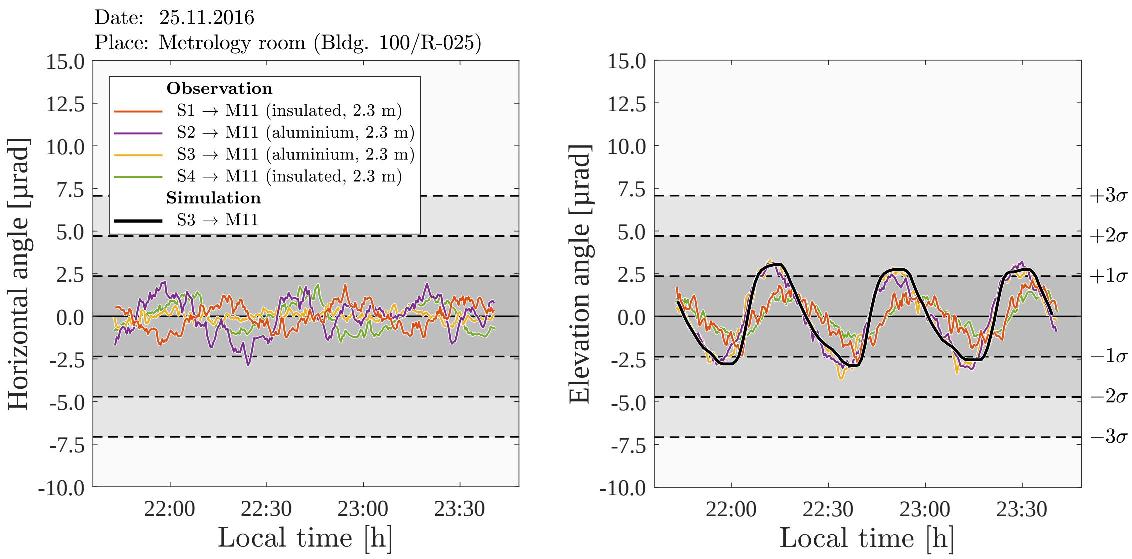

Figure 5.16: Horizontal and elevation angle variation of four theodolites observing a spherical target. The theodolites are installed on aluminium tripods at approximately 2.3 m instrument height. The tripods of the theodolites S1 and S4 were insulated with rubber sheets. The vertical displacement of the theodolite S3 has been simulated according to the configuration and the environmental conditions.

The input values in Equation 5.5 are the mean values of the four temperature sensors (T_i) and the mean value of the entire four time series (T_0). From the temperature recordings we see that the amplitude of the temperature variation is 0.31 °C. The rest of the input values are: the lineal thermal expansion coefficient (α) for aluminium, which is equal to 23.1 µm m^{-1} °C^{-1}, and the reference length of the tripod height (L_0), which is equal to 2.1 m. The computed amplitude of the height variation for the given input values is equal to 15 µm.

To compute the simulated elevation angle we follow Equation 5.6. The input height difference between the theodolite and the target is equal to 0.662 m and the horizontal distance is equal to 2.336 m. These values are precisely known from the *161125 network* solution. The amplitude of the simulated elevation angle is equal to 5.9 µrad and the period is approximately 39 min. The profile of the elevation angle variation is the inverse of the temperature variation profile, which is depicted in Figure 5.3.

In Figure 5.16, we notice that the insulated tripods (S1 and S3) demonstrate smaller amplitudes for the elevation angle variation than the non-insulated tripods (S2 and S4). Moreover, we observe that the insulation causes a time delay to the variation, and in general, a smoother vertical displacement of the theodolite. Apparently, the time series of the simulated elevation angles that corresponds to the theodolite S3 matches very well with the observations of the theodolite S3. This result verifies the assumption that the target itself did not execute a periodic vertical motion, and in case it did, this was not detectable by the specific configuration and the employed measuring system.

The variation of the horizontal angle time series also demonstrates a periodic behavior. Unfortunately, it is not possible to reconstruct the complete horizontal movement of the theodolites due to the fact that only the movement in the lateral direction with respect to the optical axis is observable. Most probably, there is a wobbling pattern related to the tilt of the tripod mounting plate, caused by the non-equal length of the tripod legs.

Third measurement

The aforementioned simulation is based on the assumption that the target on the top of the magnet is stable. This assumption is supported by the fact that the target was mounted on a stack of objects that were large in dimensions and massive, and therefore, less affected by relatively high-frequency and low-amplitude temperature variations. Moreover, the majority of these objects were made out of materials such as steel and granite with smaller expansion coefficients compared to aluminium.

To verify this assumption, we designed and executed an additional measurement, in which two theodolites were placed on the floor; one observing a target on the magnet, and the other observing a target on the floor. The configuration of the measurement is illustrated in Figure 5.9a and the result is presented in Figure 5.17. A 2 h sample of one double-face measurement every 28 s demonstrates an excellent stability for the target placed on the floor as well as for the target on the top of the magnet. During the measurement, the temperature variation had an amplitude of 0.31 °C with a period of approximately 35 min.

To quantify the level of stability, we report the standard deviations of the samples. For the horizontal angles we compute the values of 0.2 µrad and 0.5 µrad for the theodolites

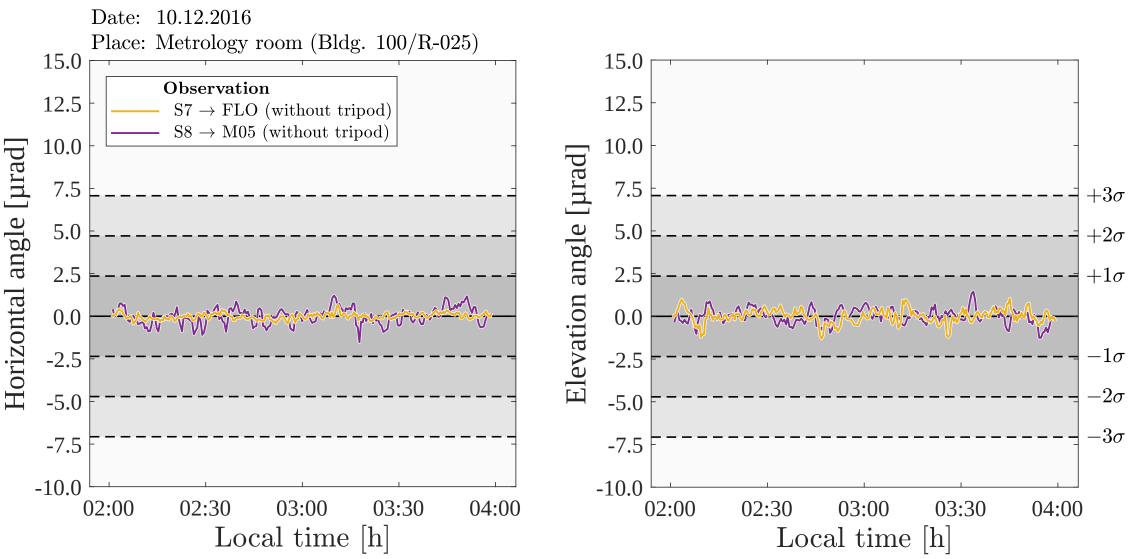

Figure 5.17: Horizontal and elevation angle variations of two theodolites directly mounted on the floor. The theodolite S7 is observing a spherical target (FLO) also mounted on the floor, while the theodolite S8 is observing a spherical target (M05) mounted on the magnet.

S7 and S8, respectively. The standard deviations of the elevation angles are 0.4 µrad for S7 and 0.5 µrad for S8. We notice that although the standard deviations of the elevation angles are similar for the two measurements, the standard deviations of the horizontal angles significantly differ. Many parameters may have contributed to this result, e.g., lower horizontal vibrations for the target located on the floor, smaller noise levels on the horizontal circle of the theodolite observing the target on the floor, or better atmospheric conditions due to the significantly smaller height difference between the target on the floor and the theodolite.

The values of the standard deviation that have been achieved in this measurement are 5 to 10 times smaller than the standard deviation of the angular accuracy specification of the employed theodolites, which is approximately 2.4 µrad. This result is similar with the performance of the theodolites as evaluated in Chapter 3. It is clear that the achieved values can only be considered as indicators of the angular precision of the specific type of theodolite, since they correspond to only one direction in space. These values should not be confused with the angular accuracy specification, which refers to every direction and it is estimated following a specific measurement configuration as suggested in *ISO 17123-3* (2001).

Fourth measurement

The last configuration aims at demonstrating the effect that the temperature variation has on a carbon-fiber tripod, when it is fully extended. Two theodolites were installed at the maximum instrument height that can be reached with the Leica MST36 carbon-fiber tripod, which is approximately 1.3 m. Both theodolites were observing a target on the top of the magnet, according to the configuration depicted in Figure 5.9b. A sample of the measurements is presented in Figure 5.18. The sample has a 2 h 20 min duration with one double-face measurement every 28 s.

Here, we observe that the carbon-fiber tripod causes a smaller amplitude and a time delay in the elevation angle variation, compared to the aluminium tripod. For the horizontal angle variation, the maximum range corresponds to S6 (carbon-fiber tripod) and it is 3.7 µrad, or 10 µm, given the distance. The elevation angle variation of the theodolite S6 has a range of 2.6 µrad, or 7 µm, while for the theodolite S5 (aluminium tripod) the range is 4.3 µrad, or 11 µm.

It is also interesting to notice that the vertical displacement range of the aluminium tripod with an instrument height of 1.3 m is similar to that of the insulated aluminium tripod with an instrument height of 2.3 m (Figure 5.16). This result corresponds to a temperature variation of a 0.32 °C amplitude and a period of approximately 47 min.

We notice that the period of the temperature variation is different for each of the four measurements, while the amplitude remains stable at approximately 0.3 °C. As already mentioned in Section 5.2.2, these differences are most probably caused by the operation of the air-conditioning system.

A simulation was also performed for this sample, concerning the theodolite S5, which is mounted on the aluminium tripod. The input values were: 23.1 µm m^{-1} °C^{-1} for the linear thermal expansion coefficient (α), 1.1 m for the reference length (L_0) of the tripod height, 0.277 m for the height difference and 2.620 m for the horizontal distance between the theodolite and the target.

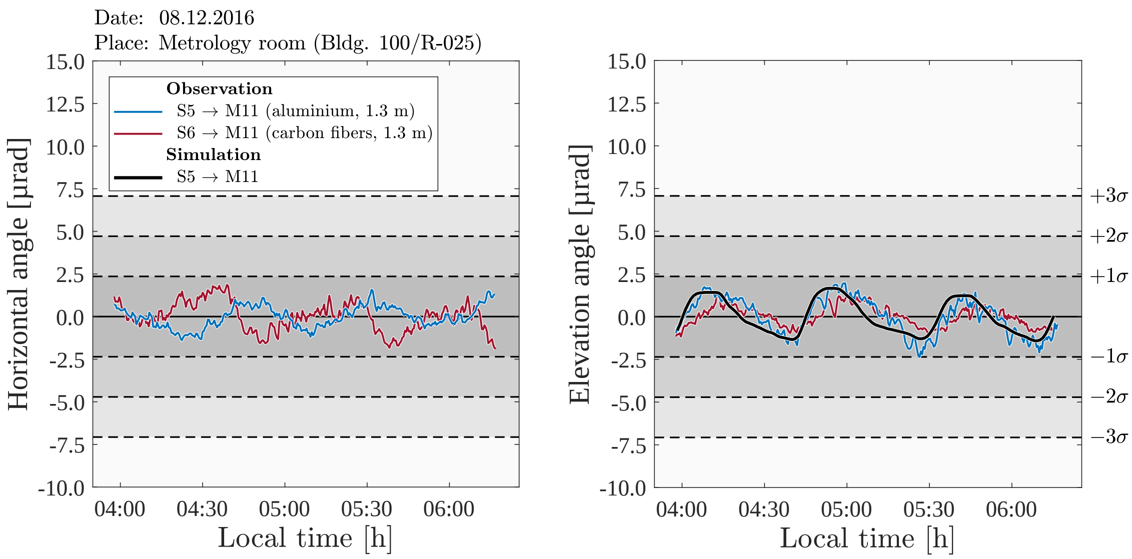

Figure 5.18: Horizontal and elevation angle variations of two theodolites; one mounted on an aluminium tripod, the other on a carbon-fiber tripod. The theodolites are installed at approximately 1.3 m instrument height, both observing a spherical target mounted on the magnet. The vertical displacement of the theodolite S5 has been simulated according to the configuration and the environmental conditions.

The result of the simulation also matches very well with the observed data of the theodolite S5. The amplitude of the temperature variation (0.32 °C) results in a height-variation amplitude of 8 µm, and consequently, in a 3.1 µrad amplitude for the elevation angle variation.

5.4.2 Analysis of the *161125 network* case study

Least-squares adjustment of the observations

The functional model of the *161125 network* is already described in Section 5.3.4. For the stochastic model the observations were grouped into: horizontal angles to the targets, zenith angles to the targets, horizontal angles to the wire and zenith angles to the wire. The initial values of the *a priori* standard deviation $\sigma_{i,G}$ was set equal to 0.15 mgon, for each observation i of each group G of observations. After a few repetitions of the adjustment, and by updating the *a priori* standard deviation values (see Equation 4.79), we end up with the values in Table 5.1, while the *a posteriori* standard deviation components $\hat{\sigma}_G$ are converging to the unit value.

The *a priori* standard deviation values in Table 5.1 indicate that the observations are slightly worse than it is expected by the specifications of the theodolite. Mainly, two sources of uncertainty contribute to the higher standard deviation values. The first source is the instrument height variation due to the temperature variation, which is already demonstrated, while the second source is the different light conditions for each target,

Table 5.1: The *a priori* and *a posteriori* reference standard deviations (σ_0, $\hat{\sigma}_0$), the standard deviations $\sigma_{i,G}$ for each observation i of each group G of observations and the *a posteriori* standard deviation components $\hat{\sigma}_G$ for the *161125 network*. The observations are grouped into horizontal and zenith angles to the targets (H_t, Z_t) and to the wire (H_w, Z_w).

161125 network

			target observations		wire observations	
Reference	[mgon]	Components	H_t [mgon]	Z_t [mgon]	H_w [mgon]	Z_w [mgon]
σ_0	1.00	$\sigma_{i,G}$	0.22	0.39	0.19	0.21
$\hat{\sigma}_0$	1.00	$\hat{\sigma}_G$	1.00	1.00	0.98	0.99

which resulted in various systematic effects in the target detection and measurement process (see Appendix E).

The estimated residuals $\hat{v}$ of the four aforementioned groups of observations are depicted in different colors in Figure 5.19. The residuals demonstrate a pattern of systematic errors that is very well repeated between the four sequential series of measurements, which were performed under theoretically identical conditions. Details on the behavior of the wire observation residuals are presented in Section 5.4.3, in which we analyze the *170407 network*. The probable source of the pattern of the residuals and of the correlation between the horizontal and the zenith angle residuals of the wire observations are more evident in the *170407 network* due to the large spatial spread of the observations along the wire.

In Figure 5.20, we present the estimated standard residuals $\hat{w}$ of the observations. Approximately 6.2 % of the values are out of the ±1.96 interval which corresponds to the 95 % of the *normal* distribution. The observations exceeding this threshold are those that were automatically reweighted according to the Biber weight function (Equation 4.89).

In Figure 5.21, we see the number of observations that were reweighted (approximately 6.2 %) and the magnitude of the p_Biber weight factors. We also observe that the p_Biber weight factors of the horizontal and zenith angle observations to the wire are fully

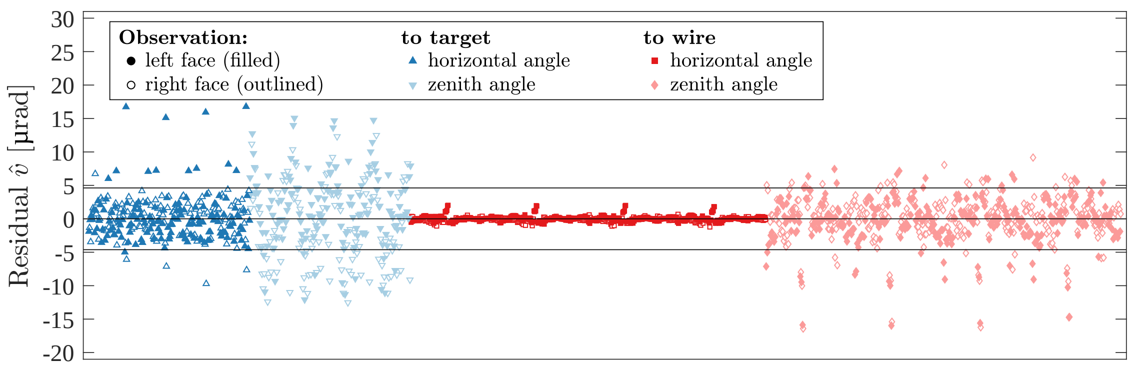

Figure 5.19: Estimated residuals $\hat{v}$ of the *161125 network*. The horizontal black lines represent the 95 % confidence interval of the angular precision of the theodolite according to the manufacturer.

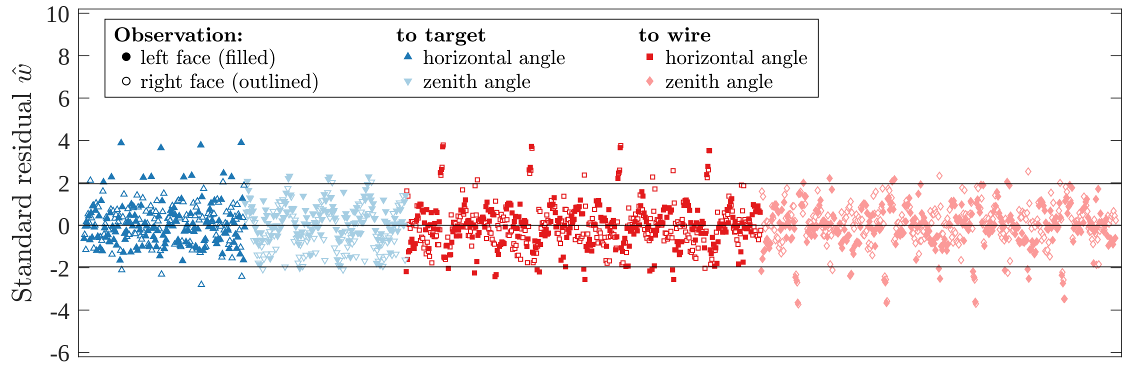

Figure 5.20: Estimated standard residuals $\hat{w}$ of the *161125 network*. The horizontal black lines represent the selected constant for the Biber function, which is equal to 1.96 and it corresponds to a probability of 95 %.

correlated due to the correlation of the respective standard residuals, as we will discuss in Section 5.4.3 and as shown in Figure 5.35.

The partial redundancy z of the observations (see Section 4.6.3) are depicted in Figure 5.22. Focusing on the observations to the targets, we notice that the partial redundancy of the vast majority of the zenith angles is more than 0.75, while for the horizontal angles there is a considerable amount of observations between 0.25 and 0.75. The horizontal angles to the targets are less redundant as a result of the fact that the targets mounted on the sides of the magnet were only observed by two instrument positions, creating a weak configuration.

For the wire observations, the horizontal angles are entirely below the value of 0.25, while for the zenith angles the partial redundancy is always above the 0.75 threshold. The values of the partial redundancy are related to the apparent orientation of the wire in the image plane, as we will demonstrate in Section 5.4.3 and as shown in Figure 5.37.

In Figure 5.23b, we focus on the wire, in the region of the observations. Here, we visualize the observation rays as they intersect the vertical plane and the lateral surface that are defined by the wire axis. The lateral surface is horizontal in the lateral direction

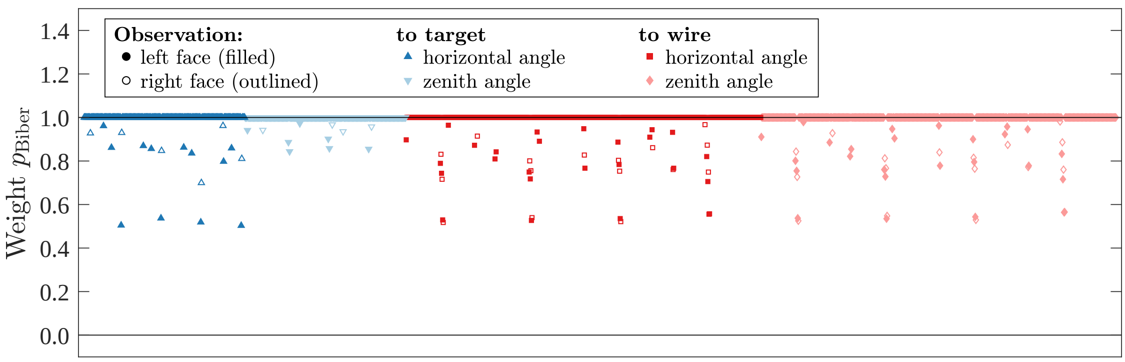

Figure 5.21: Weight factors p_{Biber} of the *161125 network*, according to the Biber weighting function.

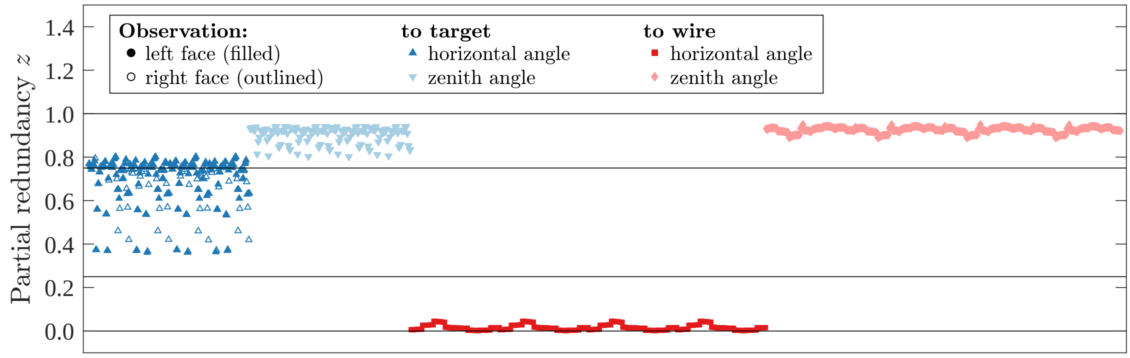

Figure 5.22: Partial redundancy z of the *161125 network*. The horizontal black lines represent the 0.25 and 0.75 thresholds used to consider the level of contribution or the level of redundancy of an observation.

and follows the wire curvature in the longitudinal direction. The observation rays are plotted in colors that are different for each theodolite position, according to Figure 5.23a.

The residuals of the wire observations can be expressed in units of lengths with respect to the estimated wire axis. To do so, we compute the vertical deviation dV and the lateral deviation dL, which are the distances between the observation ray and the wire axis with respect to the vertical plane and the lateral surface of the wire (see also Section 6.2.4 and Figure 6.6a). The vertical and lateral deviations are presented in Figure 5.24 with respect to the actual diameter of the wire, which is 0.1 mm.

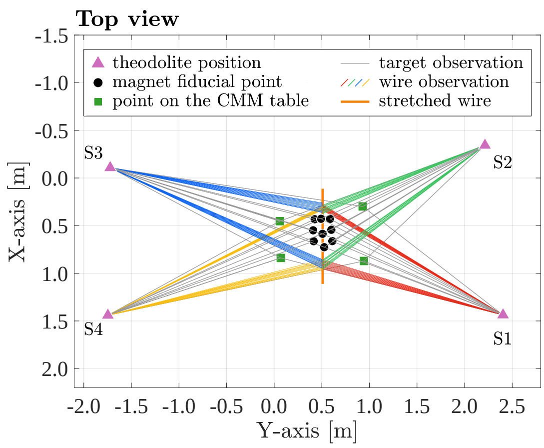

(a)

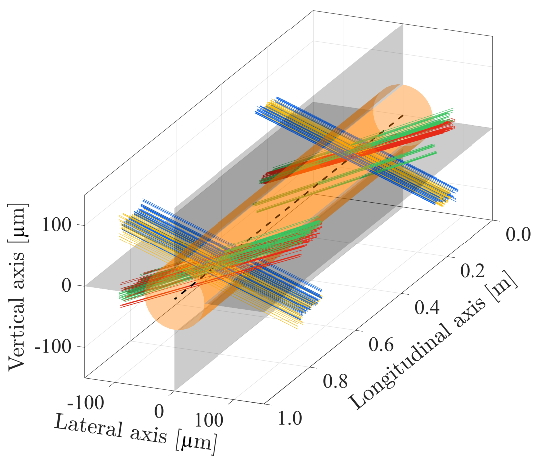

(b)

Figure 5.23: Configuration of the *161125 network*. (a) Top view of the network, in which the wire observations from each instrument position are depicted in different colors. (b) Detail of the network in the region of the wire, where the observation rays intersect the vertical plane of the wire and the surface that is perpendicular to the vertical plane and follows the wire curvature.

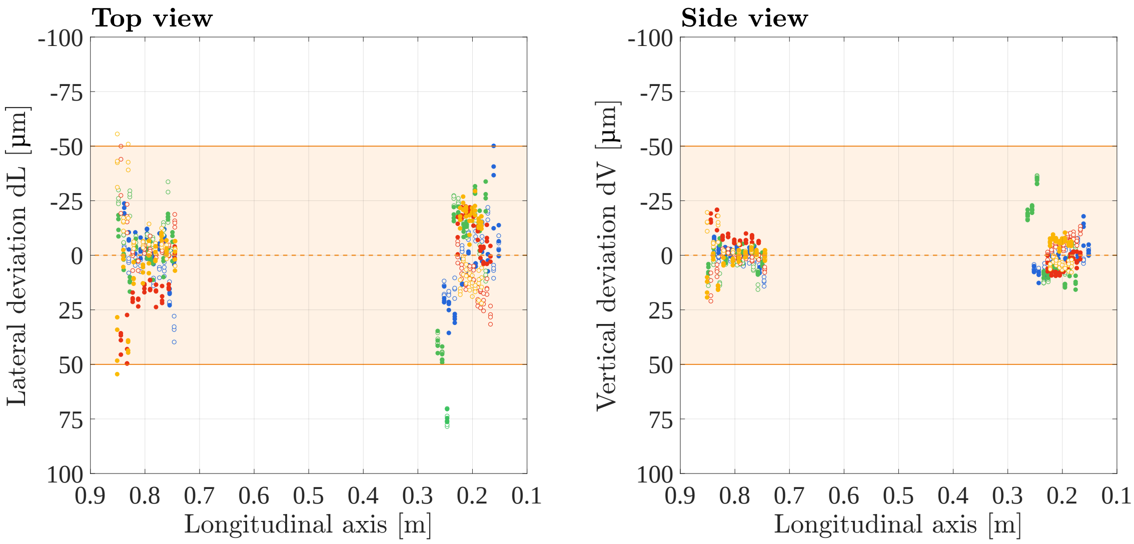

(a) **(b)**

Figure 5.24: (a) Lateral deviations dL and (b) vertical deviations dV of the observation rays with respect to the estimated wire axis.

The vertical deviations dV demonstrate less dispersion than the lateral deviations dL due to the unfavorable configuration of the network in the lateral direction, i.e., the obtuse intersection of the observations (approximately 130°), as depicted in Figure 5.13c.

Comparison of the fiducial point coordinates

In this section, we compare the coordinates of the fiducial points as they are estimated by the micro-triangulation network (*micro-triangulation coordinates*) and as they are measured by the coordinate measuring machine (*CMM coordinates*). Prior to the comparison, we present the statistics of the expanded uncertainties of the coordinates for the *161125 network* in Table 5.2. The expanded uncertainties are computed from the standard deviation values of the coordinates multiplied by 1.96, which is the coverage factor for a 95 % probability.

Table 5.2: Statistics of the expanded uncertainties U^{95} of the estimated *micro-triangulation coordinates* of the *161125 network*. The expanded uncertainties refer to a 95 % confidence level with a coverage factor equal to 1.96.

161125 network

	micro-triangulation coordinates expanded uncertainty		
	U_X^{95} [µm]	U_Y^{95} [µm]	U_Z^{95} [µm]
min	2.9	6.1	5.3
max	4.4	12.3	8.6
mean	3.7	8.0	7.1
median	3.8	7.3	7.2

Table 5.3: Statistics of the coordinate differences dX, dY, dZ and the magnitudes of the horizontal vector **dr** and the 3D vector **dR** between the *micro-triangulation coordinates* of the *161125 network* solution and the *CMM coordinates*, which are used as reference values.

161125 network

	micro-triangulation coordinates − CMM coordinates				
	dX [µm]	dY [µm]	dZ [µm]	||**dr**|| [µm]	||**dR**|| [µm]
min	−4.3	−5.2	−8.4	0.8	4.1
max	6.6	7.6	5.2	8.5	12.0
mean	0.4	0.7	−0.5	4.7	6.7
median	0.7	0.3	0.2	4.2	5.2
std	3.7	4.3	5.0	2.9	2.9
rms	3.5	4.1	4.8	5.4	7.2

According to Table 5.2, we report that the maximum value of the expanded uncertainty for the position of the fiducial points is 12.3 µm for a 95 % confidence interval. The mean value of the expanded uncertainties for the X-axis is 3.7 µm, while for the Y-axis and Z-axis the mean values are 8.0 µm and 7.1 µm, respectively.

The largest uncertainty appears in the Y-axis due to the unfavorable configuration of the network. The Y-axis almost coincides with the lateral direction to the wire, and therefore, the high uncertainty in this direction will propagate into the estimation of the offsets between the fiducials and the wire, which is the final product of the fiducialization procedure.

Prior to the comparison of the two sets of fiducial point coordinates, a 3D Helmert transformation between the micro-triangulation coordinate system and the CMM coordinate system is performed, taking into account the fiducial points and the points on the CMM table.

The statistics of the differences between the two sets of coordinates are presented in Table 5.3. The root-mean-square values for the coordinate differences do not exceed 5 µm, while for the magnitude of the 3D vector **dR** the root-mean-square value is approximately 7 µm and the maximum value is 12 µm.

In Figure 5.25, we plot the 2D confidence ellipses of the fiducial points for the *161125 network*. The ellipses are computed for each plane of the coordinate system and they refer to a 95 % confidence level with a coverage factor equal to 2.45. In each plane, we also plot the projection of the 3D vector **dR** between the *micro-triangulation coordinates* and the *CMM coordinates*. The mean length of the major and the minor semi-axes for the three planes are 10.0 µm and 5.7 µm, respectively, while the corresponding maximum values are 16.2 µm and 9.5 µm.

Comparison of the stretched-wire position

Combining all the available data, we are able to compute three different wire reconstructions using essentially independent sources. The first reconstruction is the *micro-triangulation wire*, which is computed by using the parameters estimated by the *161125 network* adjustment. The second reconstruction is the *direct–CMM wire*, which is com-

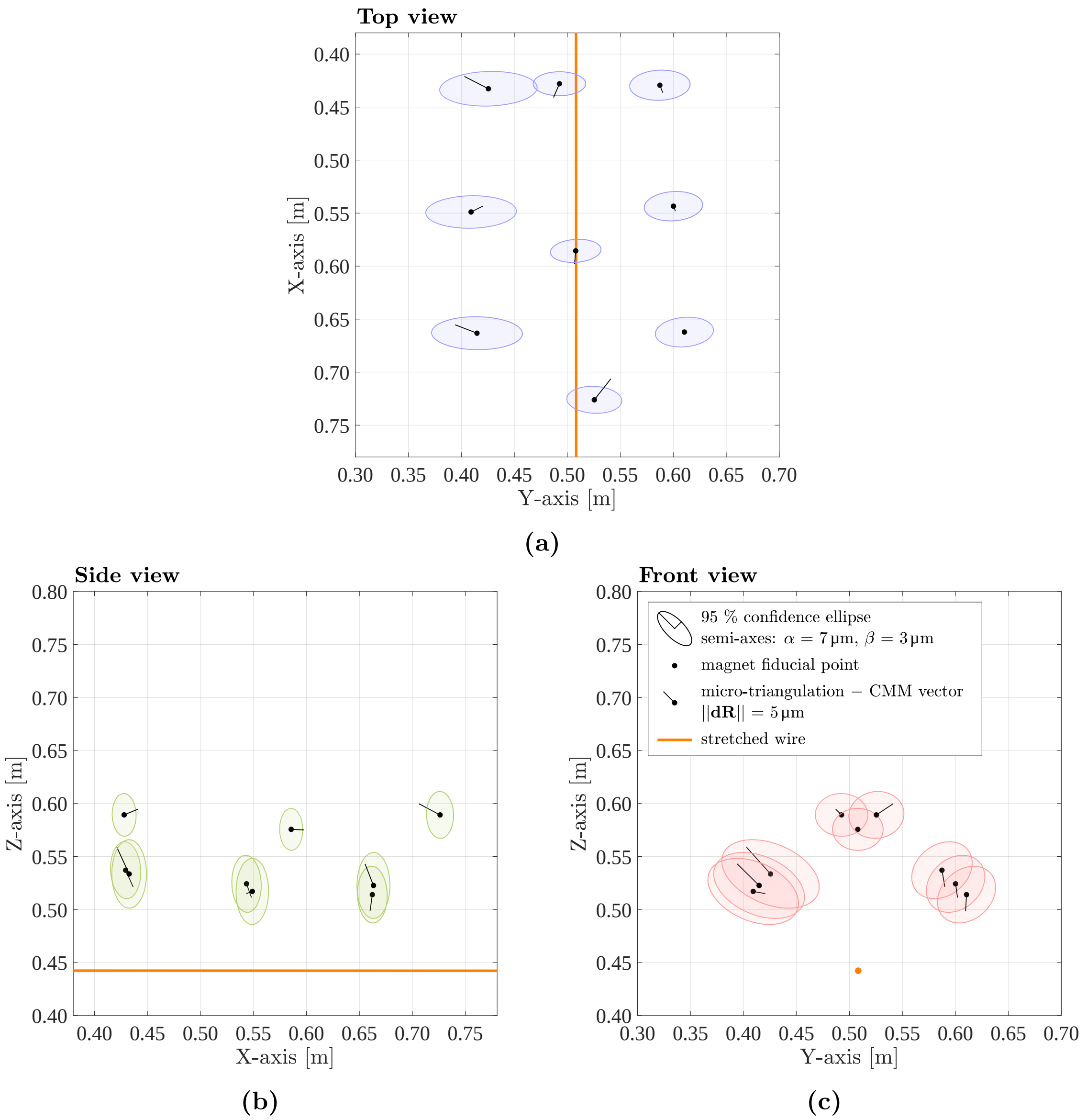

Figure 5.25: Confidence ellipses for a 95 % probability and the projections of the 3D vectors **dR** between the *micro-triangulation coordinates* and the *CMM coordinates* for the fiducial points of the *161125 network* case study.

puted by using the two points that were directly measured on the wire with the CMM optical sensor, and with the form factor as it is computed by the resonance frequency (Equation 5.10). The same form factor is used for the reconstruction of the *indirect–CMM wire*, however, for this reconstruction we use the computed points that are inferred by the wire stages (see Section 5.3.3). In Figure 5.26, we see the top view and in Figure 5.27 the side view of the three wire reconstructions.

The layout of the three wires with respect to the micro-triangulation coordinate system is depicted in Figure 5.26a. Due to the small differences in the position and direction

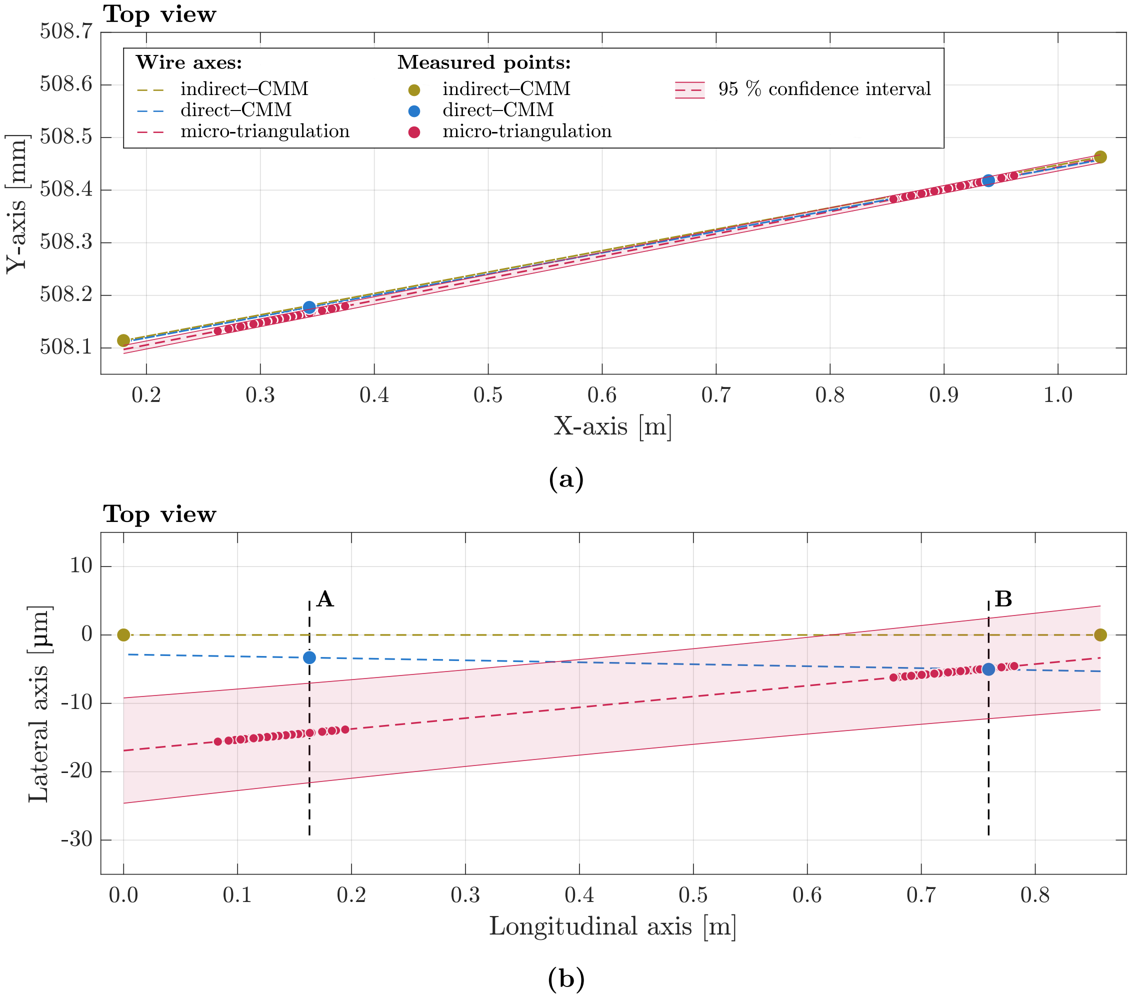

Figure 5.26: Superimposition of the horizontal position (top view) of the three reconstructed wires for the *161125 network* case study (a) with respect to the micro-triangulation coordinate system, and (b) with respect to the *indirect–CMM wire*.

between the three reconstructions we also plot the wires with respect to a reference wire. The reference wire is selected to be the *indirect–CMM wire*, which is depicted as a yellow dashed line in Figure 5.26b.

In Figures 5.26 and 5.27, we depict the wire axis for each reconstruction and the corresponding measured points that the reconstruction is based on. It is important to mention that for the micro-triangulation solution we plot the estimated points that correspond to the observations, aiming to visualize the distribution of the micro-triangulation observations on the wire. Moreover, for the *micro-triangulation wire* we plot the 95 % confidence interval in the lateral and the vertical directions. Since we do not have information on the actual precision of the CMM measurements, we cannot draw the equivalent area for the other two wire reconstructions. However, it is considered to be about an order of magnitude better than the uncertainty of the micro-triangulation measurement.

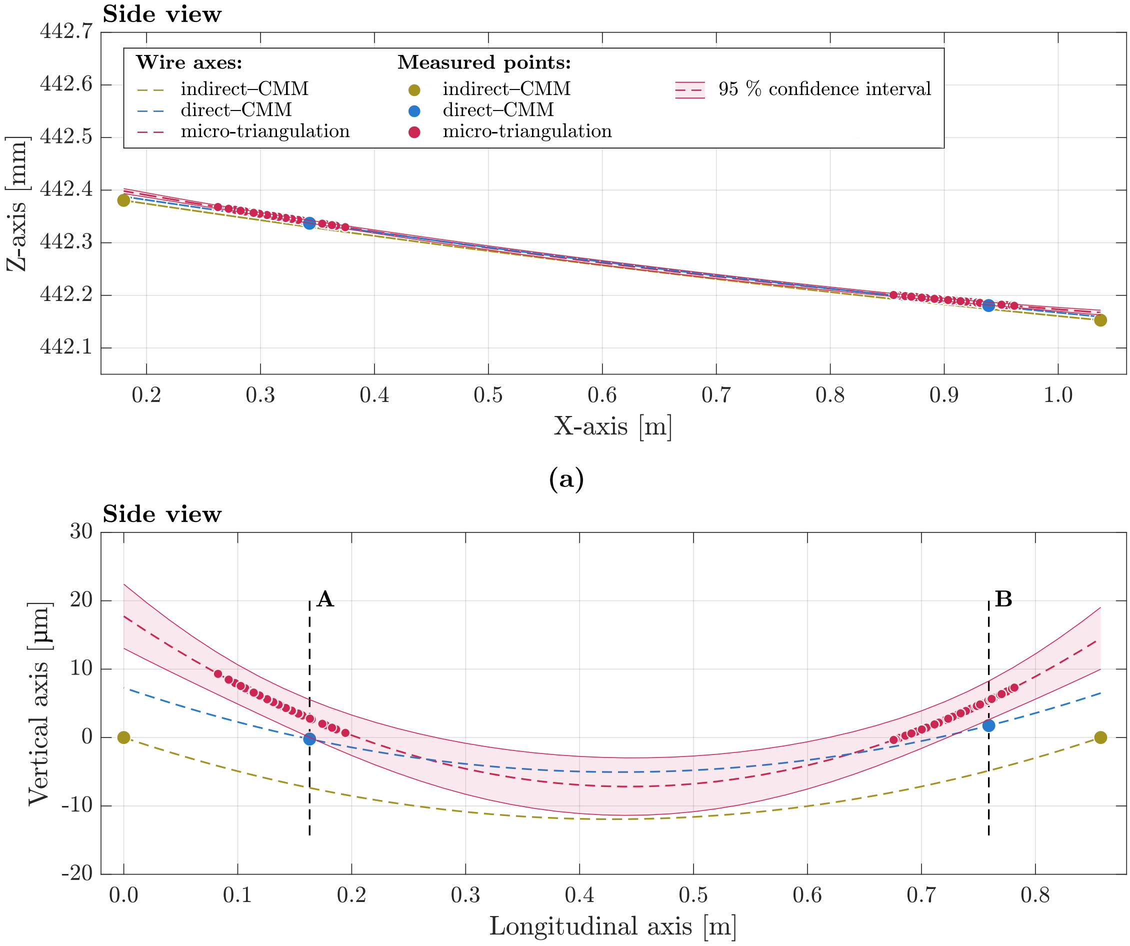

(a)

(b)

Figure 5.27: Superimposition of the vertical position (side view) of the three reconstructed wires for the *161125 network* case study (a) with respect to the micro-triangulation coordinate system, and (b) with respect to the *indirect–CMM wire*.

In the lateral direction, the differences at the extremities of the wire between the *indirect–CMM wire* and the *direct–CMM wire* are 2.9 µm and 5.3 µm. For the *micro-triangulation wire* we observe a very good agreement on one extremity — differences of 3.3 µm and 2.0 µm with respect to the *indirect–CMM wire* and to the *direct–CMM wire*, respectively — but a larger deviation on the other extremity, with differences of 16.9 µm and 14.1 µm, respectively.

For the entire length of the wire, the mean value of the lateral confidence intervals is ±7.2 µm for a 95 % probability.

The side view of the three wires is given in Figure 5.27. Due to the inclination of the wires with respect to the micro-triangulation coordinate system, their small curvature and their different positions, the reconstructed wires are not clearly visible in Figure 5.27a.

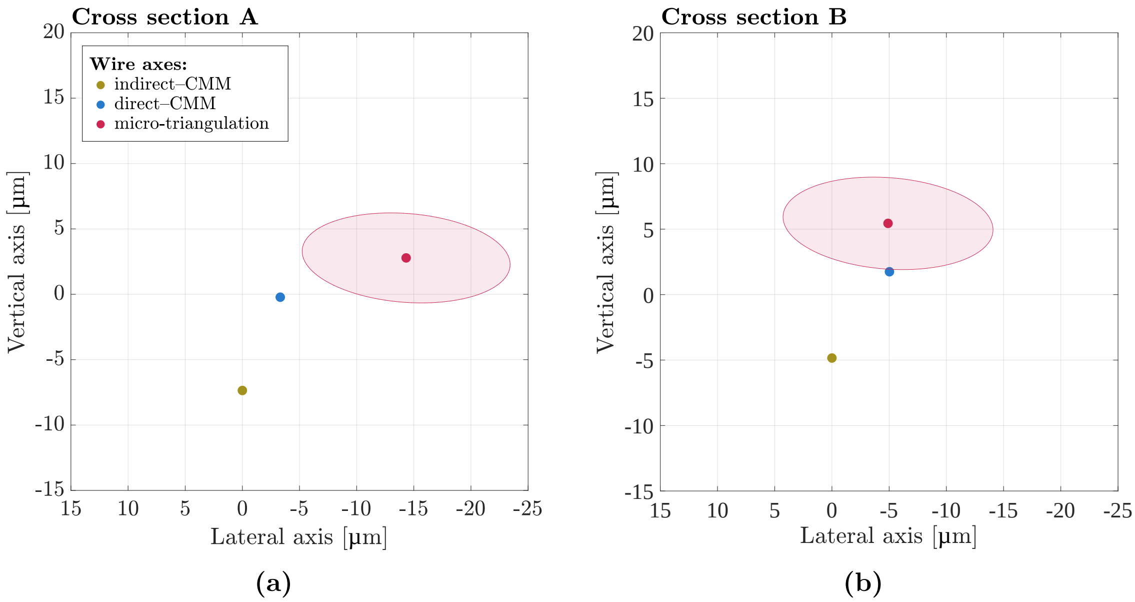

Figure 5.28: Cross sections (see Figure 5.27b) of the three reconstructed wires for the *161125 network* case study. The cross sections are located at the points of the *direct–CMM wire* measurements. The confidence ellipses of the *micro-triangulation wire* correspond to a 95 % confidence level with a coverage factor equal to 2.45.

Thus, we draw the wires with respect to the *indirect–CMM wire* and we rotate its axis in order to draw the suspension points at the same height.

In Figure 5.27b, we observe that there is a vertical offset in the range of 6.5 µm to 7.3 µm between the *direct–CMM wire* and the *indirect–CMM wire*. This is most probably caused by a systematic error in the calibration of the wire stages rather than by the calibration of the optical sensor of the CMM, given the fact that the measurements were performed within a few minutes, and therefore, they refer to the same measurand. This systematic offset is also verified by the results of the *170407 network* case study, as presented in Figure 5.39b.

Regarding the wire shape, we notice that the curvature of the *micro-triangulation wire* is larger than the common curvature of the other two reconstructions. In numbers, the form factor of the *direct–CMM wire* and the *indirect–CMM wire* is equal to 7699.5 m, as computed for 160.29 Hz resonance frequency, according to Equation 5.10, while the form factor for the *micro-triangulation wire* is estimated to be 3947.6 m with a ±1179.5 m confidence interval for a 95 % probability.

The large disagreement between the estimated form factor from the *161125 network* adjustment and from the resonance frequency is most probably due to the fact that the micro-triangulation observations to the wire are concentrated in two small regions along the wire. The agreement in the form factor gets improved when the angular observations cover the whole span of the wire, as it is shown for the *170407 network* case study (Section 5.4.3).

The difference in the form factor causes a deviation in the height of the *micro-triangulation wire* extremities of 8.0 µm and 10.5 µm with respect to the *direct–CMM wire*, and of 14.5 µm and 17.7 µm with respect to the *indirect–CMM wire*. In the middle of the span the height differences are much smaller at about 2.1 µm and 4.8 µm with the *direct–CMM wire* and the *indirect–CMM wire*, respectively.

The vertical confidence intervals of the *micro-triangulation wire* reconstruction are estimated to be at ±3.5 µm in the two regions of measurements (minimum value) and at ±4.7 µm in the middle of the wire span (maximum value) for a 95 % probability.

In Figure 5.28, we focus on two specific vertical planes that are perpendicular to the horizontal direction of the *indirect–CMM wire* (Figure 5.26b). The cross sections depict the relative position of the three wire reconstructions and the 95 % confidence ellipses for the *micro-triangulation wire*. The location of these two planes are defined by the measured points of the *direct–CMM wire*. These locations are suitable for comparison between the reconstructions because they also belong to the region of the micro-triangulation measurements. The planes of the cross sections are denoted in Figures 5.26b and 5.27b with black dashed lines and the letters A and B .

Comparison of the fiducial point offsets

In this section, we compare the offsets between the fiducial points and the stretched wire as they are estimate for each of the three methods. During the *161125 network* measurement, the quadrupole magnet was equipped with nine fiducial points, thus, we can compute nine vertical offsets ν, nine horizontal offsets ℓ and nine 3D offsets ρ. In Table 5.4, we list the statistics of each type of offsets. The maximum offset value does not exceed 15 cm, as a result of the width and height of the magnet used for the test bench. The statistics of the 95 % expanded uncertainty are also presented in Table 5.4. The mean value of the expanded uncertainty for the three types of the offsets is approximately 10 µm, while the maximum value is approximately 15 µm, which appears in the horizontal offsets ℓ. The uncertainty of the vertical offsets ν are indeed smaller than that of the horizontal offsets, as expected due to the configuration of the network.

In order to evaluate the quality of the estimated offsets of the *161125 network*, we compare them with the offsets calculated by the fiducial coordinates obtained by the

Table 5.4: Statistics of the vertical offsets ν, the horizontal offsets ℓ and the offsets ρ in 3D between the fiducial points and the wire as computed from the *161125 network* adjustment. The expanded uncertainties U^{95} refer to a 95 % confidence level with a coverage factor equal to 1.96.

161125 network

	micro-triangulation offsets			expanded uncertainty		
	ν [mm]	ℓ [mm]	ρ [mm]	U^{95}_{ν} [µm]	U^{95}_{ℓ} [µm]	U^{95}_{ρ} [µm]
min	71.8	0.4	123.1	5.6	8.7	5.6
max	147.0	102.2	148.0	9.3	15.2	14.8
mean	102.5	64.6	130.2	7.9	11.3	10.7
median	91.2	82.7	124.2	8.3	10.2	11.3

Table 5.5: Statistics of the vertical offset differences dν, the horizontal offset differences dℓ and the 3D offset differences dρ between the wire reconstructions. The first comparison is between the *micro-triangulation offsets* and the *direct–CMM offsets* (in blue color), and the second comparison is between the *micro-triangulation offsets* and the *indirect–CMM offsets* (in yellow color).

161125 network

	micro-triangulation − direct–CMM			*micro-triangulation − indirect–CMM*		
	dν [µm]	dℓ [µm]	dρ [µm]	dν [µm]	dℓ [µm]	dρ [µm]
min	−8.7	−16.9	−17.8	−15.8	−20.5	−25.4
max	7.3	8.5	9.2	0.4	12.1	8.1
mean	0.6	−3.5	−0.9	−6.4	−3.8	−6.3
median	2.2	−3.4	−1.2	−4.7	−7.3	−8.3
std	5.3	9.0	9.5	5.3	12.7	11.8
rms	5.0	9.2	9.0	8.1	12.6	12.8

CMM measurements, and by the *indirect–CMM wire* and *direct–CMM wire* parameters, respectively. In Table 5.5, we list the statistics of the differences for each type of offsets.

The first remark on the offset comparison is that the differences between the *micro-triangulation offsets* and the *direct–CMM offsets* are smaller than the differences between the *micro-triangulation offsets* and the *indirect–CMM offsets*. This result is expected due to the better agreement between the *micro-triangulation wire* and the *direct–CMM wire*, which is presented in the previous section.

Moreover, in Table 5.5, we observe that the differences in the vertical offsets dν are smaller than the differences in the horizontal offsets dℓ for both comparisons. One more time, this result is due to the configuration of the micro-triangulation network, which provides a better estimation in the vertical direction.

In general, the accuracy of the offsets obtained with the *micro-triangulation method with direct wire observations* is on average 10 µm rms, compared with the two different methods that we applied in order to compute the stretched-wire offsets from the CMM measurements. This result is obtained with an unfavorable configuration for the micro-triangulation network and under unfavorable ambient conditions, i.e., the vertical periodic movement of the theodolites and the poor light conditions. Therefore, we could characterize this result as conservative and for sure promising that the micro-triangulation method is capable of achieving even better results, suitable for demanding in precision fiducialization applications.

5.4.3 Analysis of the *170407 network* case study

Least-squares adjustment of the observations

The major difference between the present and the previous configuration is that the magnet has been removed, and therefore, the entire suspending part of the stretched wire was visible to the theodolites and accessible by the CMM probe. Although the configuration is unrealistic for magnet fiducialization applications due to the absence of the magnet, it is advantageous to further study some aspects of the new methodologies, i.e., the direct wire

Table 5.6: The *a priori* and *a posteriori* reference standard deviations (σ_0, $\hat{\sigma}_0$), the standard deviations $\sigma_{i,G}$ for each observation i of each group G of observations, and the *a posteriori* standard deviation components $\hat{\sigma}_G$ for the *170407 network*. The observations are grouped into horizontal and zenith angles to the targets (H_t, Z_t) and to the wire (H_w, Z_w).

170407 network

			target observations		wire observations	
Reference	[mgon]	Components	H_t [mgon]	Z_t [mgon]	H_w [mgon]	Z_w [mgon]
σ_0	1.00	$\sigma_{0,G}$	0.17	0.31	0.89	0.66
$\hat{\sigma}_0$	1.00	$\hat{\sigma}_{0,G}$	0.98	1.00	1.13	1.00

observations with the QDaedalus measuring system and with the coordinate measuring machine.

The same four groups of observations are considered for the stochastic model as with the previous network. The *a priori* reference standard deviation σ_0 and the *a priori* standard deviation $\sigma_{i,G}$ for each observation i of each group G of observations was initially set to 0.15 mgon. After a few repetitions, the values converge at those given in Table 5.6. We notice that the standard deviation for the observations to the targets are close to the specifications of the theodolite, while for the observations to the wire the large values indicate the existence of systematic errors (see also Appendix E).

In Figure 5.29, we observe a systematic pattern of the residuals concerning the observations to the wire. The pattern has an excellent repeatability between the three series of observations that were taken into account for the *170407 network* adjustment, as it is better visualized for the zenith angles in Figure 5.30b.

In Figure 5.31, we focus on the residuals of the zenith angles to the wire for the first series of measurements acquired from the theodolite position S02. In addition, the median values of the background pixel intensities in the proximity of the wire are shown

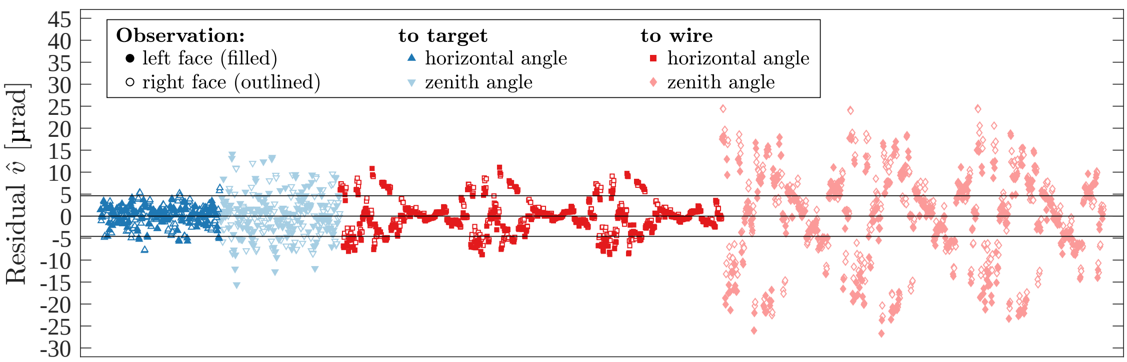

Figure 5.29: Estimated residuals $\hat{v}$ of the *170407 network*. The horizontal black lines represent the 95 % confidence interval of the angular precision of the theodolite, according to the manufacturer.

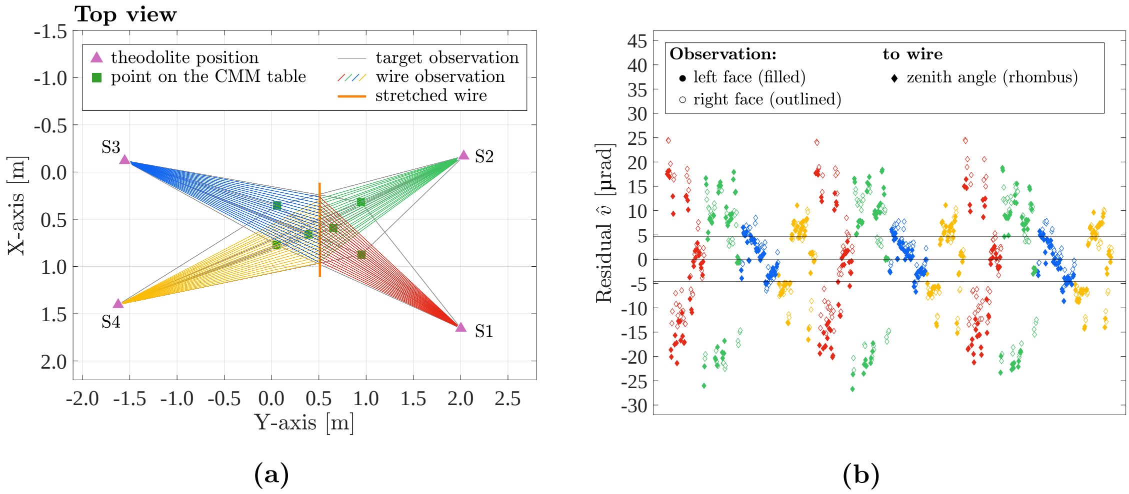

Figure 5.30: (a) Top view of the *170407 network*, in which the wire observations from each instrument position are in different colors. (b) The systematic behavior of the residuals appears to follow a pattern that is related to the background intensities of the images (see Appendix E).

in Figure 5.32. These values are calculated from the respective sample images given in Figure E.4.

The comparison of the patterns depicted in Figures 5.31 and 5.32 reveals that the vast majority of the abrupt changes in the residuals are in agreement with the corresponding changes in the background intensities. This is also valid for the observations to the wire from all the theodolite positions, as it is demonstrated in Appendix E.

The available data indicate a correspondence between the magnitude of the residual of a zenith angle to the wire and its background intensity value. In most of the cases, the wire detection algorithm introduced a bias to the zenith angle observation, which is relevant either to the light conditions or to the background intensity. This outcome is expected for optical measurements, especially for measurements based on passive optical systems. It is also in an immediate compliance with the results of the experimental evaluation of the wire detection algorithm, as presented in Chapter 3, in which we demonstrated the influence that the light conditions and the background intensities have on the quality of the angle observations.

Similar patterns are also noticeable for the *161125 network*, however, for the *170407 network* the interpretation is more evident due to the larger spread of the observations along the wire, which results in large and abrupt variations in the light conditions and in the background intensities. In any case, better light conditions are expected to improve the performance of the image detection algorithms.

Despite the large residuals due to the systematic errors of the wire observations, the reweighted observations (Figure 5.33) are approximately 4 % due to the fact that the standard residuals $\hat{w}$ (Figure 5.34) — that are used as a criterion for the computation of the weights (Equation 4.89) — are divided by the *a priori* standard deviation $\sigma_{i,G}$ for each group of observations.

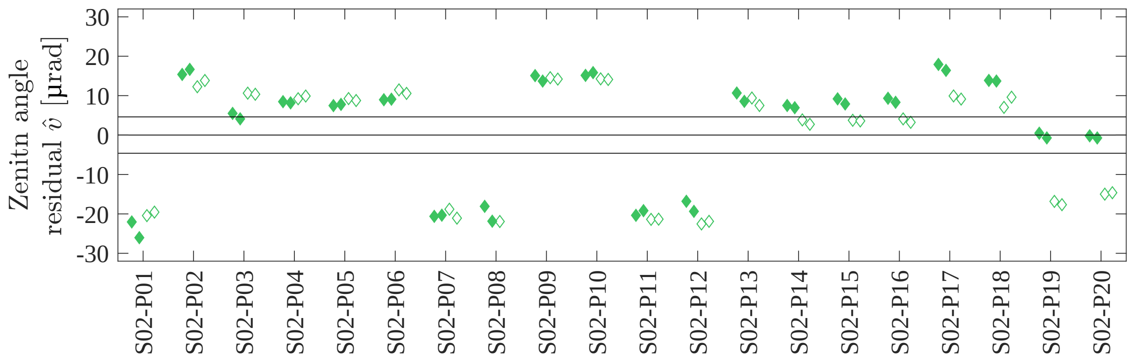

Figure 5.31: Residuals of the zenith angle observations for sequential point targets on the wire observed from the theodolite position S02.

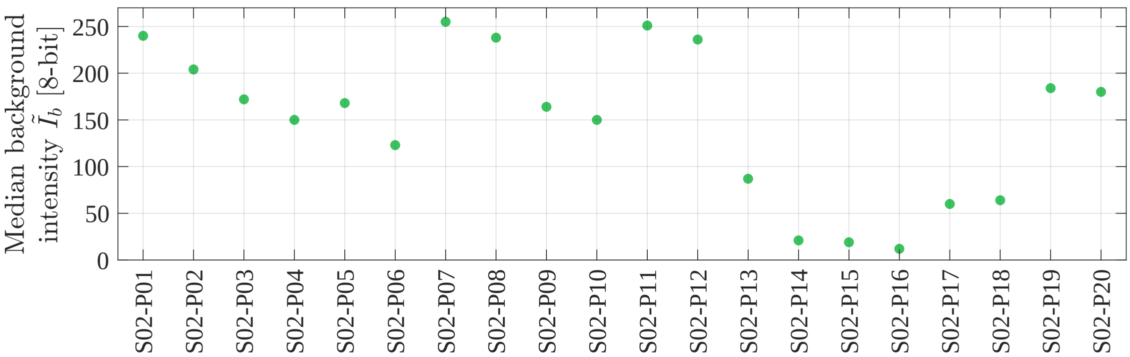

Figure 5.32: Median of the background pixel intensities in the proximity of the wire. The values correspond to the sample images in Figure E.4, acquired from the theodolite position S02.

As it is observed in Figures 5.29 and 5.34, the residuals $\hat{v}$ between the horizontal and the zenith angle observations to the wire are correlated, and as a consequence, the standard residuals $\hat{w}$ are correlated, too. Figure 5.35 reveals a linear correlation only for the wire observations. The color code is in accordance to the network configuration depicted in Figure 5.30a.

More specifically, in Figure 5.35a, the direction of the slope for each theodolite position is related to the apparent orientation of the wire in the acquired image. Therefore, small deviations of the lines of correlation are related to the orientation variations of the wire in the images due to the variations of the angles of incidence between the wire axis and the optical axis of the theodolite (see Figures E.1, E.4, E.7 and E.10).

The observed correlation is expected due to the fact that the observation rays that are intersecting the vertical longitudinal plane of the wire in a position that is, for example, below the wire axis will always intersect the plane either on the left side or on the right side of the wire axis, depending on the inclination of the wire in the image. In this case, we always obtain negative residuals for the zenith angles to the wire, according to Equation 4.9, and always positive —or, respectively, always negative— residuals for the horizontal angles to the wire.

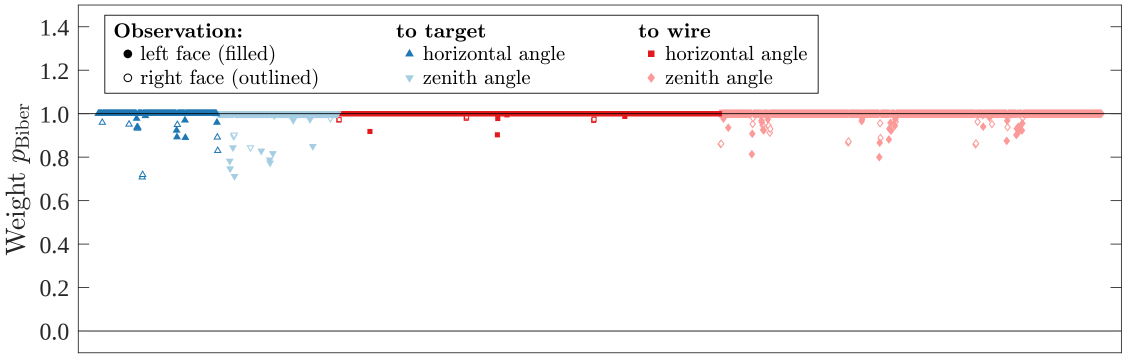

Figure 5.33: Weight factors p_{Biber} of the *170407 network*, according to the Biber weighting function.

The small discrepancies around the lines of correlation that we observe in Figure 5.35a do not appear in the case of the standard residuals $\hat{w}$ (Figure 5.35b). This is due to the fact that the influence of the geometry on the standard residuals is eliminated with the division by the factor $q_{v_i v_i}$, which represents the geometry of the network. The diversion of the lines of correlation from the diagonals actually represents the ratio between the standard deviation components $\sigma_{i,G}$ of the two group of observations.

The spread of the wire observations along the wire makes the *170407 network* suitable for the investigation of the patterns that the values of the partial redundancy z of the observations exhibit. In Figure 5.36, we notice that the partial redundancy of the zenith angles to the wire are much higher than those of the horizontal angles. This pattern is expected to be related to the wire orientation on the image plane.

From a theoretical point of view, for a wire that appears horizontal on the image plane the zenith angle contributes more than the horizontal angle to the estimation of the position and orientation of the wire. In this case, it is expected for the partial redundancy of the zenith angle to be greater than that of the horizontal angle. The opposite is true in the case that the observed wire appears vertical in the image plane.

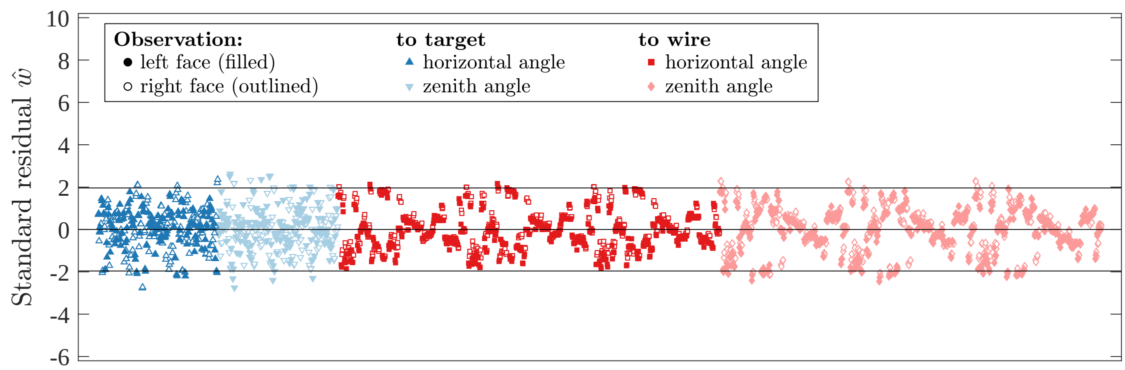

Figure 5.34: Estimated standard residuals $\hat{w}$ of the *170407 network*. The horizontal black lines represent the selected constant for the Biber function, which is equal to 1.96 and it corresponds to a probability of 95 %.

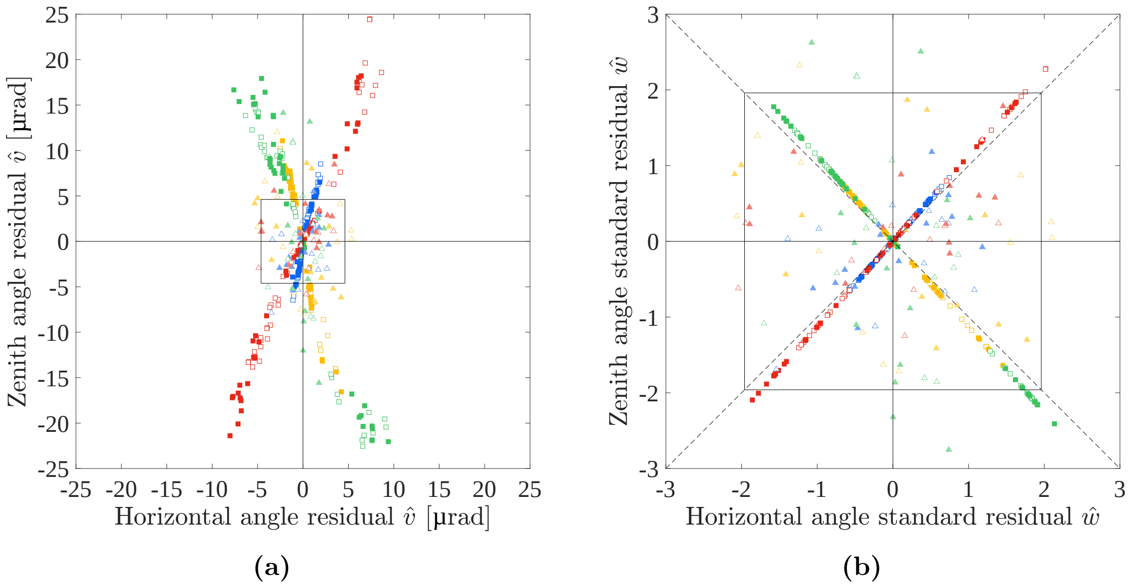

Figure 5.35: (a) Correlation between the estimated residuals $\hat{v}$ of the horizontal angles and the zenith angles. (b) Correlation between the estimated standard residuals $\hat{w}$ of the horizontal angles and the zenith angles.

As a consequence, trying to discover the exact relation between the orientation of the wire image (angle ω in Figure 5.37b) and the partial redundancy z of the observations, we concluded that there is a correlation between z and $\sin^2(\omega)$, as it is demonstrated in Figure 5.37a. From a theoretical point of view, the sine function indicates that the partial redundancy is related to the angle of incidence between the wire axis and the observation ray, otherwise, related to the projection of the observation ray to the wire axis. Moreover, the partial redundancy is a ratio of variances (Equation 4.80), which explains the relation to a quadratic function.

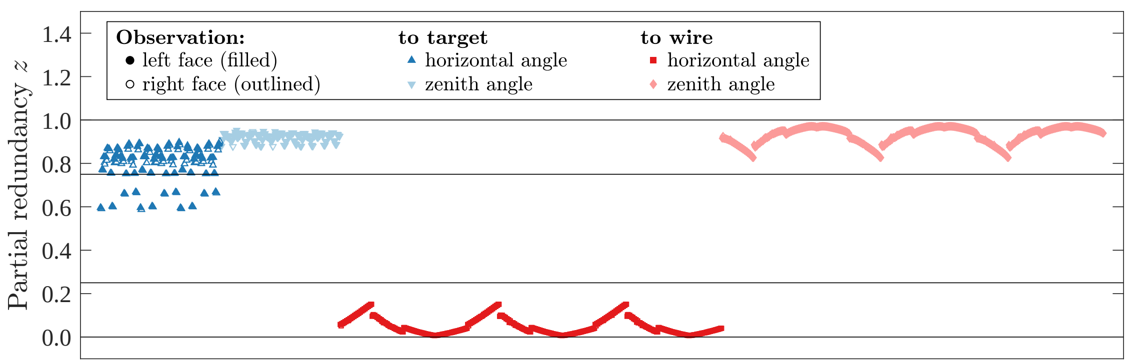

Figure 5.36: Partial redundancy z of the *170407 network*. The horizontal black lines represent the 0.25 and 0.75 thresholds used to consider the level of contribution or the level of redundancy of an observation.

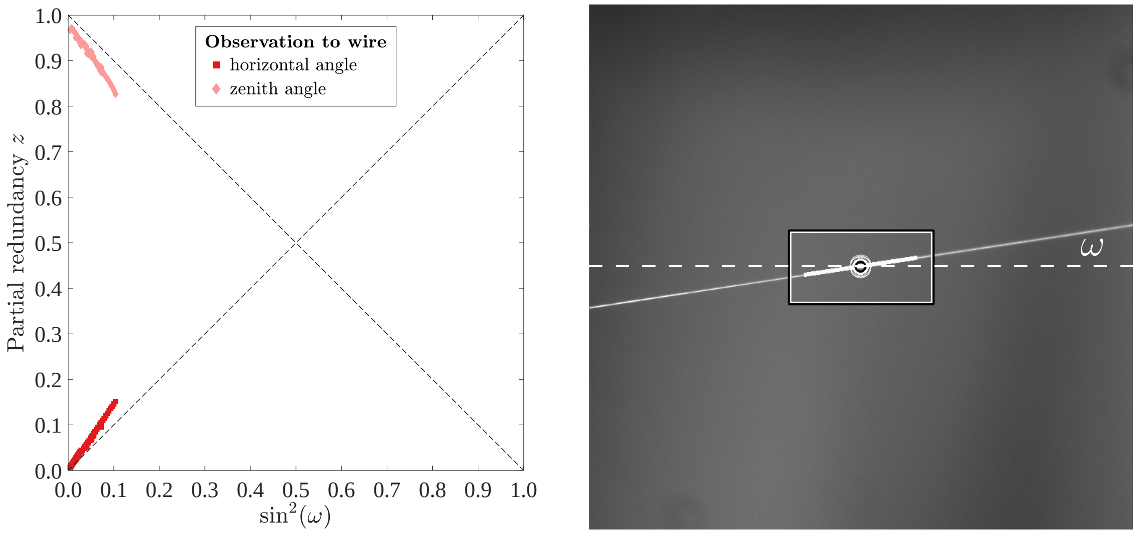

(a) (b)

Figure 5.37: (a) Correlation between the partial redundancy z of the wire observations and the angle ω. (b) The projection of the wire onto the image plane forms the angle ω with respect to the horizontal direction of the coordinate system of the image.

Following the correlation lines, we verify that as the angle ω increases, the partial redundancy of the horizontal angle also increases, while the partial redundancy of the zenith angle decreases. This correlation is confirmed by the observations of the micro-triangulation network in the LHC tunnel that is examined in Chapter 6 (see Figure 6.13b). The diversion of the lines of correlation from the diagonals represents the ratio between the standard deviation components $\sigma_{i,G}$ for the two group of observations, which is also the case for the lines of correlation of the standard residuals $\hat{w}$, in Figure 5.35b.

Comparison of the stretched-wire position

For the measurement campaign presented in this section we compute and compare three reconstructions of the stretched wire, as we also did for the measurement campaign presented in Section 5.4.2. The major difference in this case is that the direct wire observations with the QDaedalus measuring system and with the coordinate measuring machine were evenly distributed along the entire length of the suspending wire.

Due to the absence of the magnet the micro-triangulation observations of the *170407 network* were well distributed along the wire, in contrast to the observations of the *161125 network* that were concentrated into two regions on either side of the magnet. Moreover, 29 well distributed points were measured with the CMM optical sensors (blue points in Figures 5.38 and 5.39), instead of the two points measured in the previous measurement campaign. In this case study, the *direct–CMM wire* parameters are estimated by fitting the catenary model to the 29 measured points, and as a consequence, each of the three form factors is obtained by an independent source.

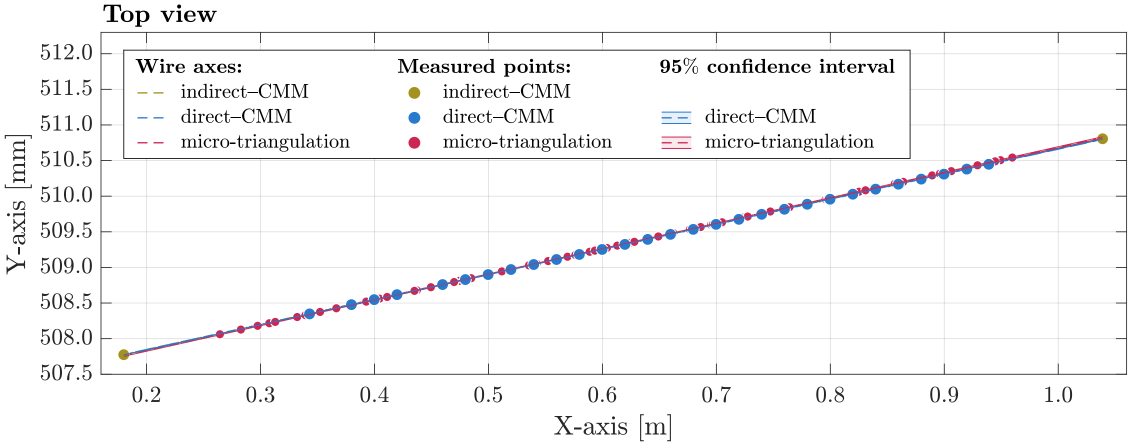

(a)

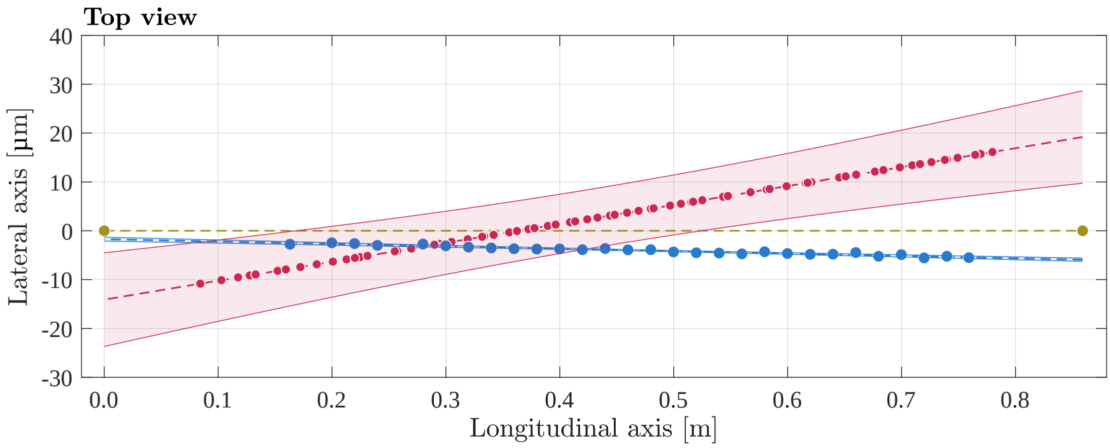

(b)

Figure 5.38: Superimposition of the horizontal position (top view) of the three reconstructed wires for the *170407 network* case study (a) with respect to the micro-triangulation coordinate system and (b) with respect to the *indirect–CMM wire*.

The 3D Helmert transformation between the micro-triangulation coordinate system and the CMM coordinate system, which takes place before the comparison, is now based on the six common targets located on the CMM table. The distance between the targets and the wire, which is at least 0.5 m (Figure 5.14), creates a lever arm that amplifies the effect that the uncertainty of the transformation parameters has on the transformation of the *direct–CMM wire* and the *indirect–CMM wire* position to the micro-triangulation coordinate system.

The layout of the three wires with respect to the micro-triangulation coordinate system is depicted in Figure 5.38a, while in Figure 5.38b the wires are plotted with respect to the *indirect–CMM wire*, which is selected to be the reference wire (yellow dashed line).

In Figure 5.38b, we observe a larger deviation of the horizontal orientation of the *micro-triangulation wire* with respect to the other two wires, in comparison to the previous case

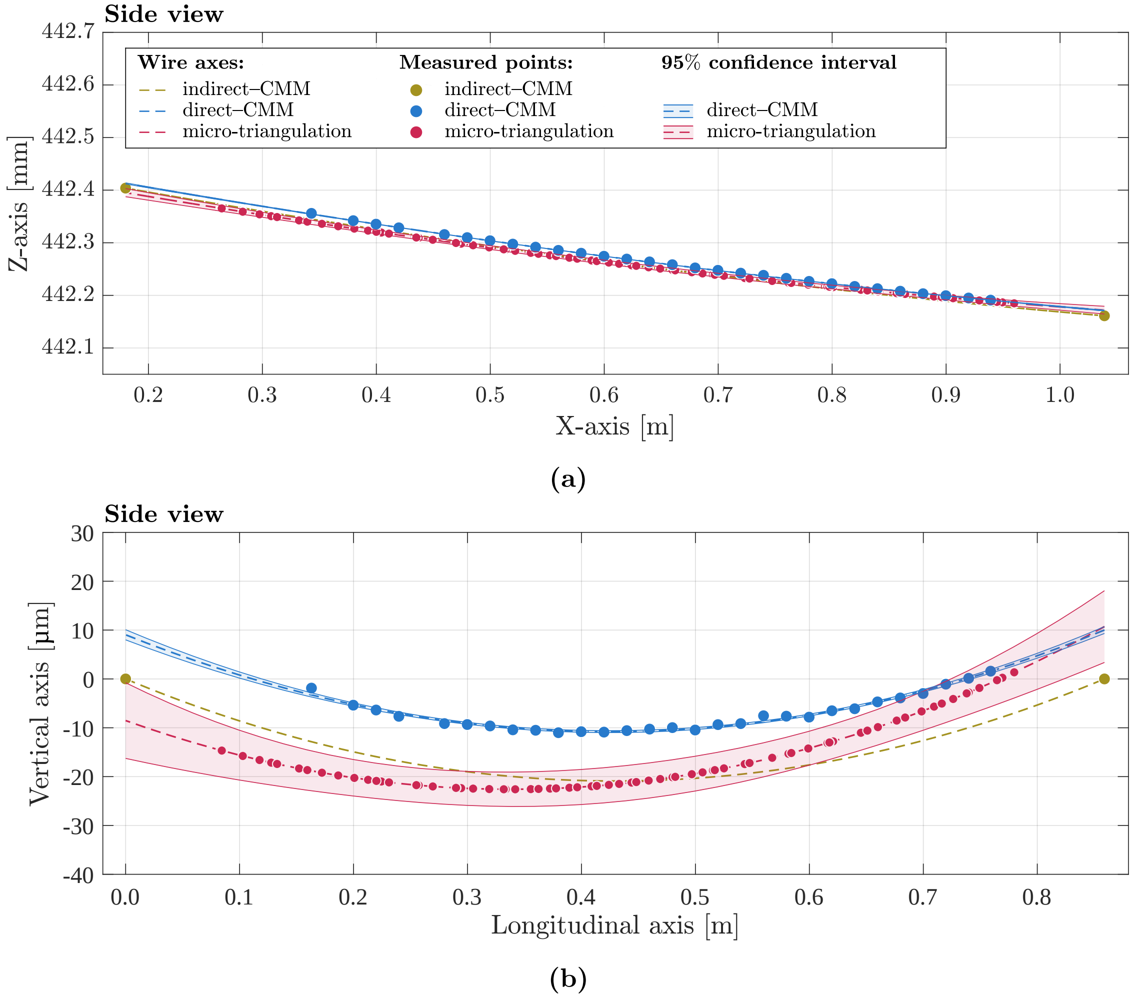

Figure 5.39: Superimposition of the vertical position (side view) of the three reconstructed wires for the *170407 network* case study (a) with respect to the micro-triangulation coordinate system and (b) with respect to the *indirect–CMM wire*.

study. This deterioration is most probably caused by the lever arm that is created due to the distance between the wire and the targets, when the transformation between the CMM coordinate system and the micro-triangulation coordinate system is applied.

The side view of the three wires is given in Figure 5.39a with respect to the micro-triangulation coordinate system. In Figure 5.39b the wires are depicted with respect to the *indirect–CMM wire* (yellow dashed line). The tilt between the *micro-triangulation wire* and the other two wires also indicates the aforementioned lever arm that is acting on the wire position and orientation due to the uncertainty of the transformation parameters.

Small deterioration is also observed in the uncertainty of the *micro-triangulation wire* reconstruction. For the *micro-triangulation wire* of the *170407 network* the maximum 95 % confidence intervals are ±9.6 µm and ±7.7 µm in the lateral and vertical direction, respectively. The corresponding values for the *161125 network* are ±7.7 µm and ±4.7 µm.

The precision of the reconstruction is most probably reduced due to the existence of significant systematic errors in the angle observations to the wire, caused by the variation of the light conditions and of the image background intensity (see also Appendix E).

Here, it is important to mention that for this measurement we also observe a systematic difference between the *indirect–CMM wire* and the *direct–CMM wire* that is in the range of 1.9 µm to 5.9 µm in the lateral direction, and in the range of 9.0 µm to 10.0 µm in the vertical direction. This systematic deviation between the two measurements of the CMM confirms the result of the previously described case study, demonstrating similar values (see Figures 5.26b and 5.27b).

Moreover, for the *direct–CMM wire*, we compute the confidence intervals of the reconstructed axis — as estimated from the fit of the 29 points that were measured by the CMM optical probes — for a 95 % probability. The mean values of the confidence intervals are ±0.2 µm and ±0.4 µm in the lateral and vertical direction, respectively, while the maximum values are ±0.4 µm and ±1.0 µm.

The last interesting magnitude to compare is the catenary form factor, which expresses the shape of the wire. For each reconstruction a form factor was computed by independent measurements.

More specifically, for the *micro-triangulation wire* the value of the form factor is 4068.4 m with ±1370.7 m confidence interval for a 95 % probability, as estimated from the adjustment of the *170407 network*. For the *direct–CMM wire* the value is 4539.3 m with ±206.5 m confidence interval for a 95 % probability, as estimated from the fit of the 29 points that were measured by the CMM optical probes. Lastly, for the *indirect–CMM wire* the value of the form factor is 4412.5 m, as computed from the resonance frequency (Equation 5.10), which was 121.11 Hz.

These results indicate that for the *170407 network* case study the value of the form factor estimated with the micro-triangulation method is closer to the other two estimations, in comparison to the *161125 network* case study. The good agreement is most probably the result of the larger distribution of the micro-triangulation observations along the wire.

5.5 Discussion and conclusions

In this chapter, we successfully demonstrated the feasibility of the *micro-triangulation method with direct wire observations* in a metrology room for magnet fiducialization applications. A permanent installation around a calibration bench is the ideal application for a measuring system with multiple theodolites in order to cope with the complexity of the installation and the laborious parameter configuration of the targets, especially for the QDaedalus system as its is currently implemented. Moreover, in the case of a permanent configuration, better solutions could be considered for the supporting devices of the theodolites, e.g., concrete pillars instead of aluminium tripods.

The metrology room operates at 20 °C with a temperature variation of approximately 0.3 °C amplitude and 40 min period. This temperature variation results in a periodic motion with a maximum amplitude of 18 µm in the vertical direction and 10 µm in the horizontal direction when the theodolites are installed on aluminium tripods at 2.3 m height.

The insulation of the aluminium tripod with a 20 mm rubber sheet resulted in a reduced amplitude of approximately 11 µm in the vertical direction for the same range of temperature variation and for the same instrument height. We also found that the temperature variation caused a similar range of displacement to a 2.3 m height insulated aluminium tripod as to a 1.3 m height aluminium tripod without insulation. Moreover, the 1.3 m height carbon-fiber tripod reduces the effect to 7 µm amplitude when the temperature amplitude is 0.3 °C.

The precision evaluation of the micro-triangulation network shows a mean expanded uncertainty of approximately 7.5 µm for a 95 % confidence level, for the coordinates of the fiducial points. This value corresponds to the lateral (Y-axis) and vertical (Z-axis) directions with respect to the wire axis that are important for the fiducialization of a particle accelerator component. The accuracy of the micro-triangulation coordinates is at 5 µm rms, with respect to the coordinate measuring machine measurements, while in three dimensions the maximum difference is 12 µm.

The precision of the wire reconstruction with the micro-triangulation method — i.e., the precision with which we can estimate the position of an arbitrary point on the wire — is estimated by the covariance matrix of the relevant unknown parameters of the adjustment. A typical value of the expanded uncertainty is 7 µm in the lateral direction and 5 µm in the vertical direction for a 95 % confidence level, for both the networks studied in this chapter. This level of precision is similar to that achieved by the standard fiducialization method at CERN.

For both the lateral and the vertical offsets between the fiducial targets and the stretched wire, the micro-triangulation method provides a mean expanded uncertainty of 10 µm for a 95 % confidence level.

The root-mean-square values of the differences between the offsets computed with the micro-triangulation measurement and the offsets computed with the direct wire measurements of the coordinate measuring machine are approximately 5 µm in the lateral direction and 9 µm in the vertical direction. These values indicate the accuracy of the offsets obtained with the micro-triangulation method, given the fact that the precision of the wire reconstruction from the direct wire measurements of the CMM is better than 1 µm for a 95 % confidence level, therefore, about 10 times better than the precision of the micro-triangulation method.

A repeatable difference was observed between the indirect and the direct method of the coordinate measuring machine for the estimation of the wire position. For both measurements examined in this chapter, the mean value of the deviation is on average approximately 4 µm in the lateral direction and approximately 8 µm in the vertical direction, for the whole length of the suspending wire. This deviation is beyond the expected precision of the employed CMM and it seems to be systematic. Given the high-precision wire reconstruction from the direct wire measurements of the CMM, which is better than 1 µm for a 95 % confidence level, we assume that the deviation is caused by the calibration of the wire supports that was performed in a coordinate machine providing lower precision measurements.

Finally, despite the unrealistic configuration — since the magnet was removed —, the second case study was rather helpful in order to clarify various aspects of the micro-triangulation networks with direct wire observations. Firstly, the variations of the light conditions and the background intensities was identified as sources of significant systematic errors that have a large influence on the angle observations to the wire. Secondly, a more accurate estimation of the catenary form factor was achieved due to the larger distribution of the angle observations. Lastly, the correlation of the residuals and the standard residuals between the horizontal and the vertical angles to the wire were better shown, as well as the relation between the partial redundancy of an observation and the apparent angle of the wire in the image plane.

Chapter 6

Validation of micro-triangulation for alignment applications in the LHC tunnel

In this chapter, we aim to validate the micro-triangulation method with direct wire observations for alignment applications in the LHC tunnel. The concept of the test measurement is described in Section 6.1. An elongated surveying network consisting of fiducial targets and a stretched wire was measured with the QDaedalus measuring systmem, a laser tracker and an ecartometer as described is Section 6.2. The results presented in Section 6.3 demonstrated precision of approximately 60 µm for a 95 % confidence level for the horizontal offsets between the fiducial points and the stretched wire in a length of approximately 55 m. The most important findings of this test measurement are summarize in Section 6.4.

6.1 Introduction

Stretched wires are used at CERN as reference for the alignment of the accelerator components, together with the *ecartometry* method, which has been developed and used at CERN for over 50 years (*Quesnel et al.*, 2008). Ecartometry is based on the measurement of the horizontal distance (offset) between a stretched wire and a reference point (fiducial) located on a particle accelerator component, e.g., a magnet. Currently, ecartometry is the standard method used for the alignment of the Large Hadron Collider (LHC) and it is also considered for the alignment of the upgrade project of the LHC; the High Luminosity LHC (HL – LHC).

Ecartometry is applied with the use of a special measuring device called *ecartometer*. The device is a digital caliper with a microscope mounted on the slider of the caliper (Figure 6.4a). The ecartometer is mounted in the socket of the fiducial point and the microscope is used to target the wire from above. The length between the socket and the wire is measured on the horizontal scale and the indication is displayed on the device.

The resolution of the offset measurement is at approximately 15 µm to 20 µm, while the precision is estimated to be at about 40 µm (standard deviation) after an adjustment (*Quesnel et al.*, 2008). The method is relatively fast and easy to apply, with low com-

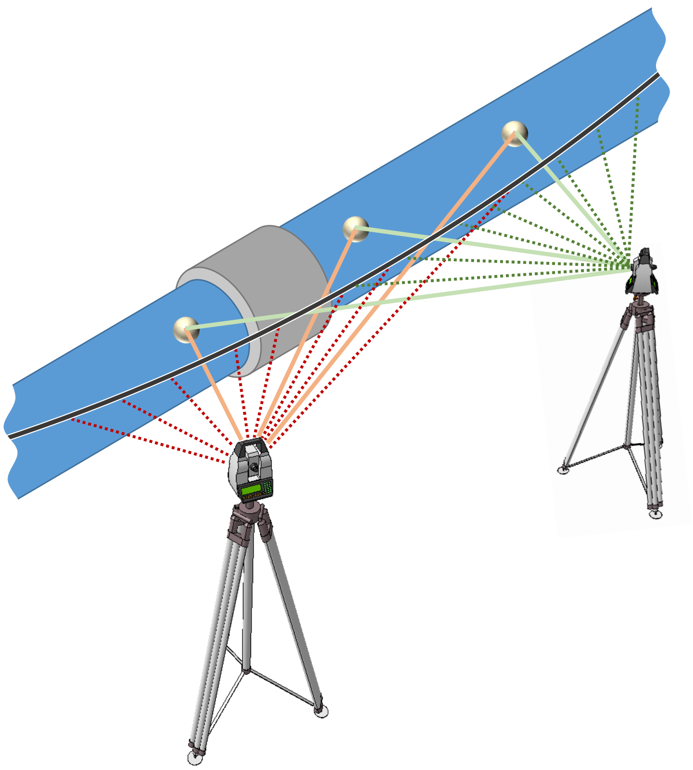

Figure 6.1: Concept of micro-triangulation with targets and wires in the LHC tunnel. An image-assisted theodolite observes the fiducial points (white spheres) and the stretched wire (black line) from different positions, creating a surveying network.

putational workload. Significant limitations of the method could be considered the facts that: a) it can measure only the horizontal offset between a fiducial and a wire, b) the wire should be stretched on approximately the same height as the fiducials, following the slope of the accelerator components, and c) it cannot be used for complex configurations with multiple wires.

In the last few years, much research at CERN has focused on alternative solutions that can overcome the aforementioned limitations. The required measuring system should be portable, accurate at the level of a few tens of micrometers, and able to establish a geometrical link between the fiducials and the wire(s) by conducting non-contact wire measurements. Three new methods are currently under development at CERN based on the photogrammetry (*Mergelkuhl et al.*, 2018), on the optical wire positioning system (oWPS) technology (*Fuchs et al.*, 2018), and on the micro-triangulation (Figure 6.1).

After the validation of the *micro-triangulation method with direct wire measurements* for magnet *fiducialization* applications with an accuracy of approximately 10 µm rms for the offsets between the wire and the fiducial points (Chapter 5), we decided to proceed in the validation of the method for *alignment* applications of particle accelerator components. The ideal place to test the method in real working and environmental conditions, and with realistic spatial and time constraints, is the LHC tunnel. A measurement campaign was organized by the survey section of the EN-SMM group (Engineering Department - Survey, Mechatronics and Measurements) at CERN, in February and March 2018, during the annual Year-End Technical Stop (YETS) of the LHC. This campaign was part of the R&D studies for the upgrade project of the LHC; the High Luminosity LHC (HL – LHC). The aim of the measurement campaign was to evaluate the feasibility and the accuracy of various stretched-wire measurement methods, including the *micro-triangulation method with direct wire measurements*. More information about this campaign and a discussion on the performance and the comparison of the methods under evaluation can be found in *Fuchs et al.* (2018).

The main objective is to examine the feasibility and the efficiency of the micro-triangulation method with direct wire observations in the special environmental conditions and space limitations of the LHC tunnel. Moreover, we aim to estimate the accuracy of the method for alignment applications, in comparison with the results of the laser tracker and of the standard ecartometry method. Therefore, two surveying networks were measured, consisting of common targets. The first network consists of angle and distance observations measured by a laser tracker. Due to the type of the employed laser tracker, hereafter, this surveying networks is called *AT402 network*. The second surveying network is a micro-triangulation network measured by the QDaedalus measuring system, and consisting of angles to targets and to the wire. This network will be called *QDaedalus network*.

The reason that we consider two different networks is technical and related to the fact that a standard software cannot process angle observations to non-corresponding points, i.e., the observations to the wire. Moreover, the software we developed to solve micro-triangulation networks that include observations to lines, catenaries, etc., could not process distance observations by the time this study took place.

For both, the *AT402 network* and the *QDaedalus network*, we use a truncated functional model that omits the Earth's curvature and makes no correction for the atmospheric refraction. This decision is imposed by the fact that the software that we developed was initially developed to solve micro-triangulation networks with a volume of a few metres. Evidently, the truncated model does not significantly affect the horizontal coordinates of the networks, which are used for the comparisons of this chapter.

For the evaluation, we firstly compare the target coordinates estimated by the micro-triangulation measurements and by the laser tracker measurements. Subsequently, we proceed to the comparison of the horizontal distances (offsets) between the fiducials and the wire. Thus, we compare the horizontal distances that are calculated by the parameters of the micro-triangulation network with the offsets measured directly with the ecartometry method. In this comparison, we are only compare the horizontal offsets, because this is the quantity that the ecartometry can only measure.

The results demonstrate that the combination of the micro-triangulation method and the QDaedalus measuring system is able to provide coordinates with approximately 55 µm precision for a 95 % confidence level in the lateral direction to the wire axis, which is the most important direction for alignment applications. This level of precision is comparable to the coordinate precision that we obtained with the laser tracker. Concerning the horizontal offsets between the fiducials and the stretched wire, the micro-triangulation method provides a precision of approximately 60 µm for a 95 % confidence level, which is comparable to the precision of the ecartometry. A preliminary analysis of this study can be found in (*Vlachakis and Fuchs*, 2018).

6.2 Materials and methods

In this section, we describe the equipment employed for the required measurements, the configuration of the network, the measurement procedure, and the methodology followed to analyze the acquired data. The data analysis starts with the least-squares adjustment of the two surveying networks, continues with the detection of a displacement of the wire between the two days of measurements, and ends with the comparison of the target coordinates between the laser tracker and the micro-triangulation measurements, and the comparison of the offsets between the micro-triangulation and ecartometry.

6.2.1 Equipment

The basic equipment used in the LHC tunnel for this validation measurement is depicted in Figure 6.2, while the actual setup is described here:

- **Theodolite and tripod.** The Leica Nova TS60 theodolite was used for this measurement. According to the manufacturer specifications, the angular accuracy is 0.15 mgon (1σ, ISO17123-3) — which is approximately 2.4 µrad or 2.4 $\mu\mathrm{m\,m}^{-1}$ — and the reference to the vertical is less than 0.1 mgon. The TS60 was mounted on a Leica AT21 aluminium tripod. Both, the theodolite and the tripod were left in the tunnel for a few days in advance to acclimatize.
- **QDaedalus measuring system.** The automated micro-triangulation technique was applied in combination with the QDaedalus measuring system. The focusing mechanism of the QDaedalus measuring system was not installed on the theodolite owing to the internal focusing system of the theodolite. However, the front divergence lens was installed on the objective lens of the theodolite due to the fact that the range

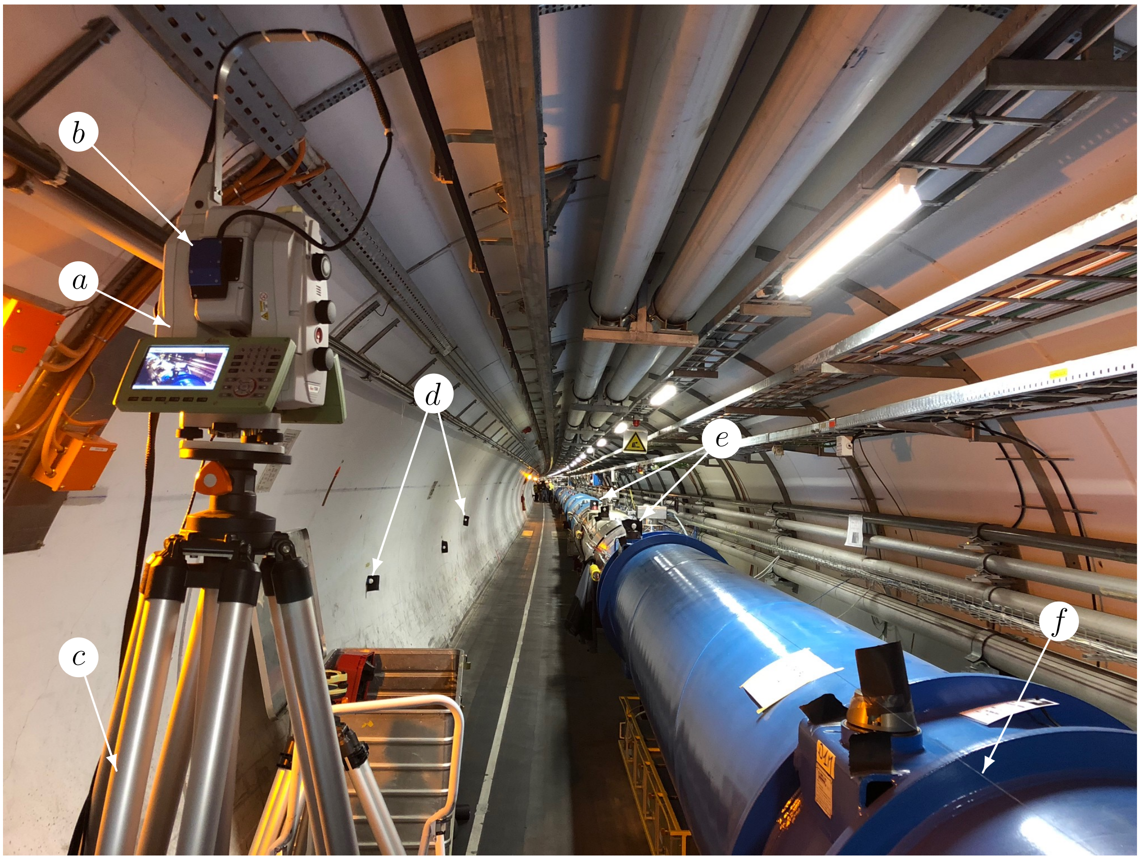

Figure 6.2: Micro-triangulation measurements in the LHC tunnel. The Leica Nova TS60 theodolite (a), was equipped with the QDaedalus system (b) and mounted on the Leica AT21 aluminium tripod (c). Moreover, spherical targets were mounted on the wall (d) and on the magnets (e), and a wire was stretched along the selected accelerator sector (f). (Source: Jean-Frederic Fuchs, CERN).

between the theodolite and the targets exceeded 13 m. For this measurement, we used the *Circle matching* algorithm to observe the spherical fiducial points *Guillaume et al.* (2012), and the *Line matching* algorithm (described in Chapter 2) to observe the wire. To ensure the portability of the system and the fast movement between the theodolite stations, we used a rolling desk for the laptop, the cabling, the batteries and other necessary tools and accessories.

- **Targets and supports.** White ceramic spheres, made by Zirconium dioxide (ZrO_2), were used as fiducial points. The spheres have 1 µm sphericity (Grade 40, ISO3290) and 38.1 mm (1.5 inch) diameter. They were attached by magnetic force on aluminium supports that were inserted in the standards sockets of the magnets (Figure 6.3b). Aluminium supports were also affixed on the tunnel wall with a two-part epoxy glue, a week before the measurement in order to let the glue set (Figure 6.3c). The advantage of the ceramic spheres is that they can be observed from

(a)

(b)

(c)

Figure 6.3: Targets and supports used for the validation measurement in the LHC tunnel. (a) A corner cube retroreflector inserted in a spherical adapter with equal size to a Taylor Hobson sphere. (b) A ceramic sphere of 1.5 inch diameter on an aluminium support used as adapter to reach approximately the same height as a Taylor Hobson sphere. (c) A ceramic sphere of 1.5 inch diameter mounted with magnetic force in an aluminium support affixed to the wall with a two-part epoxy glue. (Source: Jean-Frederic Fuchs, CERN).

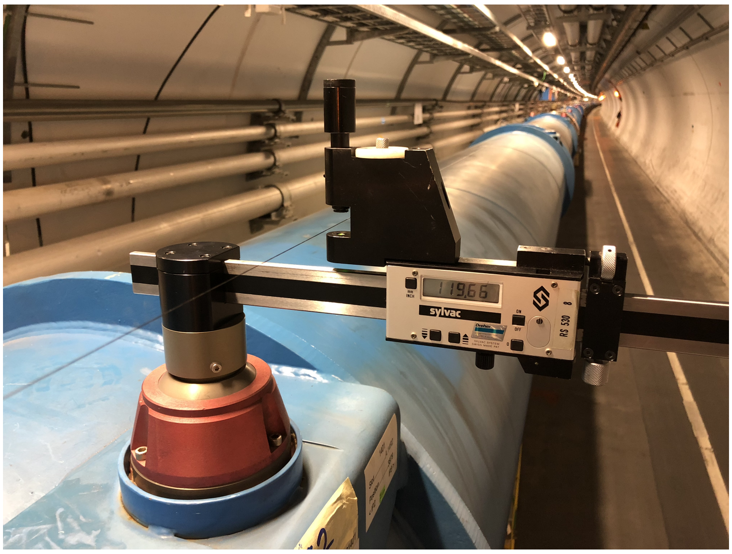

(a)

(b)

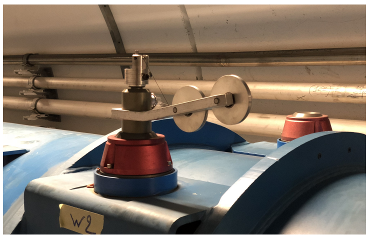

(c)

Figure 6.4: (a) Digital ecartometer. (b and c) Standard wire-stretching devices developed at CERN. The relative position and orientation of the wire was arranged to be suitable for ecartometry measurements. (Source: Jean-Frederic Fuchs, CERN).

every direction, so there is no need to manually orient the target, as happens with a standard corner cube retroreflector (CCR) used for the laser tracker measurement (Figure 6.3a).

- **Wire and supports.** A black, multi-thread, vectran wire of 0.4 mm diameter was stretched for about 86 m. Standard stretching devices, developed at CERN, were used at the two extremities to keep the wire stretched under stable tension (Figures 6.4b and 6.4c). The wire was stretched in the direction of the tunnel axis, at about 20 cm in the lateral direction and at approximately 20 cm higher than the sockets of the fiducial points in order to enable the ecartometry measurements (Figure 6.4a). The height difference between the wire suspending points (Figures 6.4b and 6.4c) was approximately 1.1 m (Figure 6.5b), forming a sagitta of approximately 2 cm (Figure 6.15b).

6.2.2 Measurement procedure

Many measuring systems were used by members of the surveying group during the measurement campaign, which lasted for about two weeks. The list of these systems include an ecartometer, optical wire positioning system (oWPS) devices, a digital camera, a laser tracker and the aforementioned theodolite. Next, we will describe in detail the measurements that are relevant to our analysis, i.e., the ecartometer, the laser tracker and the theodolite.

Ecartometry

Several ecartometry measurements were performed during the two-weeks campaign by Julien Labarthe-Vacquier, a member of the surveying group. The measurements of the 13 fiducial points acquired on 26/02/2018 (one day before the beginning of the micro-triangulation measurements) were used for the comparison in this chapter. Ecartometry measurements were also performed during the micro-triangulation measurements on the extremities of the wire, but not on the fiducials in the area of interest. Therefore, although these measurements were synchronous to the micro-triangulation measurements, they cannot be used for the offset comparison.

Laser tracker

A Leica AT402 laser tracker with 1.5 inch diameter corner cube retroreflectors (CCR) and the SpatialAnalyzer® data acquisition software were used for this measurement campaign. Many laser tracker measurements were performed during the days of the campaign for different purposes and by several members of the surveying group, including Mathieu Duquenne, Vivien Rude and Jean-Frederic Fuchs. The laser tracker measurements used in the analysis of this study were acquired on 06/03/2018 (four stations) and on 08/03/2018 (two stations). It is also worth mentioning that a fast measurement was performed a few days before the micro-triangulation measurements that was used only to obtain approximate coordinates of the network at the level of 0.1 mm. The approximate network coordinates were used in order to facilitate and expedite the configuration and the acquisition of the micro-triangulation measurements.

Micro-triangulation

The micro-triangulation measurements took place on 27 and 28/02/2018. The Leica Nova TS60 theodolite was used, equipped with the QDaedalus measuring system. The network was measured from several positions of the theodolite, according to the measurement procedure described next. The micro-triangulation measurements were performed synchronously with the ecartometry, the oWPS, the photogrammetry and the laser tracker measurements, causing several disruptions to the procedure.

- **Theodolite installation.** The theodolite was installed and leveled properly. Its approximate position and orientation was obtained by a resection using a corner-cube prism. This information is important in order to facilitate and expedite the next step.
- **Parameters configuration.** The approximate coordinates of the instrument position, the targets, and pre-selected points on the wire were used a) to compute the direction of the targets with respect to the station, b) to configure the focus on the targets, using a pre-calibrated distance-to-focus function, and c) to select the targets to be observed, given a range of distances (usually 5 m to 20 m).

  The procedure continues with the configuration of the user-defined parameters of the QDaedalus system, such as the camera gain, the shutter speed, the number of CCD shots to average per angle measurement, and the parameters relevant to the target detection algorithms. At the end, the measurement scenario was defined by setting the number of repeating angle measurements per target, the number of the theodolite faces and the sequence of the measurements.

  This second step used to last for about one hour, which was also enough time for the tripod to settle.
- **Observations acquisition.** After the parameters configuration, the system was ready to perform the observations. This part used to take about 20 min, given the number of shots per angle measurement and the number of angle measurements per target. In our case, we selected to acquire 10 CCD shots for each angle measurement to a target and five CCD shots for each angle measurement to the wire.

  In surveying, a series of measurements is completed when all the selected targets are observed in both, the *left face* and the *right face* of the theodolite. In our case, the theodolite was set to perform two sequential series of measurements from each position. Each series was later considered as a different station with different estimated coordinates, orientation and systematic errors. Following this technique, we practically reduce the observation time for each station, in an attempt to reduce errors caused by dynamic effects such as the tripod or the wire instability due to temperature variations.

6.2.3 Network configuration

To increase the reliability of the comparison, it was decided to measure 13 fiducial points in an arc of about 55 m in the LHC tunnel that consists of two quadrupole magnets and three dipole magnets. Thus, an elongated surveying network of approximately 85 m length, 2 m width, and 2 m height was created (Figure 6.5).

The network consists of the 13 fuducial points, the stretched wire, and 10 additional targets mounted on the available tunnel wall, opposite to the magnets with respect to the corridor. The additional targets were introduced to strengthen the network geometry due its elongated shape, and to allow for a much better constraint of the network scale in the

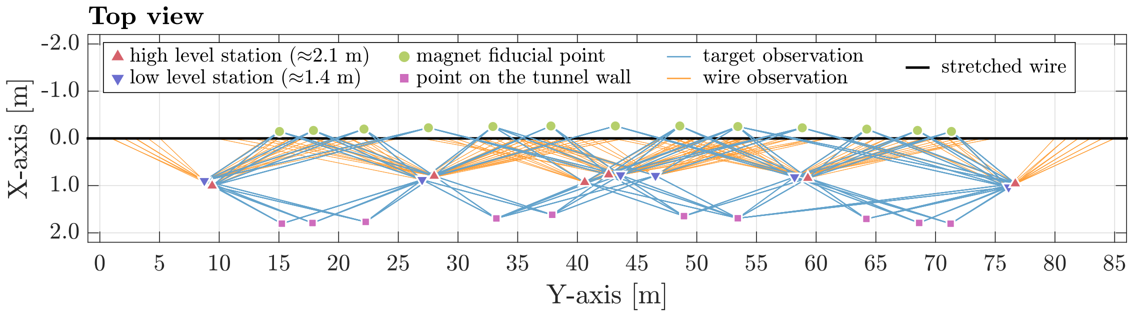

(a)

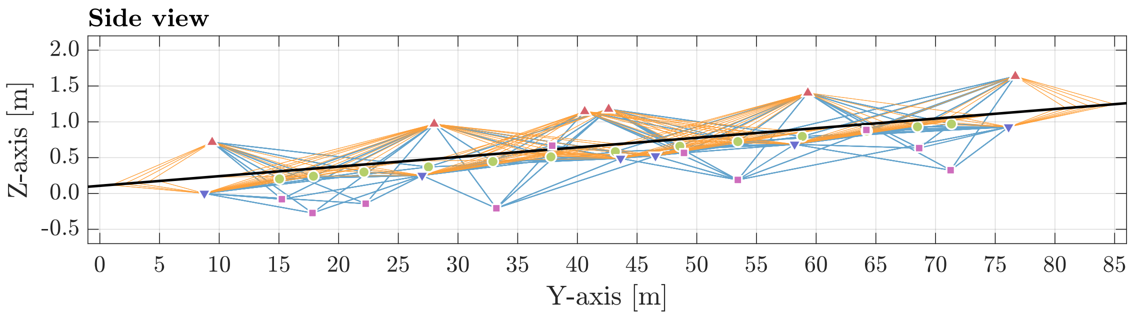

(b)

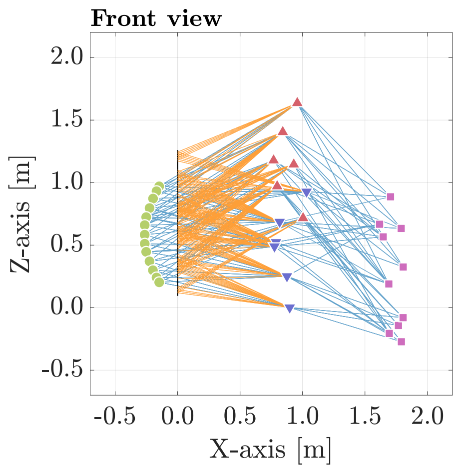

(c)

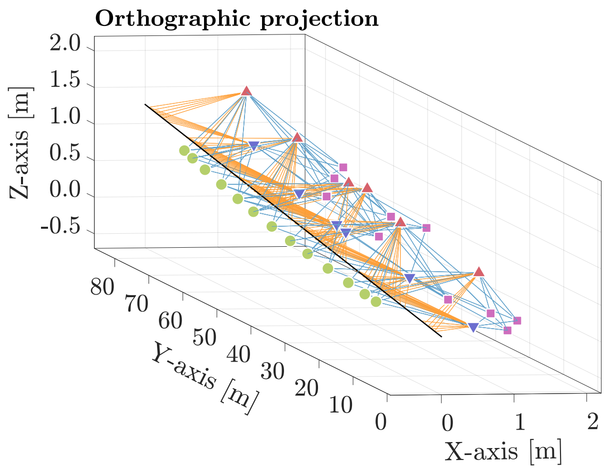

(d)

Figure 6.5: Configuration of the surveying network. The 85 m long network consists of 13 fiducial points on the magnets, the stretched wire on the side of the magnets, 10 additional targets mounted on the tunnel wall and the theodolite positions in the LHC tunnel corridor. Angle observations to the targets and to the wire are depicted in different colors.

lateral direction to the wire axis. These targets were mounted approximately opposite to the fiducials in order to facilitate the selection of the theodolite stations, and in various heights (see magenta squares in Figure 6.5).

During the preparation phase, before the measurement campaign, a numerical simulation was carried out to ensure that the network can be solved in terms of least-squares adjustment and that it has the required redundancy. The partial redundancy z was computed to be over 0.75 for the vast majority of the observations and with no observation under the 0.25 threshold, except for the horizontal angles to the wire that cannot be well controlled by the network due to the approximately horizontal wire configuration (see Figure 6.10).

The positions of the theodolite in the lateral direction (X-axis) were lying in an approximately straight line, following the tunnel axis. The theodolite positions in the longitudinal direction (Y-axis) were chosen in accordance to the constraint that the targets ought to be in the range of 3 m to 30 m. In this range the optical system — i.e., the combination of the telescope, the camera and the additional front lens — is able to perform measurements to the targets and the wire with the previously specified size.

Measurements from two positions with different heights are required in order to estimate the parameters of an approximately horizontal wire, according to the proposed micro-triangulation method. Therefore, the theodolite was positioned at the minimum height allowed by the employed tripod (approximately 1.4 m) and at the maximum height allowed by the tunnel ceiling (approximately 2.1 m).

Given the aforementioned geometrical constraints, five areas were selected to be suitable for the installation of the theodolite. Taking into account our prior experience with the QDaedalus measuring system and the available time — which was two days — we estimated that it was feasible to install, configure and perform measurements from 10 positions, i.e., five pairs of a low instrument height and a high instrument height positions. During the measurement, we realized that the available time was enough to perform measurements from an additional pair of a low and a high instrument height positions. These stations were added in the middle of the working area in order to further strengthen the network.

6.2.4 Data analysis

The acquired data can be divided into three sets: a) the ecartometry measurements, b) the laser tracker measurements, and c) the micro-triangulation measurements. The ecartometry data set consists of the independently measured horizontal distances between the selected fiducial points and the stretched wire, thus, they cannot be processed any further. Hence, we proceed with the analysis of the surveying observations with the least-squares adjustment method.

AT402 network analysis

A detailed description of the *AT402 network* includes:

- **Functional model.** Includes horizontal and vertical angles, and distances that are already reduced (average of the left and the right faces). The functional model used for the *AT402 network* adjustment is based on a topocentric system and it does not include corrections for the Earth's curvature or the atmospheric refraction.

- **Observations.** The network consists of 222 reduced observations between 23 targets (13 fiducials and 10 targets on the tunnel wall), and six stations.
- **Unknowns.** In total, 93 unknown parameters are estimated for this network. They consist of the three coordinates for each station and target, plus the six horizontal orientation parameters, one for each station.
- **Constraints.** The datum defect for such a network is four (three for the position and one for the horizontal orientation), thus, an equal amount of constraints was set in order to get a minimum constraint solution. More specifically, the position of the network was constrained in the middle fiducial point (at the longitudinal position of about 43 m) and the orientation at the last fiducial point (at about 71 m), as depicted in Figure 6.5a.

QDaedalus network analysis

A detailed description of the *QDaedalus network* includes:

- **Functional model.** The functional model used in this case is an expanded model, including three systematic errors for each theodolite position and each series of measurements, and the catenary parameters of the stretched wire (Section 4.3). The model is based on a topocentric system and it does not include corrections for the Earth's curvature or the atmospheric refraction.
- **Observations.** The network consists of 23 targets, 24 stations and the stretched wire. It contains 4312 angle observations, grouped into 420 quadruples of observations to the targets and 658 quadruples of observations to the wire (Figure 6.5). Each quadruple of observations combines two pairs of horizontal and zenith angles, one for the *left face* and one for the *right face* of the theodolite.
- **Unknowns.** There are seven unknown parameters for each theodolite station (three coordinates, the horizontal orientation and three theodolite systematic errors), three unknown coordinates for each targets, seven unknown parameters for each wire that is modeled as a catenary and one unknown parameter t_p for each pair of horizontal and zenith angle observations to the wire (see Section 4.3). Therefore, there are 168 unknown parameters for the 24 stations, 69 unknown parameters for the targets and 1330 unknown parameters for the wire.
- **Constraints.** Partial trace minimization constraints were introduced as Helmert conditions to cover the datum defect, which is five for a three dimensional triangulation network (three for the position, one for the horizontal orientation and one for the scale). Another two constraints were added for each wire: one for the longitudinal position and one for the directional vector components (Section 4.5.2). The coordinates obtained by the adjustment of the AT402 network were used to constrain the micro-triangulation solution. In this case, the accuracy of the scale of the triangulation network is inherited from the accuracy of the scale provided by the laser tracker.

Verification of the wire model

The interpretation of the least-squares analysis is mainly based on the residuals of the observations. For example, the statistics of the residuals can reveal potential problems of the functional model used to describe the observations. In a standard surveying network, the residuals refer to the station from where the observations were performed and to the observed targets. Therefore, we rely on their statistics, while there is no need to visualize their values in space.

This is also true in case of a wire, where the statistics of the angle observation residuals can surely indicate modeling issues. However, the visualization of the residuals in space might reveal more information about the exact source of the problem. In order to achieve a meaningful visualization, we compute the vertical and lateral deviations between the estimated wire position and the rays of the observations in space.

More specifically, the vertical deviation dV is computed as the vertical distance between the intersection $\mathcal{V}$ of the observation ray with the vertical plane of the wire and the point $\mathcal{V}'$ on the wire (Figure 6.6a). In a similar sense, the lateral deviation dL is computed as the horizontal distance between the intersection $\mathcal{L}$ of the ray with the surface that it is formed by the wire and it is perpendicular to the vertical plane and the point $\mathcal{L}'$, which is the projection of $\mathcal{L}$ on the wire.

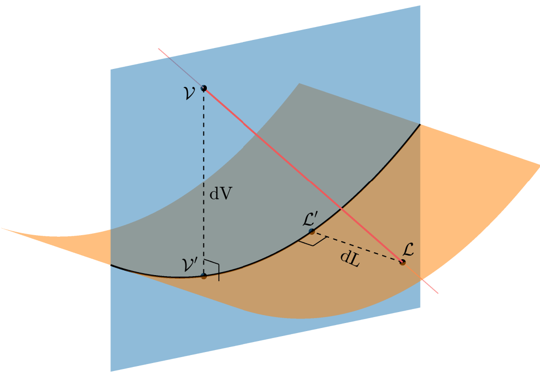

(a)

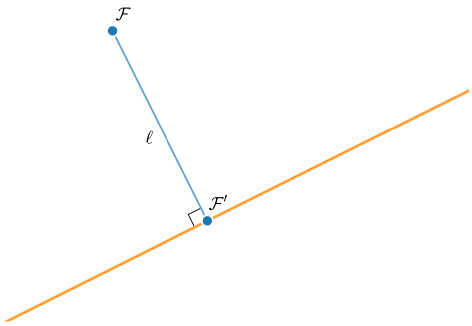

(b)

Figure 6.6: (a) Lateral deviation dL and vertical deviation dV between the observation ray (red line) and the estimated wire (black curve). (b) Top view of the horizontal distance (offset) ℓ between the fiducial and the wire.

Comparison of the coordinates

This comparison concerns the difference of the estimated position of the targets (on the magnets and on the tunnel wall) measured by the laser tracker (*AT402 network*) and by the QDaedalus measuring system (*QDaedalus network*). The comparison will indicate whether the micro-triangulation method can give results comparable to a laser tracker — which is nowadays the standard instrument — in such a difficult environment, especially considering the poor light conditions.

Comparison of the wire offsets

The comparison of the wire offsets takes place between the ecartometry measurements and the corresponding horizontal distances that are derived from the estimated parameters of the catenary and the estimated coordinates of the *QDaedalus network* adjustment.

Firstly, we calculate the horizontal distance ℓ between the fiducial $\mathcal{F}$ and its projection onto the wire $\mathcal{F}'$ (Figure 6.6b). Following the law of uncertainty propagation, the 95 % confidence interval of each horizontal distance (offset) is calculated based on the relevant elements of the covariance matrix of the network solution (see Section 4.7.1).

Subsequently, we compute the difference $d\ell$ of the horizontal offsets ℓ between the micro-triangulation method and the ecartometry method, and its 95 % confidence interval, taking into account the standard uncertainty of each one of the two methods.

6.3 Results

6.3.1 AT402 network solution

As mentioned earlier, the *AT402 network* consists of three types of observations, i.e., the horizontal and zenith angles, and the distances. After a few repetitions of the adjustment, we obtained representative values for the *a priori* variance values $\sigma^2_{i,G}$ for each observation i of each group G of observations, by updating the stochastic model according to the respective *a posteriori* variance components $\hat{\sigma}^2_G$ (see Section 4.6.2).

The *a priori* values for the reference standard deviation and the standard deviation for each group of observations are shown in Table 6.1, in which we can also see that the *a posteriori* values are close to the unit.

Table 6.1: The *a priori* and *a posteriori* reference standard deviations (σ_0, $\hat{\sigma}_0$), the standard deviation $\sigma_{i,G}$ for each observation i of each group G of observations and the *a posteriori* standard deviation components $\hat{\sigma}_G$. The observations of the *AT402 network* are grouped in horizontal angles H, zenith angles Z and distances S.

AT402 network					*06 & 08/03/2018*
Reference	[mgon, mm]	Components	H [mgon]	Z [mgon]	S [mm]
σ_0	1.00	$\sigma_{i,G}$	0.19	0.23	0.02
$\hat{\sigma}_0$	0.99	$\hat{\sigma}_G$	1.00	1.00	0.98

The standard deviation $\sigma_{i,G}$ of the zenith angles is estimated to be slightly larger than that of the horizontal angles. The difference is perhaps caused by the fact that the functional model does not account for the Earth's curvature and the atmospheric refraction effects on the observations. This particularly affects the zenith angles, leading to systematically larger residuals compared to the horizontal angles.

Concerning the precision of the estimated coordinates, we proceed with the optimistic assumption that the standard uncertainty is equal to the standard deviation computed according to the covariance matrix of the unknown parameters. With this assumption, we certainly neglect effects related to the centering and the repositioning of a target in a support. In Table 6.2, we provide the statistics of the expanded uncertainty U^{95} of the

Table 6.2: Statistics of the expanded uncertainties U^{95} for the estimated *AT402 coordinates* of the *AT402 network*.

AT402 network			*06 & 08/03/2018*
	AT402 coordinate expanded uncertainty		
	$\mathrm{U}^{95}_{\mathrm{X}}$ [mm]	$\mathrm{U}^{95}_{\mathrm{Y}}$ [mm]	$\mathrm{U}^{95}_{\mathrm{Z}}$ [mm]
min	0.029	0.027	0.043
max	0.123	0.037	0.094
mean	0.064	0.031	0.058
median	0.057	0.030	0.054

coordinates, for each axis. The expanded uncertainty is calculated by multiplying the standard deviation of each coordinate by a coverage factor that it is equal to 1.96 for a 95 % confidence level.

As expected by the fact that the configuration of the network is narrow in the X-axis and elongated in the Y-axis, the high-precision distance measurements of the laser tracker strongly contributes to the high precision in the Y-axis direction. As a result, the mean expanded uncertainty for the X-axis ($\mathrm{U}^{95}_{\mathrm{X}}$) is twice larger than that for the Y-axis ($\mathrm{U}^{95}_{\mathrm{Y}}$).

The mean expanded uncertainty for the Z-axis ($\mathrm{U}^{95}_{\mathrm{Z}}$) is worse than that of the Y-axis ($\mathrm{U}^{95}_{\mathrm{Y}}$) due to the fact that the functional model does not take into account the effects of the Earth's curvature and the atmospheric refraction on the observations.

6.3.2 QDaedalus network solution with one catenary

In the first attempt to adjust the *QDaedalus network*, the functional model was built with the assumption that only one wire was measured and that it follows the catenary shape. The adjustment resulted in very large residuals for the angle observations to the wire, which did not have a random behavior. After a few tries and by partially solving the network, we realized that the angle observations to the wire are inconsistent with the applied model.

In Table 6.3, we present the *a priori* values of the standard deviation for each type of observations. The large value of the standard deviation for the zenith angle observations

Table 6.3: The *a priori* and *a posteriori* reference standard deviations (σ_0, $\hat{\sigma}_0$), the standard deviation $\sigma_{i,G}$ for each observation i of each group G of observations and the *a posteriori* standard deviation components $\hat{\sigma}_G$ for the *QDaedalus network* solution with one catenary. The observations are grouped into horizontal and zenith angles to the targets (H_t, Z_t) and to the wire (H_w, Z_w).

QDaedalus network — solution with one catenary						*27 – 28/02/2018*
			target observations		wire observations	
Reference	[mgon]	Components	H_t [mgon]	Z_t [mgon]	H_w [mgon]	Z_w [mgon]
σ_0	1.00	$\sigma_{i,G}$	0.42	0.51	1.01	2.34
$\hat{\sigma}_0$	1.00	$\hat{\sigma}_G$	1.00	1.00	0.99	1.01

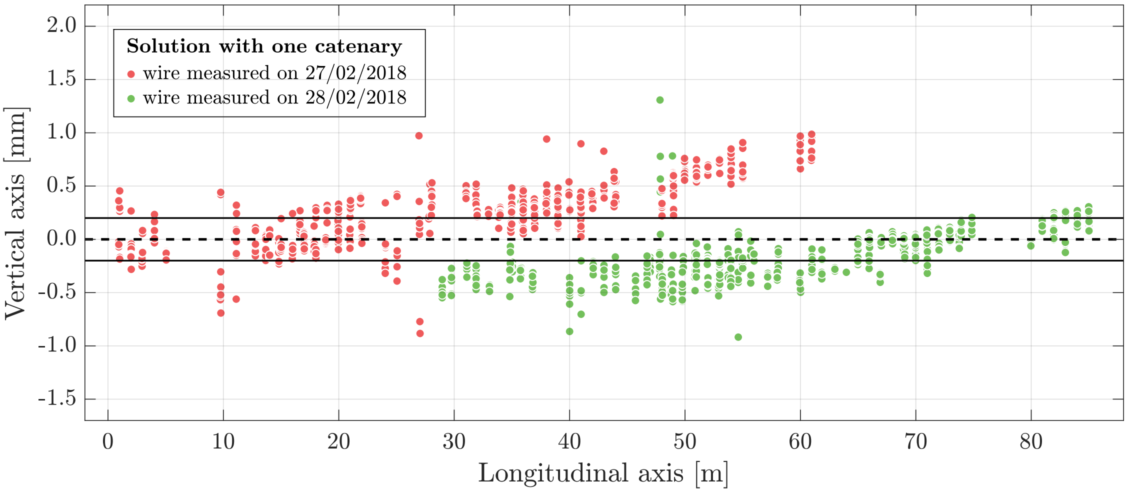

Figure 6.7: Vertical deviations dV of the observation rays from the estimated wire calculated for the solution with one catenary. Each color corresponds to one day of measurements.

to the wire reflects the problematic functional model and it does not indicate the actual precision of this type of observations.

In order to verify the exact problem of the functional model, we plot the vertical deviations dV between the observation rays and the estimated wire. In Figure 6.7, we observe that the deviations seem to belong into two groups, one extended to the forward part (on the left-hand side) and the other to the backward part (on the right-hand side) of the wire. By using different colors, one for each day of measurements, it is revealed that the groups of deviations coincide with the days of measurements.

Subsequently, a new adjustment were performed with two catenaries included in the functional model of the network; one for each day. An updated top view map of the observations to the wire is presented in Figure 6.8, being colored according to the day of measurements.

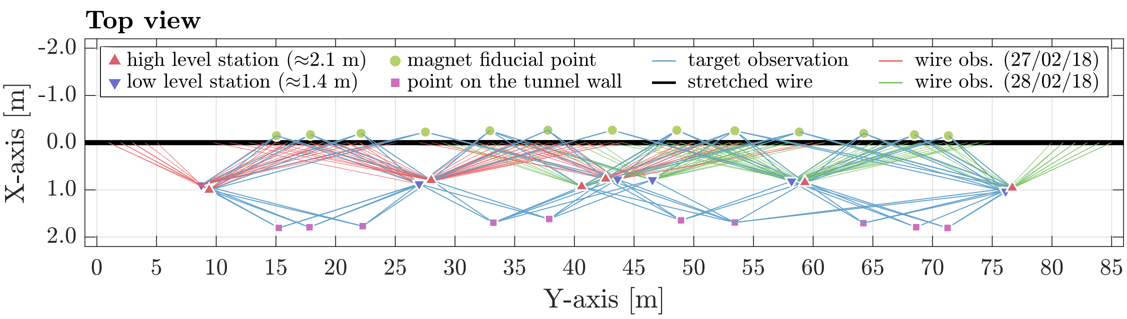

Figure 6.8: Top view of the surveying network configuration. The observations to the wire are colored according to the day of measurements.

6.3.3 QDaedalus network solution with two catenaries

Analysis of the observations

In the final adjustment of the *QDaedalus network*, the functional model is composed by two catenaries, one for each day of measurements. For this network we consider six groups of observations. The stochastic model was built according to the *a priori* standard deviation values presented in Table 6.4.

In Table 6.4, we observe that standard deviation values of the observations to the targets are approximately three times larger than the expected value according to the specifications of the theodolite. Many parameters could have contributed to this result, such as the poor light conditions, which cause instability in the circle detection algorithm, as well as the temperature variation and the unstable airflow in the tunnel during the two days of measurements.

We also notice that the standard deviation of the zenith angles is slightly larger than that of the horizontal angles. This is perhaps caused by the truncated functional model that omits the Earth's curvature and the atmospheric refraction.

Moreover, the standard deviation values of the observations to both the wires are about six times larger than the precision indicated by the manufacturer of the theodolite. The reason for such large values is certainly the fact that the wire was vibrating during the measurements, as a result of the wind flow in the tunnel caused by the ventilation system. The vibration of the wire was also verified by the oWPS sensor measurements during the measurement campaign (*Fuchs et al.*, 2018), and it was also visible to the naked eye.

The estimated residuals $\hat{v}$ for each group of observations are depicted in different colors in Figure 6.9, in which we observe that the residuals of the horizontal angles to the wire seem to have smaller scatter — and therefore, smaller standard deviation — than the zenith angles to the wire. This observation contradicts with the respective standard deviation values presented in Table 6.4, in which the values for the horizontal and the vertical angles to the wire are approximately equal. The contradiction is caused by the fact that the standard deviation component $\hat{\sigma}_G$ of each group of observations is computed

Table 6.4: The *a priori* and *a posteriori* reference standard deviations (σ_0, $\hat{\sigma}_0$), the standard deviation $\sigma_{i,G}$ for each observation i of each group G of observations and the *a posteriori* standard deviation components $\hat{\sigma}_G$ for the *QDaedalus network* solution with two catenaries. The observations are grouped in horizontal and zenith angles to the targets (H_t, Z_t), to the first wire (H_{w_1}, Z_{w_1}) and to the second wire (H_{w_2}, Z_{w_2}).

QDaedalus network — solution with two catenaries

			target observations		wire observations			
			27 – 28/02/2018		*27/02/2018*		*28/02/2018*	
Reference	[mgon]	Components	H_t [mgon]	Z_t [mgon]	H_{w_1} [mgon]	Z_{w_1} [mgon]	H_{w_2} [mgon]	Z_{w_2} [mgon]
σ_0	1.00	$\sigma_{i,G}$	0.42	0.47	0.90	0.92	0.93	0.93
$\hat{\sigma}_0$	0.99	$\hat{\sigma}_G$	1.00	0.99	0.95	0.99	1.00	1.00

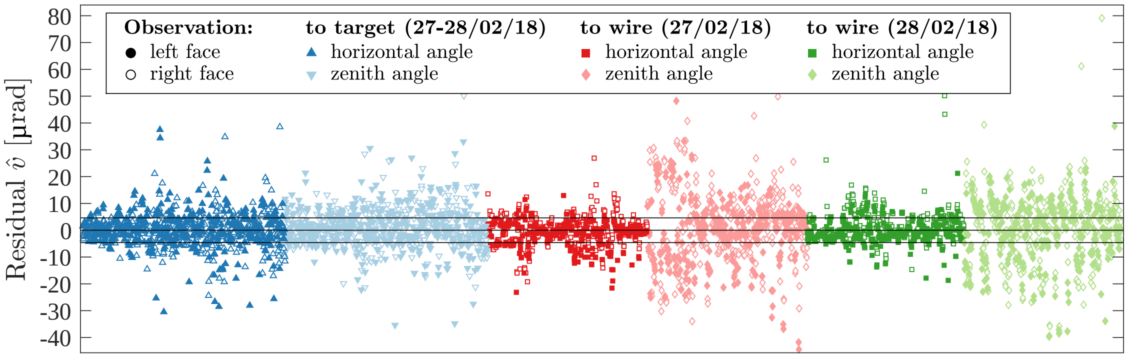

Figure 6.9: Estimated residuals $\hat{v}$ of the *QDaedalus network* for the two-catenary solution. The black horizontal lines represent the 95 % confidence interval of the angular precision of the theodolite, according to the manufacturer. The *left face* observations are denoted by filled symbols, while the *right face* observations are denoted by outlined symbols.

with Equation 4.75, in which the denominator is the partial redundancy of the particular group of observations.

In Figure 6.10, we observe that the partial redundancy z values of the horizontal angles to the wire are very small and that they lie below the critical value of 0.25 for the majority of the these observations. Due to the approximately horizontal orientation of the measured wire the horizontal angles to the wire do not significantly contribute to the network. Therefore, these observations cannot be well controlled by the network and finally it is difficult to reliably estimate their actual precision. For the other groups of observations, the standard deviation of the respective residuals is very close to the standard deviation component.

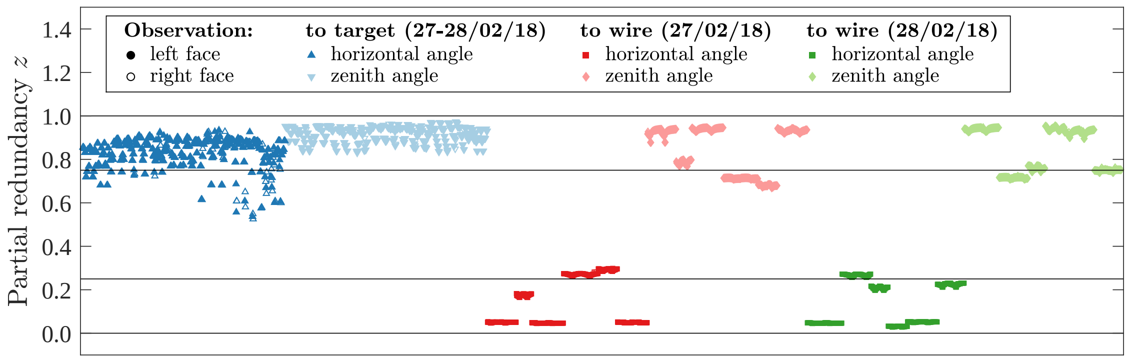

Figure 6.10: Partial redundancy z of the *QDaedalus network* for the two-catenary solution. The horizontal black lines represent the 0.25 and 0.75 thresholds used to indicate whether an observation is well or poorly controlled by the network. The *left face* observations are denoted by filled symbols, while the *right face* observations are denoted by outlined symbols.

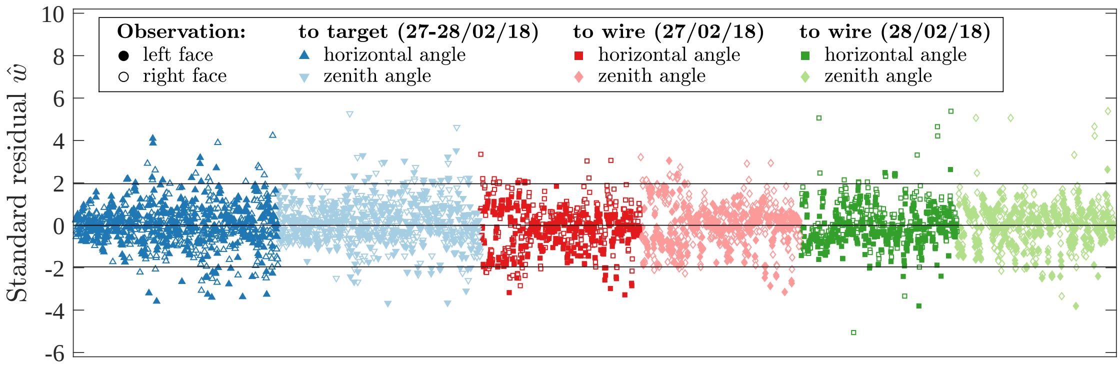

Figure 6.11: Estimated standard residuals $\hat{w}$ of the *QDaedalus network* for the two-catenary solution. The black horizontal lines represent the selected constant for the Biber function, equal to 1.96, which corresponds to a 95 % probability. The *left face* observations are denoted by filled symbols, while the *right face* observations are denoted by outlined symbols.

Despite the narrow and elongated configuration of the network, in Figure 6.10, we observe that except from the horizontal angles to the wire, all the other groups of observations are very well controlled with values more than 0.75 for the vast majority of the observations. This is the result of the large number of observations acquired by many stations with the a wide horizontal distribution and a large vertical separation.

A useful quantity for the iteratively reweighted least-squares adjustment is the estimated standard residual $\hat{w}$ of each observation (Equation 4.84). In this study, we apply the Biber function to compute the weight factors for the observations with respect to the estimated standard residuals $\hat{w}$ (depicted in Figure 6.11). Approximately 5.6 % of the values are out of the ± 1.96 interval, which corresponds to the 95 % of the *normal* distribution. The observations exceeding this threshold are those that are automatically reweighted according to the Biber weight function (Equation 4.89).

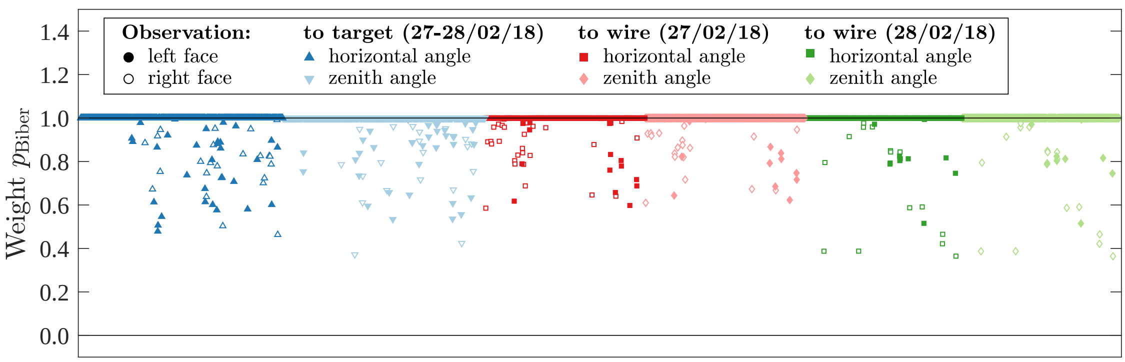

Figure 6.12: Weight factors p_{Biber} (according to the Biber weighting function) of the *QDaedalus network* for the two-catenary solution. The *left face* observations are denoted by filled symbols, while the *right face* observations are denoted by outlined symbols.

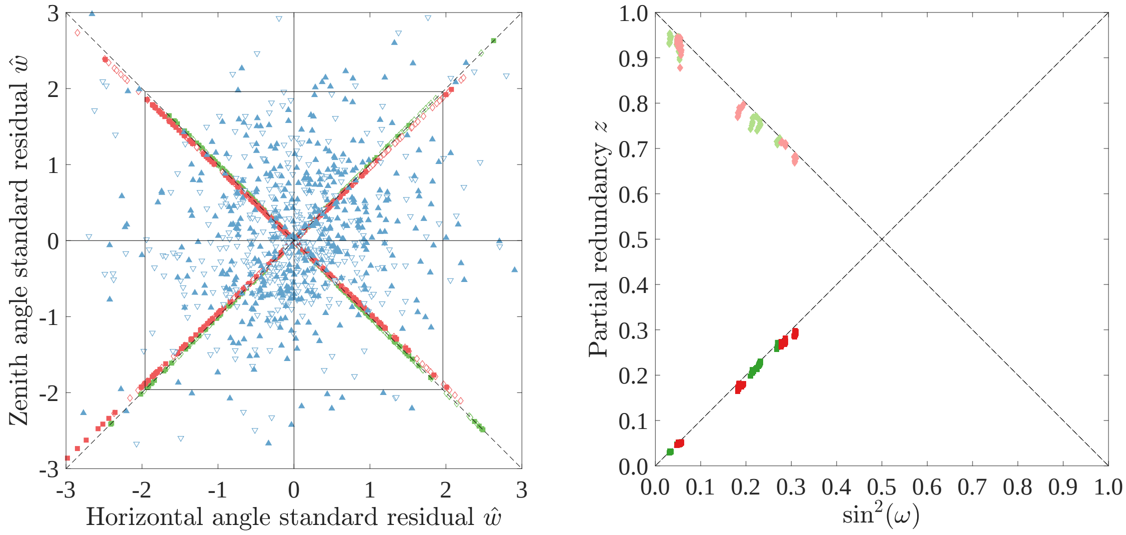

(a) **(b)**

Figure 6.13: (a) Correlation between the estimated standard residuals $\hat{w}$ of the horizontal angles and the zenith angles. (b) Correlation between the partial redundancy z of the wire observations and the angle ω of the wire in the image plane for each observation.

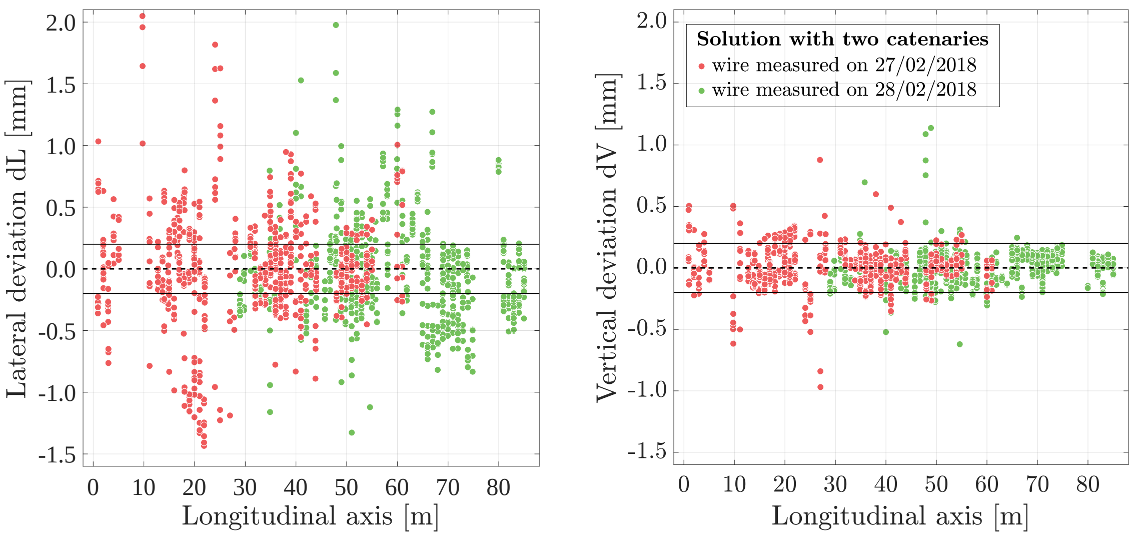

(a) **(b)**

Figure 6.14: (a) Lateral deviations dL and (b) vertical deviations dV of the observation rays to the estimated wires, calculated for the solution with two catenaries. Each color corresponds to one day of measurements.

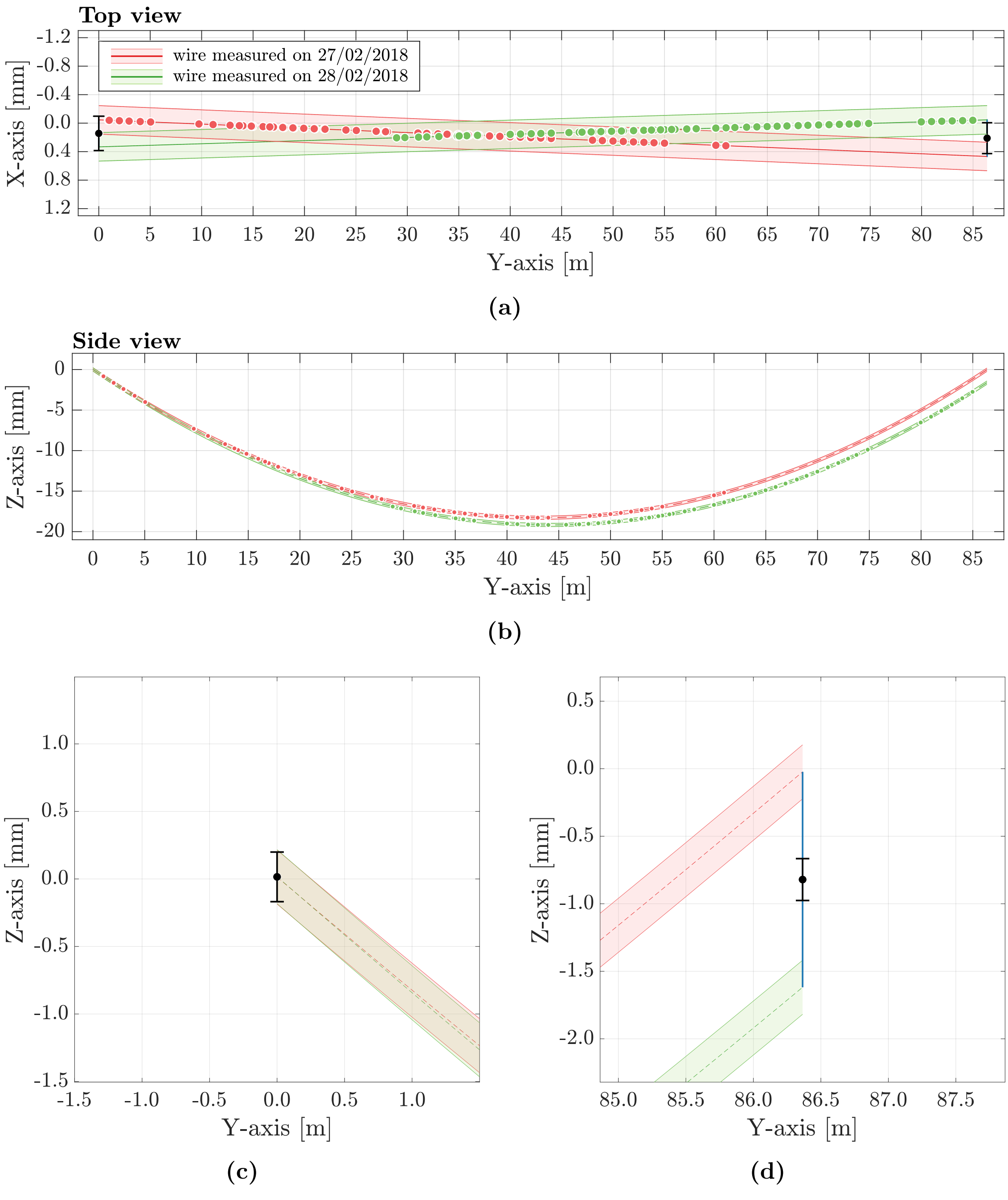

Figure 6.15: Estimated horizontal (a) and vertical (b) position of the two catenaries by the least-squares adjustment of the *QDaedalus network*. Estimated height difference and expanded uncertainty (for a 95 % confidence level) of the vertical position of the wires for the right-hand side (c) and for the right-hand side (d) extremities. The diameter of the wire is depicted in the actual scale of each graph.

In Figure 6.12, we present the calculated weight factors p_{Biber}. We notice that for the two catenaries the weights of the horizontal and zenith angles are correlated, while this is not true for the weights of the horizontal and zenith angles to the targets. The correlation of the p_{Biber} weight factors is expected due to the correlation of the standard residuals that it is discussed in Section 5.4.3 and it is shown in Figure 5.35b.

In Section 5.4.3, we discussed two interesting results related to the wire observations. The first result concerns the correlation of the standard residuals $\hat{w}$ between the horizontal and the vertical angle observations to the wire. The second result concerns the relation between the partial redundancy z of the angle observations to the wire and the apparent orientation of the wire in the image plane (see Figure 5.37). In order to confirm these two results, we repeat the relevant computations and we plot Figures 6.13a and 6.13b.

The vertical and the lateral deviations for the solution with the two catenaries are presented in Figure 6.14. In this case, we do not observe any bias due to the wire modeling. The vertical deviations dV show very small dispersion compared to the diameter of the wire (0.4 mm), which is represented by the two horizontal black lines. For the lateral deviations dL, we observe a much larger scatter that it is most probably caused by the unfavorable configuration of the network, especially regarding the vertical separation between the theodolite positions and the wire.

The reconstruction of each wire in the three dimensions is possible owing to the estimated wire parameters from the network adjustment. In Figure 6.15, we present the top view and the side view of the two catenaries for the entire suspending length (approximately 85 m). In Figure 6.15b, we select to depict the vertical position of both catenaries with respect to the straight line connecting the extremities of the red catenary. This reduction helps us to visualize the sagitta of approximately 2 cm over the height difference of about 1.1 m. The exact diameter of the wire is depicted in the actual scale, which is different for each graph.

In the lateral direction (X-axis), the differences in the position of the two catenaries are estimated to be 0.379 mm on the left-hand side and 0.514 mm on the right-hand side, forming an angle of about 10.3 µrad (Figure 6.15a). The uncertainty in the estimation of the horizontal deviations is 0.241 mm and 0.216 mm for a 95 % confidence level, respectively. This result suggests that the wire had changed its lateral position between the two days of measurements, and certainly the wire extremity on the right-hand side (85 m on the Y-axis).

In the vertical direction, we observe that the estimated height difference between the two catenaries is 0.003 mm on the left-hand side (Figure 6.15c) and 1.595 mm on the right-hand side (Figure 6.15d), with uncertainties of 0.184 mm and 0.155 mm for a 95 % confidence level, respectively. This result is explained by the fact that the wire had to be lowered at the right-hand side suspending point to allow ecartometry measurements on that part of the wire.

6.3.4 Coordinate comparison

In this section, we compare the coordinates of all targets as estimated by the *QDaedalus network* and the *AT402 network*. Prior to the comparison, we present in Table 6.5 the statistics of the expanded uncertainties of the *QDaedalus coordinates*. The expanded

Table 6.5: Statistics of the expanded uncertainties U^{95} for the estimated *QDaedalus coordinates* of the *Qdaedalus network*.

QDaedalus network			*27 – 28/02/2018*
QDaedalus coordinate expanded uncertainty			
	U^{95}_X [mm]	U^{95}_Y [mm]	U^{95}_Z [mm]
min	0.045	0.186	0.020
max	0.075	0.766	0.045
mean	0.055	0.350	0.029
median	0.053	0.313	0.028

uncertainties are computed by the standard deviation of the coordinates multiplied by 1.96, which is the coverage factor for a 95 % probability.

Compared to the corresponding statistics for the *AT402 network* (Table 6.2), we notice that the expanded uncertainties for the X-axis (U^{95}_X) are comparable between the two networks (median values at 0.053 mm and 0.057 mm, respectively), for the Y-axis (U^{95}_Y) the *QDaedalus network* provides approximately 10 times worse precision (median values at 0.313 mm and 0.030 mm, respectively), and for the Z-axis (U^{95}_Z) the *QDaedalus network* provides approximately two times better precision (median values at 0.028 mm and 0.054 mm, respectively). Such a result is expected, given the fact that the high-precision distance measurements of the laser tracker make a major contribution to the precision in the Y-axis direction, and by the fact that the *QDaedalus network* consists of much larger number of observations that contribute in the high precision of the X-axis and Z-axis.

Before we compare the two sets of the coordinates, it is required to perform a 3D Helmert transformation due to the fact that the two networks refer to different topocentric reference systems. The statistics of the coordinate differences (dX, dY, dZ) and the respective magnitudes of the horizontal vectors and the 3D vectors (**dr**, **dR**) are presented in Table 6.6. Here, it is worth emphasizing that the measurements of the *AT402 network* took place about 10 days after the *QDaedalus network* measurements.

In Figure 6.16, we plot the 2D confidence ellipses for the *QDaedalus network* in the Y-X plane (top view) and in the Y-Z plane (side view). The ellipses are computed for a 95 % confidence level, thus, the semi-axes of each ellipse are multiplied by a coverage

Table 6.6: Statistics of the coordinate differences dX, dY, dZ and the magnitudes of the horizontal vectors **dr** and the 3D vectors **dR** between the *QDaedalus coordinates* and the *AT402 coordinates*, which are used as reference values.

QDaedalus coordinates − AT402 coordinates					
	dX [mm]	dY [mm]	dZ [mm]	$\|\|\mathbf{dr}\|\|$ [mm]	$\|\|\mathbf{dR}\|\|$ [mm]
min	−0.125	−0.975	−0.081	0.029	0.063
max	0.118	0.387	0.103	0.975	0.979
mean	0.000	0.000	0.000	0.245	0.250
median	−0.001	0.092	0.004	0.146	0.149
std	0.061	0.323	0.047	0.212	0.212
rms	0.059	0.316	0.046	0.321	0.325

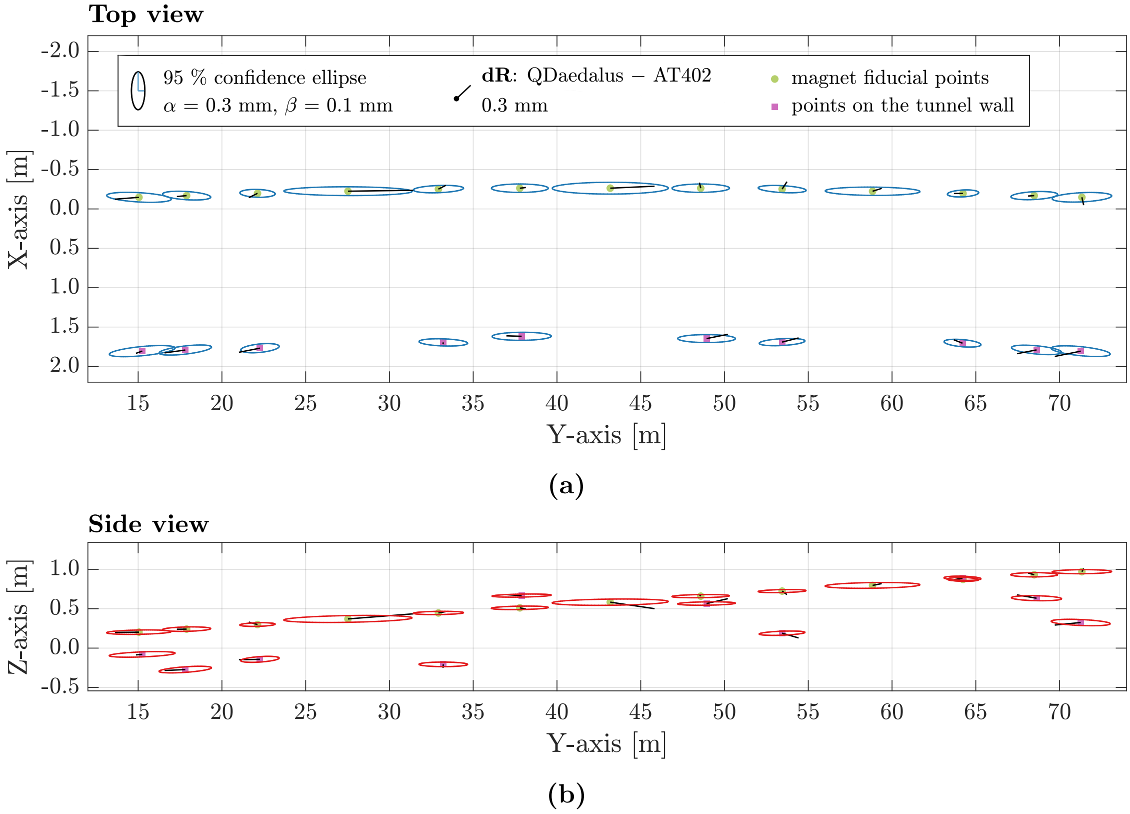

Figure 6.16: Confidence ellipses for the *QDaedalus network* for a 95 % confidence level and the projection of the 3D vectors **dR** between the *QDaedalus coordinates* and the *AT402 coordinates*. (Scale according to the legend).

factor that is equal to 2.45. We also plot the projection in each plane of the 3D vectors **dR** between the *QDaedalus coordinates* and the *AT402 coordinates*. In Figure 6.16, we observe that the projection of the vectors **dR** to the two planes are systematically oriented to the Y-axis and that the vast majority lies within the area of the confidence ellipses.

6.3.5 Offset comparison with ecartometry

For each catenary, we compute the offsets from the fiducial points that are located in the range of the angle observations for each day of measurements. More specifically, according to Figure 6.8, the wire measurements on the first day expand from 0 m to 55 m in the Y-axis, while on the second day, the wire measurements expand from 30 m to 75 m in the Y-axis. Therefore, the first group consists of the offsets between the wire measured on 27/02/2018 and the first nine fiducials (see also Figure 6.17), while the second group consists of the offsets between the wire measured on 28/02/2018 and the last nine fiducials. The two groups of offsets have an overlap of five fiducials in the middle part of the wire.

The horizontal offsets ℓ are computed according to Equation 4.98 without taking into account the vertical component of the equation. The horizontal offsets are in the range

Table 6.7: Statistics of the horizontal offsets ℓ, as computed from the estimated unknown parameters of the *QDaedalus network* for the two catenaries. The expanded uncertainties U_{ℓ}^{95} refer to a 95 % confidence level with a coverage factor equal to 1.96.

QDaedalus offsets

	wire measured on 27/02/2018		wire measured on 28/02/2018	
	ℓ [mm]	U_{ℓ}^{95} [mm]	ℓ [mm]	U_{ℓ}^{95} [mm]
min	147.597	0.048	147.955	0.047
max	263.919	0.071	263.851	0.089
mean	226.183	0.058	225.986	0.059
median	251.970	0.054	251.797	0.050

of approximately 150 mm to 260 mm (Table 6.7), as a result of the length of the LHC arc sector that was selected for this test measurement.

In order to estimate the uncertainty of an offset ℓ we apply the law of propagation (as described in Section 4.7.1) for the part of the covariance matrix (Equation 4.101) that is relevant to the horizontal components of the catenary parameters and to the horizontal coordinates of the specific fiducial point.

The statistics of the expanded uncertainties for a 95 % confidence level are presented in Table 6.7. The mean values of U_{ℓ}^{95} are approximately 60 µm for both groups of offsets, while the maximum value is less than 90 µm, which corresponds to a standard deviation of approximately 45 µm. This value is at the level of the standard deviation of the ecartomerty method, which is estimated to be equal to 40 µm, as reported in *Quesnel et al.* (2008).

Next, we compare the offsets calculated by the micro-triangulation network with those measured by the ecartometry method one day before the start of the micro-triangulation measurements. For each fiducial point the horizontal offset difference $\mathrm{d}\ell$ is computed by subtracting the *Ecartometry offset* from the *Qdaedalus offset*. The expanded uncertainty $\mathrm{U}_{\mathrm{d}\ell}^{95}$ for each difference is calculated with the law of uncertainty propagation, taking into consideration that the standard deviation of the ecartomerty method is equal to 40 µm.

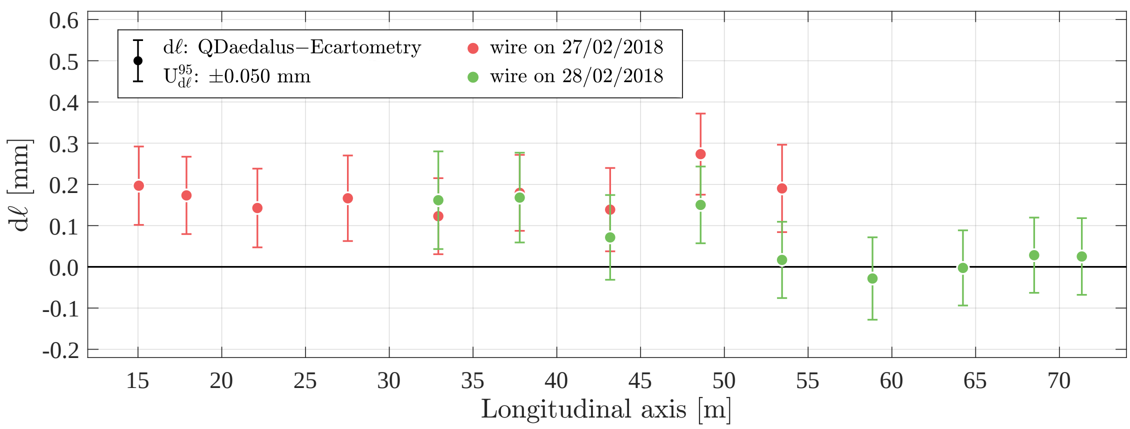

Figure 6.17: Differences $\mathrm{d}\ell$ between the *QDaedalus offsets* and the *Ecartometry offsets*, and their expanded uncertainties $\mathrm{U}_{\mathrm{d}\ell}^{95}$. (Scale according to the legend).

Table 6.8: Statistics of the horizontal offset differences $\mathrm{d}\ell$ between the *QDaedalus offsets* and the *Ecartometry offsets* for the two catenaries. The expanded uncertainties $\mathrm{U}^{95}_{\mathrm{d}\ell}$ of the offset differences are computed according to the precision of the two methods.

QDaedalus – Ecartometry

	wire measured on 27/02/2018		wire measured on 28/02/2018	
	$\mathrm{d}\ell$ [mm]	$\mathrm{U}^{95}_{\mathrm{d}\ell}$ [mm]	$\mathrm{d}\ell$ [mm]	$\mathrm{U}^{95}_{\mathrm{d}\ell}$ [mm]
min	0.123	0.092	−0.028	0.091
max	0.273	0.106	0.168	0.118
mean	0.176	0.098	0.066	0.099
median	0.173	0.095	0.028	0.093
std	0.044	—	0.076	—
rms	0.181	—	0.097	—

The differences $\mathrm{d}\ell$ are depicted in Figure 6.17 as points at the exact longitudinal position and in different colors according to the day of the measurements. The error bars correspond to the expanded uncertainty for each difference $\mathrm{d}\ell$ ($\mathrm{U}^{95}_{\mathrm{d}\ell}$). The statistics of the offsets differences $\mathrm{d}\ell$ are presented in Table 6.8, together with the statistics of the expanded uncertainties $\mathrm{U}^{95}_{\mathrm{d}\ell}$ for each group of offsets.

In Table 6.8, we notice that the mean value of the offset differences $\mathrm{d}\ell$ for the first wire (in red color) is approximately three times larger than that of the second wire (in green color), while the respective standard deviation value is approximately half. The results of the comparison suggest that most probably the measurand, i.e., the position of the wire, is different for each day of measurements. This assumption is also supported by the demonstrated displacement of the wire between the two days by the micro-triangulation measurements and by the fact that the wire was being displaced at least once per day (usually before or after the measurements of the other systems) in order to enable the ecartometry measurements. The inconsistency of the comparison for the two groups of offsets is also visible in Figure 6.17 and in the large difference of the root-mean-square values.

To report a value for the accuracy of the offsets measured by the micro-triangulation method with respect to the ecartometry method, we would choose the best of the results that is approximately 0.1 mm rms for the group of offsets concerning the wire measurements on 28/02/2018. This choice is made under the assumption that in the case that the two measurands were different, at least they were closer to each other.

6.4 Discussion and conclusions

In this chapter, we successfully demonstrated the feasibility of the *micro-triangulation method with direct wire observations* in the LHC tunnel for alignment applications. Concerning the efficiency, the micro-triangulation method cannot compete with the standard ecartometry method in terms of simplicity and productivity, especially for networks with a large longitudinal size. The limiting factors in the efficiency of the micro-triangulation method could be seen in the complicated and rather difficult moving of the hardware, and the semi-automated procedure of the measurement configuration in the QDaedalus software for each theodolite station.

However, the proposed method is advantageous, especially in cases that not only the horizontal offsets are required but the vertical offsets, too. This is feasible due to the fact that the network is measured and computed in the three dimensions, in a single coordinate system that is precisely linked to the gravity field owing to the use of theodolites. Moreover, the proposed method could be considered as a solution for complex configurations with multiple wires in various directions and height differences. It is important to mention that the method can definitely be rather performant in permanent configurations with multiple theodolites and especially in applications that they require frequent and automated monitoring.

The numerical results of this evaluation measurement demonstrate that for the target coordinates the precision of the micro-triangulation network in the lateral direction to the wire axis (X-axis) is similar to the laser tracker network, i.e., a precision of approximately 55 µm for a 95 % confidence level. However, in the longitudinal direction (Y-axis) the mean coordinate uncertainty of the micro-triangulation network is approximately 0.3 mm for a 95 % confidence level due to the unfavorable network configurations in relation with the nature of the angle observations. The comparison with the laser tracker network coordinates resulted in differences of approximately 60 µm rms in the lateral direction to the wire axis, which is usually the most important direction for alignment applications.

The micro-triangulation method provides a precision comparable to that of the ecartometry for the horizontal offsets between the fiducials and the stretched wire. The precision of the proposed method is approximately 60 µm for a 95 % confidence level and for about 55 m wire length. The result is six times less precise than that achieved in the metrology room, most probably, due to the much larger scale of this application and due to the fact that the wire was vibrating during the measurement, owing to the ventilation system of the tunnel.

Although there is a reasonable doubt about the comparability of the offsets obtained by the different measuring methods due to the changes in the position of the wire during the measurement campaign, the accuracy of the offsets computed by the *QDaedalus network* is approximately 0.1 mm rms in comparison with the ecartometry measurements.

Finally, it is demonstrated that the proposed method, based on the *micro-triangulation with direct angle observations to the wire* in combination with the QDaedalus measuring system, can be applied for in-situ alignment applications for particle accelerator components, providing results comparable to the standard ecartometry method in terms of precision.

Chapter 7

Conclusions and outlook

The concluding chapter briefly presents the developments of this study in Section 7.1 and the most important experimental results in Section 7.2. The advantages and disadvantages of the proposed methodology and the employed measuring system are discussed in Section 7.3 and in Section 7.4, respectively. Finally, Section 7.5 is devoted to ideas for further improvements that could enhance the performance of the proposed metrology solution.

The aim of this study is to propose an alternative metrology solution for the fiducialization and the alignment of particle accelerator components. The proposed solution is based on the automated micro-triangulation method and utilizes image-assisted theodolite systems.

Two significant novelties characterize the proposed methodology: the direct observation to surveying targets and stretched wires at the same time and location, and the least-squares adjustment of these observations, according to a unified mathematical model and in a single coordinate system. These unique features enable the precise measurement of complex configurations with multiple wires that are stretched in various locations, directions and height differences, which was not possible beforehand.

Before the experimental validation and the performance evaluation of the new methodology, it was necessary to proceed to the development of two important tools: a wire detection algorithm to enable the automated observation of the stretched wire, and a least-squares adjustment software that is based on an expanded mathematical model and is capable of processing the angle observations to the targets and the wires.

This thesis presents the successful development, validation and precision evaluation of a portable metrology solution that is able to perform fast, accurate, contactless, automated and remotely-controlled measurements to the reference targets on a particle accelerator component and the stretched wire, which is used as reference for fiducialization and alignment applications.

7.1 Developments

The QDaedalus measuring system, which was employed for the experimental part of the present study, is accompanied with a data acquisition software. At the time that this study started, the software was already able to automatically detect and measure the fiducial spherical targets with a circle detection algorithm. However, no algorithm was available to enable the automated measurement of the stretched wire. Therefore, we developed a new wire detection algorithm that we also implemented into the QDaedalus software.

The new algorithm is based on the Canny edge detector, on a robust best-line fit and on geometrical calculations to precisely measure the position and orientation of the wire in the image coordinate system. The implementation of the new algorithm respects all the software-related requirements that were set in order to successfully integrate the algorithm into the QDaedalus software. The wire detection algorithm is able to work independently and in cooperation with the existing QDaedalus detection algorithms.

A qualitative evaluation of the developed wire detection algorithm demonstrated that it is able to detect and measure the wire under various configurations that are usually met in a triangulation network. Specifically, the algorithm adequately performed measurements in different angles of incidence between the theodolite optical axis and the wire for a large range of contrasts between the wire image and its background, and with the wire being depicted in different orientations in the image.

A standard surveying software cannot adjust a triangulation network with targets and wires due to the fact that we cannot distinguish targets on a wire that has a uniform surface, and therefore, the angle observations from different theodolite positions cannot correspond to the exact same point. As a result, we developed a new functional model in order to integrate the angle observations to the wire, and a new software to enable the least-squares adjustment of such triangulation networks.

The new observation equations for the horizontal and zenith angles to the stretched wire are formulated by integrating the straight line or the catenary parametric equations into the standard observation equations used in surveying.

The developed software is able to handle all the necessary types of observations, i.e., the horizontal and vertical angle observations to targets, straight lines and catenaries. For each observation, the software automatically adds the corresponding unknown parameters and computes the first derivatives of the corresponding observation equation. Moreover, the software computes the datum constraints, according to the selection of the user, and it adds the constraints that correspond to the selected model for each observed stretched wire. Finally, the software applies an iteratively reweighted adjustment, which is used to update the weights of the observations according to the given loss function. The most important feature of the developed software is the capability to adjust networks that consist of a large number of instrument positions, targets and stretched wires in different shapes.

After the development of these two essential tools for this study, we proceeded to the experimental validation and the performance evaluation of the proposed methodology.

7.2 Experimental results

The experimental evaluation of the wire detection algorithm and the circle detection algorithm demonstrated that high-precision angle measurements can be performed. The standard deviation values that were obtained in different experiments are in the range of 0.25 µrad to 1.25 µrad. These values correspond to double-face measurements in one direction in space. The results are considered as fully satisfactory for the quality of the detection algorithms, given the fact that in the worst case the standard deviation is approximately two times better than the specified angular accuracy of the employed theodolite. The obtained angular precision is indicative of the spatial precision that such a measuring system could reach with an optimal configuration of the network geometry and under stable environmental conditions.

The two detection algorithms were tested against variations of the user-defined parameter values and environmental conditions. The wire detection algorithm demonstrated excellent robustness against changes in the user-defined parameter values such as the exposure time, the sensor gain, the sensitivity of the edge detection, etc. However, the algorithm is susceptible to biases caused by variations of the light conditions and the background intensity in the image. Moreover, the analysis of the micro-triangulation networks revealed that large changes in the image background cause abrupt changes in the residuals of the observations to the wire. For the circle detection algorithm biases appear with long exposure times and high values for the sensor gain, as well as when the target is not centered in the image.

The proposed methodology was successfully validated for fiducialization applications. The final product of the fiducialization process is the offsets between the fiducial targets and the stretched wire. The micro-triangulation method achieved a mean expanded uncertainty of 10 µm for a 95 % confidence level for both, the lateral and the vertical offsets.

The accuracy of the offsets is approximately 5 µm rms in the lateral direction and approximately 9 µm rms in the vertical direction, in comparison to the offsets computed by the direct CMM measurement of the stretched wire.

Moreover, the developed methodology was validated for alignment applications in the accelerator tunnel, where a stretched wire is used as a reference. The results demonstrated a precision of approximately 60 µm for a 95 % confidence level in the estimation of the horizontal offsets between the fiducial points and the stretched wire for a length of approximately 55 m. This result can be characterized as conservative — given the already demonstrated better performance of the measuring system and of the overall methodology in laboratory conditions — because it is influenced by the poor network configuration and the unfavorable environmental conditions, which are factors that can be easily improved.

7.3 Advantages

The experimental part of this study revealed the advantages of the proposed methodology, compared to the existing solutions, and exhibited a high potential.

The most important feature of the proposed methodology is that it relies on passive optical measurements that are performed without requiring contact with the targets. This feature enables the direct measurement of freely suspended stretched wires. In combination with the fact that the theodolites can observe targets at practically any direction, the methodology gains an unprecedented advantage; the direct measurement of the fiducial targets and the stretched wire with a single measuring system, in a single coordinate system and at the same time and location.

Another advantage of the use of theodolites is the performance of high-precision observations that are potentially free of systematic errors when specific measurement and analysis practices are followed. The most accurate theodolite has an angular accuracy specification of approximately 2.4 µm m^{-1} (1σ). In this study, we achieved up to 10 times better angular precision in terms of standard deviation for measurements in single direction. It is left to be proven that this precision can be achieved for angle measurement in various directions.

The aforementioned high precision measurements are most probably the result of the automated target detection algorithms. These algorithms enhance the precision of the final result of the measurement, while at the same time they reduce potential gross errors. Moreover, the entire set of measurements for this study was acquired remotely. The remotely-controlled measurements are nowadays feasible due to the available software tools and the internet connectivity at almost any location.

The combination of the automation and the remote control has the advantage that the measuring system is able to effortlessly enlarge the number of acquired measurements per unit of time, while it contributes to the precision by the capability of performing measurements during specific hours of the day in order to avoid high levels of induced seismicity caused by human activity.

The short duration of the measurement is also essential for a high quality result. The faster a measurement is completed, the smaller the influence of the environmental conditions to the measured object and the measuring system will be, and therefore, the more precise the measurement result will be. In this study, we achieved the acquisition of a complete series of observations for fiducialization in approximately 10 min. The total acquisition time surely depends on the number of the points measured, however, the crucial parameters are the exposure time, the number of shots and the number of angle measurements per target. Fortunately, improvements that are relevant to these three parameters can drastically enhance the performance of the QDaedalus system.

Finally, the portability of the proposed methodology is another key feature. This should be combined with the fact that there is no limitation on the size and the weight of the measured component as it exists in the case of the coordinate measuring machine. The advantage in this case is that both the fiducialization and the alignment of a component can be performed in the tunnel and potentially under the operating conditions (e.g., temperature) of the accelerator component, avoiding deformations of the component that may occur during the transportation or due to differences in the ambient temperature.

7.4 Disadvantages

The first disadvantage of the proposed methodology is the lack of scale definition, which is inherited by the triangulation method. There are numerous solutions to this problem, depending on the exact application and the required precision. In all the micro-triangulation networks examined in this study, the least-squares solution was constrained by the coordinates of a set of targets. For the fiducialization application the coordinates were provided by the CMM measurements, with a precision at the level of a micrometre or better, while for the alignment application the coordinates were provided by the laser tracker measurements, with a precision at the level of approximately 5 µm.

The second disadvantage of the proposed methodology is relevant to the employed QDaedalus measuring system, which could be better described as a research product than as an industrial product. The fields of Surveying and Large-Scale metrology have already entered into the era of high-automation processes with instrumentation that increasingly follows the *plug-and-play* philosophy. On the contrary, the employed Qdaedalus measuring system requires a great amount of time and effort for the installation and the configuration of the user-defined parameters for the measurements. Moreover, a significant level of expertise is required in order to fully exploit the potential precision of the system. As a consequence, the system is currently more suitable for permanent configurations, e.g., in applications that a large amount of similar objects has to be sequentially measured.

7.5 Proposed improvements

Based on the experience gained during this study, we propose a few improvements in order to both increase the versatility of the proposed methodology and upgrade the QDaedalus measuring system to become more user-friendly, more efficient, more reliable, and potentially, more precise.

The initial aim of this study was to validate the proposed metrology solution only for the fiducialization process. Therefore, the mathematical model that describes the angle observations to the wire and the accompanied least-squares adjustment software were developed without modeling or applying corrections for the atmospheric refraction and the Earth's curvature. This decision was taken due to the small working volume. However, the successful validation of the proposed methodology for alignment applications, which are typically extended in much larger working volumes, demand a more complete approach that will improve the quality of the micro-triangulation network, especially in the vertical direction.

Moreover, given the fact that the scale can be inserted in the adjustment in the form of distance observations or in the form of physical constraints, it would be a useful improvement for the software to be able to handle this information. In addition, the mathematical model and the software could be expanded with the observation equation of a distance measurement to the wire, although such a measurement is not currently feasible in the sense of a trilateration network, at the best of our knowledge. The parameterization of this observation equation should be similar to that already developed in this study in order to tackle the problem of the non-corresponding measured points on the wire.

Interesting would also be a research and development study for the parameterization of observation equations that describe a wire that is stretched in a non-homogeneous gravity field. This development might be proved useful for extremely long stretched wires, especially in alignment applications for linear accelerators and colliders.

Several software upgrades can improve the overall performance of the QDaedalus measuring system. Firstly, an automated adjustment of the contrast between the wire and it background will optimize the exposure time for each shot. This upgrade will reduce the duration of the acquisition and it will simplify the parameters configuration of the measurements by eliminating two user-defined parameters: the shutter speed and the sensor gain. Secondly, the development of an algorithm that is able to automatically control the number of the acquired repeated observations will also reduce the duration of the acquisition. The new algorithm could be based on user-defined criteria such as the minimum number of required measurements and the maximum permissible standard deviation of the pixel detection. Lastly, an auto-focus algorithm, in cooperation with the existing distance-to-focus function, will provide images that are always in focus and, at the same time, it will facilitate the parameters configuration of the measurements by eliminating the current focusing process.

The last and certainly most important improvement to be considered for the near future is the development of an illumination system that could consist of either multiple light sources spread around the object to be measured or a light source that is approximately coaxial to the optical axis of the theodolite. Such a development will definitely improve the precision of the angle observations both, by mitigating potential biases of the observations that are caused by changes in the light conditions, and by optimizing the acquisition parameters, resulting in very fast measurements.

Bibliography

Aicheler, M., et al. (2012), A Multi-TeV Linear Collider Based on CLIC Technology: CLIC Conceptual Design Report, *Tech. Rep. CERN-2012-007. SLAC-R-985. KEK-Report-2012-1. PSI-12-01. JAI-2012-001*, CERN, Geneva, Switzerland.

Arpaia, P., D. Caiazza, C. Petrone, and S. Russenschuck (2015), Performance of the Stretched- and Vibrating-Wire Techniques and Correction of Background Fields in Locating Quadrupole Magnetic Axes, in *XXI IMEKO World Congress "Measurement in Research and Industry", Prague, Czech Republic, August 30–September 4, 2015.*

Artoos, K., M. Modena, and H. Mainaud Durand (2013), CLIC Quadrupole Module final report, *Tech. Rep. EuCARD-REP-2013-019*, CERN.

Becker, F., W. Coosemans, R. Pittin, and I. H. Wilson (2003), An Active Pre-Alignment System and Metrology Network for CLIC, *Tech. Rep. CERN-OPEN-2003-011*, CERN, Geneva, Switzerland.

Behrens, A., D. Mergelkuhl, and C. Vendeuvre (2016), Evaluation of Streched Wire Measurement Based on Photogrammetry in the Context of CERN, in *14th International Workshop on Accelerator Alignment, ESRF, Grenoble, France, October 3–7, 2016.*

Berry, D. W. (1961), Precise Surveying in the Construction of "Nimrod"—the 7 GeV Proton Synchrotron, *Land surveying and mining surveying*, pp. 566–574.

Bestmann, P., J. Bensinger, and K. Hashemi (2010), Validation of an optical WPS system, in *11th International Workshop on Accelerator Alignment, DESY, Hamburg, Germany, September 13–17, 2010.*

Boland, M. J., et al. (2016), Updated baseline for a staged Compact Linear Collider, *Tech. Rep. CERN-2016-004*, CERN, Geneva, Switzerland.

Bottura, L., M. Buzio, S. Pauletta, and N. Smirnov (2006), Measurement of magnetic axis in accelerator magnets: Critical comparison of methods and instruments, in *23rd IEEE Instrumentation and Measurement Technology Conference (IMTC 2006), Sorrento, Italy, April 24–27, 2006*, pp. 765–770, doi:10.1109/IMTC.2006.328154.

Breed, C., A. Bone, and B. Barry (1971), *Surveying*, vol. III, 3rd ed., Wiley.

Brüning, O. S., P. Collier, P. Lebrun, S. Myers, R. Ostojic, J. Poole, and P. Proudlock (2004), LHC Design Report, *Tech. Rep. CERN-2004-003-V-2*, CERN, Geneva, Switzerland.

Budagov, J., V. Glagolev, M. Lyablin, G. Shirkov, H. Mainaud Durand, and G. Stern (2014), A laser based fiducial line for high precision multipoint alignment system, *Physics of Particles and Nuclei Letters*, *11*(3), 286–293, doi:10.1134/S1547477114030042.

Bürki, B., S. Guillaume, P. Sorber, and H. P. Oesch (2010), DAEDALUS: A versatile usable digital clip-on measuring system for Total Stations, in *International conference on Indoor Positioning and Indoor Navigation, Zurich, Switzerland, September 15-–17, 2010*, pp. 1–10, doi:10.1109/IPIN.2010.5646270.

Caiazza, D. (2017), Metrological performance enhancement of wire methods for magnetic field measurements in particle accelerators, Ph.D. thesis, University of Sannio, Benevento.

Caiazza, D., N. Catalan Lasheras, H. Mainaud Durand, M. Modena, C. Sanz, D. Tshilumba, V. Vlachakis, M. Wendt, and S. Zorzetti (2017), New solution for the high accuracy alignment of accelerator components, *Phys. Rev. Accel. Beams*, *20*(8), doi:10.1103/PhysRevAccelBeams.20.083501.

Candamo, J., and D. Goldgof (2008), Wire detection in low-altitude, urban, and low-quality video frames, in *2008 19th International Conference on Pattern Recognition*, pp. 1–4, doi:10.1109/ICPR.2008.4761566.

Candamo, J., R. Kasturi, D. Goldgof, and S. Sarkar (2009), Detection of Thin Lines using Low-Quality Video from Low-Altitude Aircraft in Urban Settings, *IEEE Transactions on Aerospace and Electronic Systems*, *45*(3), 937–949, doi:10.1109/TAES.2009.5259175.

Chan, T.-O., and D. D. Lichti (2011), 3D catenary curve fitting for geometric calibration, *ISPRS - International Archives of the Photogrammetry, Remote Sensing and Spatial Information Sciences*, *XXXVIII-5/W12*, 259–264, doi:10.5194/isprsarchives-XXXVIII-5-W12-259-2011.

Chan, T. O., D. D. Lichti, and C. L. Glennie (2013), Multi-feature based boresight self-calibration of a terrestrial mobile mapping system, *ISPRS Journal of Photogrammetry and Remote Sensing*, *82*, 112–124, doi:10.1016/j.isprsjprs.2013.04.005.

Charalampous, E., et al. (2015), Measuring sub-mm structural displacements using QDaedalus: a digital clip-on measuring system developed for total stations, *Applied Geomatics*, *7*(2), 91–101, doi:10.1007/s12518-014-0150-z.

Clerc, J. (2015), Automated measurement of passive targets for dam monitoring using an image-assisted theodolite, Master's thesis, ETH Zurich.

CLIC (2017), CLIC accelerator footprint, (OPEN-PHO-ACCEL-2017-027).

CLIC@CERN (2018), CLIC accelerator, `http://clicdp.web.cern.ch/content/clic-accelerator`, accessed: 2018-06-20.

Crandall, C. (1906), *Text-Book on Geodesy and Least Squares*, Sobert Drummond, New York, reprint from the collection of the University of Michigan Library.

Dermanis, A. (1986), *Adjustment of Observations and Estimation Theory. Volume 1*, vol. 1, Ziti Publications, in Greek.

Dermanis, A. (1987), *Adjustment of Observations and Estimation Theory. Volume 2*, vol. 2, Ziti Publications, in Greek.

Duquenne, M., et al. (2014), Determination of the Magnetic Axis of a CLIC Drive Beam Quadrupole with respect to External Alignment Targets using a Combination of WPS, CMM and Laser Tracker Measurements, in *5^{th} International Particle Accelerator Conference, Dresden, Germany, June 15–20, 2014*.

Farkhondeh, M., S. P. Holmberg, W. W. Sapp, and J. D. Zumbro (1991), Fiducialization of Magnets for the MIT-Bates SHR, in *14^{th} IEEE Particle Accelerator Conference, San Francisco, CA, USA, May 6–9, 1991*, pp. 634–636, doi:10.1109PAC.1991.164387.

Flesia, A. G., G. Ames, G. Bergues, L. Canali, and C. Schurrer (2014), Sub-pixel straight lines detection for measuring through machine vision, in *2014 IEEE International Instrumentation and Measurement Technology Conference (I2MTC) Proceedings*, pp. 402–406, doi:10.1109/I2MTC.2014.6860776.

Franceschini, F., M. Galetto, D. Maisano, L. Mastrogiacomo, and B. Pralio (2011), *Distributed Large-Scale Dimensional Metrology: New Insights*, SpringerLink: Bücher, Springer London.

Frangez, V., U. Kälin, M. Xiao, and Y. Xu (2017), Determination of High-Precise Heights, *Tech. rep.*, CERN & ETH Zurich, report for the Geodetic Project Course.

Fu, L., and S. Lu (2011), Obstacle detection algorithms for aviation, in *2011 IEEE International Conference on Computer Science and Automation Engineering*, vol. 4, pp. 710–714, doi:10.1109/CSAE.2011.5952944.

Fuchs, J.-F., V. Rude, M. Duquenne, C. Vendeuvre, and V. Vlachakis (2018), Validation of Wire Measurements in the LHC Tunnel, in *15^{th} International Workshop on Accelerator Alignment, Fermi National Accelerator Laboratory, Batavia, IL, USA, October 8–12, 2018*.

Geraldes, R., R. J. Leão, G. Cernicchiaro, R. T. Neuenschwander, J. F. Citadini, and A. R. D. Rodrigues (2016), New sensor and non-contact geometrical survey for the vibrating wire technique, *Nuclear Instruments and Methods in Physics Research Section A: Accelerators, Spectrometers, Detectors and Associated Equipment*, *811*, 115–123, doi:10.1016/j.nima.2015.12.016.

Ghilani, C. (2010), *Adjustment Computations: Spatial Data Analysis*, 5^{th} ed., John Wiley & Sons.

Gonzalez, R., and R. Woods (2008), *Digital Image Processing*, Pearson/Prentice Hall.

Griffet, S. (2010), Literature Review of Fiducialization Methods and Pre-alignment of Components on a Common Support, *Tech. Rep. EDMS 1096102 v.1*, CERN, Geneva, Switzerland.

Griffet, S. (2012), Inter-comparaison par des mesures sur la maquette CLIC TM0: Micro-Triangulation et Laser Tracker AT401, *Tech. Rep. EDMS 1177171 v.1*, CERN, Geneva, Switzerland.

Guelch, E. (1995), Line photogrammetry: a tool for precise localization of 3D points and lines in automated object reconstruction, in *Integrating Photogrammetric Techniques with Scene Analysis and Machine Vision II*, vol. 2486, pp. 2–12, doi:10.1117/12.213108.

Guillaume, S. (2015), Determination of a Precise Gravity Field for the CLIC Feasibility Studies, Ph.D. thesis, ETH Zurich.

Guillaume, S. (2018), *Geodetic Network and Parameter Estimation*, Lecture notes, Institute of Geodesy and Photogrammetry, ETH Zurich.

Guillaume, S., B. Bürki, S. Griffet, and H. Mainaud Durand (2012), QDaedalus: Augmentation of Total Stations by CCD Sensor for Automated Contactless High-Precision Metrology, in *FIG Working Week, Rome, Italy, May 6–11, 2012*.

Guillaume, S., B. Burki, and J. Clerc (2015), *QDaedalus: Digital Clip-on Measuring System for Total Stations*, Geodesy and Geodynamics Laboratory, ETH Zurich, user's manual.

Guillaume, S., J. Clerc, C. Leyder, J. Ray, and M. Kistler (2016a), Contribution of the Image-Assisted Theodolite System QDaedalus to Geodetic Static and Dynamic Deformation Monitoring, in *3^{rd} Joint International Symposium on Deformation Monitoring, Vienna, Austria, March 30–April 1, 2016*.

Guillaume, S., A. Geiger, and M. Scaramuzza (2016b), Automated High Precision Optical Tracking of Aircrafts and non-cooperative Flying Objects, in *29^{th} International Technical Meeting of the Satellite Division of The Institute of Navigation, Portland, OR, USA, September 12–16, 2016*, pp. 2315–2317, doi:https://doi.org/10.33012/2016.14604.

Hartley, R., and A. Zisserman (2004), *Multiple View Geometry in Computer Vision*, 2^{nd} ed., Cambridge University Press.

Hatibovic, A. (2014), Derivation of Equations for Conductor and Sag Curves of an Overhead Line Based on a Given Catenary Constant, *Periodica Polytechnica Electrical Engineering and Computer Science*, *58*(1), 23–27, doi:10.3311/PPee.6993.

Hauk, M., C. Hirt, and C. Ackermann (2017), Experiences with the QDaedalus system for astrogeodetic determination of deflections of the vertical, *Survey Review*, *49*(355), 294–301, doi:10.1080/00396265.2016.1171960.

Hauth, S., M. Schlüter, and F. Thiery (2012), Modular Imaging Total Stations—Sensor Fusion for high precision alignment, in *3^{rd} International Conference on Machine Control & Guidance, Stuttgart, Germany, March 27–29, 2012*, pp. 202–210.

Herty, A., H. Mainaud Durand, and A. Marin (2004), Test and Calibration Facility for HLS and WPS Sensor, in *8^{th} International Workshop on Accelerator Alignment, CERN, Geneva, Switzerland, October 4–7, 2004*.

HEXAGON (2011), *Leitz CMM Technical Data – Overview*, HEXAGON Manufacturing Intelligence, product brochure.

HEXAGON (2015), *PRECITEC LR Optical sensor for ultra-precision surfaces*, HEXAGON Manufacturing Intelligence, product brochure.

Hirt, C., S. Guillaume, A. Wisbar, B. Bürki, and H. Sternberg (2010), Monitoring of the refraction coefficient in the lower atmosphere using a controlled setup of simultaneous reciprocal vertical angle measurements, *Journal of Geophysical Research: Atmospheres*, *115*(D21), doi:10.1029/2010JD014067.

Holland, P. W., and R. E. Welsch (1977), Robust regression using iteratively reweighted least-squares, *Communications in Statistics - Theory and Methods*, *6*(9), 813–827, doi:10.1080/03610927708827533.

Hopping, J. N., and D. D. Jacobus (1967), Precision surveying in radioactive areas with tv camera on a theodolite, in *Annual Meeting of the American Society of Mechanical Engineers, Pittsburgh, PA, USA, November 12–17, 1967*.

Huang, L., R. Xie, and Y. Xu (2015), Invasion detection on transmission lines using saliency computation, in *2015 IEEE International Symposium on Signal Processing and Information Technology (ISSPIT)*, pp. 320–325, doi:10.1109/ISSPIT.2015.7394352.

Hugon, P. (2010), Études des méthodes optiques et méca-niques pour le transfert du réseau géodésique en surface au réseau sou-terrain, dans le cadre du projet CLIC au CERN, Master's thesis, Institut National des Sciences Appliquées de Strasbourg (INSA).

Hübscher, F., B. Kramis, and R. Pott (2017), Water tower 3D-Movements & Vertical height transfer, *Tech. rep.*, CERN & ETH Zurich, report for the Geodetic Project Course.

Ingensand, H., and S. Kyle (1992), Modern survey techniques, in *CAS – CERN Accelerator School: Specialised course on Magnets: Magnetic measurement and alignment, Montreux, Switzerland, March 16–20, 1992*, pp. 296–319, doi:10.5170/CERN-1992-005.296.

Ishikawa, K., S. Ono, J. ichi Takiguchi, Y. Amano, and T. Hashizume (2009), Aerial cable localization and managemAerial cable localization and management using a mobile mapping system, in *2009 ICCAS-SICE*, pp. 2491–2495.

ISO 10360-2 (2001), Geometrical Product Specifications (GPS) — Acceptance and reverification tests for coordinate measuring machines (CMM) — Part 2: CMMs used for measuring size, *ISO 10360-2:2001*, International Organization for Standardization, Geneva, Switzerland.

ISO 17123-3 (2001), Optics and optical instruments – Field procedures for testing geodetic and surveying instruments – Part 3: Theodolites, *ISO 17123-3:2001*, International Organization for Standardization, Geneva, Switzerland.

ISO 3290-1 (2001), Rolling bearings — Balls — Dimensions and tolerances, *ISO 3290:2001*, International Organization for Standardization, Geneva, Switzerland.

ISR@CERN (2018), The intersecting storage rings, `https://home.cern/science/accelerators/intersecting-storage-rings`, accessed: 2018-09-30.

Jain, A., M. Anerella, G. Ganetis, P. He, P. Joshi, P. Kovach, S. Plate, S. J., and A. Temnykh (2008), Vibrating Wire R&D for Alignment of Multipole Magnets in NSLS-II, in *10^{th} International Workshop on Accelerator Alignment, KEK, Tsukuba, Japan, February 11–15, 2008*.

Jones, M. (2000), Geodetic Definition (Datum Parameters) of the CERN Coordinate System, *Tech. Rep. EDMS 107981 v.1*, CERN, Geneva, Switzerland.

Jwa, Y., G. Sohn, and H. Kim (2009), Automatic 3D Powerline Reconstruction Using Airborne LIDAR Data, *ISPRS - International Archives of the Photogrammetry, Remote Sensing and Spatial Information Sciences*, *XXXVIII-3/W8*, 105–110.

Kamugasa, S. W. (2018), Development and Validation of a Frequency Scanning Interferometry Network for Compact Linear Collider Component Fiducialization, Ph.D. thesis, ETH Zurich.

Kleeven, W. J. G. M., J. I. M. Botman, J. L. Delhez, H. L. Hagedoorn, C. J. Timmermans, and G. A. Webers (1993), Emittance Growth in Nonlinear Beam Guiding and Focusing Elements, in *13^{th} International Conference on Cyclotrons and their Applications, Vancouver, BC, Canada, July 6–10, 1992*, pp. 384–387.

Knoblach, S. (2009), Entwicklung, Kalibrierung und Erprobung eines kameraunterstützten Hängetachymeters, Ph.D. thesis, Technische Universität Dresden.

Le Bec, G. (2016), Advances on magnetic measurements by stretched wires at the ESRF, in *2^{nd} PACMAN Workshop, Debrecen, Hungary, June 13–15, 2016*.

Lehmann, R. (2013), 3σ-Rule for Outlier Detection from the Viewpoint of Geodetic Adjustment, *Journal of Surveying Engineering*, *139*(4), 157–165, doi:10.1061/(ASCE)SU.1943-5428.0000112.

LEICA (2002), *Leica Industrial Theodolites and Total Stations - TPS5000 Instruments*, LEICA Geosystems AG, product brochure.

Leão, R. J., C. R. Baldo, M. L. Reis, J. L. Trabanco, F. Rodrigues, and R. T. Neuenschwander (2017), Magnet alignment on a common girder: Development of a length artefact for measurement accuracy improvement, *Precision Engineering*, *50*, 53–62, doi:10.1016/j.precisioneng.2017.04.013.

Luhmann, T., S. Robson, S. Kyle, and J. Boehm (2014), *Close-Range Photogrammetry and 3D Imaging*, De Gruyter Textbook, 2^{nd} ed., De Gruyter.

Mainaud Durand, H. (2004a), The CLIC Alignment Studies: Past, Present and Future, in *8^{th} International Workshop on Accelerator Alignment, CERN, Geneva, Switzerland, October 4–7, 2004*.

Mainaud Durand, H. (2004b), Micrometric alignment metrology: means, developments and applications, *Tech. Rep. TS-Note-2004-038*, CERN, Geneva, Switzerland.

Mainaud Durand, H., and T. Touzé (2006), The Active Prealignment of the CLIC Components, in *9th International Workshop on Accelerator Alignment, Stanford, CA, USA, September 26–29, 2006*.

Mainaud Durand, H., T. Touzé, S. Griffet, J. Kemppinen, and F. Lackner (2010), CLIC active pre-alignment system: proposal for CDR and program for TDR, in *11th International Workshop on Accelerator Alignment, DESY, Hamburg, Germany, September 13–17, 2010*.

Mainaud Durand, H., M. Anastasopoulos, N. Chritin, S. Griffet, J. Kemppinen, M. Sosin, and T. Touzé (2011), Theoretical and practical feasibility demonstration of a micrometric remotely controlled pre-alignment system for the CLIC linear collider, in *2nd International Particle Accelerator Conference, San Sebastian, Spain, September 4–9, 2011*, pp. 547–549.

Mainaud Durand, H., M. Duquenne, J. Sandomierski, M. Sosin, and V. Rude (2014), Drive Beam Quadrupoles for the CLIC Project: a Novel Method of Fiducialisation and a New Micrometric Adjustment System, in *13th International Workshop on Accelerator Alignment, Beijing, China, October 13–17, 2014*.

Mainaud Durand, H., et al. (2015), Status of the PACMAN Project, in *4th International Beam Instrumentation Conference, Melbourne, Australia, September 13–17, 2015*, doi: 10.18429/JACoW-IBIC2015-TUPB062.

Mainaud Durand, H., et al. (2017), Main Achievements of the PACMAN Project for the Alignment at Micrometric Scale of Accelerator Components, in *8th International Particle Accelerator Conference, Copenhagen, Denmark, May 14–19, 2017*, doi: 10.18429/JACoW-IPAC2017-TUPIK077.

Mayoud, M. (1987), Geodetic metrology of particle accelerators and physics equipment, in *2nd Industrial and Engineering Survey Conference, London, UK, September 2–4, 1987*, pp. 1–15.

McLaughlin, R. A. (2006), Extracting transmission lines from airborne LIDAR data, *IEEE Geoscience and Remote Sensing Letters*, *3*(2), 222–226, doi:10.1109/LGRS.2005.863390.

Mergelkuhl, D., S. Missiaen, C. Vendeuvre, and S. Lapardhaja (2018), Recent developments for a photogrammetric system to measure offsets to stretched wires at CERN, in *15th International Workshop on Accelerator Alignment, Fermi National Accelerator Laboratory, Batavia, IL, USA, October 8–12, 2018*.

Mikhail, E., and F. Ackermann (1976), *Observations and least squares*, IEP series in civil engineering, IEP.

Mikhail, E., and G. Gracie (1981), *Analysis and adjustment of survey measurements*, Van Nostrand Reinhold Co.

Molnár, B. (2010), Direct linear transformation based photogrammetry software on the web, *ISPRS - International Archives of the Photogrammetry, Remote Sensing and Spatial Information Sciences*, *XXXVIII-5*, 462–465.

Mulawa, D., and E. Mikhail (1988), Photogrammetric Treatment of Linear Features, *ISPRS - International Archives of the Photogrammetry, Remote Sensing and Spatial Information Sciences*, *Volume XXVII Part B3*, 383–394.

Neff, P. (2016), Automated high precision optical tracking of flying objects, Master's thesis, ETH Zurich.

Nixon, M., and R. Loveland (2005), Passive power line detection system for aircraft, Google Patents, US Patent 6,940,994.

Nüssli, T., and R. Salzgeber (2015), Automated high precision optical aircraft tracking, Master's thesis, ETH Zurich.

Ogundare, J. (2016), *Precision Surveying: The Principles and Geomatics Practice*, EBL-Schweitzer, Wiley.

PACMAN@CERN (2018), PACMAN Innovative Doctoral Program, `https://pacman.web.cern.ch/`, accessed: 2018-06-20.

Petrone, C. (2013), Wire methods for measuring field harmonics, gradients and magnetic axes in accelerator magnets, Ph.D. thesis, University of Sannio, Benevento.

Quesnel, J.-P., H. Mainaud Durand, and T. Touzé (2008), Stretched Wire Offset Measurements: 40 Years of Practice of This Technique at CERN, in *10th International Workshop on Accelerator Alignment, KEK, Tsukuba, Japan, February 11–15, 2008.*

Sanders-Reed, J. N., D. J. Yelton, C. C. Witt, and R. R. Galetti (2009), Passive obstacle detection system (PODS) for wire detection, in *Enhanced and Synthetic Vision 2009*, vol. 7328, pp. 33–44, doi:10.1117/12.815543.

Sanz, C., A. Cherif, H. Mainaud Durand, P. Morantz, and P. Shore (2015), Characterisation and measurement to the sub-micron scale of a reference wire position, in *17^{e} Congrès International de Métrologie, Paris, France, September 21–24, 2015*, CERN-ACC-2015-0075.

Schmid, M., M. Wanner, and M. Manyoky (2010), Suitability of the Daedalus system for Micro-triangulation, *Tech. rep.*, CERN & ETH Zurich, report for the Geodetic Project Course.

Silverman, B. (1986), Wire and wire like object detection system, Google Patents, US Patent 4,572,662.

Sinha, P. (2012), *Image Acquisition and Preprocessing for Machine Vision Systems*, SPIE Press.

Song, B., and X. Li (2014), Power line detection from optical images, *Neurocomputing*, *129*, 350–361, doi:10.1016/j.neucom.2013.09.023.

Sonka, M., V. Hlavac, and R. Boyle (2014), *Image Processing, Analysis, and Machine Vision*, Cengage Learning.

Stern, G. (2016), Study and development of a laser based alignment system for the compact linear collider, Ph.D. thesis, ETH Zurich.

Tan, W. (2005), Inner constraints for 3-D survey networks, *Journal of Spatial Science*, *50*(1), 91–94, doi:10.1080/14498596.2005.9635040.

Temnykh, A. (1997), Vibrating wire field-measuring technique, *Nuclear Instruments and Methods in Physics Research Section A: Accelerators, Spectrometers, Detectors and Associated Equipment*, *399*(2), 185–194, doi:https://doi.org/10.1016/S0168-9002(97) 00972-8.

Teunissen, P. (2000), *Adjustment Theory: An Introduction*, Series on mathematical geodesy and positioning, Delft University Press.

Teunissen, P. (2006), *Network Quality Control*, Series on mathematical geodesy and positioning, VSSD.

Torge, W., and J. Müller (2012), *Geodesy*, De Gruyter Textbook, 4^{th} ed., De Gruyter.

Touzé, T. (2011), Proposition d'une méthode d'alignement de l'accélérateur linéaire CLIC, Ph.D. thesis, Paris-Est U.

Tóth, G., and l. Völgyesi (2016),), Data Processing of QDaedalus Measurements, *Geosciences and Engineering*, *5*(8), 149–166.

van Heijningen, J. (2012), Precision Improvement in Optical Alignment Systems of Linear Colliders, Master's thesis, Delft University of Technology (TUDelft).

Vlachakis, V., and J.-F. Fuchs (2018), Validation of micro-triangulation with direct wire measurements in the LHC tunnel, in *15^{th} International Workshop on Accelerator Alignment, Fermi National Accelerator Laboratory, Batavia, IL, USA, October 8–12, 2018.*

Vlachakis, V., J.-F. Fuchs, and H. Mainaud Durand (2016), Recent development of micro-triangulation for magnet fiducialisation, in *14^{th} International Workshop on Accelerator Alignment, European Synchrotron Radiation Facility, Grenoble, France, October 3–7, 2016*, CERN-ACC-NOTE-2016-0068.

Vorozhtsov, A., and M. Modena (2011), Design and Manufacture of a Main Beam Quadrupole Model for CLIC, in *22^{nd} International Conference on Magnet Technology, Marseille, France, September 12–16, 2011.*

Vranković, V., C. Wouters, S. Sidorov, P. Chevtsov, R. Deckardt, M. Emmenegger, M. Dach, and S. Sanfilippo (2014), A Method for the Submicrometer Accuracy Determination of Quadrupole Magnetic Axis, *IEEE Transactions on Applied Superconductivity*, *24*(3), doi:10.1109/TASC.2013.2290995.

Wagner, A. (2017), New Geodetic Monitoring Approaches using Image Assisted Total Stations, Ph.D. thesis, Technical University of Munich.

Walckiers, L. (2011), Magnetic measurement with coils and wires, in *CAS – CERN Accelerator School: Specialised course on Magnets: Bruges, Belgium, June 16–25, 2009*, doi:10.5170/CERN-2010-004.357.

Wiedemann, H. (2007), *Particle Accelerator Physics*, SpringerLink: Springer e-Books, 3^{rd} ed., Springer Berlin Heidelberg.

Wille, K., and J. McFall (2000), *The Physics of Particle Accelerators: An Introduction*, Oxford University Press.

Wilson, R. (1971), *Land Surveying*, The M & E handbook series, Macdonald & Evans.

Wolf, Z. (2005), A Vibrating Wire System For Quadrupole Fiducialization, *Tech. Rep. SLAC-TN-10-087. LCLS-TN-05-11*, SLAC National Accelerator Lab., Menlo Park, CA, USA.

Wouters, C., M. Calvi, V. Vranković, S. Sidorov, and S. Sanfilippo (2012), Vibrating Wire Technique and Phase Lock Loop for Finding the Magnetic Axis of Quadrupoles, *IEEE Transactions on Applied Superconductivity*, *22*(3), doi:10.1109/TASC.2011.2178015.

Yu, C., S. Sharma, M. Ilardo, and M. Ke (2018), Fiducialization Precision of Mechanical Method, in *15^{th} International Workshop on Accelerator Alignment, Fermi National Accelerator Laboratory, Batavia, IL, USA, October 8–12, 2018.*

Zeiske, K. (2004), *Surveying made easy*, LEICA Geosystems AG, user's guide.

Zhang, C., C. Mitsuda1, and K. Kajimoto (2016), An Eigenfrequency Wire Alignment System under Development for Magnet Fiducialization, in *14^{th} International Workshop on Accelerator Alignment, ESRF, Grenoble, France, October 3–7, 2016.*

Zhu, Z., Y. Yuan, and X. Zhang (2011), Theodolite-camera videometrics system based on total station, in *International Symposium on Photoelectronic Detection and Imaging 2011: Advances in Imaging Detectors and Applications, Beijing, China, May 24–26, 2011*, vol. 8194, doi:10.1117/12.900859.

Zielinski, H. (1993), Object Reconstruction with Digital Line Photogrammetry, Ph.D. thesis, Royal Institute of Geodesy and Photogrammetry Stockholm.

Appendix A

Source code of the wire detection algorithm

This appendix contains the course code of the wire detection algorithm. The algorithm has been developed in the *Qt* environment, using the *C++* programming language and the open-source computer-vision library *OpenCV*. The source code is divided into three sections: the data structure declaration and function prototyping in Section A.1, the wire detection algorithm in Section A.2, and the robust 2D line fitting algorithm in Section A.3. The algorithm is described in detail in Chapter 2 and especially in Sections 2.3 and 2.4. The performance evaluation of the developed algorithm is presented in Chapter 3.

A.1 Data structure declaration and function prototyping

```
// *** START DATA STRUCTURE DECLARATION *** //

    // 2D parametric line data structure
    typedef struct
    {
        double x;   // x coordinate of a point on the line (in pixels)
        double y;   // y coordinate of a point on the line (in pixels)
        double nX;  // x component of the unit vector of the line
        double nY;  // y component of the unit vector of the line
        double npX; // x component of the perpendicular to the line unit vector
        double npY; // y component of the perpendicular to the line unit vector
    } parametric2DLine;

    // User parameters data structure
    typedef struct
    {
        int minEdgePnts;    // minimum number of points participating to the line fit
        int halfWidthROI;   // half-width of the region of interest (ROI) (in pixels)
        int halfHeightROI;  // half-height of the region of interest (ROI) (in pixels)
        double maxResidual; // maximum permissible residual for the line fit (in pixels)
        int cannyThreshold; // Canny edge detector high threshold [0-255]
    } userParameters;

    // Wire data structure
    typedef struct
    {
        parametric2DLine coarseLine;   // coarse line
        parametric2DLine positiveLine; // positive line
        parametric2DLine negativeLine; // negative line
        parametric2DLine fineLine;     // fine line
        int coarsePnts;                // number of edge points of the coarse line
        int positivePnts;              // number of edge points of the positive line
        int negativePnts;              // number of edge points of the negative line
        double wireWidth;              // width of the wire in the region of the detection (in pixels)
    } wireDetectionData;

// *** END DATA STRUCTURE DECLARATION *** //


// *** START FUNCTION PROTOTYPING *** //

    // Function to detect and measure the position of the wire in the image
    bool wireDetection(IplImage* imgInput,      // imgInput: input/output raw wire image
                       userParameters param,    // param:    input user parameters
                       wireDetectionData* wire, // wire:     output computed wire data
                       IplImage** imgCanny);    // imgCanny: output canny edge image

    // Function to robust fit a 2D line
    bool robustFit2DLine(int minEdgePnts,
                         int maxResidual,
                         parametric2DLine* line,
                         std::vector<double> *x,
                         std::vector<double> *y);

    // minEdgePnts: input minimum number of points participating to the line fit
    // maxResidual: input maximum permissible residual for the line fit (in pixels)
    // line:        output fitted line parameters
    // x:           input/output x coordinates of the edge points (in pixels)
    // y:           input/output y coordinates of the edge points (in pixels)

// *** END FUNCTION PROTOTYPING *** //
```

A.2 Wire detection algorithm

```
// Function to detect and measure the position of the wire in the image
bool PilotOpenCV::wireDetection(IplImage* imgInput, userParameters userParam, wireDetectionData* wire,
     IplImage** imgCanny)
{

// *** START VARIABLE DECLARATION *** //

    // centre of image x, y coordinates
    int imgCenterX = 0;
    int imgCenterY = 0;

    CvRect ROI;                  // region of interest (x, y, width, height)
    IplImage* imgEdges;          // image that accommodates the Canny edges
    CvScalar scTemp;             // used to store the edge pixel intensity value (=255).

```

```
    // data structure for the coarse line
    parametric2DLine* coarseLine = new parametric2DLine();
    std::vector<double> initX;   // vector of x component of the coarse line edge points
    std::vector<double> initY;   // vector of y component of the coarse line edge points

    // data structure for the positive line
    parametric2DLine* posLine = new parametric2DLine();
    std::vector<double> posX;    // vector of x component of the positive line edge points
    std::vector<double> posY;    // vector of y component of the positive line edge points

    // data structure for the negative line
    parametric2DLine* negLine = new parametric2DLine();
    std::vector<double> negX;    // vector of x component of the negative line edge points
    std::vector<double> negY;    // vector of y component of the negative line edge points

    // data structure for the fine line
    parametric2DLine* fineLine = new parametric2DLine();

    //bool robustFit2DLineReturn;  // boolean to check if robust line fit succeded

    double bisVectX = 0;              // x component of the bisector vector
    double bisVectY = 0;              // y component of the bisector vector
    double bisVectN = 0;              // norm of the bisector vector
    double negInterPntX = 0;          // x component of a point on the negative line
    double negInterPntY = 0;          // y component of a point on the negative line
    double posInterPntX = 0;          // x component of a point on the positive line
    double posInterPntY = 0;          // y component of a point on the positive line

    // matrices to be used in the fine lime position
    CvMat* sysMat = cvCreateMat(2, 2, CV_64FC1);
    CvMat* sysMatInv = cvCreateMat(2, 2, CV_64FC1);
    CvMat* sysVect = cvCreateMat(2, 1, CV_64FC1);
    CvMat* solVect = cvCreateMat(2, 1, CV_64FC1);

// *** END VARIABLE DECLARATION *** //


// *** START ROI CALCULATION *** //

    // calculate the center point of the image
    imgCenterX = (int)imgInput->width/2;
    imgCenterY = (int)imgInput->height/2;

    // calculate the ROI (CvRect)
    ROI.x = imgCenterX - userParam.halfWidthROI;
    ROI.y = imgCenterY - userParam.halfHeightROI;
    ROI.width = 2 * userParam.halfWidthROI;
    ROI.height = 2 * userParam.halfHeightROI;

// *** END ROI CALCULATION *** //


// *** START CANNY EDGE DETECTION *** //

    // create an image for the Canny edges by cloning the input image
    imgEdges = cvCloneImage(imgInput);

    // apply the ROI mask to both raw image and canny edges images
    cvSetImageROI(imgEdges, ROI);
    cvSetImageROI(imgInput, ROI);

    // calculate canny edges image in the ROI according to the canny threshold given by the user
    cvCanny(imgInput, imgEdges, userParam.cannyThreshold, userParam.cannyThreshold/3, 3);

    // remove the ROI mask from the two images for visualisation purposes;
    cvResetImageROI(imgEdges);
    cvResetImageROI(imgInput);

    // copy (clone) the Canny edge image to output for visualisation
    *imgCanny = cvCloneImage(imgEdges);

// *** END CANNY EDGE DETECTION *** //


// *** START EDGE POINT REGISTRATION *** //

    // horizontally scan the ROI for edge points
    for (double i = ROI.x; i < ROI.x + ROI.width; i++)
    {
        // vertically scan the ROI for edge points
        for (double j = ROI.y; j < ROI.y + ROI.height; j++)
        {
            // get pixel intensity
            scTemp = cvGet2D(imgEdges, j, i);

            // if pixel intensity == 255 (white)
            if(scTemp.val[0] == 255)
            {
```

```
                // append pixel coordinates in vectors (initX, initY)
                initX.push_back(i);
                initY.push_back(j);
            }
        }
    }

    // after edge points registation, delete (release) the Canny edge image
    cvReleaseImage(&imgEdges);

// *** END EDGE POINT REGISTRATION *** //


// *** START COARSE LINE ROBUST FIT *** //

    // check if the robust fit of the coarse line is succesful.
    if (robustFit2DLine(userParam.minEdgePnts, userParam.maxResidual, coarseLine, &initX, &initY))
    {
        // if robust fit succeeds, copy data from the line data structure to the wire data structure
        wire->coarseLine.x = coarseLine->x;
        wire->coarseLine.y = coarseLine->y;
        wire->coarseLine.nX = coarseLine->nX;
        wire->coarseLine.nY = coarseLine->nY;
        wire->coarseLine.npX = coarseLine->npX;
        wire->coarseLine.npY = coarseLine->npY;
        wire->coarsePnts = initX.size();
    }
    else
    {
        // if robust fit fails, exit the function returning false
        return false;
    }

// *** END COARSE LINE ROBUST FIT *** //


// *** START EDGE POINT SEPARATION IN TWO GROUPS *** //

    // loop for the points left after the robust fit
    for (int i = 0; i < initX.size(); i++)
    {
        // check the z-component of the cross-product and separate the points in two groups
        if ((initX[i] - coarseLine->x) * coarseLine->nY - (initY[i] - coarseLine->y) * coarseLine->nX >= 0)
        {
            // if positive, append point coordinates in the positive group
            posX.push_back(initX[i]);
            posY.push_back(initY[i]);
        }
        else
        {
            // if negative, append point coordinates in the negative group
            negX.push_back(initX[i]);
            negY.push_back(initY[i]);
        }
    }

// *** END EDGE POINT SEPARATION IN TWO GROUPS *** //


// *** START POSITIVE LINE ROBUST FIT *** //

    // calculate the positive line
    if (robustFit2DLine(userParam.minEdgePnts, 1, posLine, &posX, &posY))
    {
        // copy data from the line data structure to the wire data structure
        wire->positiveLine.x = posLine->x;
        wire->positiveLine.y = posLine->y;
        wire->positiveLine.nX = posLine->nX;
        wire->positiveLine.nY = posLine->nY;
        wire->positiveLine.npX = posLine->npX;
        wire->positiveLine.npY = posLine->npY;
        wire->positivePnts = posX.size();
    }
    else
    {
        // if robust fit fails, exit the function returning false
        return false;
    }

// *** END POSITIVE LINE ROBUST FIT *** //


// *** START NEGATIVE LINE ROBUST FIT *** //

    // Calculate the negative line
    if (robustFit2DLine(userParam.minEdgePnts, 1, negLine, &negX, &negY))
    {
        // copy data from the line data structure to the wire data structure
```

```
        wire->negativeLine.x = negLine->x;
        wire->negativeLine.y = negLine->y;
        wire->negativeLine.nX = negLine->nX;
        wire->negativeLine.nY = negLine->nY;
        wire->negativeLine.npX = negLine->npX;
        wire->negativeLine.npY = negLine->npY;
        wire->negativePnts = negX.size();
    }
    else
    {
        // if robust fit fails, exit the function returning false
        return false;
    }

// *** END NEGATIVE LINE ROBUST FIT *** //


// *** START FINE LINE VECTOR CALCULATION *** //

    // calculate the x-axis and y-axis components of the bisector vector
    bisVectX = (posLine->nX + negLine->nX);
    bisVectY = (posLine->nY + negLine->nY);

    // calculate the norm of the bisector vector
    bisVectN = sqrt(bisVectX*bisVectX + bisVectY*bisVectY);

    // normalize the bisector vector to become a unit vector
    fineLine->nX = bisVectX/bisVectN;
    fineLine->nY = bisVectY/bisVectN;

    // calculate the perpendicular to the bisector unit vector for further use
    fineLine->npX = -fineLine->nY;
    fineLine->npY = fineLine->nX;

// *** END FINE LINE VECTOR CALCULATION *** //


// *** START POSITIVE LINE INTERSECTION POINT CALCULATION *** //

    // create the matrix of the linear system
    cvmSet(sysMat, 0, 0, fineLine->npX);
    cvmSet(sysMat, 0, 1, -posLine->nX);
    cvmSet(sysMat, 1, 0, fineLine->npY);
    cvmSet(sysMat, 1, 1, -posLine->nY);

    // invert the matrix of the linear system
    cvInvert(sysMat, sysMatInv, CV_LU);

    // create the vector of the linear system
    cvmSet(sysVect, 0, 0, posLine->x - coarseLine->x);
    cvmSet(sysVect, 1, 0, posLine->y - coarseLine->y);

    // multiply the inverted matrix with the vector
    cvGEMM(sysMatInv, sysVect, 1, NULL, 0, solVect);

    // get the necessary parameter
    scTemp = cvGet2D(solVect,1,0);

    // calculate the intersection point on the positive line
    posInterPntX = posLine->x + scTemp.val[0]* posLine->nX;
    posInterPntY = posLine->y + scTemp.val[0]* posLine->nY;

// *** END POSITIVE LINE INTERSECTION POINT CALCULATION *** //


// *** START NEGATIVE LINE INTERSECTION POINT CALCULATION *** //

    // create the matrix of the linear system
    cvmSet(sysMat, 0, 0, fineLine->npX);
    cvmSet(sysMat, 0, 1, -negLine->nX);
    cvmSet(sysMat, 1, 0, fineLine->npY);
    cvmSet(sysMat, 1, 1, -negLine->nY);

    // invert the matrix of the linear system
    cvInvert(sysMat, sysMatInv, CV_LU);

    // create the vector of the linear system
    cvmSet(sysVect, 0, 0, negLine->x - coarseLine->x);
    cvmSet(sysVect, 1, 0, negLine->y - coarseLine->y);

    // multiply the inverted matrix with the vector
    cvGEMM(sysMatInv, sysVect, 1, NULL, 0, solVect);

    // get the necessary parameter
    scTemp = cvGet2D(solVect,1,0);

    // calculate the intersection point on the negative line
    negInterPntX = negLine->x + scTemp.val[0]*negLine->nX;
```

```
    negInterPntY = negLine->y + scTemp.val[0]*negLine->nY;

    // delete (release) matrices
    cvReleaseMat(&sysMat);
    cvReleaseMat(&sysMatInv);
    cvReleaseMat(&sysVect);
    cvReleaseMat(&solVect);

// *** END NEGATIVE LINE INTERSECTION POINT CALCULATION *** //


// *** START FINE LINE POINT CALCULATION *** //

    // Calculate a point on the final line
    // This point belongs to the wire axis and could be concidered as the measurement
    fineLine->x = (posInterPntX + negInterPntX)/2;
    fineLine->y = (posInterPntY + negInterPntY)/2;

    // store values to the fine line data structure
    wire->fineLine.x = fineLine->x;
    wire->fineLine.y = fineLine->y;
    wire->fineLine.nX = fineLine->nX;
    wire->fineLine.nY = fineLine->nY;
    wire->fineLine.npX = fineLine->npX;
    wire->fineLine.npY = fineLine->npY;

    // calculate the width of the wire in pixels
    wire->wireWidth = sqrt(pow(posInterPntX-negInterPntX,2) + pow(posInterPntY-negInterPntY,2));

// *** END FINE LINE POINT CALCULATION *** //

    // if the detection is successful, return true
    return true;
}
```

A.3 Robust 2D line fitting algorithm

```
// Function to robust fit a 2D line
bool PilotOpenCV::robustFit2DLine(int minEdgePnts, int maxResidual, parametric2DLine* line, std::vector<
      double> *x, std::vector<double> *y)
{

// *** START VARIABLE DECLARATION *** //

    // flag indicator for the outlier detection
    bool isRobust = false;

    // temporary coodinates of the edge points in a local frame
    double localX = 0;
    double localY = 0;

    // elements of the covariance matrix
    double cov11 = 0;
    double cov12 = 0;
    double cov22 = 0;

    CvMat* cov = cvCreateMat(2, 2, CV_64FC1);      // covariance matrix
    CvMat* eigVect = cvCreateMat(2, 2, CV_64FC1);  // eigenvector matrix
    CvMat* eigVal = cvCreateMat(2, 1, CV_64FC1);   // eigenvalue vector

    CvScalar scTemp;   // temporary variable to extract values from the matrices

    std::vector<double> dist;                      // vector of distance between each point and the line
    std::vector<double>::iterator maxDist;         // maximum distance for the outlier detection
    int cooToErase;                                // index of the point with the maximum distance

// *** END VARIABLE DECLARATION *** //


    // loop while the fit is robust and the points are more than the user defined value
    while (isRobust == false && x->size() >= minEdgePnts)
    {

// *** START COVARIANCE MATRIX CALCULATION *** //

        // calculate the mean point of best fit line)
        line->x = std::accumulate(x->begin(), x->end(), 0.0);
        line->x = line->x / x->size ();

        line->y = std::accumulate(y->begin(), y->end(), 0.0);
        line->y = line->y / y->size ();

```

```
        // loop for all edge points
        for (int i = 0; i < x->size(); i++)
        {
            // subtract the mean point to set the new coordinate system to (0,0)
            localX = x->at(i) - line->x;
            localY = y->at(i) - line->y;

            // calculate the covariance matrix elements
            cov11 += localX * localX;
            cov12 += localX * localY;
            cov22 += localY * localY;
        }

        // create the covariance matrix
        cvmSet(cov, 0, 0, cov11/(x->size()-1));
        cvmSet(cov, 0, 1, cov12/(x->size()-1));
        cvmSet(cov, 1, 0, cov12/(x->size()-1));
        cvmSet(cov, 1, 1, cov22/(x->size()-1));

// *** END COVARIANCE MATRIX CALCULATION *** //


// *** START EIGENVECTOR CALCULATION *** //

        // calculate the eigenvalues and the eigenvectors (unit vectors of line)
        cvEigenVV(cov, eigVect, eigVal, DBL_EPSILON);

        // store values to the line data structure
        scTemp = cvGet2D(eigVect,0,0);
        line->nX = scTemp.val[0];
        scTemp = cvGet2D(eigVect,0,1);
        line->nY = scTemp.val[0];
        scTemp = cvGet2D(eigVect,1,0);
        line->npX = scTemp.val[0];
        scTemp = cvGet2D(eigVect,1,1);
        line->npY = scTemp.val[0];

// *** END EIGENVECTOR CALCULATION *** //


// *** START OUTLIER DETECTION *** //

        dist.clear();       // initialize the distance vector
        isRobust = true;    // set isRobust flag to true. In case there are outliers it turns to false

        // loop for the number of the edge points
        for (int i = 0; i < x->size(); i++)
        {
            // calculate the distance between the line and each point
            dist.push_back(fabs((x->at(i) - line->x)* line->npX + (y->at(i) - line->y)* line->npY));
        }


        maxDist = std::max_element(dist.begin(), dist.end());  // the maximum distance
        cooToErase = std::distance(dist.begin(),maxDist);      // the index (location) of the point with
             the maximun distance

        // check if the maximum distance is larger than the user defined maximum permissible residual
        if (*maxDist > maxResidual)
        {
            // erase the  point that is detected as outlier
            x->erase(x->begin()+cooToErase);
            y->erase(y->begin()+cooToErase);

            // initialise the line data structure
            line->x = 0;
            line->y = 0;
            line->nX = 0;
            line->nY = 0;
            line->npX = 0;
            line->npY = 0;

            // set the isRobust flag to false in order to repeat the fitting process without the outlier
            isRobust = false;
        }
    }

// *** END OUTLIER DETECTION *** //

    // Release images
    cvReleaseMat(&cov);
    cvReleaseMat(&eigVect);
    cvReleaseMat(&eigVal);

    // if the fit is successful, return true
    return isRobust;
}
```

Appendix B

Confidence intervals and statistical tests for the experimental evaluation of the wire detection and the circle detection algorithms

The theory and the actual formulas used in the analysis of Chapter 3 to compute the confidence intervals and to perform the statistical tests are presented is Section B.1 and Section B.2, respectively. For the experimental evaluation of the *wire detection algorithm* the numerical results of the measurements, the confidence intervals and the statistical tests are listed in the tables in Section B.3. Similarly, the tables in Section B.4 contain the numerical results of the measurements, the confidence intervals and the statistical tests for the experimental evaluation of the *circle detection algorithm*.

B.1 Confidence intervals

Assuming that the reduced angle observation x follows the *normal* distribution with known expectation μ and known variance σ^2, we can compute the confidence interval for a unique measurement and a given confidence level $1 - \alpha$.

$$P(\mu - \sigma \cdot \mathrm{z}^{\alpha/2} < x \leq \mu + \sigma \cdot \mathrm{z}^{\alpha/2}) = 1 - \alpha \tag{B.1}$$

where $\mathrm{z}^{\alpha/2}$ is the percentile for the *normal* distribution for a given significance level α.

By replacing in Equation B.1 x with r and μ with $\bar{r}$, which is by definition equal to zero (see Equation 3.10), the confidence interval of the residual r becomes

$$P(-\sigma \cdot \mathrm{z}^{\alpha/2} < r \leq +\sigma \cdot \mathrm{z}^{\alpha/2}) = 1 - \alpha \tag{B.2}$$

The graphs in Chapter 3 depict the $\pm 1\sigma$, $\pm 2\sigma$ and $\pm 3\sigma$ confidence intervals that correspond to the following significance levels (α) or their respective probabilities (P):

$$\begin{aligned} \mathrm{z}^{\alpha/2} = 1 &\Rightarrow \alpha = 0.3174 \Rightarrow P = 68.26\% \\ \mathrm{z}^{\alpha/2} = 2 &\Rightarrow \alpha = 0.0456 \Rightarrow P = 95.44\% \\ \mathrm{z}^{\alpha/2} = 3 &\Rightarrow \alpha = 0.0026 \Rightarrow P = 99.74\% \end{aligned} \tag{B.3}$$

The confidence interval $\mathcal{I}^{\alpha/2}$ for the sample mean of the the residuals $\bar{r}_{\mathcal{P}_k}$ for each parameter value p_k is computed as

$$P(\bar{r}_{\mathcal{P}_k} - \frac{s_{\mathcal{P}_k}}{\sqrt{n_k}} \cdot t_f^{\alpha/2} < \bar{r}_{\mathcal{P}_k} \leq \bar{r}_{\mathcal{P}_k} + \frac{s_{\mathcal{P}_k}}{\sqrt{n_k}} \cdot t_f^{\alpha/2}) = 1 - \alpha \tag{B.4}$$

where $t_f^{\alpha/2}$ is the percentile of the *Student's t* distribution for significance level α and for f degrees of freedom:

$$f = n_k - 1 \tag{B.5}$$

The values for a 95 % ($\alpha = 0.05$) confidence interval $\mathcal{I}^{0.025}$ are presented in the tables of this appendix and they are also depicted as vertical lines, centered in the corresponding mean values, in the graphs of Chapter 3.

B.2 Statistical tests

In order to evaluate the potential influence of the different parameter values to the measurement results, we perform two statistical tests: one for the sample variance and another for the sample mean.

B.2.1 Statistical test for the sample variable

The first statistical test concerns the sample variance $s^2_{\mathcal{P}_k}$ of the measurements for each parameter value p_k. Each sample variance is compared with the variance σ^2, which corresponds to angular precision of the theodolite, as provided by the manufacturer (i.e., 0.15 mgon at 1σ). This statistical test aims to indicate parameter values that influence the measurement process, causing a larger variance than that expected by the theodolite precision.

Initially, we test the null hypothesis H_0 against the alternative hypothesis H_a,

$$H_0 : s^2_{\mathcal{P}_k} = \sigma^2, \quad H_a : s^2_{\mathcal{P}_k} \neq \sigma^2 \tag{B.6}$$

The null hypothesis H_0 is accepted if

$$\chi^2_{1-\alpha/2,f} \leq u \leq \chi^2_{\alpha/2,f} \tag{B.7}$$

where

$$u = \frac{s^2_{\mathcal{P}_k} \cdot f}{\sigma^2} \tag{B.8}$$

and $\chi^2_{1-\alpha/2,f}$, $\chi^2_{\alpha/2,f}$ are the percentiles of the χ^2 distribution for significance level α and for f degrees of freedom (Equation B.5).

In case that the null hypothesis H_0 is rejected, we either perform the test:

$$H_0 : s^2_{\mathcal{P}_k} = \sigma^2, \quad H_a : s^2_{\mathcal{P}_k} > \sigma^2 \tag{B.9}$$

where the null hypothesis H_0 is accepted if

$$u \leq \chi^2_{\alpha,f} \tag{B.10}$$

or we perform the test:

$$H_0 : s^2_{\mathcal{P}_k} = \sigma^2, \quad H_a : s^2_{\mathcal{P}_k} < \sigma^2 \tag{B.11}$$

where the null hypothesis H_0 is accepted if

$$\chi^2_{1-\alpha,f} \leq u \tag{B.12}$$

The confidence level $1 - \alpha$ is selected to be 95 % for the statistical test of the sample variable. The values of the aforementioned quantities are presented in the following tables for each parameter under examination and for both, the wire detection algorithm and the circle detection algorithm measurements.

B.2.2 Statistical test for the sample mean

The second statistical test concerns the sample mean $\bar{x}_{\mathcal{P}_k}$ (or equivalently the quantity $\bar{r}_{\mathcal{P}_k}$) of the measurements for each parameter value p_k. Each sample mean $\bar{r}_{\mathcal{P}_k}$ is compared to the sample mean that corresponds to the respective reference parameter value $\bar{r}_{\mathcal{P}_{ref}}$, according to Appendices C and D. This statistical test aims to reveal parameter values that cause biases to the measurements.

The null hypothesis H_0 and the alternative hypothesis H_a are:

$$H_0 : \bar{r}_{\mathcal{P}_k} - \bar{r}_{\mathcal{P}_{ref}} = 0 \Leftrightarrow \bar{r}_{\mathcal{P}_k} = \bar{r}_{\mathcal{P}_{ref}}, \quad H_a : \bar{r}_{\mathcal{P}_k} \neq \bar{r}_{\mathcal{P}_{ref}} \tag{B.13}$$

The null hypothesis H_0 is accepted if

$$|t| \leq t_\nu^{\alpha/2} \tag{B.14}$$

where

$$t = \frac{\bar{r}_{\mathcal{P}_{ref}} - \bar{r}_{\mathcal{P}_k}}{\sqrt{\dfrac{s^2_{\mathcal{P}_{ref}}}{n_{ref}} + \dfrac{s^2_{\mathcal{P}_k}}{n_k}}} \tag{B.15}$$

and $t_\nu^{\alpha/2}$ is the percentile of the *Student's t* distribution for significance level α and for ν degrees of freedom:

$$\nu = \frac{\left(s^2_{\mathcal{P}_{ref}}/n_1 + s^2_{\mathcal{P}_k}/n_k\right)^2}{\dfrac{\left(s^2_{\mathcal{P}_{ref}}/n_1\right)^2}{n_{ref}-1} + \dfrac{\left(s^2_{\mathcal{P}_k}/n_k\right)^2}{n_k-1}} \tag{B.16}$$

The confidence level $1-\alpha$ for the statistical test of the sample mean is selected to be 99 %, therefore, more tolerant (less strict) than that for the statistical test of the sample variance in order to accommodate potential drifts of the mean values due to the extended in time measurements. The values of the aforementioned quantities are presented in the following tables for each parameter under examination and for both, the wire detection algorithm and the circle detection algorithm measurements.

The theory and the actual formulas concerning the confidence intervals and statistical tests can be found in the classic and the modern bibliography in the field of the observation adjustment theory. An indicative list of books used in this chapter contains *Mikhail and Ackermann* (1976), *Mikhail and Gracie* (1981), *Dermanis* (1986) and *Ghilani* (2010).

B.3 Values for the evaluation of the wire detection algorithm

shots parameter — elevation angle to the wire

Table B.1: Confidence intervals for the mean values of the elevation angle to the wire (in blue color), and statistical tests for the variance (in red color) and for the mean values (in green color). Each row corresponds to a different value of the user-defined parameter *# shots* (see Section 3.4.1).

p_k	n_k	f	$\bar{r}_{\mathcal{P}_k}$ [µrad]	$s^2_{\mathcal{P}_k}$ [µrad^2]	$s_{\mathcal{P}_k}$ [µrad]	$s^2_{\bar{r}_{\mathcal{P}_k}}$ [µrad^2]	$s_{\bar{r}_{\mathcal{P}_k}}$ [µrad]	$t_f^{0.025}$	$\mathcal{I}^{0.025}$ [µrad]
3	10	9	0.45	0.7932	0.89	0.0793	0.28	2.262	±0.64
5	10	9	0.02	0.8138	0.90	0.0814	0.29	2.262	±0.65
10	10	9	-0.47	0.8903	0.94	0.0890	0.30	2.262	±0.67

χ^2_f	$\chi^2_{0.975,f}$	$\chi^2_{0.025,f}$	$\chi^2_{0.95,f}$	$\chi^2_{0.05,f}$		$\|t\|$	ν	$t_\nu^{0.005}$	
1.286	2.700	19.023	3.325	16.919	$s^2_{\mathcal{P}_1} < \sigma^2$	1.080	18.00	2.878	$\bar{r}_{\mathcal{P}_1} = \bar{r}_{\mathcal{P}_2}$
1.319	2.700	19.023	3.325	16.919	$s^2_{\mathcal{P}_2} < \sigma^2$				
1.443	2.700	19.023	3.325	16.919	$s^2_{\mathcal{P}_3} < \sigma^2$	1.194	17.96	2.879	$\bar{r}_{\mathcal{P}_3} = \bar{r}_{\mathcal{P}_2}$

Std shot parameter — elevation angle to the wire

Table B.2: Confidence intervals for the mean values of the elevation angle to the wire (in blue color), and statistical tests for the variance (in red color) and for the mean values (in green color). Each row corresponds to a different value of the user-defined parameter *Std shot* (see Section 3.4.1).

p_k [pixel]	n_k	f	$\bar{r}_{\mathcal{P}_k}$ [µrad]	$s^2_{\mathcal{P}_k}$ [µrad^2]	$s_{\mathcal{P}_k}$ [µrad]	$s^2_{\bar{r}_{\mathcal{P}_k}}$ [µrad^2]	$s_{\bar{r}_{\mathcal{P}_k}}$ [µrad]	$t_f^{0.025}$	$\mathcal{I}^{0.025}$ [µrad]
0.05	10	9	-0.08	0.8547	0.92	0.0855	0.29	2.262	$\pm$0.66
0.10	10	9	-0.12	1.4034	1.18	0.1403	0.37	2.262	$\pm$0.85
0.20	10	9	0.20	0.7377	0.86	0.0738	0.27	2.262	$\pm$0.61

χ^2_f	$\chi^2_{0.975,f}$	$\chi^2_{0.025,f}$	$\chi^2_{0.95,f}$	$\chi^2_{0.05,f}$		$\lvert t \rvert$	ν	$t_\nu^{0.005}$	
1.386	2.700	19.023	3.325	16.919	$s^2_{\mathcal{P}_1} < \sigma^2$	0.090	17.00	2.898	$\bar{r}_{\mathcal{P}_1} = \bar{r}_{\mathcal{P}_2}$
2.275	2.700	19.023	3.325	16.919	$s^2_{\mathcal{P}_2} < \sigma^2$				
1.196	2.700	19.023	3.325	16.919	$s^2_{\mathcal{P}_3} < \sigma^2$	0.694	16.41	2.911	$\bar{r}_{\mathcal{P}_3} = \bar{r}_{\mathcal{P}_2}$

Shutter parameter — elevation angle to the wire

Table B.3: Confidence intervals for the mean values of the elevation angle to the wire (in blue color), and statistical tests for the variance (in red color) and for the mean values (in green color). Each row corresponds to a different value of the user-defined parameter *Shutter* (see Section 3.4.2).

p_k [ms]	n_k	f	$\bar{r}_{\mathcal{P}_k}$ [µrad]	$s^2_{\mathcal{P}_k}$ [µrad^2]	$s_{\mathcal{P}_k}$ [µrad]	$s^2_{\bar{r}_{\mathcal{P}_k}}$ [µrad^2]	$s_{\bar{r}_{\mathcal{P}_k}}$ [µrad]	$t_f^{0.025}$	$\mathcal{I}^{0.025}$ [µrad]
210	10	9	-0.10	0.4266	0.65	0.0427	0.21	2.262	$\pm$0.47
240	10	9	0.26	0.3505	0.59	0.0351	0.19	2.262	$\pm$0.42
270	10	9	-0.28	0.5060	0.71	0.0506	0.22	2.262	$\pm$0.51
300	10	9	0.05	0.7038	0.84	0.0704	0.27	2.262	$\pm$0.60
330	10	9	0.25	0.2448	0.49	0.0245	0.16	2.262	$\pm$0.35
360	10	9	0.06	0.3076	0.55	0.0308	0.18	2.262	$\pm$0.40
390	10	9	-0.24	0.4637	0.68	0.0464	0.22	2.262	$\pm$0.49

χ^2_f	$\chi^2_{0.975,f}$	$\chi^2_{0.025,f}$	$\chi^2_{0.95,f}$	$\chi^2_{0.05,f}$		$\lvert t \rvert$	ν	$t_\nu^{0.005}$	
0.692	2.700	19.023	3.325	16.919	$s^2_{\mathcal{P}_1} < \sigma^2$	0.452	16.98	2.899	$\bar{r}_{\mathcal{P}_1} = \bar{r}_{\mathcal{P}_4}$
0.568	2.700	19.023	3.325	16.919	$s^2_{\mathcal{P}_2} < \sigma^2$	0.658	16.18	2.916	$\bar{r}_{\mathcal{P}_2} = \bar{r}_{\mathcal{P}_4}$
0.820	2.700	19.023	3.325	16.919	$s^2_{\mathcal{P}_3} < \sigma^2$	0.948	17.53	2.887	$\bar{r}_{\mathcal{P}_3} = \bar{r}_{\mathcal{P}_4}$
1.141	2.700	19.023	3.325	16.919	$s^2_{\mathcal{P}_4} < \sigma^2$				
0.397	2.700	19.023	3.325	16.919	$s^2_{\mathcal{P}_5} < \sigma^2$	0.655	14.59	2.959	$\bar{r}_{\mathcal{P}_5} = \bar{r}_{\mathcal{P}_4}$
0.499	2.700	19.023	3.325	16.919	$s^2_{\mathcal{P}_6} < \sigma^2$	0.038	15.61	2.931	$\bar{r}_{\mathcal{P}_6} = \bar{r}_{\mathcal{P}_4}$
0.752	2.700	19.023	3.325	16.919	$s^2_{\mathcal{P}_7} < \sigma^2$	0.858	17.27	2.893	$\bar{r}_{\mathcal{P}_7} = \bar{r}_{\mathcal{P}_4}$

Gain parameter — elevation angle to the wire

Table B.4: Confidence intervals for the mean values of the elevation angle to the wire (in blue color), and statistical tests for the variance (in red color) and for the mean values (in green color). Each row corresponds to a different value of the user-defined parameter *Gain* (see Section 3.4.2).

p_k	n_k	f	$\bar{r}_{\mathcal{P}_k}$ [µrad]	$s^2_{\mathcal{P}_k}$ [µrad^2]	$s_{\mathcal{P}_k}$ [µrad]	$s^2_{\bar{r}\mathcal{P}_k}$ [µrad^2]	$s_{\bar{r}\mathcal{P}_k}$ [µrad]	$t_f^{0.025}$	$\mathcal{I}^{0.025}$ [µrad]
110	10	9	0.22	0.5761	0.76	0.0576	0.24	2.262	±0.54
140	10	9	0.09	0.7549	0.87	0.0755	0.27	2.262	±0.62
170	10	9	-0.43	1.1159	1.06	0.1116	0.33	2.262	±0.76
200	10	9	0.10	0.5266	0.73	0.0527	0.23	2.262	±0.52
230	10	9	-0.06	1.3113	1.15	0.1311	0.36	2.262	±0.82
260	10	9	0.15	0.4005	0.63	0.0400	0.20	2.262	±0.45
290	10	9	-0.07	0.6300	0.79	0.0630	0.25	2.262	±0.57

χ^2_f	$\chi^2_{0.975,f}$	$\chi^2_{0.025,f}$	$\chi^2_{0.95,f}$	$\chi^2_{0.05,f}$		$\lvert t\rvert$	ν	$t_\nu^{0.005}$	
0.934	2.700	19.023	3.325	16.919	$s^2_{\mathcal{P}_1} < \sigma^2$	0.365	17.96	2.879	$\bar{r}_{\mathcal{P}_1} = \bar{r}_{\mathcal{P}_4}$
1.224	2.700	19.023	3.325	16.919	$s^2_{\mathcal{P}_2} < \sigma^2$	0.007	17.45	2.889	$\bar{r}_{\mathcal{P}_2} = \bar{r}_{\mathcal{P}_4}$
1.809	2.700	19.023	3.325	16.919	$s^2_{\mathcal{P}_3} < \sigma^2$	1.307	15.95	2.922	$\bar{r}_{\mathcal{P}_3} = \bar{r}_{\mathcal{P}_4}$
0.854	2.700	19.023	3.325	16.919	$s^2_{\mathcal{P}_4} < \sigma^2$				
2.126	2.700	19.023	3.325	16.919	$s^2_{\mathcal{P}_5} < \sigma^2$	0.362	15.22	2.941	$\bar{r}_{\mathcal{P}_5} = \bar{r}_{\mathcal{P}_4}$
0.649	2.700	19.023	3.325	16.919	$s^2_{\mathcal{P}_6} < \sigma^2$	0.172	17.67	2.885	$\bar{r}_{\mathcal{P}_6} = \bar{r}_{\mathcal{P}_4}$
1.021	2.700	19.023	3.325	16.919	$s^2_{\mathcal{P}_7} < \sigma^2$	0.490	17.86	2.881	$\bar{r}_{\mathcal{P}_7} = \bar{r}_{\mathcal{P}_4}$

Focus parameter — elevation angle to the wire

Table B.5: Confidence intervals for the mean values of the elevation angle to the wire (in blue color), and statistical tests for the variance (in red color) and for the mean values (in green color). Each row corresponds to a different value of the user-defined parameter *Focus* (see Section 3.4.2).

p_k [step]	n_k	f	$\bar{r}_{\mathcal{P}_k}$ [µrad]	$s^2_{\mathcal{P}_k}$ [µrad^2]	$s_{\mathcal{P}_k}$ [µrad]	$s^2_{\bar{r}\mathcal{P}_k}$ [µrad^2]	$s_{\bar{r}\mathcal{P}_k}$ [µrad]	$t_f^{0.025}$	$\mathcal{I}^{0.025}$ [µrad]
108000	9	8	-0.13	0.7547	0.87	0.0839	0.29	2.306	±0.67
108100	10	9	-0.47	0.4815	0.69	0.0482	0.22	2.262	±0.50
108200	10	9	0.25	0.3174	0.56	0.0317	0.18	2.262	±0.40
108300	10	9	0.01	0.7946	0.89	0.0795	0.28	2.262	±0.64
108400	10	9	-0.25	0.4133	0.64	0.0413	0.20	2.262	±0.46
108500	10	9	0.23	0.3760	0.61	0.0376	0.19	2.262	±0.44
108600	9	8	0.38	1.0246	1.01	0.1138	0.34	2.306	±0.78

χ^2_f	$\chi^2_{0.975,f}$	$\chi^2_{0.025,f}$	$\chi^2_{0.95,f}$	$\chi^2_{0.05,f}$		$\lvert t\rvert$	ν	$t_\nu^{0.005}$	
1.088	2.180	17.535	2.733	15.507	$s^2_{\mathcal{P}_1} < \sigma^2$	0.332	16.88	2.901	$\bar{r}_{\mathcal{P}_1} = \bar{r}_{\mathcal{P}_4}$
0.781	2.700	19.023	3.325	16.919	$s^2_{\mathcal{P}_2} < \sigma^2$	1.348	16.98	2.899	$\bar{r}_{\mathcal{P}_2} = \bar{r}_{\mathcal{P}_4}$
0.515	2.700	19.023	3.325	16.919	$s^2_{\mathcal{P}_3} < \sigma^2$	0.733	15.20	2.941	$\bar{r}_{\mathcal{P}_3} = \bar{r}_{\mathcal{P}_4}$
1.288	2.700	19.023	3.325	16.919	$s^2_{\mathcal{P}_4} < \sigma^2$				
0.670	2.700	19.023	3.325	16.919	$s^2_{\mathcal{P}_5} < \sigma^2$	0.743	16.37	2.912	$\bar{r}_{\mathcal{P}_5} = \bar{r}_{\mathcal{P}_4}$
0.610	2.700	19.023	3.325	16.919	$s^2_{\mathcal{P}_6} < \sigma^2$	0.653	15.96	2.922	$\bar{r}_{\mathcal{P}_6} = \bar{r}_{\mathcal{P}_4}$
1.476	2.180	17.535	2.733	15.507	$s^2_{\mathcal{P}_7} < \sigma^2$	0.846	16.10	2.918	$\bar{r}_{\mathcal{P}_7} = \bar{r}_{\mathcal{P}_4}$

HW ROI parameter — elevation angle to the wire

Table B.6: Confidence intervals for the mean values of the elevation angle to the wire (in blue color), and statistical tests for the variance (in red color) and for the mean values (in green color). Each row corresponds to a different value of the user-defined parameter *HW ROI* (see Section 3.4.3).

p_k [pixel]	n_k	f	$\bar{r}_{\mathcal{P}_k}$ [µrad]	$s^2_{\mathcal{P}_k}$ [µrad^2]	$s_{\mathcal{P}_k}$ [µrad]	$s^2_{\bar{r}_{\mathcal{P}_k}}$ [µrad^2]	$s_{\bar{r}_{\mathcal{P}_k}}$ [µrad]	$t_f^{0.025}$	$\mathcal{I}^{0.025}$ [µrad]
50	10	9	0.51	0.9272	0.96	0.0927	0.30	2.262	±0.69
100	10	9	-0.21	0.8720	0.93	0.0872	0.30	2.262	±0.67
150	10	9	-0.43	1.4435	1.20	0.1444	0.38	2.262	±0.86
200	10	9	-0.27	0.4751	0.69	0.0475	0.22	2.262	±0.49
250	10	9	-0.18	0.8543	0.92	0.0854	0.29	2.262	±0.66
300	10	9	0.21	0.4177	0.65	0.0418	0.20	2.262	±0.46
350	10	9	0.37	0.6243	0.79	0.0624	0.25	2.262	±0.57

χ^2_f	$\chi^2_{0.975,f}$	$\chi^2_{0.025,f}$	$\chi^2_{0.95,f}$	$\chi^2_{0.05,f}$		$\lvert t\rvert$	ν	$t_\nu^{0.005}$	
1.503	2.700	19.023	3.325	16.919	$s^2_{\mathcal{P}_1} < \sigma^2$	2.090	16.31	2.914	$\bar{r}_{\mathcal{P}_1} = \bar{r}_{\mathcal{P}_4}$
1.414	2.700	19.023	3.325	16.919	$s^2_{\mathcal{P}_2} < \sigma^2$	0.183	16.56	2.908	$\bar{r}_{\mathcal{P}_2} = \bar{r}_{\mathcal{P}_4}$
2.340	2.700	19.023	3.325	16.919	$s^2_{\mathcal{P}_3} < \sigma^2$	0.357	14.35	2.966	$\bar{r}_{\mathcal{P}_3} = \bar{r}_{\mathcal{P}_4}$
0.770	2.700	19.023	3.325	16.919	$s^2_{\mathcal{P}_4} < \sigma^2$				
1.385	2.700	19.023	3.325	16.919	$s^2_{\mathcal{P}_5} < \sigma^2$	0.254	16.65	2.906	$\bar{r}_{\mathcal{P}_5} = \bar{r}_{\mathcal{P}_4}$
0.677	2.700	19.023	3.325	16.919	$s^2_{\mathcal{P}_6} < \sigma^2$	1.630	17.93	2.880	$\bar{r}_{\mathcal{P}_6} = \bar{r}_{\mathcal{P}_4}$
1.012	2.700	19.023	3.325	16.919	$s^2_{\mathcal{P}_7} < \sigma^2$	1.937	17.67	2.885	$\bar{r}_{\mathcal{P}_7} = \bar{r}_{\mathcal{P}_4}$

Canny thres parameter — elevation angle to the wire

Table B.7: Confidence intervals for the mean values of the elevation angle to the wire (in blue color), and statistical tests for the variance (in red color) and for the mean values (in green color). Each row corresponds to a different value of the user-defined parameter *Canny thres* (see Section 3.4.3).

p_k [8-bit]	n_k	f	$\bar{r}_{\mathcal{P}_k}$ [µrad]	$s^2_{\mathcal{P}_k}$ [µrad^2]	$s_{\mathcal{P}_k}$ [µrad]	$s^2_{\bar{r}_{\mathcal{P}_k}}$ [µrad^2]	$s_{\bar{r}_{\mathcal{P}_k}}$ [µrad]	$t_f^{0.025}$	$\mathcal{I}^{0.025}$ [µrad]
60	9	8	-0.03	0.2581	0.51	0.0287	0.17	2.306	±0.39
80	10	9	0.01	1.4314	1.20	0.1431	0.38	2.262	±0.86
100	10	9	0.06	0.6758	0.82	0.0676	0.26	2.262	±0.59
120	10	9	0.04	0.6470	0.80	0.0647	0.25	2.262	±0.58
140	10	9	-0.42	1.1870	1.09	0.1187	0.34	2.262	±0.78
160	10	9	-0.04	1.5730	1.25	0.1573	0.40	2.262	±0.90
180	10	9	0.37	0.8443	0.92	0.0844	0.29	2.262	±0.66

χ^2_f	$\chi^2_{0.975,f}$	$\chi^2_{0.025,f}$	$\chi^2_{0.95,f}$	$\chi^2_{0.05,f}$		$\lvert t\rvert$	ν	$t_\nu^{0.005}$	
0.372	2.180	17.535	2.733	15.507	$s^2_{\mathcal{P}_1} < \sigma^2$	0.247	15.35	2.937	$\bar{r}_{\mathcal{P}_1} = \bar{r}_{\mathcal{P}_4}$
2.320	2.700	19.023	3.325	16.919	$s^2_{\mathcal{P}_2} < \sigma^2$	0.067	15.76	2.927	$\bar{r}_{\mathcal{P}_2} = \bar{r}_{\mathcal{P}_4}$
1.096	2.700	19.023	3.325	16.919	$s^2_{\mathcal{P}_3} < \sigma^2$	0.050	17.99	2.879	$\bar{r}_{\mathcal{P}_3} = \bar{r}_{\mathcal{P}_4}$
1.049	2.700	19.023	3.325	16.919	$s^2_{\mathcal{P}_4} < \sigma^2$				
1.924	2.700	19.023	3.325	16.919	$s^2_{\mathcal{P}_5} < \sigma^2$	1.072	16.56	2.908	$\bar{r}_{\mathcal{P}_5} = \bar{r}_{\mathcal{P}_4}$
2.550	2.700	19.023	3.325	16.919	$s^2_{\mathcal{P}_6} < \sigma^2$	0.176	15.33	2.938	$\bar{r}_{\mathcal{P}_6} = \bar{r}_{\mathcal{P}_4}$
1.369	2.700	19.023	3.325	16.919	$s^2_{\mathcal{P}_7} < \sigma^2$	0.861	17.69	2.884	$\bar{r}_{\mathcal{P}_7} = \bar{r}_{\mathcal{P}_4}$

Background condition — elevation angle to the wire

Table B.8: Confidence intervals for the mean values of the elevation angle to the wire (in blue color), and statistical tests for the variance (in red color) and for the mean values (in green color). Each row corresponds to a different case of the *Background* intensity, as described in Section 3.4.4: (a) grey, (b) dark (black), and (c) bright (white).

p_k	n_k	f	$\bar{r}_{\mathcal{P}_k}$ [µrad]	$s^2_{\mathcal{P}_k}$ [µrad^2]	$s_{\mathcal{P}_k}$ [µrad]	$s^2_{\bar{r}_{\mathcal{P}_k}}$ [µrad^2]	$s_{\bar{r}_{\mathcal{P}_k}}$ [µrad]	$t_f^{0.025}$	$\mathcal{I}^{0.025}$ [µrad]
a	10	9	-1.37	0.4773	0.69	0.0477	0.22	2.262	±0.49
b	10	9	1.63	0.9634	0.98	0.0963	0.31	2.262	±0.70
c	10	9	-0.26	0.5323	0.73	0.0532	0.23	2.262	±0.52

χ^2_f	$\chi^2_{0.975,f}$	$\chi^2_{0.025,f}$	$\chi^2_{0.95,f}$	$\chi^2_{0.05,f}$		$\lvert t\rvert$	ν	$t_\nu^{0.005}$	
0.774	2.700	19.023	3.325	16.919	$s^2_{\mathcal{P}_1} < \sigma^2$				
1.562	2.700	19.023	3.325	16.919	$s^2_{\mathcal{P}_2} < \sigma^2$	7.898	16.16	2.917	$\bar{r}_{\mathcal{P}_2} \neq \bar{r}_{\mathcal{P}_1}$
0.863	2.700	19.023	3.325	16.919	$s^2_{\mathcal{P}_3} < \sigma^2$	3.507	17.95	2.879	$\bar{r}_{\mathcal{P}_3} \neq \bar{r}_{\mathcal{P}_1}$

Light condition — elevation angle to the wire

Table B.9: Confidence intervals for the mean values of the elevation angle to the wire (in blue color), and statistical tests for the variance (in red color) and for the mean values (in green color). Each row corresponds to a different case of the *Light* condition, as described in Section 3.4.4: (a) laboratory ceiling lights switched on, (b) laboratory security lights switched on, (c) LED 1 switched on, (d) LED 2 switched on, (e) LED 3 switched on, (f) LED 4 switched on, and (g) all four LED lights switched on.

p_k	n_k	f	$\bar{r}_{\mathcal{P}_k}$ [µrad]	$s^2_{\mathcal{P}_k}$ [µrad^2]	$s_{\mathcal{P}_k}$ [µrad]	$s^2_{\bar{r}_{\mathcal{P}_k}}$ [µrad^2]	$s_{\bar{r}_{\mathcal{P}_k}}$ [µrad]	$t_f^{0.025}$	$\mathcal{I}^{0.025}$ [µrad]
a	10	9	2.02	0.2258	0.48	0.0226	0.15	2.262	±0.34
b	10	9	1.56	0.4656	0.68	0.0466	0.22	2.262	±0.49
c	10	9	2.83	0.2571	0.51	0.0257	0.16	2.262	±0.36
d	10	9	1.56	0.1535	0.39	0.0154	0.12	2.262	±0.28
e	10	9	-2.48	0.1663	0.41	0.0166	0.13	2.262	±0.29
f	10	9	-4.73	0.6031	0.78	0.0603	0.25	2.262	±0.56
g	10	9	-0.77	0.4118	0.64	0.0412	0.20	2.262	±0.46

χ^2_f	$\chi^2_{0.975,f}$	$\chi^2_{0.025,f}$	$\chi^2_{0.95,f}$	$\chi^2_{0.05,f}$		$\lvert t\rvert$	ν	$t_\nu^{0.005}$	
0.366	2.700	19.023	3.325	16.919	$s^2_{\mathcal{P}_1} < \sigma^2$				
0.755	2.700	19.023	3.325	16.919	$s^2_{\mathcal{P}_2} < \sigma^2$	1.756	16.07	2.919	$\bar{r}_{\mathcal{P}_2} = \bar{r}_{\mathcal{P}_1}$
0.417	2.700	19.023	3.325	16.919	$s^2_{\mathcal{P}_3} < \sigma^2$	3.670	17.92	2.880	$\bar{r}_{\mathcal{P}_3} \neq \bar{r}_{\mathcal{P}_1}$
0.249	2.700	19.023	3.325	16.919	$s^2_{\mathcal{P}_4} < \sigma^2$	2.370	17.37	2.891	$\bar{r}_{\mathcal{P}_4} = \bar{r}_{\mathcal{P}_1}$
0.270	2.700	19.023	3.325	16.919	$s^2_{\mathcal{P}_5} < \sigma^2$	22.723	17.60	2.886	$\bar{r}_{\mathcal{P}_5} \neq \bar{r}_{\mathcal{P}_1}$
0.978	2.700	19.023	3.325	16.919	$s^2_{\mathcal{P}_6} < \sigma^2$	23.439	14.91	2.949	$\bar{r}_{\mathcal{P}_6} \neq \bar{r}_{\mathcal{P}_1}$
0.668	2.700	19.023	3.325	16.919	$s^2_{\mathcal{P}_7} < \sigma^2$	11.042	16.59	2.907	$\bar{r}_{\mathcal{P}_7} \neq \bar{r}_{\mathcal{P}_1}$

B.4 Values for the evaluation of the circle detection algorithm

shots parameter — horizontal angle to the *Up* target

Table B.10: Confidence intervals for the mean values of the horizontal angle to the *Up* target (in blue color), and statistical tests for the variance (in red color) and for the mean values (in green color). Each row corresponds to a different value of the user-defined parameter # *shots* (see Section 3.5.1).

p_k	n_k	f	$\bar{r}_{\mathcal{P}_k}$ [µrad]	$s^2_{\mathcal{P}_k}$ [µrad^2]	$s_{\mathcal{P}_k}$ [µrad]	$s^2_{\bar{r}_{\mathcal{P}_k}}$ [µrad^2]	$s_{\bar{r}_{\mathcal{P}_k}}$ [µrad]	$t_f^{0.025}$	$\mathcal{I}^{0.025}$ [µrad]
3	9	8	-0.03	0.0864	0.29	0.0096	0.10	2.306	±0.23
5	10	9	0.00	0.1609	0.40	0.0161	0.13	2.262	±0.29
10	10	9	0.03	0.1815	0.43	0.0182	0.13	2.262	±0.30

χ^2_f	$\chi^2_{0.975,f}$	$\chi^2_{0.025,f}$	$\chi^2_{0.95,f}$	$\chi^2_{0.05,f}$		$\lvert t\rvert$	ν	$t_\nu^{0.005}$	
0.124	2.180	17.535	2.733	15.507	$s^2_{\mathcal{P}_1} < \sigma^2$	0.186	16.38	2.912	$\bar{r}_{\mathcal{P}_1} = \bar{r}_{\mathcal{P}_2}$
0.261	2.700	19.023	3.325	16.919	$s^2_{\mathcal{P}_2} < \sigma^2$				
0.294	2.700	19.023	3.325	16.919	$s^2_{\mathcal{P}_3} < \sigma^2$	0.137	17.93	2.880	$\bar{r}_{\mathcal{P}_3} = \bar{r}_{\mathcal{P}_2}$

shots parameter — elevation angle to the *Up* target

Table B.11: Confidence intervals for the mean values of the elevation angle to the *Up* target (in blue color), and statistical tests for the variance (in red color) and for the mean values (in green color). Each row corresponds to a different value of the user-defined parameter # *shots* (see Section 3.5.1).

p_k	n_k	f	$\bar{r}_{\mathcal{P}_k}$ [µrad]	$s^2_{\mathcal{P}_k}$ [µrad^2]	$s_{\mathcal{P}_k}$ [µrad]	$s^2_{\bar{r}_{\mathcal{P}_k}}$ [µrad^2]	$s_{\bar{r}_{\mathcal{P}_k}}$ [µrad]	$t_f^{0.025}$	$\mathcal{I}^{0.025}$ [µrad]
3	9	8	0.11	0.2808	0.53	0.0312	0.18	2.306	±0.41
5	10	9	-0.06	0.6147	0.78	0.0615	0.25	2.262	±0.56
10	10	9	-0.03	0.7674	0.88	0.0767	0.28	2.262	±0.63

χ^2_f	$\chi^2_{0.975,f}$	$\chi^2_{0.025,f}$	$\chi^2_{0.95,f}$	$\chi^2_{0.05,f}$		$\lvert t\rvert$	ν	$t_\nu^{0.005}$	
0.405	2.180	17.535	2.733	15.507	$s^2_{\mathcal{P}_1} < \sigma^2$	0.558	15.86	2.924	$\bar{r}_{\mathcal{P}_1} = \bar{r}_{\mathcal{P}_2}$
0.997	2.700	19.023	3.325	16.919	$s^2_{\mathcal{P}_2} < \sigma^2$				
1.244	2.700	19.023	3.325	16.919	$s^2_{\mathcal{P}_3} < \sigma^2$	0.075	17.78	2.883	$\bar{r}_{\mathcal{P}_3} = \bar{r}_{\mathcal{P}_2}$

Std shot parameter — horizontal angle to the *Up* target

Table B.12: Confidence intervals for the mean values of the horizontal angle to the *Up* target (in blue color), and statistical tests for the variance (in red color) and for the mean values (in green color). Each row corresponds to a different value of the user-defined parameter *Std shot* (see Section 3.5.1).

p_k [pixel]	n_k	f	$\bar{r}_{\mathcal{P}_k}$ [µrad]	$s^2_{\mathcal{P}_k}$ [µrad^2]	$s_{\mathcal{P}_k}$ [µrad]	$s^2_{\bar{r}_{\mathcal{P}_k}}$ [µrad^2]	$s_{\bar{r}_{\mathcal{P}_k}}$ [µrad]	$t_f^{0.025}$	$\mathcal{I}^{0.025}$ [µrad]
0.05	10	9	0.03	0.2288	0.48	0.0229	0.15	2.262	±0.34
0.10	10	9	-0.09	0.2903	0.54	0.0290	0.17	2.262	±0.39
0.20	10	9	0.06	0.4045	0.64	0.0404	0.20	2.262	±0.45

χ^2_f	$\chi^2_{0.975,f}$	$\chi^2_{0.025,f}$	$\chi^2_{0.95,f}$	$\chi^2_{0.05,f}$		$\lvert t\rvert$	ν	$t_\nu^{0.005}$	
0.371	2.700	19.023	3.325	16.919	$s^2_{\mathcal{P}_1} < \sigma^2$	0.513	17.75	2.883	$\bar{r}_{\mathcal{P}_1} = \bar{r}_{\mathcal{P}_2}$
0.471	2.700	19.023	3.325	16.919	$s^2_{\mathcal{P}_2} < \sigma^2$				
0.656	2.700	19.023	3.325	16.919	$s^2_{\mathcal{P}_3} < \sigma^2$	0.546	17.53	2.888	$\bar{r}_{\mathcal{P}_3} = \bar{r}_{\mathcal{P}_2}$

Std shot parameter — elevation angle to the *Up* target

Table B.13: Confidence intervals for the mean values of the elevation angle to the *Up* target (in blue color), and statistical tests for the variance (in red color) and for the mean values (in green color). Each row corresponds to a different value of the user-defined parameter *Std shot* (see Section 3.5.1).

p_k [pixel]	n_k	f	$\bar{r}_{\mathcal{P}_k}$ [µrad]	$s^2_{\mathcal{P}_k}$ [µrad^2]	$s_{\mathcal{P}_k}$ [µrad]	$s^2_{\bar{r}_{\mathcal{P}_k}}$ [µrad^2]	$s_{\bar{r}_{\mathcal{P}_k}}$ [µrad]	$t_f^{0.025}$	$\mathcal{I}^{0.025}$ [µrad]
0.05	10	9	0.17	0.8779	0.94	0.0878	0.30	2.262	±0.67
0.10	10	9	-0.38	0.2991	0.55	0.0299	0.17	2.262	±0.39
0.20	10	9	0.20	0.4730	0.69	0.0473	0.22	2.262	±0.49

χ^2_f	$\chi^2_{0.975,f}$	$\chi^2_{0.025,f}$	$\chi^2_{0.95,f}$	$\chi^2_{0.05,f}$		$\lvert t\rvert$	ν	$t_\nu^{0.005}$	
1.423	2.700	19.023	3.325	16.919	$s^2_{\mathcal{P}_1} < \sigma^2$	1.597	14.50	2.961	$\bar{r}_{\mathcal{P}_1} = \bar{r}_{\mathcal{P}_2}$
0.485	2.700	19.023	3.325	16.919	$s^2_{\mathcal{P}_2} < \sigma^2$				
0.767	2.700	19.023	3.325	16.919	$s^2_{\mathcal{P}_3} < \sigma^2$	2.085	17.13	2.895	$\bar{r}_{\mathcal{P}_3} = \bar{r}_{\mathcal{P}_2}$

Shutter parameter — horizontal angle to the *Up* target

Table B.14: Confidence intervals for the mean values of the horizontal angle to the *Up* target (in blue color), and statistical tests for the variance (in red color) and for the mean values (in green color). Each row corresponds to a different value of the user-defined parameter *Shutter* (see Section 3.5.2).

p_k [ms]	n_k	f	$\bar{r}_{\mathcal{P}_k}$ [µrad]	$s^2_{\mathcal{P}_k}$ [µrad^2]	$s_{\mathcal{P}_k}$ [µrad]	$s^2_{\bar{r}_{\mathcal{P}_k}}$ [µrad^2]	$s_{\bar{r}_{\mathcal{P}_k}}$ [µrad]	$t_f^{0.025}$	$\mathcal{I}^{0.025}$ [µrad]
100	10	9	0.05	0.0899	0.30	0.0090	0.09	2.262	$\pm$0.21
150	10	9	-0.30	0.0643	0.25	0.0064	0.08	2.262	$\pm$0.18
200	10	9	-0.07	0.3234	0.57	0.0323	0.18	2.262	$\pm$0.41
250	10	9	-0.17	0.0731	0.27	0.0073	0.09	2.262	$\pm$0.19
300	10	9	-0.05	0.2959	0.54	0.0296	0.17	2.262	$\pm$0.39
350	10	9	0.06	0.4925	0.70	0.0493	0.22	2.262	$\pm$0.50
400	10	9	0.49	0.2838	0.53	0.0284	0.17	2.262	$\pm$0.38

χ^2_f	$\chi^2_{0.975,f}$	$\chi^2_{0.025,f}$	$\chi^2_{0.95,f}$	$\chi^2_{0.05,f}$		$\lvert t\rvert$	ν	$t_\nu^{0.005}$	
0.146	2.700	19.023	3.325	16.919	$s^2_{\mathcal{P}_1} < \sigma^2$	1.661	17.81	2.882	$\bar{r}_{\mathcal{P}_1} = \bar{r}_{\mathcal{P}_4}$
0.104	2.700	19.023	3.325	16.919	$s^2_{\mathcal{P}_2} < \sigma^2$	1.176	17.93	2.880	$\bar{r}_{\mathcal{P}_2} = \bar{r}_{\mathcal{P}_4}$
0.524	2.700	19.023	3.325	16.919	$s^2_{\mathcal{P}_3} < \sigma^2$	0.478	12.87	3.017	$\bar{r}_{\mathcal{P}_3} = \bar{r}_{\mathcal{P}_4}$
0.119	2.700	19.023	3.325	16.919	$s^2_{\mathcal{P}_4} < \sigma^2$				
0.480	2.700	19.023	3.325	16.919	$s^2_{\mathcal{P}_5} < \sigma^2$	0.581	13.19	3.005	$\bar{r}_{\mathcal{P}_5} = \bar{r}_{\mathcal{P}_4}$
0.798	2.700	19.023	3.325	16.919	$s^2_{\mathcal{P}_6} < \sigma^2$	0.969	11.61	3.073	$\bar{r}_{\mathcal{P}_6} = \bar{r}_{\mathcal{P}_4}$
0.460	2.700	19.023	3.325	16.919	$s^2_{\mathcal{P}_7} < \sigma^2$	3.460	13.35	2.999	$\bar{r}_{\mathcal{P}_7} \neq \bar{r}_{\mathcal{P}_4}$

Shutter parameter — elevation angle to the *Up* target

Table B.15: Confidence intervals for the mean values of the elevation angle to the *Up* target (in blue color), and statistical tests for the variance (in red color) and for the mean values (in green color). Each row corresponds to a different value of the user-defined parameter *Shutter* (see Section 3.5.2).

p_k [ms]	n_k	f	$\bar{r}_{\mathcal{P}_k}$ [µrad]	$s^2_{\mathcal{P}_k}$ [µrad^2]	$s_{\mathcal{P}_k}$ [µrad]	$s^2_{\bar{r}_{\mathcal{P}_k}}$ [µrad^2]	$s_{\bar{r}_{\mathcal{P}_k}}$ [µrad]	$t_f^{0.025}$	$\mathcal{I}^{0.025}$ [µrad]
100	10	9	-1.80	0.6465	0.80	0.0646	0.25	2.262	$\pm$0.58
150	10	9	-1.82	0.3221	0.57	0.0322	0.18	2.262	$\pm$0.41
200	10	9	-1.67	0.4690	0.68	0.0469	0.22	2.262	$\pm$0.49
250	10	9	-1.29	0.2151	0.46	0.0215	0.15	2.262	$\pm$0.33
300	10	9	-0.29	0.5900	0.77	0.0590	0.24	2.262	$\pm$0.55
350	10	9	2.56	0.1666	0.41	0.0167	0.13	2.262	$\pm$0.29
400	10	9	4.32	0.7330	0.86	0.0733	0.27	2.262	$\pm$0.61

χ^2_f	$\chi^2_{0.975,f}$	$\chi^2_{0.025,f}$	$\chi^2_{0.95,f}$	$\chi^2_{0.05,f}$		$\lvert t\rvert$	ν	$t_\nu^{0.005}$	
1.048	2.700	19.023	3.325	16.919	$s^2_{\mathcal{P}_1} < \sigma^2$	1.736	14.39	2.964	$\bar{r}_{\mathcal{P}_1} = \bar{r}_{\mathcal{P}_4}$
0.522	2.700	19.023	3.325	16.919	$s^2_{\mathcal{P}_2} < \sigma^2$	2.267	17.31	2.892	$\bar{r}_{\mathcal{P}_2} = \bar{r}_{\mathcal{P}_4}$
0.760	2.700	19.023	3.325	16.919	$s^2_{\mathcal{P}_3} < \sigma^2$	1.465	15.82	2.925	$\bar{r}_{\mathcal{P}_3} = \bar{r}_{\mathcal{P}_4}$
0.349	2.700	19.023	3.325	16.919	$s^2_{\mathcal{P}_4} < \sigma^2$				
0.956	2.700	19.023	3.325	16.919	$s^2_{\mathcal{P}_5} < \sigma^2$	3.522	14.79	2.953	$\bar{r}_{\mathcal{P}_5} \neq \bar{r}_{\mathcal{P}_4}$
0.270	2.700	19.023	3.325	16.919	$s^2_{\mathcal{P}_6} < \sigma^2$	19.702	17.71	2.884	$\bar{r}_{\mathcal{P}_6} \neq \bar{r}_{\mathcal{P}_4}$
1.188	2.700	19.023	3.325	16.919	$s^2_{\mathcal{P}_7} < \sigma^2$	18.212	13.86	2.981	$\bar{r}_{\mathcal{P}_7} \neq \bar{r}_{\mathcal{P}_4}$

Gain parameter — horizontal angle to the *Side* target

Table B.16: Confidence intervals for the mean values of the horizontal angle to the *Side* target (in blue color), and statistical tests for the variance (in red color) and for the mean values (in green color). Each row corresponds to a different value of the user-defined parameter *Gain* (see Section 3.5.2).

p_k	n_k	f	$\bar{r}_{\mathcal{P}_k}$ [µrad]	$s^2_{\mathcal{P}_k}$ [µrad^2]	$s_{\mathcal{P}_k}$ [µrad]	$s^2_{\bar{r}_{\mathcal{P}_k}}$ [µrad^2]	$s_{\bar{r}_{\mathcal{P}_k}}$ [µrad]	$t_f^{0.025}$	$\mathcal{I}^{0.025}$ [µrad]
50	10	9	-0.10	0.2288	0.48	0.0229	0.15	2.262	$\pm$0.34
100	10	9	-0.13	0.3398	0.58	0.0340	0.18	2.262	$\pm$0.42
150	10	9	0.19	0.1238	0.35	0.0124	0.11	2.262	$\pm$0.25
200	10	9	-0.02	0.1827	0.43	0.0183	0.14	2.262	$\pm$0.31
250	10	9	-0.08	0.2506	0.50	0.0251	0.16	2.262	$\pm$0.36
300	10	9	0.03	0.1178	0.34	0.0118	0.11	2.262	$\pm$0.25
350	8	7	0.13	0.2852	0.53	0.0357	0.19	2.365	$\pm$0.45

χ^2_f	$\chi^2_{0.975,f}$	$\chi^2_{0.025,f}$	$\chi^2_{0.95,f}$	$\chi^2_{0.05,f}$		$\lvert t\rvert$	ν	$t_\nu^{0.005}$	
0.371	2.700	19.023	3.325	16.919	$s^2_{\mathcal{P}_1} < \sigma^2$	0.400	17.78	2.883	$\bar{r}_{\mathcal{P}_1} = \bar{r}_{\mathcal{P}_4}$
0.551	2.700	19.023	3.325	16.919	$s^2_{\mathcal{P}_2} < \sigma^2$	0.458	16.51	2.909	$\bar{r}_{\mathcal{P}_2} = \bar{r}_{\mathcal{P}_4}$
0.201	2.700	19.023	3.325	16.919	$s^2_{\mathcal{P}_3} < \sigma^2$	1.226	17.36	2.891	$\bar{r}_{\mathcal{P}_3} = \bar{r}_{\mathcal{P}_4}$
0.296	2.700	19.023	3.325	16.919	$s^2_{\mathcal{P}_4} < \sigma^2$				
0.406	2.700	19.023	3.325	16.919	$s^2_{\mathcal{P}_5} < \sigma^2$	0.285	17.57	2.887	$\bar{r}_{\mathcal{P}_5} = \bar{r}_{\mathcal{P}_4}$
0.191	2.700	19.023	3.325	16.919	$s^2_{\mathcal{P}_6} < \sigma^2$	0.322	17.20	2.894	$\bar{r}_{\mathcal{P}_6} = \bar{r}_{\mathcal{P}_4}$
0.360	1.690	16.013	2.167	14.067	$s^2_{\mathcal{P}_7} < \sigma^2$	0.663	13.30	3.001	$\bar{r}_{\mathcal{P}_7} = \bar{r}_{\mathcal{P}_4}$

Gain parameter — elevation angle to the *Side* target

Table B.17: Confidence intervals for the mean values of the elevation angle to the *Side* target (in blue color), and statistical tests for the variance (in red color) and for the mean values (in green color). Each row corresponds to a different value of the user-defined parameter *Gain* (see Section 3.5.2).

p_k	n_k	f	$\bar{r}_{\mathcal{P}_k}$ [µrad]	$s^2_{\mathcal{P}_k}$ [µrad^2]	$s_{\mathcal{P}_k}$ [µrad]	$s^2_{\bar{r}_{\mathcal{P}_k}}$ [µrad^2]	$s_{\bar{r}_{\mathcal{P}_k}}$ [µrad]	$t_f^{0.025}$	$\mathcal{I}^{0.025}$ [µrad]
50	10	9	-1.38	0.6208	0.79	0.0621	0.25	2.262	$\pm$0.56
100	10	9	-1.34	0.2958	0.54	0.0296	0.17	2.262	$\pm$0.39
150	10	9	-0.94	0.3483	0.59	0.0348	0.19	2.262	$\pm$0.42
200	10	9	-1.08	0.4482	0.67	0.0448	0.21	2.262	$\pm$0.48
250	10	9	-0.79	0.3693	0.61	0.0369	0.19	2.262	$\pm$0.43
300	10	9	1.80	0.4085	0.64	0.0409	0.20	2.262	$\pm$0.46
350	8	7	4.66	0.3100	0.56	0.0387	0.20	2.365	$\pm$0.47

χ^2_f	$\chi^2_{0.975,f}$	$\chi^2_{0.025,f}$	$\chi^2_{0.95,f}$	$\chi^2_{0.05,f}$		$\lvert t\rvert$	ν	$t_\nu^{0.005}$	
1.006	2.700	19.023	3.325	16.919	$s^2_{\mathcal{P}_1} < \sigma^2$	0.929	17.54	2.887	$\bar{r}_{\mathcal{P}_1} = \bar{r}_{\mathcal{P}_4}$
0.479	2.700	19.023	3.325	16.919	$s^2_{\mathcal{P}_2} < \sigma^2$	0.953	17.27	2.893	$\bar{r}_{\mathcal{P}_2} = \bar{r}_{\mathcal{P}_4}$
0.565	2.700	19.023	3.325	16.919	$s^2_{\mathcal{P}_3} < \sigma^2$	0.485	17.72	2.884	$\bar{r}_{\mathcal{P}_3} = \bar{r}_{\mathcal{P}_4}$
0.727	2.700	19.023	3.325	16.919	$s^2_{\mathcal{P}_4} < \sigma^2$				
0.599	2.700	19.023	3.325	16.919	$s^2_{\mathcal{P}_5} < \sigma^2$	1.013	17.83	2.882	$\bar{r}_{\mathcal{P}_5} = \bar{r}_{\mathcal{P}_4}$
0.662	2.700	19.023	3.325	16.919	$s^2_{\mathcal{P}_6} < \sigma^2$	9.821	17.96	2.879	$\bar{r}_{\mathcal{P}_6} \neq \bar{r}_{\mathcal{P}_4}$
0.391	1.690	16.013	2.167	14.067	$s^2_{\mathcal{P}_7} < \sigma^2$	19.856	15.96	2.922	$\bar{r}_{\mathcal{P}_7} \neq \bar{r}_{\mathcal{P}_4}$

Focus parameter — horizontal angle to the *Front* target

Table B.18: Confidence intervals for the mean values of the horizontal angle to the *Front* target (in blue color), and statistical tests for the variance (in red color) and for the mean values (in green color). Each row corresponds to a different value of the user-defined parameter *Focus* (see Section 3.5.2).

p_k [step]	n_k	f	$\bar{r}_{\mathcal{P}_k}$ [µrad]	$s^2_{\mathcal{P}_k}$ [µrad^2]	$s_{\mathcal{P}_k}$ [µrad]	$s^2_{\bar{r}_{\mathcal{P}_k}}$ [µrad^2]	$s_{\bar{r}_{\mathcal{P}_k}}$ [µrad]	$t_f^{0.025}$	$\mathcal{I}^{0.025}$ [µrad]
107100	9	8	-0.20	0.3123	0.56	0.0347	0.19	2.306	±0.43
107200	10	9	-0.28	0.1686	0.41	0.0169	0.13	2.262	±0.29
107300	10	9	-0.18	0.2169	0.47	0.0217	0.15	2.262	±0.33
107400	10	9	-0.17	0.1382	0.37	0.0138	0.12	2.262	±0.27
107500	10	9	0.22	0.5144	0.72	0.0514	0.23	2.262	±0.51
107600	10	9	0.06	0.3944	0.63	0.0394	0.20	2.262	±0.45
107700	10	9	0.54	0.5331	0.73	0.0533	0.23	2.262	±0.52

χ^2_f	$\chi^2_{0.975,f}$	$\chi^2_{0.025,f}$	$\chi^2_{0.95,f}$	$\chi^2_{0.05,f}$		$\lvert t\rvert$	ν	$t_\nu^{0.005}$	
0.450	2.180	17.535	2.733	15.507	$s^2_{\mathcal{P}_1} < \sigma^2$	0.147	13.71	2.987	$\bar{r}_{\mathcal{P}_1} = \bar{r}_{\mathcal{P}_4}$
0.273	2.700	19.023	3.325	16.919	$s^2_{\mathcal{P}_2} < \sigma^2$	0.613	17.83	2.882	$\bar{r}_{\mathcal{P}_2} = \bar{r}_{\mathcal{P}_4}$
0.352	2.700	19.023	3.325	16.919	$s^2_{\mathcal{P}_3} < \sigma^2$	0.069	17.16	2.895	$\bar{r}_{\mathcal{P}_3} = \bar{r}_{\mathcal{P}_4}$
0.224	2.700	19.023	3.325	16.919	$s^2_{\mathcal{P}_4} < \sigma^2$				
0.834	2.700	19.023	3.325	16.919	$s^2_{\mathcal{P}_5} < \sigma^2$	1.537	13.51	2.993	$\bar{r}_{\mathcal{P}_5} = \bar{r}_{\mathcal{P}_4}$
0.639	2.700	19.023	3.325	16.919	$s^2_{\mathcal{P}_6} < \sigma^2$	1.010	14.62	2.958	$\bar{r}_{\mathcal{P}_6} = \bar{r}_{\mathcal{P}_4}$
0.864	2.700	19.023	3.325	16.919	$s^2_{\mathcal{P}_7} < \sigma^2$	2.728	13.37	2.998	$\bar{r}_{\mathcal{P}_7} = \bar{r}_{\mathcal{P}_4}$

Focus parameter — elevation angle to the *Front* target

Table B.19: Confidence intervals for the mean values of the elevation angle to the *Front* target (in blue color), and statistical tests for the variance (in red color) and for the mean values (in green color). Each row corresponds to a different value of the user-defined parameter *Focus* (see Section 3.5.2).

p_k [step]	n_k	f	$\bar{r}_{\mathcal{P}_k}$ [µrad]	$s^2_{\mathcal{P}_k}$ [µrad^2]	$s_{\mathcal{P}_k}$ [µrad]	$s^2_{\bar{r}_{\mathcal{P}_k}}$ [µrad^2]	$s_{\bar{r}_{\mathcal{P}_k}}$ [µrad]	$t_f^{0.025}$	$\mathcal{I}^{0.025}$ [µrad]
107100	9	8	-0.06	0.5495	0.74	0.0611	0.25	2.306	±0.57
107200	10	9	0.19	0.3637	0.60	0.0364	0.19	2.262	±0.43
107300	10	9	-0.20	0.5250	0.72	0.0525	0.23	2.262	±0.52
107400	10	9	0.12	0.2139	0.46	0.0214	0.15	2.262	±0.33
107500	10	9	-0.05	0.6010	0.78	0.0601	0.25	2.262	±0.55
107600	10	9	-0.04	0.3510	0.59	0.0351	0.19	2.262	±0.42
107700	10	9	0.03	0.4361	0.66	0.0436	0.21	2.262	±0.47

χ^2_f	$\chi^2_{0.975,f}$	$\chi^2_{0.025,f}$	$\chi^2_{0.95,f}$	$\chi^2_{0.05,f}$		$\lvert t\rvert$	ν	$t_\nu^{0.005}$	
0.792	2.180	17.535	2.733	15.507	$s^2_{\mathcal{P}_1} < \sigma^2$	0.646	13.15	3.006	$\bar{r}_{\mathcal{P}_1} = \bar{r}_{\mathcal{P}_4}$
0.590	2.700	19.023	3.325	16.919	$s^2_{\mathcal{P}_2} < \sigma^2$	0.276	16.87	2.901	$\bar{r}_{\mathcal{P}_2} = \bar{r}_{\mathcal{P}_4}$
0.851	2.700	19.023	3.325	16.919	$s^2_{\mathcal{P}_3} < \sigma^2$	1.181	15.29	2.939	$\bar{r}_{\mathcal{P}_3} = \bar{r}_{\mathcal{P}_4}$
0.347	2.700	19.023	3.325	16.919	$s^2_{\mathcal{P}_4} < \sigma^2$				
0.974	2.700	19.023	3.325	16.919	$s^2_{\mathcal{P}_5} < \sigma^2$	0.587	14.69	2.956	$\bar{r}_{\mathcal{P}_5} = \bar{r}_{\mathcal{P}_4}$
0.569	2.700	19.023	3.325	16.919	$s^2_{\mathcal{P}_6} < \sigma^2$	0.672	17.00	2.898	$\bar{r}_{\mathcal{P}_6} = \bar{r}_{\mathcal{P}_4}$
0.707	2.700	19.023	3.325	16.919	$s^2_{\mathcal{P}_7} < \sigma^2$	0.377	16.12	2.918	$\bar{r}_{\mathcal{P}_7} = \bar{r}_{\mathcal{P}_4}$

Hz direction parameter — horizontal angle to the *Side* target

Table B.20: Confidence intervals for the mean values of the horizontal angle to the *Side* target (in blue color), and statistical tests for the variance (in red color) and for the mean values (in green color). Each row corresponds to a different value of the user-defined parameter *Hz direction* (see Section 3.5.2).

p_k [°]	n_k	f	$\bar{r}_{\mathcal{P}_k}$ [µrad]	$s^2_{\mathcal{P}_k}$ [µrad^2]	$s_{\mathcal{P}_k}$ [µrad]	$s^2_{\bar{r}_{\mathcal{P}_k}}$ [µrad^2]	$s_{\bar{r}_{\mathcal{P}_k}}$ [µrad]	$t_f^{0.025}$	$\mathcal{I}^{0.025}$ [µrad]
−0.20	11	10	-3.83	0.0637	0.25	0.0058	0.08	2.228	±0.17
−0.10	11	10	-1.82	0.1482	0.39	0.0135	0.12	2.228	±0.26
−0.05	11	10	-0.88	0.1406	0.38	0.0128	0.11	2.228	±0.25
0.00	11	10	-0.10	0.1601	0.40	0.0146	0.12	2.228	±0.27
+0.05	11	10	0.75	0.3852	0.62	0.0350	0.19	2.228	±0.42
+0.10	11	10	1.69	0.2287	0.48	0.0208	0.14	2.228	±0.32
+0.20	11	10	4.18	0.4702	0.69	0.0427	0.21	2.228	±0.46

χ^2_f	$\chi^2_{0.975,f}$	$\chi^2_{0.025,f}$	$\chi^2_{0.95,f}$	$\chi^2_{0.05,f}$		$\lvert t\rvert$	ν	$t_\nu^{0.005}$	
0.115	3.247	20.483	3.940	18.307	$s^2_{\mathcal{P}_1} < \sigma^2$	26.193	16.87	2.901	$\bar{r}_{\mathcal{P}_1} \neq \bar{r}_{\mathcal{P}_4}$
0.267	3.247	20.483	3.940	18.307	$s^2_{\mathcal{P}_2} < \sigma^2$	10.316	19.97	2.846	$\bar{r}_{\mathcal{P}_2} \neq \bar{r}_{\mathcal{P}_4}$
0.253	3.247	20.483	3.940	18.307	$s^2_{\mathcal{P}_3} < \sigma^2$	4.717	19.92	2.847	$\bar{r}_{\mathcal{P}_3} \neq \bar{r}_{\mathcal{P}_4}$
0.288	3.247	20.483	3.940	18.307	$s^2_{\mathcal{P}_4} < \sigma^2$				
0.694	3.247	20.483	3.940	18.307	$s^2_{\mathcal{P}_5} < \sigma^2$	3.788	17.09	2.896	$\bar{r}_{\mathcal{P}_5} \neq \bar{r}_{\mathcal{P}_4}$
0.412	3.247	20.483	3.940	18.307	$s^2_{\mathcal{P}_6} < \sigma^2$	9.525	19.40	2.855	$\bar{r}_{\mathcal{P}_6} \neq \bar{r}_{\mathcal{P}_4}$
0.847	3.247	20.483	3.940	18.307	$s^2_{\mathcal{P}_7} < \sigma^2$	17.874	16.10	2.918	$\bar{r}_{\mathcal{P}_7} \neq \bar{r}_{\mathcal{P}_4}$

Hz direction parameter — elevation angle to the *Side* target

Table B.21: Confidence intervals for the mean values of the elevation angle to the *Side* target (in blue color), and statistical tests for the variance (in red color) and for the mean values (in green color). Each row corresponds to a different value of the user-defined parameter *Hz direction* (see Section 3.5.2).

p_k [°]	n_k	f	$\bar{r}_{\mathcal{P}_k}$ [µrad]	$s^2_{\mathcal{P}_k}$ [µrad^2]	$s_{\mathcal{P}_k}$ [µrad]	$s^2_{\bar{r}_{\mathcal{P}_k}}$ [µrad^2]	$s_{\bar{r}_{\mathcal{P}_k}}$ [µrad]	$t_f^{0.025}$	$\mathcal{I}^{0.025}$ [µrad]
−0.20	11	10	-0.28	0.5164	0.72	0.0469	0.22	2.228	±0.48
−0.10	11	10	-0.41	0.5544	0.74	0.0504	0.22	2.228	±0.50
−0.05	11	10	0.29	0.4157	0.64	0.0378	0.19	2.228	±0.43
0.00	11	10	-0.22	0.8006	0.89	0.0728	0.27	2.228	±0.60
+0.05	11	10	0.07	0.4775	0.69	0.0434	0.21	2.228	±0.46
+0.10	11	10	0.25	0.2610	0.51	0.0237	0.15	2.228	±0.34
+0.20	11	10	0.29	0.3090	0.56	0.0281	0.17	2.228	±0.37

χ^2_f	$\chi^2_{0.975,f}$	$\chi^2_{0.025,f}$	$\chi^2_{0.95,f}$	$\chi^2_{0.05,f}$		$\lvert t\rvert$	ν	$t_\nu^{0.005}$	
0.930	3.247	20.483	3.940	18.307	$s^2_{\mathcal{P}_1} < \sigma^2$	0.172	19.11	2.859	$\bar{r}_{\mathcal{P}_1} = \bar{r}_{\mathcal{P}_4}$
0.999	3.247	20.483	3.940	18.307	$s^2_{\mathcal{P}_2} < \sigma^2$	0.536	19.36	2.855	$\bar{r}_{\mathcal{P}_2} = \bar{r}_{\mathcal{P}_4}$
0.749	3.247	20.483	3.940	18.307	$s^2_{\mathcal{P}_3} < \sigma^2$	1.525	18.18	2.875	$\bar{r}_{\mathcal{P}_3} = \bar{r}_{\mathcal{P}_4}$
1.442	3.247	20.483	3.940	18.307	$s^2_{\mathcal{P}_4} < \sigma^2$				
0.860	3.247	20.483	3.940	18.307	$s^2_{\mathcal{P}_5} < \sigma^2$	0.856	18.80	2.864	$\bar{r}_{\mathcal{P}_5} = \bar{r}_{\mathcal{P}_4}$
0.470	3.247	20.483	3.940	18.307	$s^2_{\mathcal{P}_6} < \sigma^2$	1.517	15.89	2.923	$\bar{r}_{\mathcal{P}_6} = \bar{r}_{\mathcal{P}_4}$
0.557	3.247	20.483	3.940	18.307	$s^2_{\mathcal{P}_7} < \sigma^2$	1.594	16.72	2.904	$\bar{r}_{\mathcal{P}_7} = \bar{r}_{\mathcal{P}_4}$

Zen angle parameter — horizontal angle to the *Side* target

Table B.22: Confidence intervals for the mean values of the horizontal angle to the *Side* target (in blue color), and statistical tests for the variance (in red color) and for the mean values (in green color). Each row corresponds to a different value of the user-defined parameter *Zen angle* (see Section 3.5.2).

p_k [°]	n_k	f	$\bar{r}_{\mathcal{P}_k}$ [µrad]	$s^2_{\mathcal{P}_k}$ [µrad^2]	$s_{\mathcal{P}_k}$ [µrad]	$s^2_{\bar{r}_{\mathcal{P}_k}}$ [µrad^2]	$s_{\bar{r}_{\mathcal{P}_k}}$ [µrad]	$t_f^{0.025}$	$\mathcal{I}^{0.025}$ [µrad]
−0.20	11	10	-0.08	0.1087	0.33	0.0099	0.10	2.228	±0.22
−0.10	11	10	0.10	0.2458	0.50	0.0223	0.15	2.228	±0.33
−0.05	11	10	0.01	0.2043	0.45	0.0186	0.14	2.228	±0.30
0.00	11	10	0.13	0.2010	0.45	0.0183	0.14	2.228	±0.30
+0.05	11	10	0.22	0.1080	0.33	0.0098	0.10	2.228	±0.22
+0.10	11	10	0.08	0.0805	0.28	0.0073	0.09	2.228	±0.19
+0.20	11	10	-0.46	0.4370	0.66	0.0397	0.20	2.228	±0.44

χ^2_f	$\chi^2_{0.975,f}$	$\chi^2_{0.025,f}$	$\chi^2_{0.95,f}$	$\chi^2_{0.05,f}$		$\lvert t\rvert$	ν	$t_\nu^{0.005}$	
0.196	3.247	20.483	3.940	18.307	$s^2_{\mathcal{P}_1} < \sigma^2$	1.296	18.37	2.872	$\bar{r}_{\mathcal{P}_1} = \bar{r}_{\mathcal{P}_4}$
0.443	3.247	20.483	3.940	18.307	$s^2_{\mathcal{P}_2} < \sigma^2$	0.173	19.80	2.848	$\bar{r}_{\mathcal{P}_2} = \bar{r}_{\mathcal{P}_4}$
0.368	3.247	20.483	3.940	18.307	$s^2_{\mathcal{P}_3} < \sigma^2$	0.661	20.00	2.845	$\bar{r}_{\mathcal{P}_3} = \bar{r}_{\mathcal{P}_4}$
0.362	3.247	20.483	3.940	18.307	$s^2_{\mathcal{P}_4} < \sigma^2$				
0.195	3.247	20.483	3.940	18.307	$s^2_{\mathcal{P}_5} < \sigma^2$	0.535	18.34	2.872	$\bar{r}_{\mathcal{P}_5} = \bar{r}_{\mathcal{P}_4}$
0.145	3.247	20.483	3.940	18.307	$s^2_{\mathcal{P}_6} < \sigma^2$	0.327	16.90	2.900	$\bar{r}_{\mathcal{P}_6} = \bar{r}_{\mathcal{P}_4}$
0.787	3.247	20.483	3.940	18.307	$s^2_{\mathcal{P}_7} < \sigma^2$	2.471	17.59	2.886	$\bar{r}_{\mathcal{P}_7} = \bar{r}_{\mathcal{P}_4}$

Zen angle parameter — elevation angle to the *Side* target

Table B.23: Confidence intervals for the mean values of the elevation angle to the *Side* target (in blue color), and statistical tests for the variance (in red color) and for the mean values (in green color). Each row corresponds to a different value of the user-defined parameter *Zen angle* (see Section 3.5.2).

p_k [°]	n_k	f	$\bar{r}_{\mathcal{P}_k}$ [µrad]	$s^2_{\mathcal{P}_k}$ [µrad^2]	$s_{\mathcal{P}_k}$ [µrad]	$s^2_{\bar{r}_{\mathcal{P}_k}}$ [µrad^2]	$s_{\bar{r}_{\mathcal{P}_k}}$ [µrad]	$t_f^{0.025}$	$\mathcal{I}^{0.025}$ [µrad]
−0.20	11	10	2.18	0.4767	0.69	0.0433	0.21	2.228	±0.46
−0.10	11	10	0.19	0.6887	0.83	0.0626	0.25	2.228	±0.55
−0.05	11	10	0.03	0.2428	0.49	0.0221	0.15	2.228	±0.33
0.00	11	10	-0.06	0.4109	0.64	0.0374	0.19	2.228	±0.43
+0.05	11	10	0.29	0.2386	0.49	0.0217	0.15	2.228	±0.33
+0.10	11	10	-0.36	0.6818	0.83	0.0620	0.25	2.228	±0.55
+0.20	11	10	-2.27	0.6610	0.81	0.0601	0.25	2.228	±0.55

χ^2_f	$\chi^2_{0.975,f}$	$\chi^2_{0.025,f}$	$\chi^2_{0.95,f}$	$\chi^2_{0.05,f}$		$\lvert t\rvert$	ν	$t_\nu^{0.005}$	
0.859	3.247	20.483	3.940	18.307	$s^2_{\mathcal{P}_1} < \sigma^2$	7.884	19.89	2.847	$\bar{r}_{\mathcal{P}_1} \neq \bar{r}_{\mathcal{P}_4}$
1.241	3.247	20.483	3.940	18.307	$s^2_{\mathcal{P}_2} < \sigma^2$	0.773	18.80	2.864	$\bar{r}_{\mathcal{P}_2} = \bar{r}_{\mathcal{P}_4}$
0.437	3.247	20.483	3.940	18.307	$s^2_{\mathcal{P}_3} < \sigma^2$	0.358	18.76	2.865	$\bar{r}_{\mathcal{P}_3} = \bar{r}_{\mathcal{P}_4}$
0.740	3.247	20.483	3.940	18.307	$s^2_{\mathcal{P}_4} < \sigma^2$				
0.430	3.247	20.483	3.940	18.307	$s^2_{\mathcal{P}_5} < \sigma^2$	1.430	18.68	2.866	$\bar{r}_{\mathcal{P}_5} = \bar{r}_{\mathcal{P}_4}$
1.228	3.247	20.483	3.940	18.307	$s^2_{\mathcal{P}_6} < \sigma^2$	0.959	18.84	2.864	$\bar{r}_{\mathcal{P}_6} = \bar{r}_{\mathcal{P}_4}$
1.191	3.247	20.483	3.940	18.307	$s^2_{\mathcal{P}_7} < \sigma^2$	7.075	18.97	2.861	$\bar{r}_{\mathcal{P}_7} \neq \bar{r}_{\mathcal{P}_4}$

Canny thres parameter — horizontal angle to the *Front* target

Table B.24: Confidence intervals for the mean values of the horizontal angle to the *Front* target (in blue color), and statistical tests for the variance (in red color) and for the mean values (in green color). Each row corresponds to a different value of the user-defined parameter *Canny thres* (see Section 3.5.3).

p_k [8-bit]	n_k	f	$\bar{r}_{\mathcal{P}_k}$ [µrad]	$s^2_{\mathcal{P}_k}$ [µrad^2]	$s_{\mathcal{P}_k}$ [µrad]	$s^2_{\bar{r}\mathcal{P}_k}$ [µrad^2]	$s_{\bar{r}\mathcal{P}_k}$ [µrad]	$t_f^{0.025}$	$\mathcal{I}^{0.025}$ [µrad]
80	9	8	0.29	0.1196	0.35	0.0133	0.12	2.306	±0.27
100	10	9	-0.12	0.3232	0.57	0.0323	0.18	2.262	±0.41
120	10	9	-0.01	0.3585	0.60	0.0358	0.19	2.262	±0.43
140	10	9	0.17	0.3893	0.62	0.0389	0.20	2.262	±0.45
160	10	9	0.17	0.2222	0.47	0.0222	0.15	2.262	±0.34
180	10	9	-0.37	0.1306	0.36	0.0131	0.11	2.262	±0.26
200	10	9	-0.09	0.2831	0.53	0.0283	0.17	2.262	±0.38

χ^2_f	$\chi^2_{0.975,f}$	$\chi^2_{0.025,f}$	$\chi^2_{0.95,f}$	$\chi^2_{0.05,f}$		$\|t\|$	ν	$t_\nu^{0.005}$	
0.172	2.180	17.535	2.733	15.507	$s^2_{\mathcal{P}_1} < \sigma^2$	0.514	14.32	2.967	$\bar{r}_{\mathcal{P}_1} = \bar{r}_{\mathcal{P}_4}$
0.524	2.700	19.023	3.325	16.919	$s^2_{\mathcal{P}_2} < \sigma^2$	1.079	17.85	2.881	$\bar{r}_{\mathcal{P}_2} = \bar{r}_{\mathcal{P}_4}$
0.581	2.700	19.023	3.325	16.919	$s^2_{\mathcal{P}_3} < \sigma^2$	0.657	17.97	2.879	$\bar{r}_{\mathcal{P}_3} = \bar{r}_{\mathcal{P}_4}$
0.631	2.700	19.023	3.325	16.919	$s^2_{\mathcal{P}_4} < \sigma^2$				
0.360	2.700	19.023	3.325	16.919	$s^2_{\mathcal{P}_5} < \sigma^2$	0.004	16.75	2.904	$\bar{r}_{\mathcal{P}_5} = \bar{r}_{\mathcal{P}_4}$
0.212	2.700	19.023	3.325	16.919	$s^2_{\mathcal{P}_6} < \sigma^2$	2.373	14.43	2.963	$\bar{r}_{\mathcal{P}_6} = \bar{r}_{\mathcal{P}_4}$
0.459	2.700	19.023	3.325	16.919	$s^2_{\mathcal{P}_7} < \sigma^2$	0.993	17.56	2.887	$\bar{r}_{\mathcal{P}_7} = \bar{r}_{\mathcal{P}_4}$

Canny thres parameter — elevation angle to the *Front* target

Table B.25: Confidence intervals for the mean values of the elevation angle to the *Front* target (in blue color), and statistical tests for the variance (in red color) and for the mean values (in green color). Each row corresponds to a different value of the user-defined parameter *Canny thres* (see Section 3.5.3).

p_k [8-bit]	n_k	f	$\bar{r}_{\mathcal{P}_k}$ [µrad]	$s^2_{\mathcal{P}_k}$ [µrad^2]	$s_{\mathcal{P}_k}$ [µrad]	$s^2_{\bar{r}\mathcal{P}_k}$ [µrad^2]	$s_{\bar{r}\mathcal{P}_k}$ [µrad]	$t_f^{0.025}$	$\mathcal{I}^{0.025}$ [µrad]
80	9	8	-0.11	0.1701	0.41	0.0189	0.14	2.306	±0.32
100	10	9	0.48	0.2560	0.51	0.0256	0.16	2.262	±0.36
120	10	9	-0.05	0.4527	0.67	0.0453	0.21	2.262	±0.48
140	10	9	0.14	0.2692	0.52	0.0269	0.16	2.262	±0.37
160	10	9	-0.31	0.6568	0.81	0.0657	0.26	2.262	±0.58
180	10	9	0.02	0.2361	0.49	0.0236	0.15	2.262	±0.35
200	10	9	-0.19	0.2118	0.46	0.0212	0.15	2.262	±0.33

χ^2_f	$\chi^2_{0.975,f}$	$\chi^2_{0.025,f}$	$\chi^2_{0.95,f}$	$\chi^2_{0.05,f}$		$\|t\|$	ν	$t_\nu^{0.005}$	
0.245	2.180	17.535	2.733	15.507	$s^2_{\mathcal{P}_1} < \sigma^2$	1.187	16.77	2.903	$\bar{r}_{\mathcal{P}_1} = \bar{r}_{\mathcal{P}_4}$
0.415	2.700	19.023	3.325	16.919	$s^2_{\mathcal{P}_2} < \sigma^2$	1.489	17.99	2.879	$\bar{r}_{\mathcal{P}_2} = \bar{r}_{\mathcal{P}_4}$
0.734	2.700	19.023	3.325	16.919	$s^2_{\mathcal{P}_3} < \sigma^2$	0.698	16.91	2.900	$\bar{r}_{\mathcal{P}_3} = \bar{r}_{\mathcal{P}_4}$
0.436	2.700	19.023	3.325	16.919	$s^2_{\mathcal{P}_4} < \sigma^2$				
1.065	2.700	19.023	3.325	16.919	$s^2_{\mathcal{P}_5} < \sigma^2$	1.471	15.32	2.938	$\bar{r}_{\mathcal{P}_5} = \bar{r}_{\mathcal{P}_4}$
0.383	2.700	19.023	3.325	16.919	$s^2_{\mathcal{P}_6} < \sigma^2$	0.559	17.92	2.880	$\bar{r}_{\mathcal{P}_6} = \bar{r}_{\mathcal{P}_4}$
0.343	2.700	19.023	3.325	16.919	$s^2_{\mathcal{P}_7} < \sigma^2$	1.524	17.75	2.883	$\bar{r}_{\mathcal{P}_7} = \bar{r}_{\mathcal{P}_4}$

Appendix C

Parameter values and sample images for the experimental evaluation of the wire detection algorithm

This appendix lists the full set of the parameter values that were used in each experiment conducted to evaluate the *wire detection algorithm*. The reference parameter values are given in Section C.1, while the following Sections C.2 – C.5 are dedicated to the parameters under examination, grouped accordingly. In addition, sample images of each experiment are presented, aiming to illustrate how the parameter values affect the acquired raw image and, in some cases, the result of the edge detection. The detailed analysis of the experiments can be found in Chapter 3.

C.1 Reference parameters

Table C.1: Reference parameter values for the experimental evaluation of the wire detection algorithm (see Section 3.4), arranged in the same sequence as they appear in the QDaedalus software interface.

# shots	**Std shot** [pixel]	**Shutter** [ms]	**Gain**	**Hz direction** [°]	**Zen angle** [°]
5	0.10	300	200	6.7896	90.0802
Focus [step]	**Min #pts**	**HW ROI** [pixel]	**HH ROI** [pixel]	**Canny thres** [8-bit]	**Max resid** [pixel]
108300	380	200	50	120	2

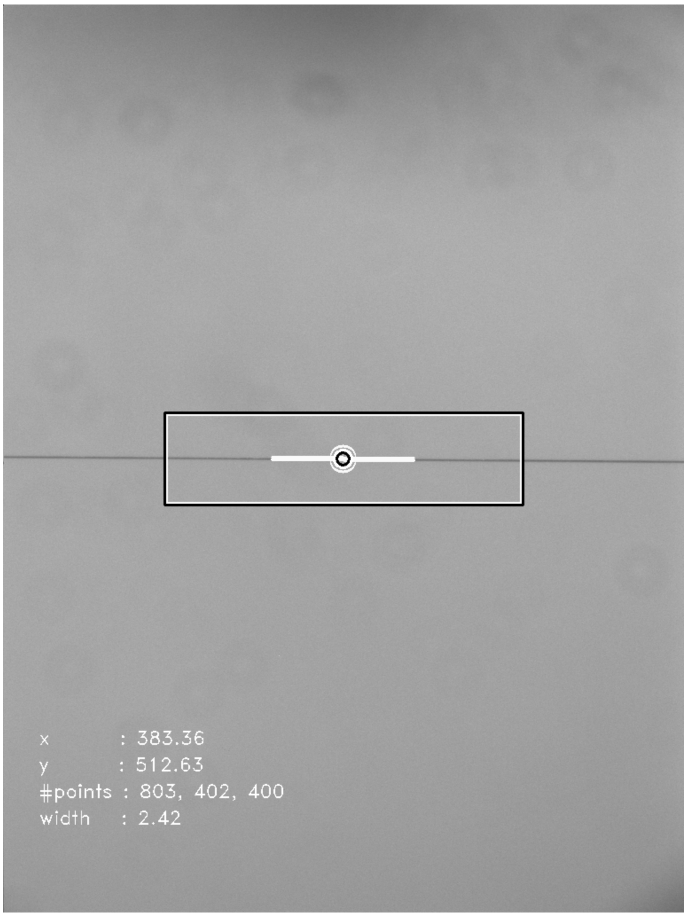

Figure C.1: Sample image of the wire detection algorithm that corresponds to the reference parameter values of Table C.1 (see Section 3.4).

C.2 Acquisition parameters

C.2.1 # *shots* parameter

Table C.2: Reference values (in blue color) and variable values (in red color) of the # *shots* parameter (see Section 3.4.1) for the experimental evaluation of the wire detection algorithm.

# shots	Std shot [pixel]	Shutter [ms]	Gain	Hz direction [°]	Zen angle [°]
3	0.10	300	200	6.7896	90.0802
5	0.10	300	200	6.7896	90.0802
10	0.10	300	200	6.7896	90.0802

Focus [step]	Min #pts	HW ROI [pixel]	HH ROI [pixel]	Canny thres [8-bit]	Max resid [pixel]
108300	380	200	50	120	2
108300	380	200	50	120	2
108300	380	200	50	120	2

C.2.2 *Std shot* parameter

Table C.3: Reference values (in blue color) and variable values (in red color) of the *Std shot* parameter (see Section 3.4.1) for the experimental evaluation of the wire detection algorithm.

# shots	Std shot [pixel]	Shutter [ms]	Gain	Hz direction [°]	Zen angle [°]
5	0.05	300	200	6.7896	90.0802
5	0.10	300	200	6.7896	90.0802
5	0.20	300	200	6.7896	90.0802

Focus [step]	Min #pts	HW ROI [pixel]	HH ROI [pixel]	Canny thres [8-bit]	Max resid [pixel]
108300	380	200	50	120	2
108300	380	200	50	120	2
108300	380	200	50	120	2

C.3 Image parameters

C.3.1 *Shutter* parameter

Table C.4: Reference values (in blue color) and variable values (in red color) of the *Shutter* parameter (see Section 3.4.2) for the experimental evaluation of the wire detection algorithm.

# shots	Std shot [pixel]	Shutter [ms]	Gain	Hz direction [°]	Zen angle [°]
5	0.10	210	200	6.7896	90.0802
5	0.10	240	200	6.7896	90.0802
5	0.10	270	200	6.7896	90.0802
5	0.10	300	200	6.7896	90.0802
5	0.10	330	200	6.7896	90.0802
5	0.10	360	200	6.7896	90.0802
5	0.10	390	200	6.7896	90.0802

Focus [step]	Min #pts	HW ROI [pixel]	HH ROI [pixel]	Canny thres [8-bit]	Max resid [pixel]
108300	380	200	50	120	2
108300	380	200	50	120	2
108300	380	200	50	120	2
108300	380	200	50	120	2
108300	380	200	50	120	2
108300	380	200	50	120	2
108300	380	200	50	120	2

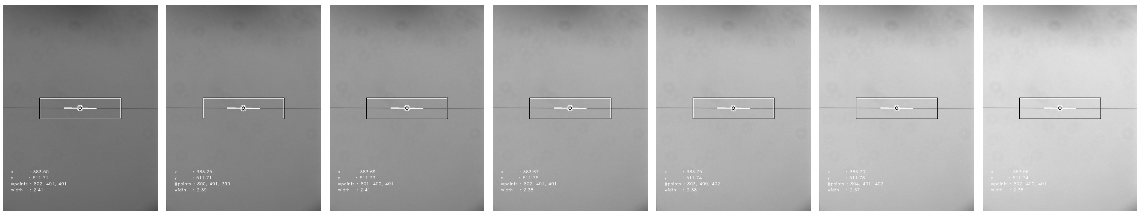

(a) (b) (c) (d) (e) (f) (g)

Figure C.2: Sample images of the wire detection algorithm that correspond to the *Shutter* experiment (see Table C.4 and Section 3.4.2). The values for the *Shutter* parameter are: (a) 210, (b) 240, (c) 270, (d) 300, (e) 330, (f) 360, and (g) 390.

C.3.2 *Gain* parameter

Table C.5: Reference values (in blue color) and variable values (in red color) of the *Gain* parameter (see Section 3.4.2) for the experimental evaluation of the wire detection algorithm.

# shots	Std shot [pixel]	Shutter [ms]	Gain	Hz direction [°]	Zen angle [°]
5	0.10	300	110	6.7896	90.0802
5	0.10	300	140	6.7896	90.0802
5	0.10	300	170	6.7896	90.0802
5	0.10	300	200	6.7896	90.0802
5	0.10	300	230	6.7896	90.0802
5	0.10	300	260	6.7896	90.0802
5	0.10	300	290	6.7896	90.0802

Focus [step]	Min #pts	HW ROI [pixel]	HH ROI [pixel]	Canny thres [8-bit]	Max resid [pixel]
108300	380	200	50	120	2
108300	380	200	50	120	2
108300	380	200	50	120	2
108300	380	200	50	120	2
108300	380	200	50	120	2
108300	380	200	50	120	2
108300	380	200	50	120	2

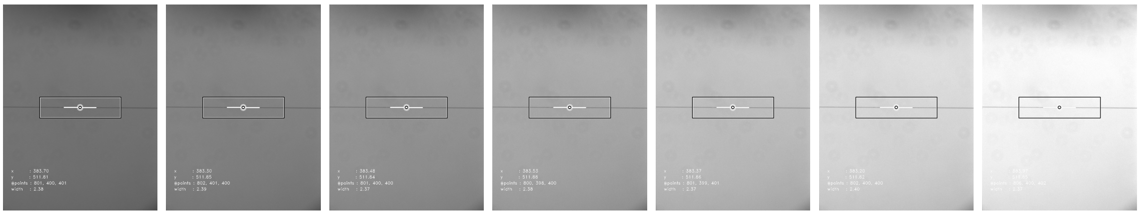

(a) (b) (c) (d) (e) (f) (g)

Figure C.3: Sample images of the wire detection algorithm that correspond to the *Gain* experiment (see Table C.5 and Section 3.4.2). The values for the *Gain* parameter are: (a) 110, (b) 140, (c) 170, (d) 200, (e) 230, (f) 260, and (g) 290.

C.3.3 *Focus* parameter

Table C.6: Reference values (in blue color) and variable values (in red color) of the *Focus* parameter (see Section 3.4.2) for the experimental evaluation of the wire detection algorithm.

# shots	Std shot [pixel]	Shutter [ms]	Gain	Hz direction [°]	Zen angle [°]
5	0.10	300	200	6.7896	90.0802
5	0.10	300	200	6.7896	90.0802
5	0.10	300	200	6.7896	90.0802
5	0.10	300	200	6.7896	90.0802
5	0.10	300	200	6.7896	90.0802
5	0.10	300	200	6.7896	90.0802
5	0.10	300	200	6.7896	90.0802

Focus [step]	Min #pts	HW ROI [pixel]	HH ROI [pixel]	Canny thres [8-bit]	Max resid [pixel]
108000	380	200	50	120	2
108100	380	200	50	120	2
108200	380	200	50	120	2
108300	380	200	50	120	2
108400	380	200	50	120	2
108500	380	200	50	120	2
108600	380	200	50	120	2

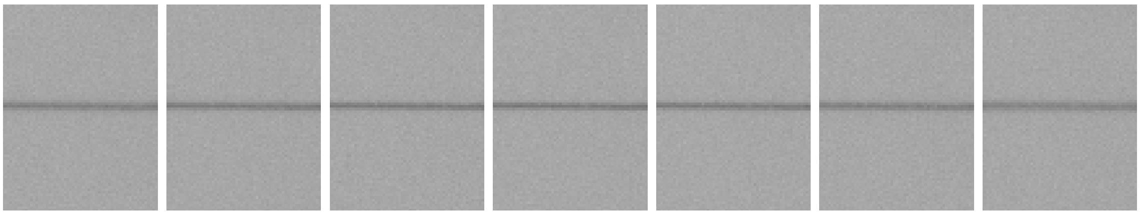

(a) (b) (c) (d) (e) (f) (g)

Figure C.4: Sample images of the wire detection algorithm that correspond to the *Focus* experiment (see Table C.6 and Section 3.4.2). The values for the *Focus* parameter are: (a) 108000, (b) 108100, (c) 108200, (d) 108300, (e) 108400, (f) 108500, and (g) 108600.

C.4 Detection parameters

C.4.1 *HW ROI* parameter

Table C.7: Reference values (in blue color) and variable values (in red color) of the *HW ROI* parameter (see Section 3.4.3) for the experimental evaluation of the wire detection algorithm. The values of the *Min #pts* parameter are selected according to the number of the detected edge points.

# shots	Std shot [pixel]	Shutter [ms]	Gain	Hz direction [°]	Zen angle [°]
5	0.10	300	200	6.7896	90.0802
5	0.10	300	200	6.7896	90.0802
5	0.10	300	200	6.7896	90.0802
5	0.10	300	200	6.7896	90.0802
5	0.10	300	200	6.7896	90.0802
5	0.10	300	200	6.7896	90.0802
5	0.10	300	200	6.7896	90.0802

Focus [step]	Min #pts	HW ROI [pixel]	HH ROI [pixel]	Canny thres [8-bit]	Max resid [pixel]
108300	80	50	50	120	2
108300	180	100	50	120	2
108300	280	150	50	120	2
108300	380	200	50	120	2
108300	480	250	50	120	2
108300	580	300	50	120	2
108300	680	350	50	120	2

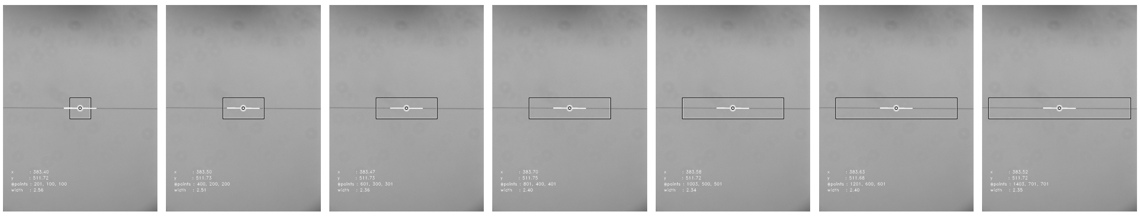

(a) (b) (c) (d) (e) (f) (g)

Figure C.5: Sample images of the wire detection algorithm that correspond to the *HW ROI* experiment (see Table C.7 and Section 3.4.3). The values for the *HW ROI* parameter are: (a) 50, (b) 100, (c) 150, (d) 200, (e) 250, (f) 300, and (g) 350.

C.4.2 *Canny thres* parameter

Table C.8: Reference values (in blue color) and variable values (in red color) of the *Canny thres* parameter (see Section 3.4.3) for the experimental evaluation of the wire detection algorithm.

# shots	Std shot [pixel]	Shutter [ms]	Gain	Hz direction [°]	Zen angle [°]
5	0.10	300	200	6.7896	90.0802
5	0.10	300	200	6.7896	90.0802
5	0.10	300	200	6.7896	90.0802
5	0.10	300	200	6.7896	90.0802
5	0.10	300	200	6.7896	90.0802
5	0.10	300	200	6.7896	90.0802
5	0.10	300	200	6.7896	90.0802

Focus [step]	Min #pts	HW ROI [pixel]	HH ROI [pixel]	Canny thres [8-bit]	Max resid [pixel]
108300	380	200	50	60	2
108300	380	200	50	80	2
108300	380	200	50	100	2
108300	380	200	50	120	2
108300	380	200	50	140	2
108300	380	200	50	160	2
108300	380	200	50	180	2

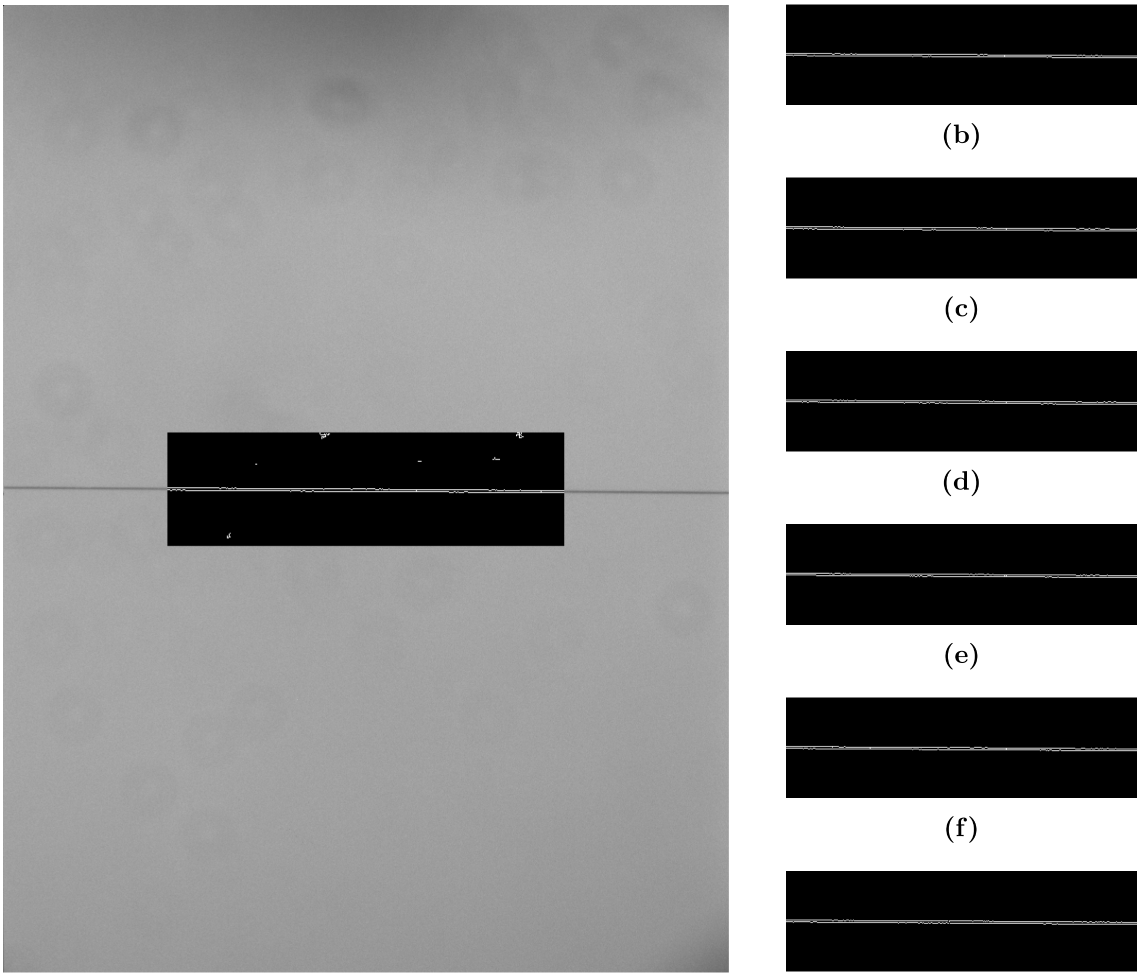

(a) (b) (c) (d) (e) (f) (g)

Figure C.6: Sample Canny edge images of the wire detection algorithm that correspond to the *Canny thres* experiment (see Table C.8 and Section 3.4.3). The values for the *Canny thres* parameter are: (a) 60, (b) 80, (c) 100, (d) 120, (e) 140, (f) 160, and (g) 180.

C.5 Environmental conditions

C.5.1 *Background* intensity

Table C.9: The parameter values remain invariable and equal to the reference values during the relevant to the *Background* intensity experimental evaluation of the wire detection algorithm (see Section 3.4.4).

# shots	Std shot [pixel]	Shutter [ms]	Gain	Hz direction [°]	Zen angle [°]
5	0.10	300	200	6.7896	90.0802
5	0.10	300	200	6.7896	90.0802
5	0.10	300	200	6.7896	90.0802

Focus [step]	Min #pts	HW ROI [pixel]	HH ROI [pixel]	Canny thres [8-bit]	Max resid [pixel]
108300	380	200	50	120	2
108300	380	200	50	120	2
108300	380	200	50	120	2

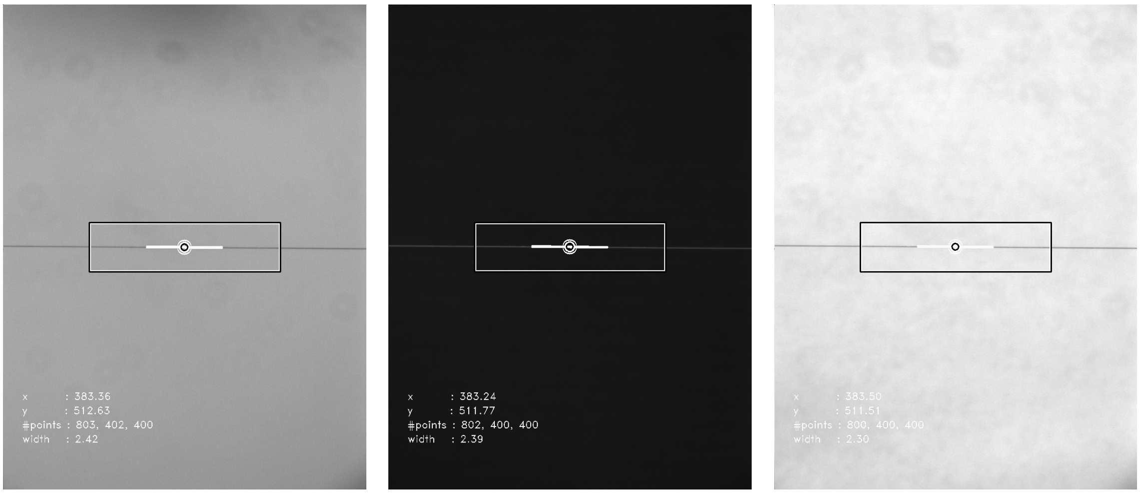

(a) (b) (c)

Figure C.7: Sample images of the wire detection algorithm that correspond to the *Background* experiment (see Table C.9 and Section 3.4.4). Three background intensities were examined: (a) grey, (b) dark (black), and (c) bright (white).

C.5.2 *Light* conditions

Table C.10: The parameter values remain invariable and equal to the reference values (except for a few values, in red color) during the relevant to the *Light* condition experimental evaluation of the wire detection algorithm (see Section 3.4.4).

# shots	Std shot [pixel]	Shutter [ms]	Gain	Hz direction [°]	Zen angle [°]
5	0.10	300	200	6.7896	90.0802
5	0.10	350	250	6.7896	90.0802
5	0.10	300	200	6.7896	90.0802
5	0.10	300	200	6.7896	90.0802
5	0.10	300	200	6.7896	90.0802
5	0.10	300	200	6.7896	90.0802
5	0.10	100	100	6.7896	90.0802

Focus [step]	Min #pts	HW ROI [pixel]	HH ROI [pixel]	Canny thres [8-bit]	Max resid [pixel]
108300	380	200	50	120	2
108300	380	200	50	50	2
108300	380	200	50	120	3
108300	380	200	50	120	2
108300	380	200	50	120	2
108300	380	200	50	120	2
108300	380	200	50	120	2

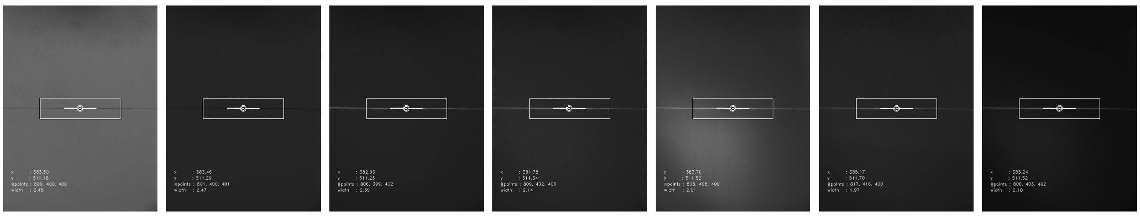

(a) (b) (c) (d) (e) (f) (g)

Figure C.8: Sample images of the wire detection algorithm relevant to the *Light* experiment (see Table C.10). Each image corresponds to one case, as described in Section 3.4.4: (a) laboratory ceiling lights switched on, (b) laboratory security lights switched on, (c) LED 1 switched on, (d) LED 2 switched on, (e) LED 3 switched on, (f) LED 4 switched on, and (g) all four LED lights switched on.

Appendix D

Parameter values and sample images for the experimental evaluation of the circle detection algorithm

This appendix lists the full set of the parameter values that were used in each experiment conducted to evaluate the *circle detection algorithm*. The reference parameter values are given in Section D.1, while the following Sections D.2 – D.4 are dedicated to the parameters under examination, grouped accordingly. In addition, sample images of each experiment are presented, aiming to illustrate how the parameter values affect the acquired raw image and, in some cases, the result of the edge detection. The detailed analysis of the experiments can be found in Chapter 3.

D.1 Reference parameters

Table D.1: Reference parameter values for the experimental evaluation of the circle detection algorithm to the *Front* target (see Section 3.5), arranged in the same sequence as they appear in the QDaedalus software interface.

# shots	Std shot [pixel]	Shutter [ms]	Gain	Hz direction [°]	Zen angle [°]
5	0.10	250	200	12.1420	91.3018
Focus [step]	**Min #pts**	**Max resid [pixel]**	**Min rad [pixel]**	**Max rad [pixel]**	**Canny thres [8-bit]**
107400	250	1	135	136	140

Table D.2: Reference parameter values for the experimental evaluation of the circle detection algorithm to the *Side* target (see Section 3.5), arranged in the same sequence as they appear in the QDaedalus software interface.

# shots	Std shot [pixel]	Shutter [ms]	Gain	Hz direction [°]	Zen angle [°]
5	0.10	250	200	13.3766	91.2578
Focus [step]	**Min #pts**	**Max resid [pixel]**	**Min rad [pixel]**	**Max rad [pixel]**	**Canny thres [8-bit]**
109000	250	1	132	133	140

Table D.3: Reference parameter values for the experimental evaluation of the circle detection algorithm to the *Up* target (see Section 3.5), arranged in the same sequence as they appear in the QDaedalus software interface.

# shots	Std shot [pixel]	Shutter [ms]	Gain	Hz direction [°]	Zen angle [°]
5	0.10	250	200	12.2161	90.0957

Focus [step]	Min #pts	Max resid [pixel]	Min rad [pixel]	Max rad [pixel]	Canny thres [8-bit]
109000	250	1	132	133	140

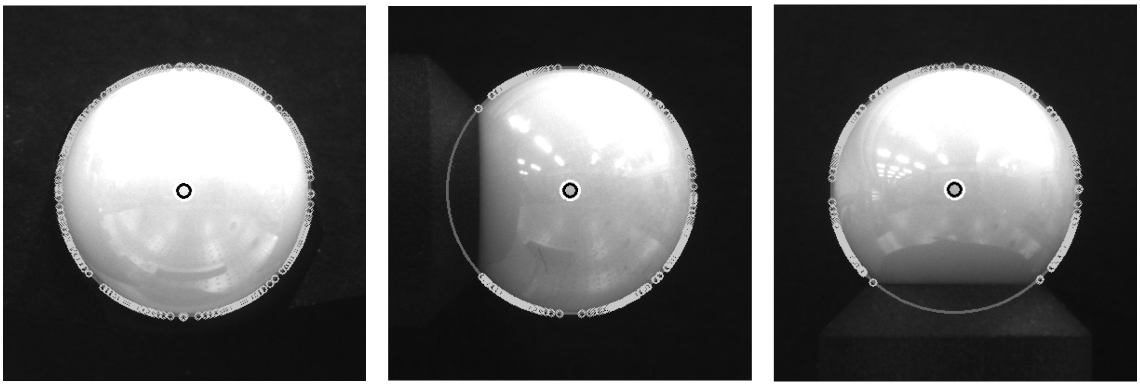

(a) (b) (c)

Figure D.1: Sample image of the circle detection algorithm for the *Front*, *Side* and *Up* targets that correspond to the reference parameter values in Tables D.1, D.2 and D.3 (see Section 3.5).

D.2 Acquisition parameters

D.2.1 # *shots* parameter

Table D.4: Reference values (in blue color) and variable values (in red color) of the # *shots* parameter to the *Up* target (see Section 3.5.1) for the experimental evaluation of the circle detection algorithm.

# shots	Std shot [pixel]	Shutter [ms]	Gain	Hz direction [°]	Zen angle [°]
3	0.10	250	200	12.2161	90.0957
5	0.10	250	200	12.2161	90.0957
10	0.10	250	200	12.2161	90.0957

Focus [step]	Min #pts	Max resid [pixel]	Min rad [pixel]	Max rad [pixel]	Canny thres [8-bit]
109000	250	1	132	133	140
109000	250	1	132	133	140
109000	250	1	132	133	140

D.2.2 *Std shot* parameter

Table D.5: Reference values (in blue color) and variable values (in red color) of the *Std shot* parameter to the *Up* target (see Section 3.5.1) for the experimental evaluation of the circle detection algorithm.

# shots	Std shot [pixel]	Shutter [ms]	Gain	Hz direction [°]	Zen angle [°]
5	0.05	250	200	12.2161	90.0957
5	0.10	250	200	12.2161	90.0957
5	0.20	250	200	12.2161	90.0957

Focus [step]	Min #pts	Max resid [pixel]	Min rad [pixel]	Max rad [pixel]	Canny thres [8-bit]
109000	250	1	132	133	140
109000	250	1	132	133	140
109000	250	1	132	133	140

D.3 Image parameters

D.3.1 *Shutter* parameter

Table D.6: Reference values (in blue color) and variable values (in red color) of the *Shutter* parameter to the *Up* target (see Section 3.5.2) for the experimental evaluation of the circle detection algorithm.

# shots	Std shot [pixel]	Shutter [ms]	Gain	Hz direction [°]	Zen angle [°]
5	0.10	100	200	12.2161	90.0957
5	0.10	150	200	12.2161	90.0957
5	0.10	200	200	12.2161	90.0957
5	0.10	250	200	12.2161	90.0957
5	0.10	300	200	12.2161	90.0957
5	0.10	350	200	12.2161	90.0957
5	0.10	400	200	12.2161	90.0957

Focus [step]	Min #pts	Max resid [pixel]	Min rad [pixel]	Max rad [pixel]	Canny thres [8-bit]
109000	250	1	132	133	140
109000	250	1	132	133	140
109000	250	1	132	133	140
109000	250	1	132	133	140
109000	250	1	132	133	140
109000	250	1	132	133	140
109000	250	1	132	133	140

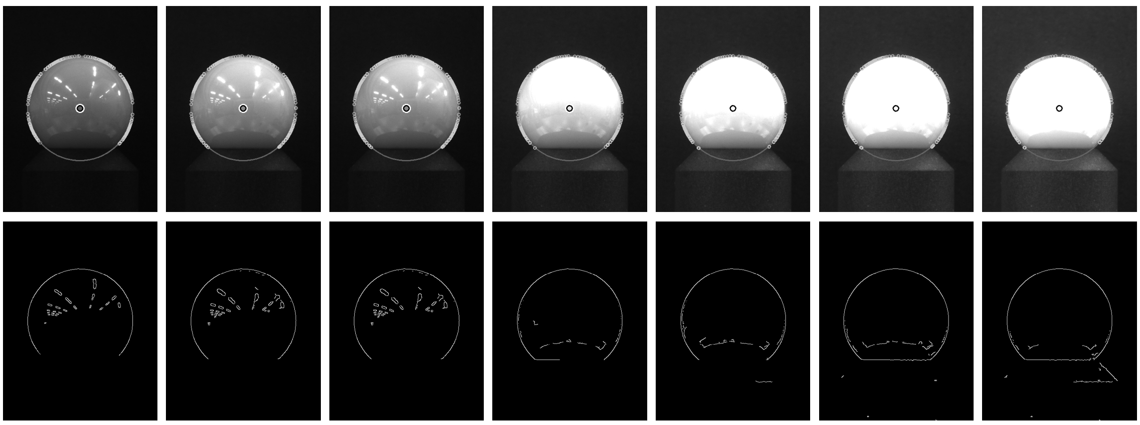

(a) (b) (c) (d) (e) (f) (g)

Figure D.2: Sample images of the circle detection algorithm and the corresponding Canny edge images for the *Shutter* experiment of the *Up* target (see Table D.6 and Section 3.5.2). The values for the *Shutter* parameter are: (a) 100, (b) 150, (c) 200, (d) 250, (e) 300, (f) 350, and (g) 400.

D.3.2 *Gain* parameter

Table D.7: Reference values (in blue color) and variable values (in red color) of the *Gain* parameter to the *Side* target (see Section 3.5.2) for the experimental evaluation of the circle detection algorithm.

# shots	Std shot [pixel]	Shutter [ms]	Gain	Hz direction [°]	Zen angle [°]
5	0.10	250	50	13.3766	91.2578
5	0.10	250	100	13.3766	91.2578
5	0.10	250	150	13.3766	91.2578
5	0.10	250	200	13.3766	91.2578
5	0.10	250	250	13.3766	91.2578
5	0.10	250	300	13.3766	91.2578
5	0.10	250	350	13.3766	91.2578
Focus [step]	**Min #pts**	**Max resid** [pixel]	**Min rad** [pixel]	**Max rad** [pixel]	**Canny thres** [8-bit]
109000	250	1	132	133	140
109000	250	1	132	133	140
109000	250	1	132	133	140
109000	250	1	132	133	140
109000	250	1	132	133	140
109000	250	1	132	133	140
109000	250	1	132	133	140

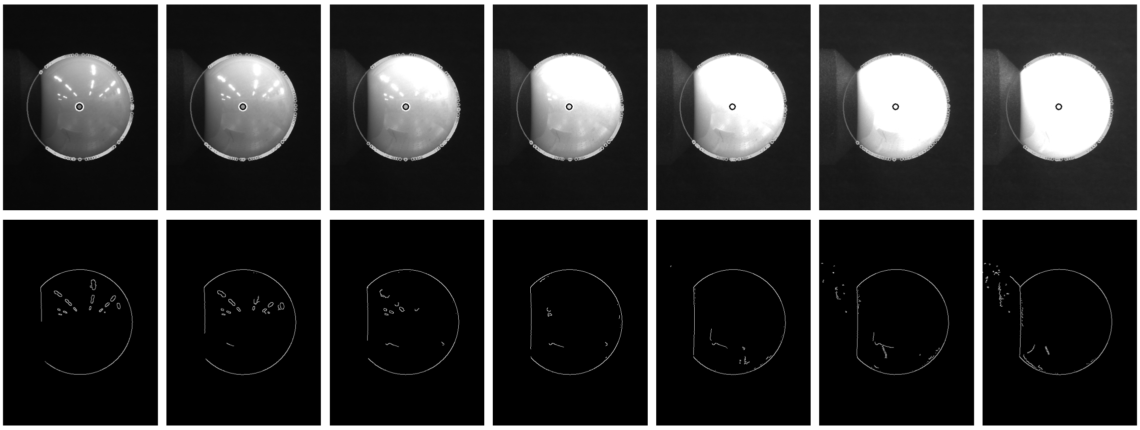

(a) (b) (c) (d) (e) (f) (g)

Figure D.3: Sample images of the circle detection algorithm and the corresponding Canny edge images for the *Gain* experiment of the *Side* target (see Table D.7 and Section 3.5.2). The values for the *Gain* parameter are: (a) 50, (b) 100, (c) 150, (d) 200, (e) 250, (f) 300, and (g) 350.

D.3.3 *Focus* parameter

Table D.8: Reference values (in blue color) and variable values (in red color) of the *Focus* parameter to the *Front* target (see Section 3.5.2) for the experimental evaluation of the circle detection algorithm.

# shots	Std shot [pixel]	Shutter [ms]	Gain	Hz direction [°]	Zen angle [°]
5	0.10	250	200	12.1420	91.3018
5	0.10	250	200	12.1420	91.3018
5	0.10	250	200	12.1420	91.3018
5	0.10	250	200	12.1420	91.3018
5	0.10	250	200	12.1420	91.3018
5	0.10	250	200	12.1420	91.3018
5	0.10	250	200	12.1420	91.3018
Focus [step]	**Min #pts**	**Max resid** [pixel]	**Min rad** [pixel]	**Max rad** [pixel]	**Canny thres** [8-bit]
107100	250	1	135	136	140
107200	250	1	135	136	140
107300	250	1	135	136	140
107400	250	1	135	136	140
107500	250	1	135	136	140
107600	250	1	135	136	140
107700	250	1	135	136	140

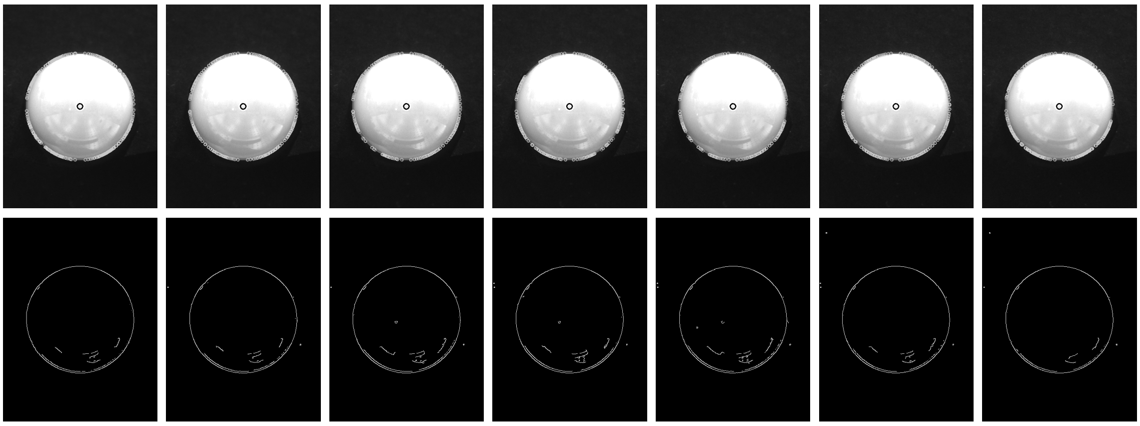

(a) (b) (c) (d) (e) (f) (g)

Figure D.4: Sample images of the circle detection algorithm and the corresponding Canny edge images for the *Focus* experiment of the *Front* target (see Table D.8 and Section 3.5.2). The values for the *Focus* parameter are: (a) 107100, (b) 107200, (c) 107300, (d) 107400, (e) 107500, (f) 107600, and (g) 107700.

D.3.4 *Hz direction* parameter

Table D.9: Reference values (in blue color) and variable values (in red color) of the *Hz direction* parameter to the *Side* target (see Section 3.5.2) for the experimental evaluation of the circle detection algorithm.

# shots	Std shot [pixel]	Shutter [ms]	Gain	Hz direction [°]	Zen angle [°]
5	0.10	250	200	13.5766	91.2578
5	0.10	250	200	13.4766	91.2578
5	0.10	250	200	13.4266	91.2578
5	0.10	250	200	13.3766	91.2578
5	0.10	250	200	13.3266	91.2578
5	0.10	250	200	13.2766	91.2578
5	0.10	250	200	13.1766	91.2578

Focus [step]	Min #pts	Max resid [pixel]	Min rad [pixel]	Max rad [pixel]	Canny thres [8-bit]
109000	250	1	132	133	140
109000	250	1	132	133	140
109000	250	1	132	133	140
109000	250	1	132	133	140
109000	250	1	132	133	140
109000	250	1	132	133	140
109000	250	1	132	133	140

(a)

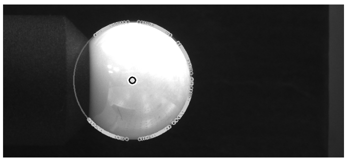

(b)

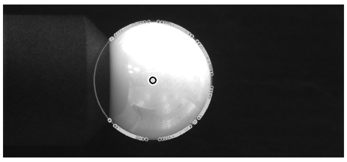

(c)

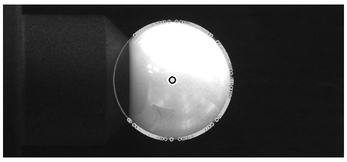

(d)

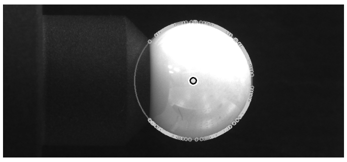

(e)

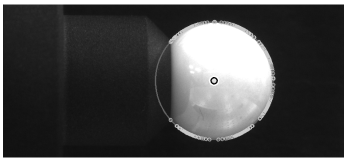

(f)

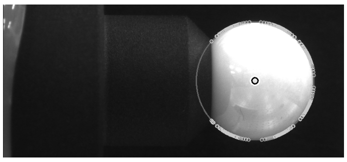

(g)

Figure D.5: Sample images of the circle detection algorithm that correspond to the *Hz direction* experiment for the *Side* target (see Table D.9 and Section 3.5.2). The horizontal angle differences with respect to the reference value for the *Hz direction* parameter are: (a) $-0.20°$, (b) $-0.10°$, (c) $-0.05°$, (d) $0°$, (e) $+0.05°$, (f) $+0.10°$, and (g) $+0.20°$.

D.3.5 *Zen angle* parameter

Table D.10: Reference values (in blue color) and variable values (in red color) of the *Zen angle* parameter to the *Side* target (see Section 3.5.2) for the experimental evaluation of the circle detection algorithm.

# shots	Std shot [pixel]	Shutter [ms]	Gain	Hz direction [°]	Zen angle [°]
5	0.10	250	200	13.3766	91.4578
5	0.10	250	200	13.3766	91.3578
5	0.10	250	200	13.3766	91.3078
5	0.10	250	200	13.3766	91.2578
5	0.10	250	200	13.3766	91.2078
5	0.10	250	200	13.3766	91.1578
5	0.10	250	200	13.3766	91.0578

Focus [step]	Min #pts	Max resid [pixel]	Min rad [pixel]	Max rad [pixel]	Canny thres [8-bit]
109000	250	1	132	133	140
109000	250	1	132	133	140
109000	250	1	132	133	140
109000	250	1	132	133	140
109000	250	1	132	133	140
109000	250	1	132	133	140
109000	250	1	132	133	140

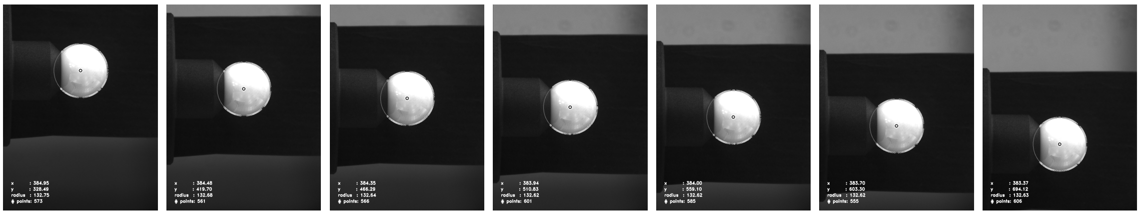

(a) (b) (c) (d) (e) (f) (g)

Figure D.6: Sample images of the circle detection algorithm that correspond to the *Zen angle* experiment for the *Side* target (see Table D.10 and Section 3.5.2). The vertical angle differences with respect to the reference value for the *Zen angle* parameter are: (a) −0.20°, (b) −0.10°, (c) −0.05°, (d) 0°, (e) +0.05°, (f) +0.10°, and (g) +0.20°.

D.4 Detection parameter

D.4.1 *Canny thres* parameter

Table D.11: Reference values (in blue color) and variable values (in red color) of the *Canny thres* parameter to the *Front* target (see Section 3.5.3) for the experimental evaluation of the circle detection algorithm.

# shots	Std shot [pixel]	Shutter [ms]	Gain	Hz direction [°]	Zen angle [°]
5	0.10	250	200	12.1420	91.3018
5	0.10	250	200	12.1420	91.3018
5	0.10	250	200	12.1420	91.3018
5	0.10	250	200	12.1420	91.3018
5	0.10	250	200	12.1420	91.3018
5	0.10	250	200	12.1420	91.3018
5	0.10	250	200	12.1420	91.3018
Focus [step]	**Min #pts**	**Max resid [pixel]**	**Min rad [pixel]**	**Max rad [pixel]**	**Canny thres [8-bit]**
107400	250	1	135	136	80
107400	250	1	135	136	100
107400	250	1	135	136	120
107400	250	1	135	136	140
107400	250	1	135	136	160
107400	250	1	135	136	180
107400	250	1	135	136	200

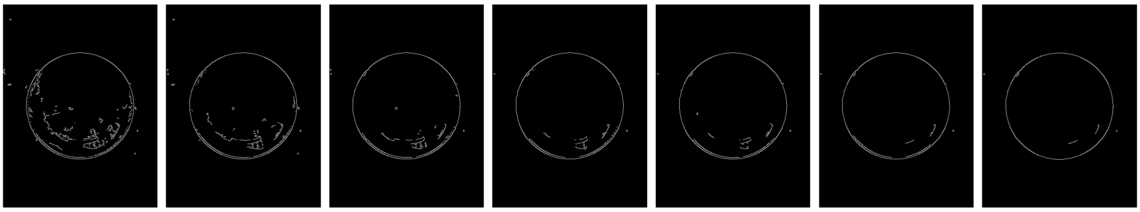

(a) (b) (c) (d) (e) (f) (g)

Figure D.7: Sample images of the circle detection algorithm that correspond to the *Canny thres* experiment for the *Front* target (see Table D.11 and Section 3.5.3). The values for the *Canny thres* parameter are: (a) 80, (b) 100, (c) 120, (d) 140, (e) 160, (f) 180, and (g) 200.

Appendix E

Parameter values and sample images of the wire detection algorithm for the micro-triangulation network

This appendix contains the input values of the *wire detection algorithm* parameters and sample images of the observations to the wire from each theodolite position, for the micro-triangulation measurement that took place in the metrology room on April 7, 2017 (see Chapter 5). We also examine the correspondence between the abrupt changes of the residuals of the zenith angle observations to the wire and the background intensities of the depicted wire.

E.1 Theodolite position S01

Table E.1: Parameter values of the wire detection algorithm for the theodolite position S01.

Target	# shots	Std shot [pixel]	Shutter [ms]	Gain	Hz direction [°]	Zen angle [°]
S01-P01	5	0.1	150	150	22.9054	115.6776
S01-P02	5	0.1	150	150	23.8247	115.5030
S01-P03	5	0.1	150	150	24.7581	115.3214
S01-P04	5	0.1	150	150	25.6996	115.1277
S01-P05	5	0.1	150	150	26.6127	114.9369
S01-P06	5	0.1	150	150	27.5229	114.7392
S01-P07	5	0.1	150	150	28.4892	114.5221
S01-P08	5	0.1	150	150	29.4159	114.3077
S01-P09	5	0.1	150	150	30.3274	114.0905
S01-P10	5	0.1	150	150	31.2798	113.8574
S01-P11	5	0.1	150	150	32.2181	113.6189
S01-P12	5	0.1	150	150	33.1225	113.3846
S01-P13	5	0.1	150	150	34.0414	113.1415
S01-P14	5	0.1	150	150	34.9879	112.8838
S01-P15	5	0.1	150	150	35.9194	112.6227
S01-P16	5	0.1	150	150	36.8316	112.3613
S01-P17	5	0.1	150	150	37.7897	112.0801
S01-P18	5	0.1	150	150	38.6824	111.8122
S01-P19	5	0.1	150	150	39.6367	111.5197
S01-P20	5	0.1	150	150	40.5575	111.2307

Target	Focus [step]	Min #pts	HW ROI [pixel]	HH ROI [pixel]	Canny thres [8-bit]	Max resid [pixel]
S01-P01	78550	120	100	50	150	5
S01-P02	78950	120	100	50	150	5
S01-P03	80150	120	100	50	150	5
S01-P04	80860	120	100	50	150	5
S01-P05	81810	120	100	50	150	5
S01-P06	82600	120	100	50	150	5
S01-P07	83650	120	100	50	150	5
S01-P08	84700	120	100	50	150	5
S01-P09	85450	120	100	50	150	5
S01-P10	86600	120	100	50	150	5
S01-P11	87700	120	100	50	150	5
S01-P12	88650	120	100	50	150	5
S01-P13	89550	120	100	50	150	5
S01-P14	90750	120	100	50	150	5
S01-P15	91850	120	100	50	150	5
S01-P16	92900	120	100	50	150	5
S01-P17	94150	120	100	50	100	5
S01-P18	95200	120	100	50	150	5
S01-P19	96450	120	100	50	150	5
S01-P20	97700	120	100	50	150	5

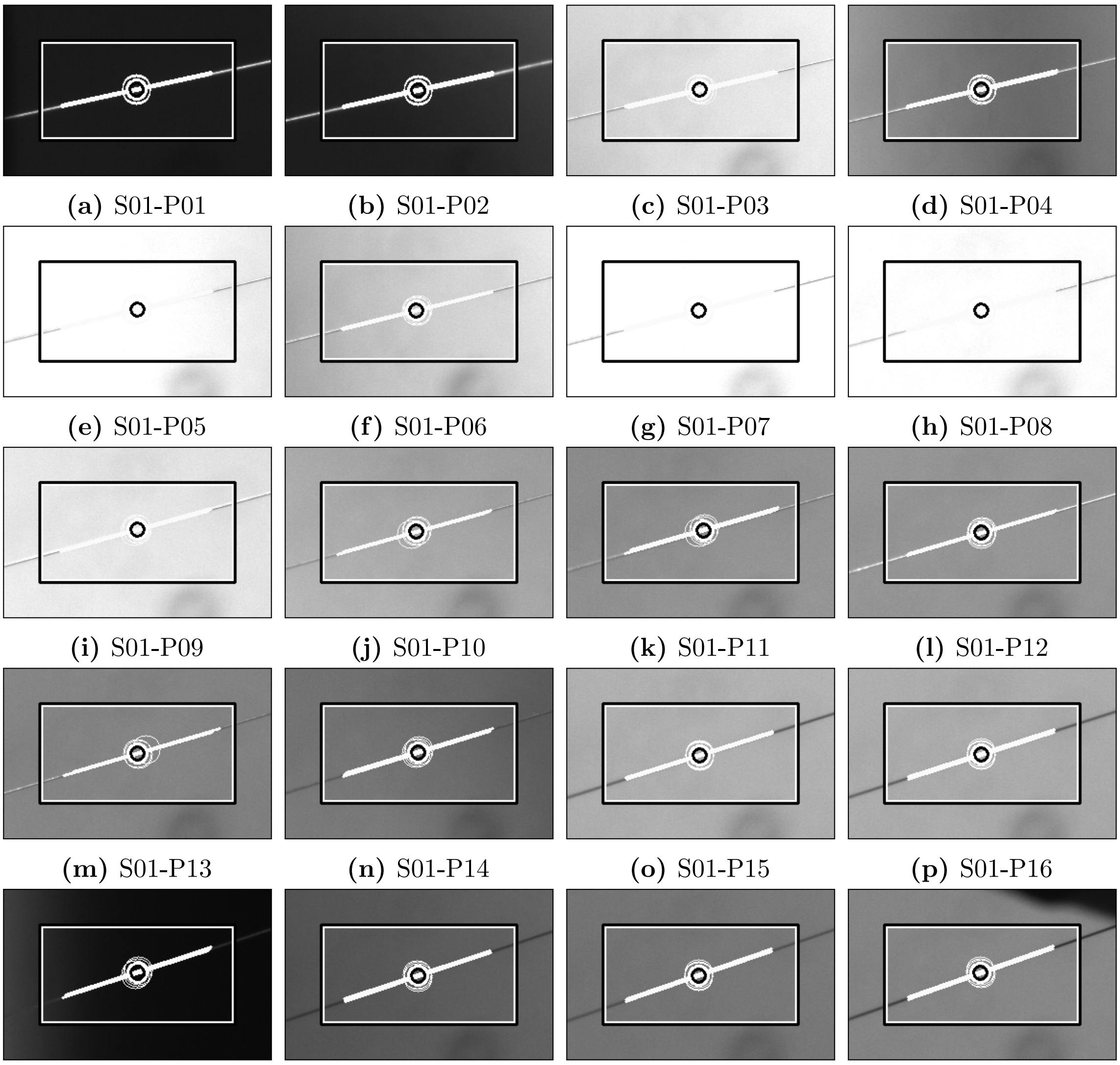

(a) S01-P01 (b) S01-P02 (c) S01-P03 (d) S01-P04

(e) S01-P05 (f) S01-P06 (g) S01-P07 (h) S01-P08

(i) S01-P09 (j) S01-P10 (k) S01-P11 (l) S01-P12

(m) S01-P13 (n) S01-P14 (o) S01-P15 (p) S01-P16

(q) S01-P17 (r) S01-P18 (s) S01-P19 (t) S01-P20

Figure E.1: Sample images of the observations to the wire acquired from the theodolite position S01.

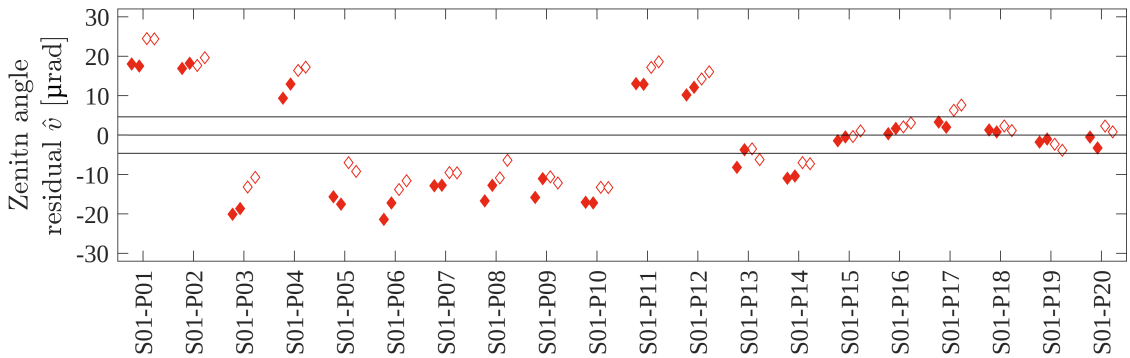

Figure E.2: Residuals of the zenith angle observations for sequential points on the wire observed from the theodolite position S01.

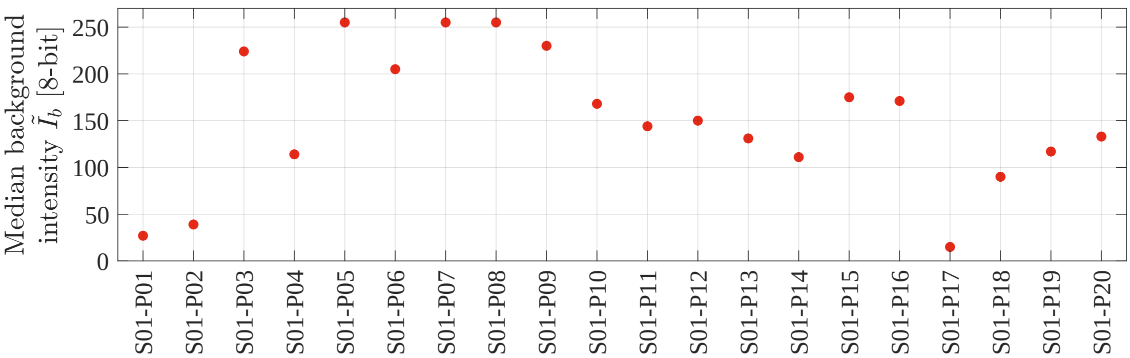

Figure E.3: Median of the background intensities in the proximity of the wire. The values correspond to the sample images in Figure E.1, acquired from the theodolite position S01.

Remarks

In Figure E.2, we observe that the abrupt changes in the residuals for the pair of images (S01-P02, S01-P03), (S01-P03, S01-P04) and (S01-P04, S01-P05) are in agreement with the corresponding changes in the background intensities, as computed from the sample images in Figure E.1 and shown in Figure E.3. Moreover, there are cases in which very small changes in the residuals correspond to very small changes in the background intensity such as for the pairs of images (S01-P01, S01-P02), (S01-P07, S01-P08) and (S01-P11, S01-P12).

On the contrary, for the pairs of images (S01-P10, S01-P11), and (S01-P12, S01-P13) the abrupt changes in the residuals do not correspond to significant changes in the background intensities. Moreover, the large changes in the background intensities for the pairs of images (S01-P16, S01-P17), and (S01-P17, S01-P18) do not match with significant changes in the corresponding residuals.

E.2 Theodolite position S02

Table E.2: Parameter values of the wire detection algorithm for the theodolite position S02.

Target	# shots	Std shot [pixel]	Shutter [ms]	Gain	Hz direction [°]	Zen angle [°]
S02-P01	5	0.1	150	150	9.8828	112.7082
S02-P02	5	0.1	150	150	10.8494	112.9521
S02-P03	5	0.1	150	150	12.1124	113.2644
S02-P04	5	0.1	150	150	12.9396	113.4621
S02-P05	5	0.1	150	150	14.1763	113.7487
S02-P06	5	0.1	150	150	15.0472	113.9437
S02-P07	5	0.1	150	150	16.2311	114.2020
S02-P08	5	0.1	150	150	17.0404	114.3718
S02-P09	5	0.1	150	150	18.1420	114.5925
S02-P10	5	0.1	150	150	19.1805	114.7946
S02-P11	5	0.1	150	150	20.2295	114.9930
S02-P12	5	0.1	150	150	21.2697	115.1798
S02-P13	5	0.1	150	150	22.4130	115.3746
S02-P14	5	0.1	150	150	23.3361	115.5265
S02-P15	5	0.1	150	150	24.3995	115.6936
S02-P16	5	0.1	150	150	25.4731	115.8540
S02-P17	5	0.1	150	150	26.2298	115.9618
S02-P18	5	0.1	150	150	27.6035	116.1476
S02-P19	5	0.1	150	150	28.5509	116.2683
S02-P20	5	0.1	150	150	29.5860	116.3920

Target	Focus [step]	Min #pts	HW ROI [pixel]	HH ROI [pixel]	Canny thres [8-bit]	Max resid [pixel]
S02-P01	91500	120	100	50	150	5
S02-P02	90400	120	100	50	150	5
S02-P03	89250	120	100	50	150	5
S02-P04	88150	120	100	50	150	5
S02-P05	87000	120	100	50	150	5
S02-P06	86050	120	100	50	150	5
S02-P07	85100	120	100	50	150	5
S02-P08	84250	120	100	50	170	5
S02-P09	83200	120	100	50	150	5
S02-P10	82350	120	100	50	150	5
S02-P11	81550	120	100	50	150	5
S02-P12	80750	120	100	50	150	5
S02-P13	79950	120	100	50	150	5
S02-P14	79200	120	100	50	150	5
S02-P15	78500	120	100	50	150	5
S02-P16	77800	120	100	50	150	5
S02-P17	77400	120	100	50	150	5
S02-P18	76800	120	100	50	80	5
S02-P19	76050	120	100	50	150	5
S02-P20	75500	120	100	50	150	5

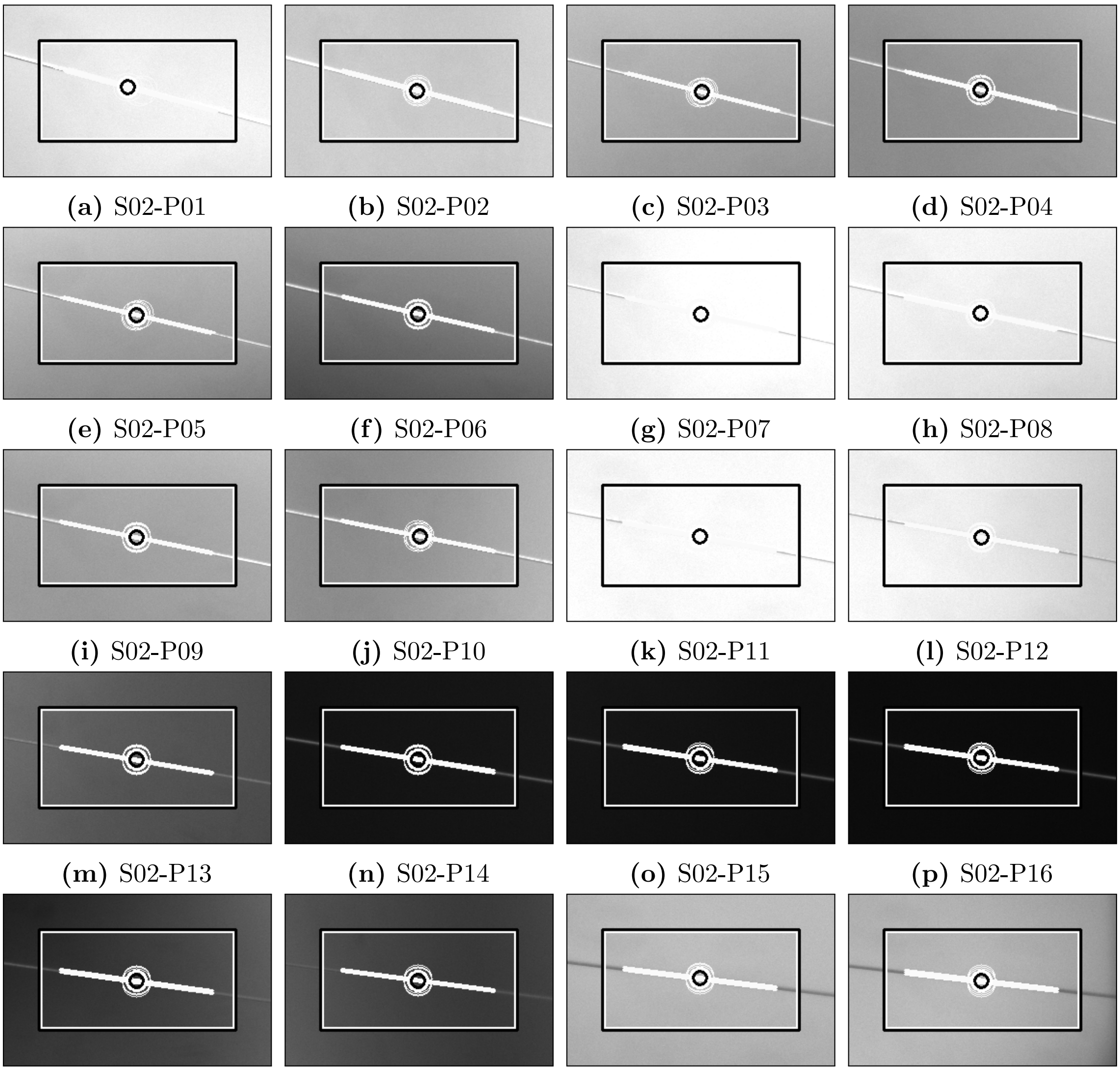

(a) S02-P01 (b) S02-P02 (c) S02-P03 (d) S02-P04

(e) S02-P05 (f) S02-P06 (g) S02-P07 (h) S02-P08

(i) S02-P09 (j) S02-P10 (k) S02-P11 (l) S02-P12

(m) S02-P13 (n) S02-P14 (o) S02-P15 (p) S02-P16

(q) S02-P17 (r) S02-P18 (s) S02-P19 (t) S02-P20

Figure E.4: Sample images of the observations to the wire acquired from the theodolite position S02.

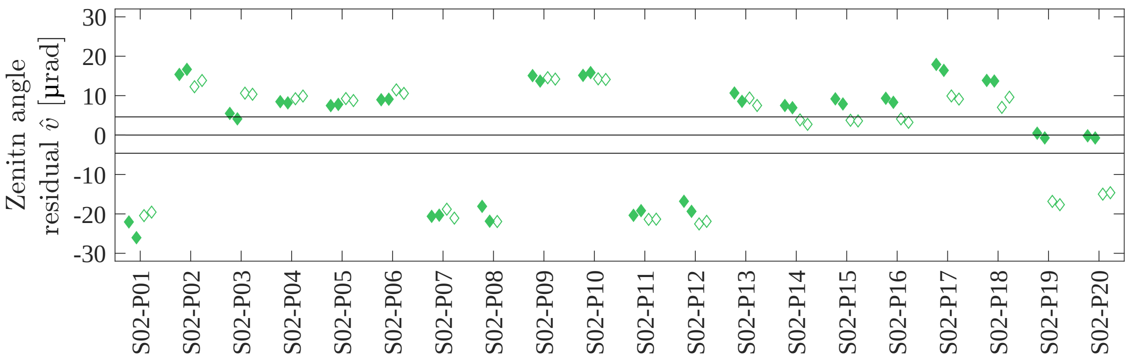

Figure E.5: Residuals of the zenith angle observations for sequential points on the wire observed from the theodolite position S02.

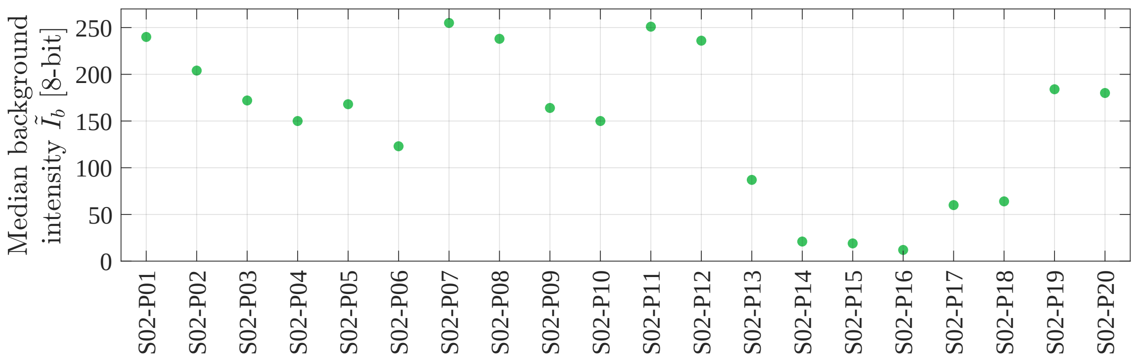

Figure E.6: Median of the background intensities in the proximity of the wire. The values correspond to the sample images in Figure E.4, acquired from the theodolite position S02.

Remarks

In Figures E.5 and E.6, we observe that the vast majority of the abrupt changes in the residuals are in agreement with the corresponding changes in the background intensities. The most obvious cases are for the pairs of images (S02-P06, S02-P07), (S02-P08, S02-P09), (S02-P10, S02-P11), (S02-P12, S02-P13), (S02-P16, S02-P17) and (S02-P18, S02-P19). Moreover, for the pairs of images (S02-P07, S02-P08), (S02-P09, S02-P10), (S02-P11, S02-P12), (S02-P14, S02-P15), (S02-P17, S02-P18) and (S02-P19, S02-P20), we do not observe any significant changes neither in the residuals nor in the background intensities.

The aforementioned examples support the assumption that there is a connection between the two magnitudes, however, there are cases such as the pair of images (S02-P01, S02-P02) that a large difference in the residuals does not correspond to a significant difference in the background intensities of the sample images.

In the case of the images S02-P01, S02-P07, S02-P08, S02-P11 and S02-P12, the large residual values seem to be caused by the very bright upper part of the wire, in combination with the large shadow underneath (Figure E.4a).

E.3 Theodolite position S03

Table E.3: Parameter values of the wire detection algorithm for the theodolite position S03.

Target	# shots	Std shot [pixel]	Shutter [ms]	Gain	Hz direction [°]	Zen angle [°]
S03-P01	5	0.1	150	150	32.6448	108.7610
S03-P02	5	0.1	150	150	31.7172	108.9070
S03-P03	5	0.1	150	150	30.8341	109.0421
S03-P04	5	0.1	150	150	29.9685	109.1702
S03-P05	5	0.1	150	150	29.0648	109.2996
S03-P06	5	0.1	150	150	28.1519	109.4251
S03-P07	5	0.1	150	150	27.2463	109.5452
S03-P08	5	0.1	150	150	26.3633	109.6576
S03-P09	5	0.1	150	150	25.4643	109.7677
S03-P10	5	0.1	150	150	24.5795	109.8714
S03-P11	5	0.1	150	150	23.6707	109.9733
S03-P12	5	0.1	150	150	22.8212	110.0641
S03-P13	5	0.1	150	150	22.0507	110.1428
S03-P14	5	0.1	150	150	20.9806	110.2469
S03-P15	5	0.1	150	150	20.0847	110.3285
S03-P16	5	0.1	150	150	19.1730	110.4070
S03-P17	5	0.1	150	150	18.2964	110.4778
S03-P18	5	0.1	150	150	17.3889	110.5464
S03-P19	5	0.1	150	150	16.4878	110.6099
S03-P20	5	0.1	150	150	15.5816	110.6688

Target	Focus [step]	Min #pts	HW ROI [pixel]	HH ROI [pixel]	Canny thres [8-bit]	Max resid [pixel]
S03-P01	107650	120	100	50	100	5
S03-P02	107350	120	100	50	100	5
S03-P03	106850	120	100	50	100	5
S03-P04	106350	120	100	50	100	5
S03-P05	106100	120	100	50	100	5
S03-P06	105000	120	100	50	100	5
S03-P07	104550	120	100	50	100	5
S03-P08	104500	120	100	50	100	5
S03-P09	103850	120	100	50	100	5
S03-P10	103400	120	100	50	100	5
S03-P11	103050	120	100	50	100	5
S03-P12	102600	120	100	50	100	5
S03-P13	102350	120	100	50	100	5
S03-P14	101850	120	100	50	100	5
S03-P15	101450	120	100	50	100	5
S03-P16	101150	120	100	50	100	5
S03-P17	100850	120	100	50	100	5
S03-P18	100550	120	100	50	100	5
S03-P19	100300	120	100	50	100	5
S03-P20	99700	120	100	50	100	5

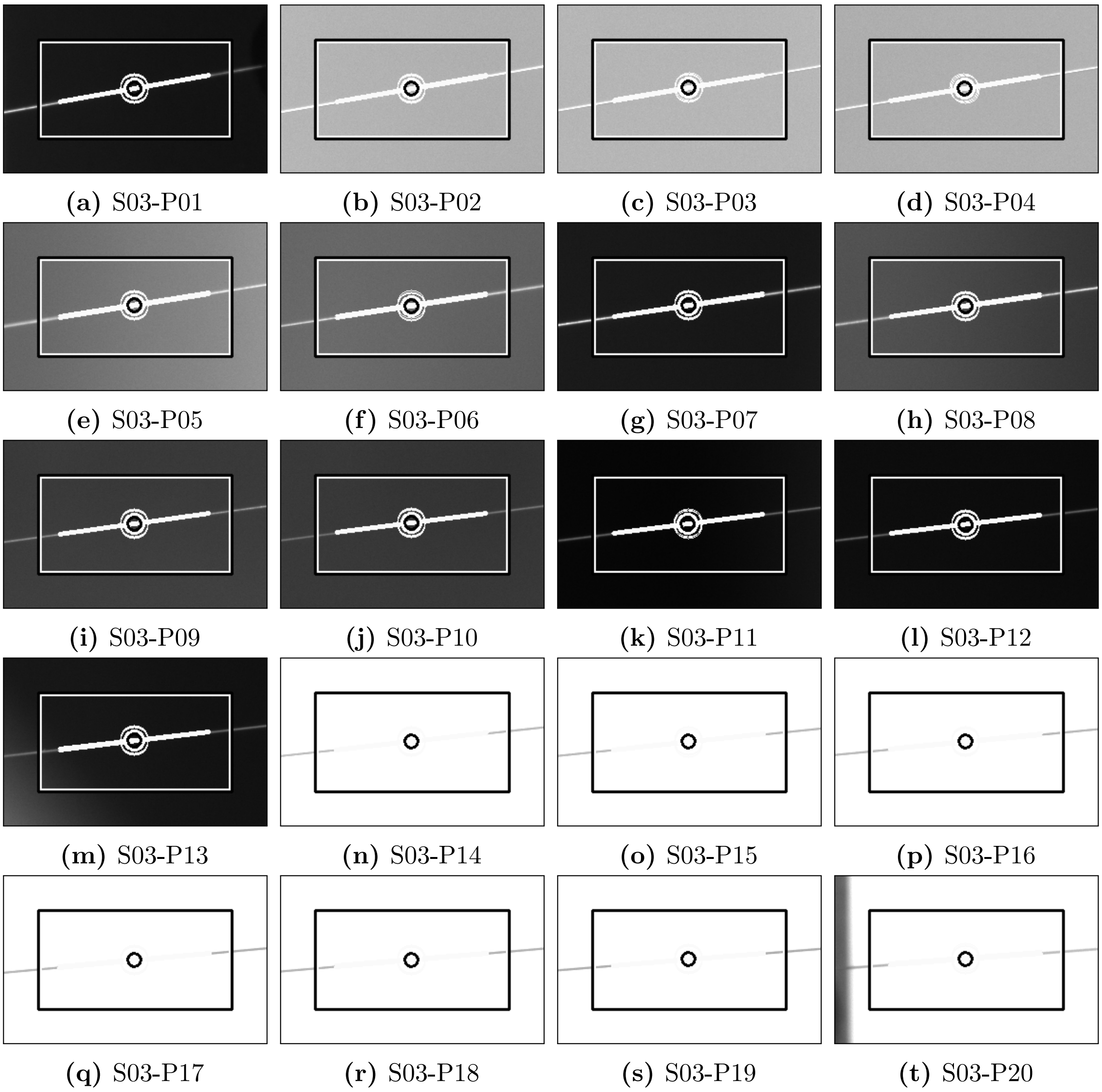

(a) S03-P01 (b) S03-P02 (c) S03-P03 (d) S03-P04
(e) S03-P05 (f) S03-P06 (g) S03-P07 (h) S03-P08
(i) S03-P09 (j) S03-P10 (k) S03-P11 (l) S03-P12
(m) S03-P13 (n) S03-P14 (o) S03-P15 (p) S03-P16
(q) S03-P17 (r) S03-P18 (s) S03-P19 (t) S03-P20

Figure E.7: Sample images of the observations to the wire acquired from the theodolite position S03.

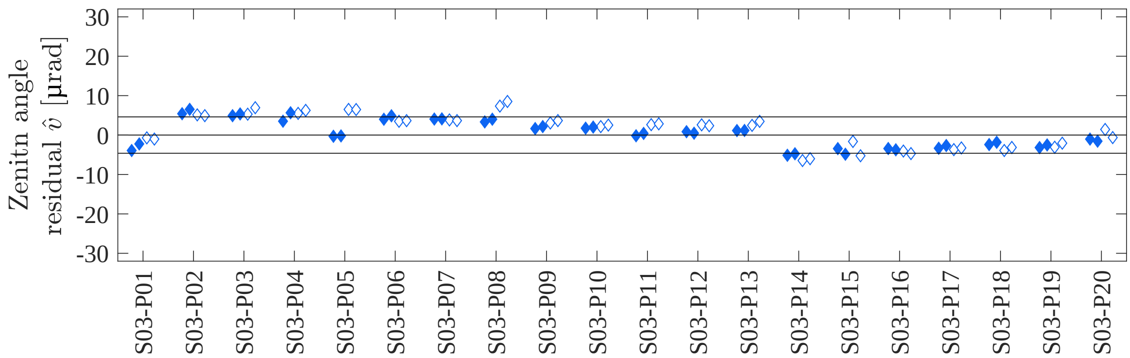

Figure E.8: Residuals of the zenith angle observations for sequential points on the wire observed from the theodolite position S03.

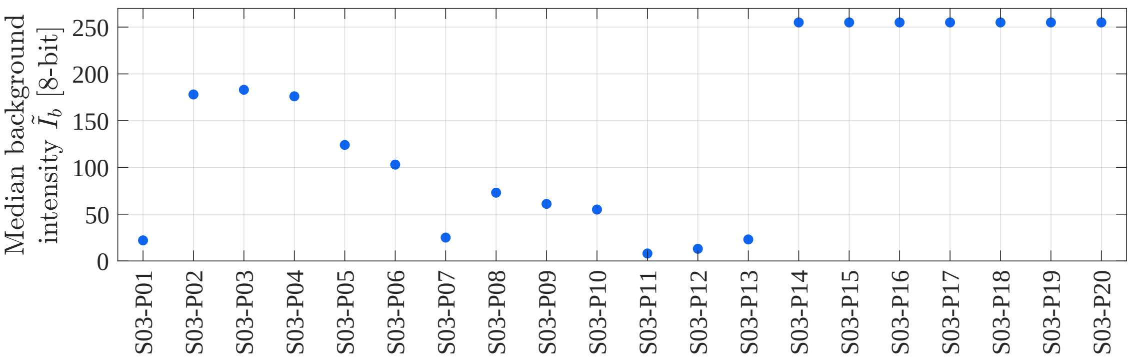

Figure E.9: Median of the background intensities in the proximity of the wire. The values correspond to the sample images in Figure E.7, acquired from the theodolite position S03.

Remarks

The performance of the wire detection algorithm exhibits excellent robustness in the case of the observations from the theodolite position S03. It is obvious that although the background intensities vary from the minimum to the maximum possible values (Figure E.9), the zenith angle residuals do not demonstrate significant biases with respect to the 95 % confidence interval that correspond to the specified precision of the employed theodolite (black horizontal lines in Figure E.8).

Despite the good performance of the algorithm, it is still noticeable that the two larger changes in the background intensity, observed for the pairs of images (S03-P01, S03-P02) and (S03-P13, S03-P14) are in agreement with the two larger changes in the residuals. It is also interesting to notice that although both the aforementioned two larger changes in the background intensities have the same sign (low to high intensity value), the corresponding changes in the residuals are not coherent.

E.4 Theodolite position S04

Table E.4: Parameter values of the wire detection algorithm for the theodolite position S04.

Target	# shots	Std shot [pixel]	Shutter [ms]	Gain	Hz direction [°]	Zen angle [°]
S04-P01	5	0.1	150	150	29.2237	110.0136
S04-P02	5	0.1	150	150	28.4352	109.9599
S04-P03	5	0.1	150	150	27.5942	109.8987
S04-P04	5	0.1	150	150	26.7801	109.8357
S04-P05	5	0.1	150	150	25.9461	109.7672
S04-P06	5	0.1	150	150	25.1132	109.6950
S04-P07	5	0.1	150	150	24.2867	109.6190
S04-P08	5	0.1	150	150	23.3858	109.5317
S04-P09	5	0.1	150	150	22.6429	109.4564
S04-P10	5	0.1	150	150	21.8053	109.3682
S04-P11	5	0.1	150	150	20.9880	109.2783
S04-P12	5	0.1	150	150	20.1687	109.1843
S04-P13	5	0.1	150	150	19.3359	109.0847
S04-P14	5	0.1	150	150	18.5063	108.9819
S04-P15	5	0.1	150	150	17.6637	108.8736
S04-P16	5	0.1	150	150	16.8653	108.7670
S04-P17	5	0.1	150	150	16.0073	108.6501
S04-P18	5	0.1	150	150	15.3372	108.5541
S04-P19	5	0.1	150	150	14.4456	108.4234
S04-P20	5	0.1	150	150	13.5455	108.2873
	Focus [step]	**Min #pts**	**HW ROI [pixel]**	**HH ROI [pixel]**	**Canny thres [8-bit]**	**Max resid [pixel]**
S04-P01	102400	120	100	50	150	5
S04-P02	102550	120	100	50	150	5
S04-P03	102750	120	100	50	150	5
S04-P04	103100	120	100	50	150	5
S04-P05	103350	120	100	50	150	5
S04-P06	103700	120	100	50	150	5
S04-P07	103900	120	100	50	150	5
S04-P08	104350	120	100	50	150	5
S04-P09	104700	120	100	50	150	5
S04-P10	105000	120	100	50	150	5
S04-P11	105350	120	100	50	150	5
S04-P12	105850	120	100	50	150	5
S04-P13	105900	120	100	50	150	5
S04-P14	106300	120	100	50	150	5
S04-P15	107150	120	100	50	150	5
S04-P16	107600	120	100	50	150	5
S04-P17	107900	120	100	50	100	5
S04-P18	108300	120	100	50	100	5
S04-P19	108800	120	100	50	100	5
S04-P20	109350	120	100	50	100	5

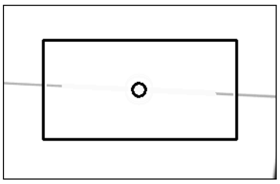
(a) S04-P01

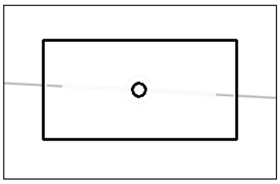
(b) S04-P02

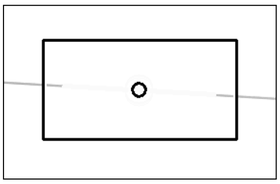
(c) S04-P03

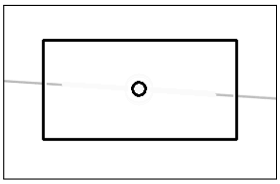
(d) S04-P04

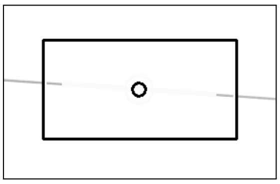
(e) S04-P05

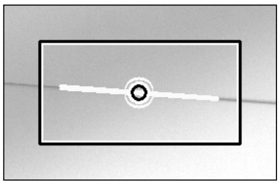
(f) S04-P06

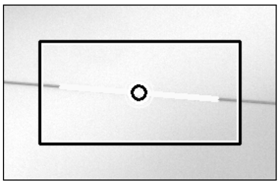
(g) S04-P07

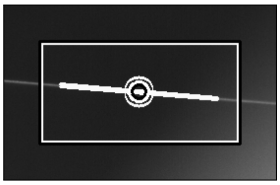
(h) S04-P08

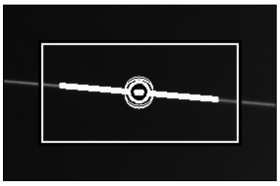
(i) S04-P09

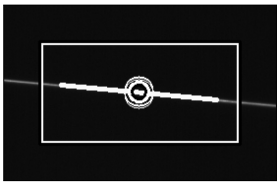
(j) S04-P10

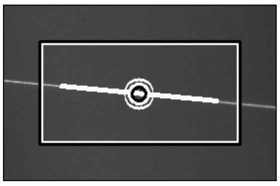
(k) S04-P11

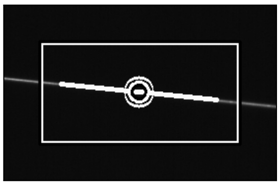
(l) S04-P12

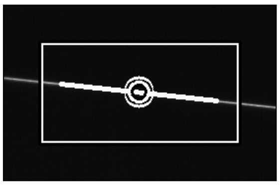
(m) S04-P13

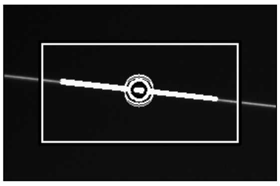
(n) S04-P14

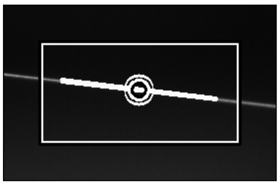
(o) S04-P15

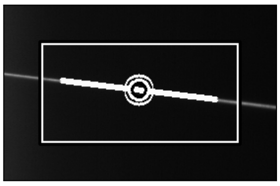
(p) S04-P16

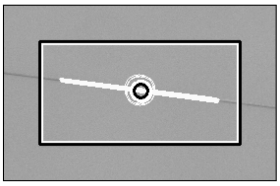
(q) S04-P17

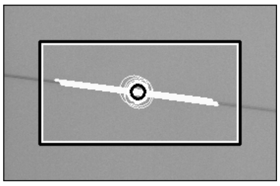
(r) S04-P18

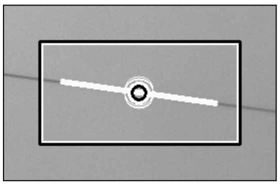
(s) S04-P19

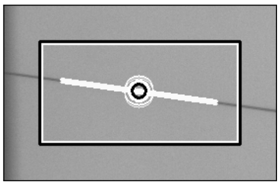
(t) S04-P20

Figure E.10: Sample images of the observations to the wire acquired from the theodolite position S04.

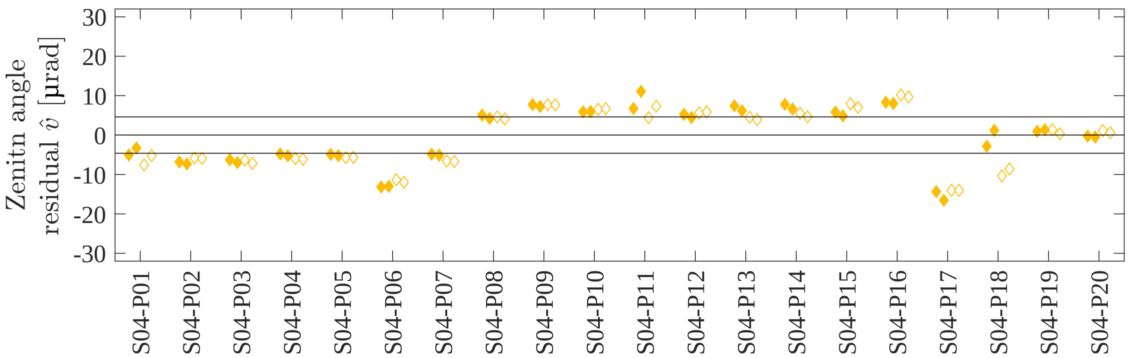

Figure E.11: Residuals of the zenith angle observations for sequential points on the wire observed from the theodolite position S04.

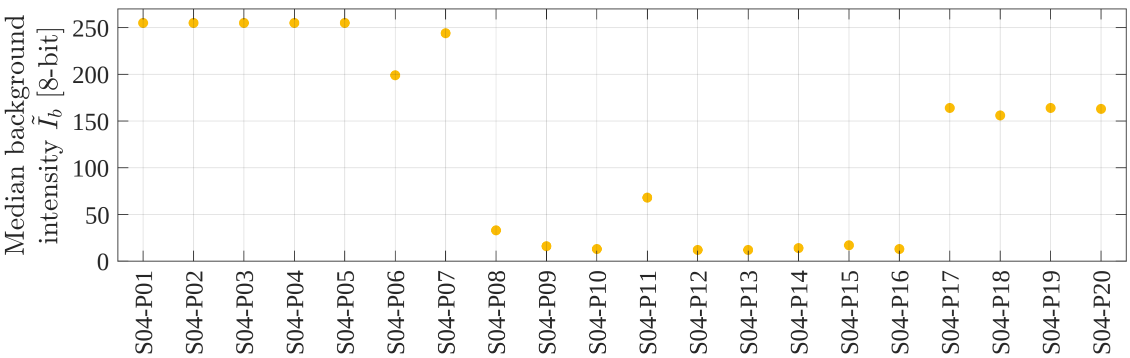

Figure E.12: Median of the background intensities in the proximity of the wire. The values correspond to the sample images in Figure E.10, acquired from the theodolite position S04.

Remarks

The comparison of Figures E.11 and E.12 verifies the correspondence between changes in the residuals and in the background intensities that we have already presented for the other theodolite positions. In this case, we can observe only one exception for the pair of images (S04-P17, S04-P18), in which a large change in the residuals does not correspond to an abrupt change for the respective background intensities.

E.5 Concluding remarks

In conclusion, there is a strong indication for a correlation between the magnitude of the residuals of the zenith angle observations to the wire and the corresponding background intensity values. The available data surely suggest an accordance, however, most probably these data are not adequate to identify a quantitative correlation. In most of the cases, the wire detection algorithm introduced a bias to the zenith angle observation, which is relevant either to the light conditions or to the background intensity. In some cases, the bias appears to be caused by the angle of incidence between the light rays that illuminate the wire and the optical axis of the camera, while in other cases the bias is caused by the contrast between the depicted wire and the background intensities.

This outcome is expected for optical measurements, especially for measurements based on passive optical systems. The accuracy and the robustness of the image detection algorithm for the wire observations is expected to be improved if a light source that is coaxial to the camera direction will be used.

Finally, the findings of this comparison are in an immediate compliance with the results of the experimental evaluation of the wire detection algorithm, as presented in Chapter 3, in which we demonstrated the influence that the light conditions and the background intensities have on the quality of the observations.

Appendix F

Parameter values and sample images of the circle detection algorithm for the micro-triangulation network

This appendix contains the input values of the *circle detection algorithm* parameters, sample images of the observations to the spherical targets from each theodolite position and the corresponding Canny edge images for the micro-triangulation measurement that took place in the metrology room on April 7, 2017 (see Chapter 5). In the following sample images, we observe intense reflections of the ceiling lights on the ceramic spheres that impose small values for the *Shutter* and *Gain* parameters. As a result, a large shadow appears on the lower part of the spheres, reducing the effective measured circumference. The poor contrast between the upper part of the spheres and the background also causes difficulties to the circle detection algorithm. To overcome the poor contrast, pieces of black paper were used as a background to the spherical targets. Diffusers on the metrology room light bodies or a light source that is coaxial to the camera direction will potentially enhance the performance of the circle detection algorithm.

F.1 Theodolite position S01

Table F.1: Input values of the circle detection parameters for the theodolite position S01.

Target	# shots	Std shot [pixel]	Shutter [ms]	Gain	Hz direction [°]	Zen angle [°]
S01-T01	5	0.1	100	150	34.1874	135.7099
S01-T02	5	0.1	100	150	49.2599	128.2513
S01-T03	5	0.1	100	150	31.3639	119.8419
S01-T04	5	0.1	100	150	21.9964	122.0703
S01-T05	5	0.1	100	150	35.8039	124.7541
S01-T06	5	0.1	100	150	29.2526	122.1638
Target	**Focus [step]**	**Min #pts**	**Max resid [pixel]**	**Min rad [pixel]**	**Max rad [pixel]**	**Canny thres [8-bit]**
S01-T01	81300	700	1	177	178	100
S01-T02	96450	500	1	153	154	100
S01-T03	114450	400	1	123	124	100
S01-T04	109800	400	1	131	133	100
S01-T05	93050	500	1	159	160	100
S01-T06	99500	400	1	148	150	100

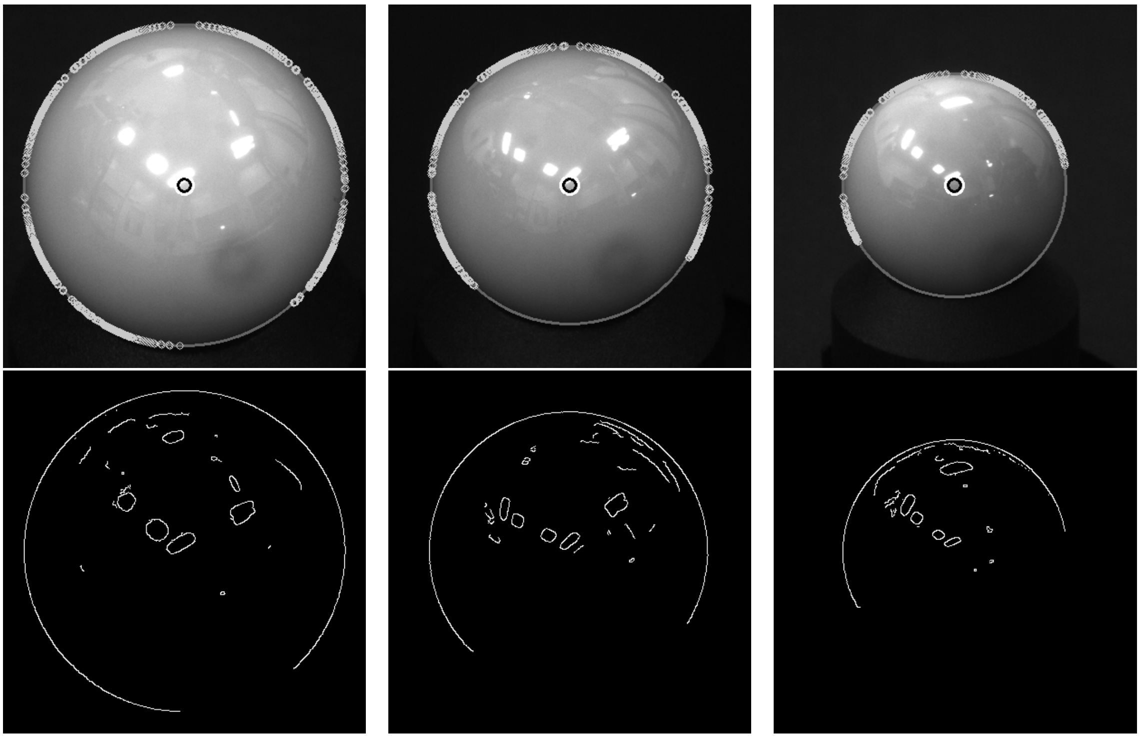

(a) S01-T01 **(b)** S01-T02 **(c)** S01-T03

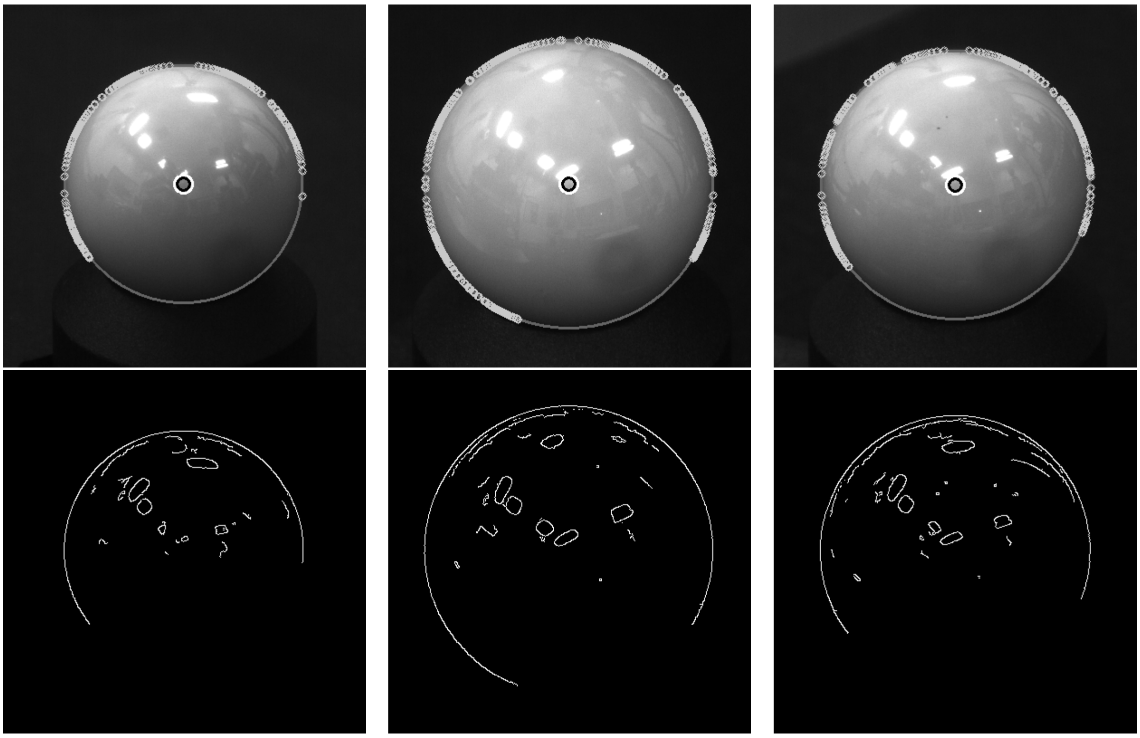

(d) S01-T04 **(e)** S01-T05 **(f)** S01-T06

Figure F.1: Sample images of the observations to the spherical targets and the corresponding Canny edge points of the circle detection algorithm, acquired from the theodolite position S01.

F.2 Theodolite position S02

Table F.2: Input values of the circle detection parameters for the theodolite position S02.

Target	# shots	Std shot [pixel]	Shutter [ms]	Gain	Hz direction [°]	Zen angle [°]
S02-T01	5	0.1	100	150	2.0979	131.6874
S02-T02	5	0.1	100	150	21.8767	138.3347
S02-T03	5	0.1	100	150	31.2385	123.2176
S02-T04	5	0.1	100	150	20.7184	121.3996
S02-T05	5	0.1	100	150	17.2099	127.0078
S02-T06	5	0.1	100	150	19.3147	122.8337

Target	Focus [step]	Min #pts	Max resid [pixel]	Min rad [pixel]	Max rad [pixel]	Canny thres [8-bit]
S02-T01	89700	400	1	165	166	100
S02-T02	76450	500	2	185	186	100
S02-T03	107550	400	1	136	137	100
S02-T04	111350	400	1	129	131	100
S02-T05	87600	450	1	168	169	100
S02-T06	98200	500	1	152	153	100

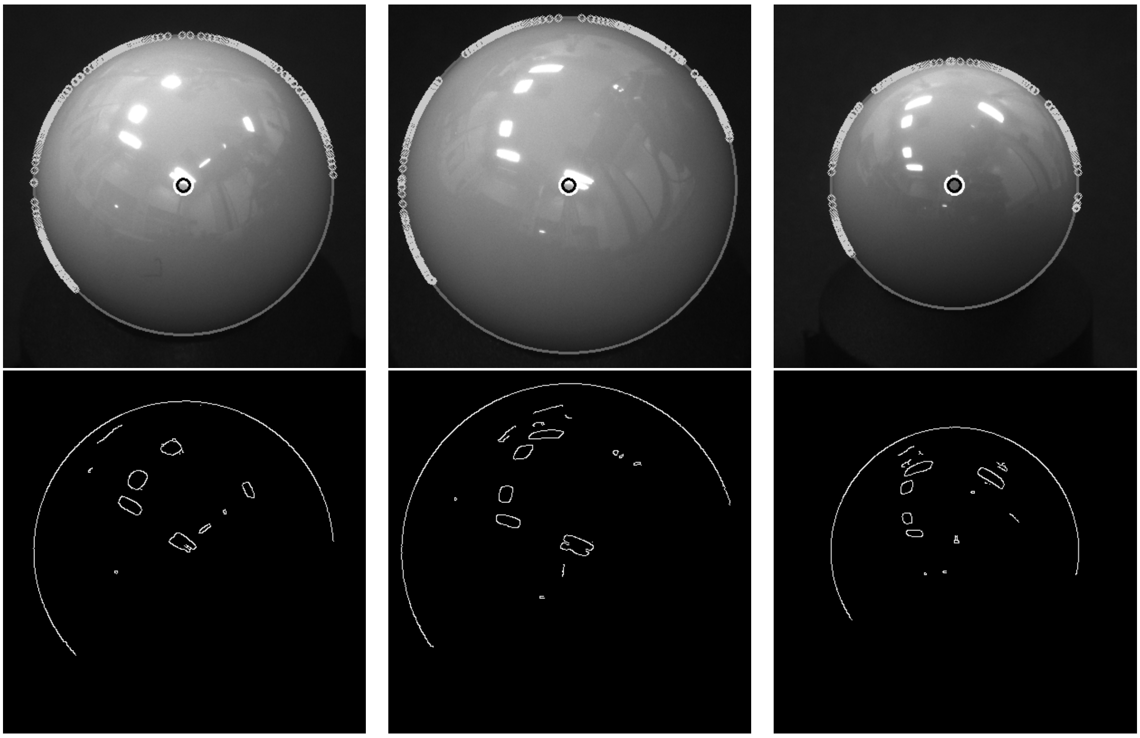

(a) S02-T01 (b) S02-T02 (c) S02-T03

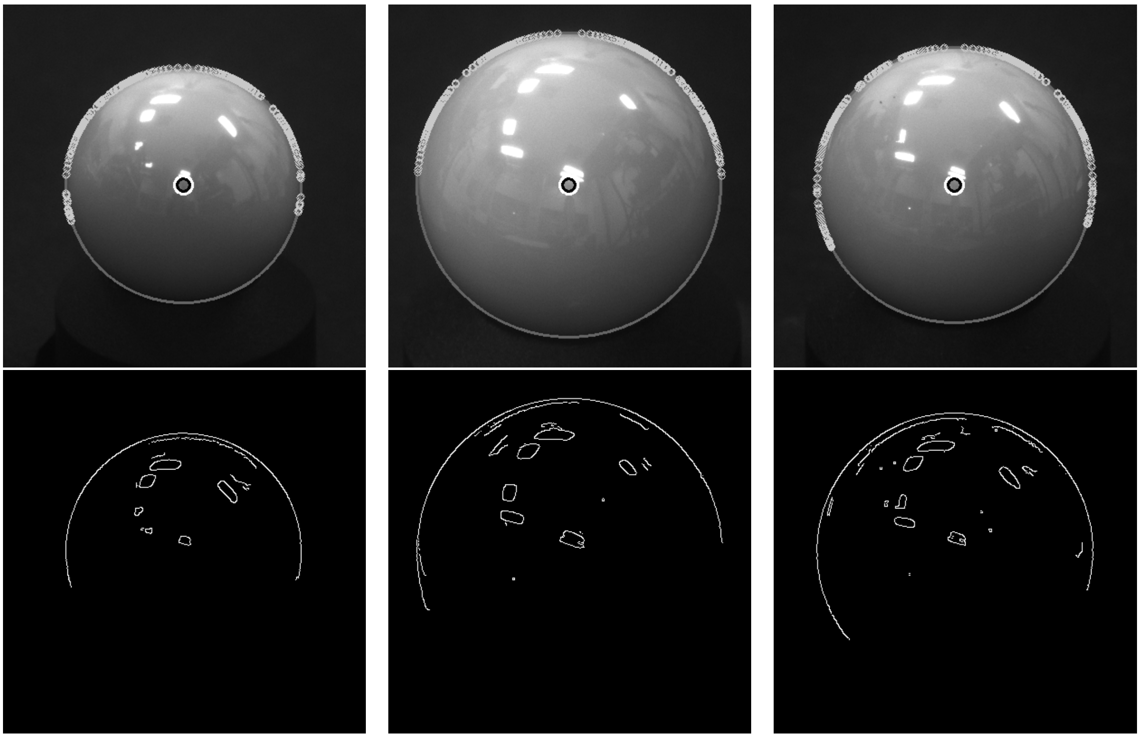

(d) S02-T04 (e) S02-T05 (f) S02-T06

Figure F.2: Sample images of the observations to the spherical targets and the corresponding Canny edge points of the circle detection algorithm, acquired from the theodolite position S02.

F.3 Theodolite position S03

Table F.3: Input values of the circle detection parameters for the theodolite position S03.

Target	# shots	Std shot [pixel]	Shutter [ms]	Gain	Hz direction [°]	Zen angle [°]
S03-T01	5	0.1	100	150	26.6709	116.4314
S03-T02	5	0.1	150	150	14.9921	117.8252
S03-T03	5	0.1	100	150	21.4296	128.5740
S03-T04	5	0.1	100	150	34.0173	126.1238
S03-T05	5	0.1	100	150	22.9112	117.1693
S03-T06	5	0.1	100	150	26.8966	119.6077

Target	Focus [step]	Min #pts	Max resid [pixel]	Min rad [pixel]	Max rad [pixel]	Canny thres [8-bit]
S03-T01	122000	300	1	111	112	100
S03-T02	118650	350	1	116	117	100
S03-T03	95800	500	1	155	156	100
S03-T04	101150	450	1	147	148	100
S03-T05	112100	400	1	128	129	100
S03-T06	106200	500	1	138	139	100

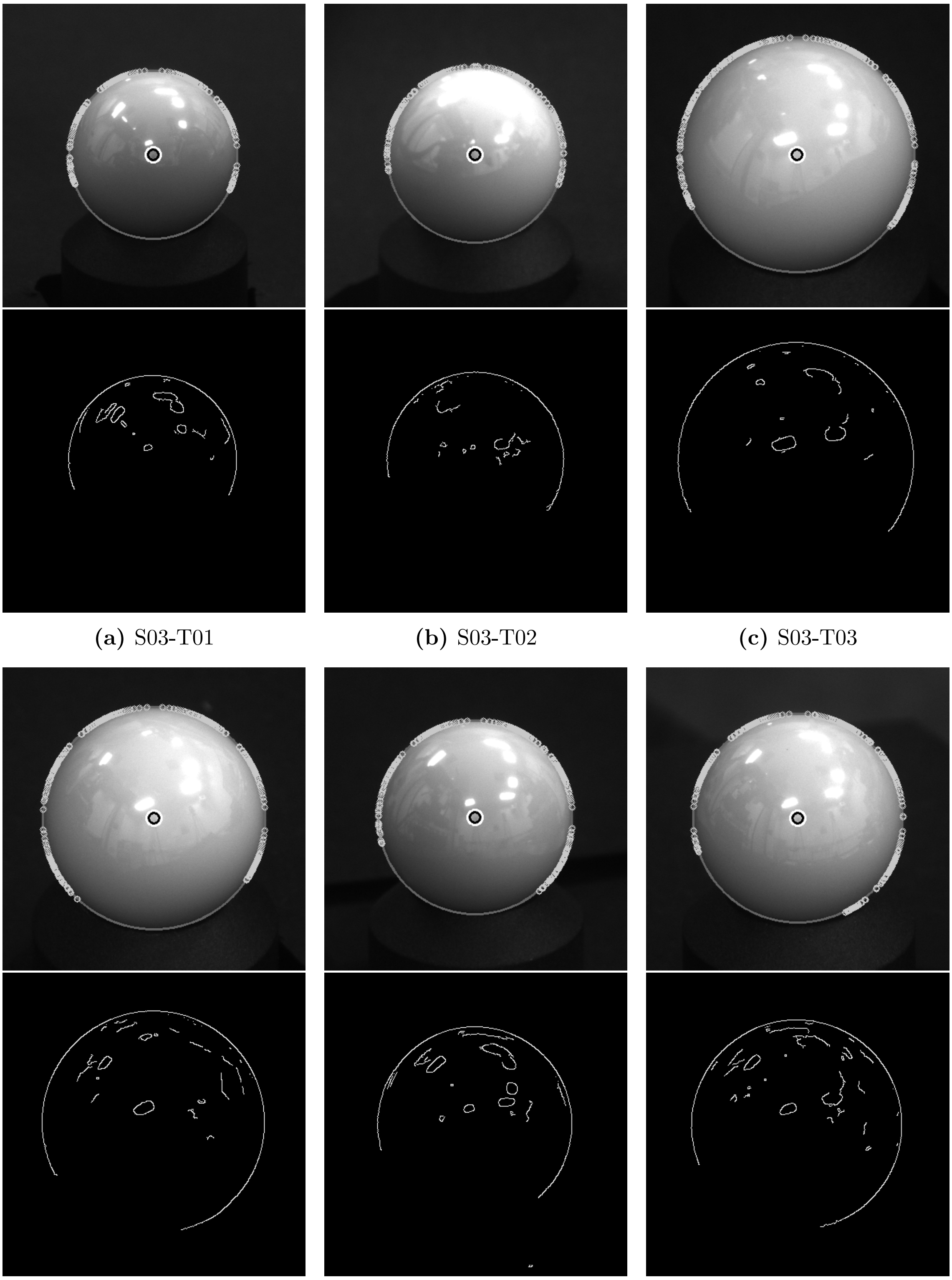

(a) S03-T01 (b) S03-T02 (c) S03-T03

(d) S03-T04 (e) S03-T05 (f) S03-T06

Figure F.3: Sample images of the observations to the spherical targets and the corresponding Canny edge points of the circle detection algorithm, acquired from the theodolite position S03.

F.4 Theodolite position S04

Table F.4: Input values of the circle detection parameters for the theodolite position S04.

Target	# shots	Std shot [pixel]	Shutter [ms]	Gain	Hz direction [°]	Zen angle [°]
S04-T01	5	0.1	100	150	29.3571	117.0531
S04-T02	5	0.1	100	150	18.0999	115.7007
S04-T03	5	0.1	100	150	8.9958	124.1137
S04-T04	5	0.1	100	150	20.2409	126.8535
S04-T05	5	0.1	100	150	21.3450	116.2669
S04-T06	5	0.1	100	150	20.6886	119.0617

Target	Focus [step]	Min #pts	Max resid [pixel]	Min rad [pixel]	Max rad [pixel]	Canny thres [8-bit]
S04-T01	120350	350	1	112	114	100
S04-T02	123250	300	1	107	108	100
S04-T03	105000	500	1	138	140	100
S04-T04	99100	500	1	148	149	100
S04-T05	114150	400	1	123	124	100
S04-T06	107100	500	1	135	136	100

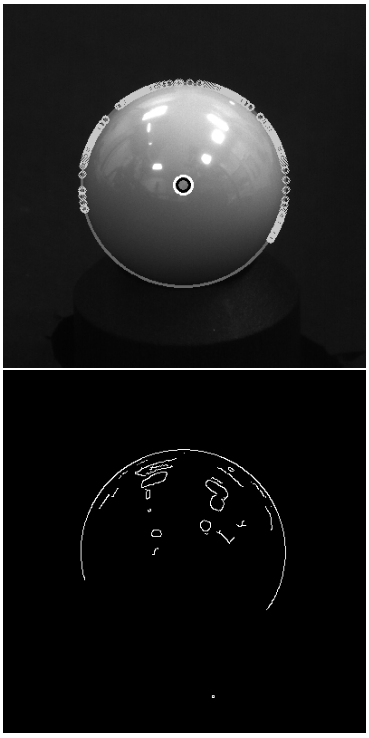

(a) S04-T01

(b) S04-T02

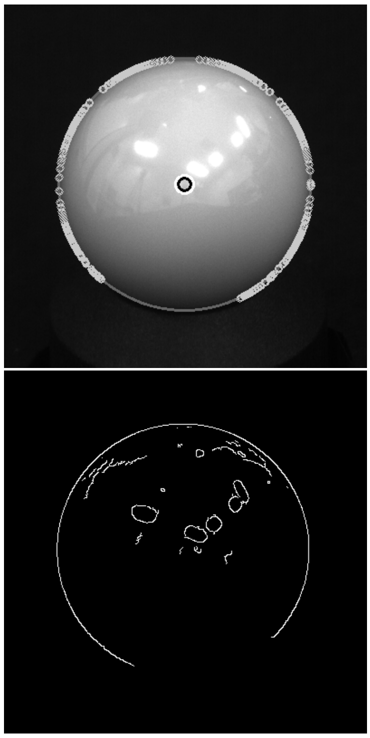

(c) S04-T03

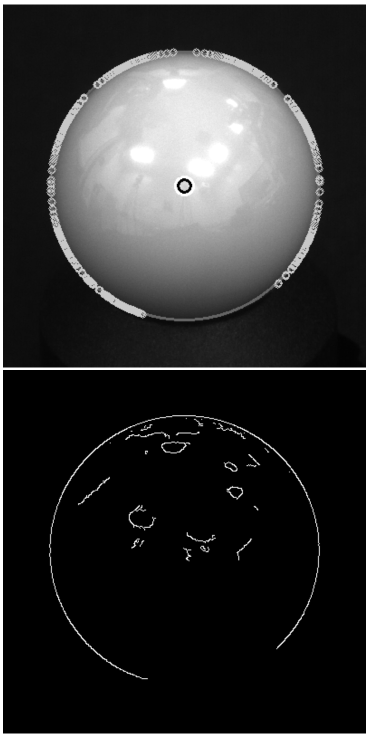

(d) S04-T04

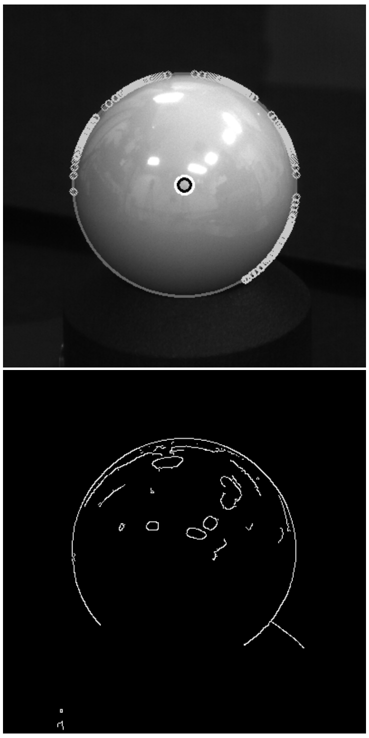

(e) S04-T05

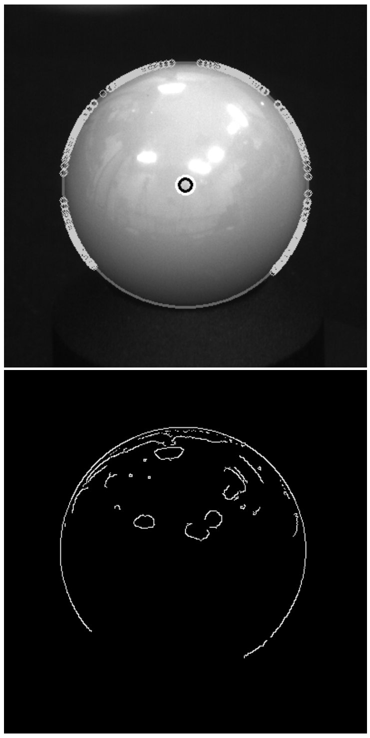

(f) S04-T06

Figure F.4: Sample images of the observations to the spherical targets and the corresponding Canny edge points of the circle detection algorithm acquired, from the theodolite position S04.